



**This electronic thesis or dissertation has been
downloaded from Explore Bristol Research,
<http://research-information.bristol.ac.uk>**

Author:
Slastanova, Anna

Title:
Polymer/surfactant Interactions at the Air-water Interface
From Synergy to Competition

General rights

Access to the thesis is subject to the Creative Commons Attribution - NonCommercial-No Derivatives 4.0 International Public License. A copy of this may be found at <https://creativecommons.org/licenses/by-nc-nd/4.0/legalcode>. This license sets out your rights and the restrictions that apply to your access to the thesis so it is important you read this before proceeding.

Take down policy

Some pages of this thesis may have been removed for copyright restrictions prior to having it been deposited in Explore Bristol Research. However, if you have discovered material within the thesis that you consider to be unlawful e.g. breaches of copyright (either yours or that of a third party) or any other law, including but not limited to those relating to patent, trademark, confidentiality, data protection, obscenity, defamation, libel, then please contact collections-metadata@bristol.ac.uk and include the following information in your message:

- Your contact details
- Bibliographic details for the item, including a URL
- An outline nature of the complaint

Your claim will be investigated and, where appropriate, the item in question will be removed from public view as soon as possible.

Polymer/surfactant Interactions at the Air-water Interface: From Synergy to Competition

Anna Slastanova



A dissertation submitted to the University of Bristol in accordance with the requirements for award of the degree of

Doctor of Philosophy

in the Faculty of Science, School of Chemistry

September 2019

Word count: 67,841

Abstract

Understanding the adsorption behaviour of polymer/surfactant mixtures at the air-water interface is of fundamental importance and has direct relevance to a variety of practical applications. Polymer/surfactant systems comprising neutral amphiphilic PEG-g-PVAc copolymer (consisting of a hydrophilic polyethylene glycol backbone with hydrophobic polyvinyl acetate grafts) with anionic sodium dodecylsulfate (SDS), cationic dodecyltrimethylammonium bromide (DTAB) and non-ionic dodecylpentaethyleneglycol ether (C₁₂E₅) were investigated at the air-water interface by a combination of dynamic and equilibrium surface tension, neutron and X-ray reflectivity (NR and XRR), and preliminary foam behaviour tests.

Surface tension data analysis revealed a transition from synergistic adsorption at low surfactant concentrations to a competitive adsorption behaviour with increasing surfactant concentration. The effect of surfactant headgroup characteristics (charge and size), and the effect of polymer architecture (PVAc graft length, number and ratio) was linked to the polymer/surfactant adsorption behaviour. Complementary NR and XRR measurements allowed elucidation of the interfacial composition and structure, revealing ~ 2 nm thick layer at the air-water interface (depending on the polymer/surfactant concentrations). The polymer was depleted from the interface with increasing surfactant concentration and formed a weakly associated layer “hanging” proximally to the interface. The thickness of this polymer layer, as well as the overall composition of the interfacial layer, played an important role in enhancing foam stability, and strongly depended on the surfactant and polymer characteristics.

Furthermore, the adsorption and complexation behaviour of anionic SDS and cationic surfactant vesicles, formed from double-tailed diethoxyester dimethylammonium chloride (DEEDMAC), were investigated in bulk and at interfaces. Dynamic light scattering and ζ -potential studies, as well as imaging techniques, indicated strong complexation of SDS/DEEDMAC in bulk. Finally, DEEDMAC bilayers were formed on mica *via* vesicle rupture, and the interactions with SDS were studied using XRR and surface force apparatus (SFA) at the solid-liquid interface, where a pronounced increase in layer thickness was observed assigned to a formation of alternating DEEDMAC/SDS strongly-interacting layers at the interface.



*“Take the Adventure, heed the call, now ere the irrevocable moment passes!’
‘Tis but a banging of the door behind you, a blithesome step forward, and you
are out of the old life and into the new!”*

— Kenneth Grahame, The Wind in the Willows

To Gerard and our adventures

Acknowledgments

Firstly, I would like to thank my supervisors Wuge Briscoe, Eric Robles, Meng Chen and Mauro Vaccaro for their involvement in the project and many stimulating discussions and guidance throughout my studies, as well as their support outside of work. Furthermore, I would like to thank the beamline scientists who I had the pleasure to meet and work with: Richard, Becky, Tom, Jonathan and Oier; and everyone who came to my experiments, took care of Leeroy and did not mind losing sleep over Polymers A and B.

While acknowledging the help I have received, I ought to mention Judith and Alan from the Wolfson Bioimaging Centre, James for his help with mica silvering, and Paul and Craig for helping with running and analysing NMR. This thanks extends to the members of the university facility teams, namely Jon and Steve, who were always happy to give me the Krüss key and have a quick chat; and Phil and Adam for their always cheerful ‘morning, y’alright?’.

I’m indebted to my parents and brother for their support while growing up and encouragement to chase my dreams whatever they were. I would not be able to achieve my ambitions without the Briscoe past and present members: from the starting line (Tim, Charlotte, Chris, Kathrin, Alex, Julia, Bea, Lizzie and Alex) to the finish line (Laura, Sarah, Patryk, Nick, Michael, Bhavesh and Gang). My special thanks goes to Liangzhi, Luisa, and Silvia who all supported me when I most needed it; and to my amazing office mates Dajana, Lauren and Holly for sharing tea and biscuits while seemingly solving all of our problems.

I cannot forget to mention my friends from outside of the research group, namely Chris, John & K and Steve & Fiona, who have always lent more than just a helping hand; everyone from Rag Morris and Bedminster Belles for providing much needed distraction from the never-ending data fitting, and Phill for introducing me to all the good things.

Finally, I would like to thank my partner Gerard, for always being my rock(star). The support, confidence and love he has given me, as well as all the cooking, is what keeps me going chasing those dreams. I truly would not have been where I am without him.

Thank you one and all.

Author's Declaration

I declare that the work in this dissertation was carried out in accordance with the requirements of the University's *Regulations and Code of Practice for Research Degree Programmes* and that it has not been submitted for any other academic award. Except where indicated by specific reference in the text, the work is the candidate's own work. Work done in collaboration with, or with the assistance of, others, is indicated as such. Any views expressed in the dissertation are those of the author.

SIGNED: DATE:.....

Publications

The following paper was authored during the course of this study, and forms the basis of Chapter 3:

*Chapter 3: A. Slastanova, R.A. Campbell, T. Snow, E. Mould, P. Li, R.J.L. Welbourn, M. Chen, E. Robles, W.H. Briscoe, *Synergy, competition, and the “hanging” polymer layer: Interactions between a neutral amphiphilic ‘tardigrade’ co-polymer with an anionic surfactant at the air-water interface*, Journal of Colloid and Interface Science, 2020, **561**, 181-194*

The following paper is finalised for submission to Langmuir:

*Chapter 4: A. Slastanova, R.A. Campbell, L. Islas, R.J.L. Welbourn, J.R.P. Webster, M. Vaccaro, M. Chen, E. Robles, W.H. Briscoe, *Interfacial structures and interactions of a neutral amphiphilic ‘tardigrade’ co-polymer with cationic surfactant at the air-water interface**

The following manuscript is in preparation:

*Chapter 5: A. Slastanova, R.A. Campbell, M. Vaccaro, M. Chen, E. Robles, W.H. Briscoe *Interfacial structures and interactions of a neutral amphiphilic ‘tardigrade’ co-polymer with non-ionic surfactant at the air-water interface**

Following papers were co-authored during the course of the study:

B. Sironi, T. Snow, C. Redeker, A. Slastanova, O. Bikondoa, T. Arnold, J. Klein, W.H. Briscoe, Structure of lipid multilayers via drop casting of aqueous liposome dispersions, *Soft Matter*, 2016, **17**, 3877-3887

L. Zhou, L. Fox, M. Wlodek, L. Islas, A. Slastanova, E. Robles, O. Bikondoa, R. Harniman, N. Fox, M. Cattelan, W.H. Briscoe, Surface structure of few layer graphene, *Carbon*, 2018, **136**, 255-261

M. Wlodek, A. Slastanova, L.J. Fox, N. Taylor, O. Bikondoa, M. Szuwarzynski, M. Kolasinska-Sojka, P. Warszynski, W.H. Briscoe, Structural evolution of supported lipid bilayers intercalated with quantum dots, *Journal of Colloid and Interface Science*, 2020, **562**, 409-417

L.J. Fox, A. Slastanova, N. Taylor, M. Wlodek, O. Bikondoa, R.M. Richardson, W.H. Briscoe, Interactions between PAMAM dendrimers and DOPC lipid multilayers: Membrane thinning and structural disorder, *Biochimica et Biophysica Acta – General Subjects*, 2020 (article in press)

Table of Contents

1	Introduction.....	1
1.1	Project Motivation.....	1
1.2	Air-water interface	3
1.2.1	Surface tension and surfactant adsorption	3
1.2.2	Micellisation	4
1.3	Polymer/surfactant interactions.....	6
1.3.1	Neutral polymers.....	7
1.3.2	Oppositely charged complexes	9
1.4	Foams	10
1.4.2	Foam generation.....	13
1.4.3	Foam destabilisation	14
1.5	Polymers and surfactants studied	15
1.5.1	PEG and PVAc	15
1.5.2	PEG-g-PVAc co-polymers.....	16
1.5.3	DEEDMAC vesicles	17
1.6	Thesis outline	18
1.7	References	19
2	Experimental methods.....	27
2.1	Surface tension	27
2.2	X-rays and neutrons	31
2.2.1	X-Ray and neutron reflectivity	32
2.2.2	XRR and NR experimental set-up	37
2.2.3	Data fitting	41
2.3	References	46

3 Synergy, competition, and the “hanging” polymer layer: Interactions between a neutral amphiphilic ‘tardigrade’ co-polymer with an anionic surfactant at the air-water interface	51
3.1 Introduction	51
3.2 Methods.....	54
3.2.1 Materials	54
3.2.2 Surface tension measurements	54
3.2.3 Neutron reflectivity (NR).....	55
3.2.4 Surface excess calculation	56
3.2.5 Foaming measurements	57
3.3 Results	57
3.3.1 Equilibrium and dynamic surface tension: From synergistic cooperative adsorption to SDS-Polymer competition	57
3.3.2 NR results: Interfacial layer composition and structure	62
3.3.3 Foaming behaviour of the polymer/surfactant mixtures: The “hanging” polymer layer affects the foamability and foam stability.....	75
3.4 Conclusions	79
3.5 References	81
4 Interfacial structures and interactions of a neutral amphiphilic ‘tardigrade’ co-polymer with cationic surfactant at the air-water interface	87
4.1 Introduction	87
4.2 Methods.....	89
4.2.1 Materials	89
4.2.2 Surface tension measurements	90
4.2.3 Neutron reflectivity (NR).....	91
4.2.4 Foaming measurements	92
4.3 Results	92
4.3.1 Equilibrium and dynamic surface tension.....	92
4.3.2 Interfacial layer composition <i>via</i> surface excess evaluation from NR low <i>Q</i> data	95

4.3.3	DTAB/PEG-g-PVAc interfacial layer structure from NR	97
4.3.4	Foam behaviour of the polymer/surfactant mixtures	105
4.4	Conclusions	108
4.5	References	110
5	Interfacial structures and interactions of a neutral amphiphilic ‘tardigrade’ co-polymer with non-ionic surfactant at the air-water interface	115
5.1	Introduction	115
5.2	Methods	117
5.2.1	Materials	117
5.2.2	Surface tension measurements	118
5.2.3	Neutron reflectivity (NR).....	118
5.2.4	Foaming measurements	119
5.3	Results	119
5.3.1	Equilibrium and dynamic surface tension measurements.....	119
5.3.2	Neutron reflectivity results	122
5.3.3	Foaming behaviour of the polymer/surfactant mixtures	130
5.4	Conclusions	133
5.5	References	134
6	Effect of polymer architecture on the interfacial structures and interactions between neutral amphiphilic comb co-polymers and surfactants at the air-water interface: XRR study	137
6.1	Introduction	137
6.1.1	Polymer/surfactant interactions	137
6.1.2	Polymer molecular structure (<i>i.e.</i> Polymer A vs Polymer B)	138
6.1.3	XRR and NR: A brief comparison.....	139
6.2	Methods.....	140
6.2.1	Materials	140
6.2.2	Surface tension.....	141

6.2.3	X-ray reflectivity (XRR).....	141
6.3	Results	142
6.3.1	Surface tension.....	142
6.3.2	Interfacial layer structure determined from XRR data fitting.....	145
6.4	Conclusions	167
6.4.1	Surface tension.....	167
6.4.2	Interfacial layer structure determined by XRR.....	167
6.5	References	169
7	Interactions of Anionic SDS with Cationic DEEDMAC Vesicles at Interfaces and Under Confinement	173
7.1	Introduction	173
7.1.1	Vesicle formation.....	174
7.2	Methods.....	176
7.2.1	Materials	176
7.2.2	Vesicle preparation	177
7.2.3	DLS and ζ -potential measurements	177
7.2.4	Surface Tension	178
7.2.5	XRR at solid-liquid and air-water interfaces	178
7.2.6	Surface force apparatus (SFA).....	178
7.2.7	Transmission electron microscopy (TEM)	187
7.2.8	Confocal Microscopy.....	189
7.3	Results	190
7.3.1	DLS and ζ -potential	190
7.3.2	Surface Tension	193
7.3.3	XRR at air-water interface	194
7.3.4	DEEDMAC/SDS adsorption at solid-liquid interface: XRR study	196
7.3.5	DEEDMAC/SDS adsorption at solid-liquid interface: SFA study	198

7.3.6	Transmission Electron Microscopy (TEM) and confocal microscopy	207
7.4	Conclusions	216
7.4.1	DEEDMAC/SDS complexation in bulk	216
7.4.2	DEEDMAC/SDS complexation at air-water interface	216
7.4.3	DEEDMAC/SDS complexation at solid-liquid interface	216
7.5	References	217
8	Conclusions and future work.....	225
8.1	Conclusions	225
8.1.1	PEG- <i>g</i> -PVAc polymer/surfactant mixtures	225
8.1.2	DEEDMAC/SDS complexes	227
8.2	Future work	228
8.2.1	PEG- <i>g</i> -PVAc polymer/surfactant mixtures	228
8.2.2	DEEDMAC/SDS complexes	229
8.3	References	230
	Appendix.....	233
A.	Polymer GPC	233
B.	NMR.....	234
C.	Supplementary material for Chapter 3	236
D.	Supplementary material for Chapter 4.....	244
E.	Supplementary material for Chapter 4	245
F.	Supplementary material for Chapter 7.....	246

List of figures

Figure 1.1 A schematic of the forces acting between water molecules in bulk and at the air-water interface. Due to the imbalance the molecules experience at the air-water interface, there is an overall pull downwards in attempt to minimise the surface area of the unfavourable interactions.	3
Figure 1.2 Schematic drawing of different processes involved in micellisation of pure surfactant, pure polymer and surfactant/polymer mixed system.	6
Figure 1.3 A schematic representation of the different length scales involved within a system of neighbouring foam bubbles.	11
Figure 1.4 An analogy of the interfacial organisation of two surface active species at the air-water interface and when stabilising a foam bubble.	11
Figure 1.5 A representation of the formation of foam bubbles. The surfactants align at the air-water interface of a gas bubble as well as on the surface of the bulk liquid phase. A lamella structure stabilised by a layer of surfactants is then formed.	14
Figure 1.6 A representation of coarsening and coalescence destabilising processes within foam systems. Figure modified from [45].	15
Figure 2.1 a) schematic representation of a reflectivity experiment setup, where the X-ray or neutron beam hits the interface at θ_i and is reflected from any structured layer at the interface. A simulated XRR curve of a 30 nm film adsorbed at interface is shown in b), as R plotted vs Q. In black are shown Kiessig fringes typical for ordered thin films. The influence of roughness, σ , on the shape of typical XRR curve is demonstrated by comparison to the simulated curve of 30 nm thick film with higher σ (5 nm, compared to 0.5 nm in black).	34
Figure 2.2 Outline of the I07 beamline. Figure taken from [39].	38
Figure 2.3 Schematic of the FIGARO beamline, highlighting the main components. Figure taken from [61].	40
Figure 2.4 A schematic representation of the INTER beamline. Figure is taken from [63]. ...	41

Figure 3.1 Molecular structures (with corresponding schematics) of SDS and PEG-g-PVAc copolymer.54

Figure 3.2. a) Equilibrium surface tension γ vs. surfactant or polymer concentration (in their respective cmc and cac determined experimentally) using the Wilhelmy plate method. Four sets of data are shown for pure SDS (∇), pure polymer (O), and the polymer (0.2 \square and 2 cac \blacktriangle) mixed with SDS at different concentrations. Data points labelled 1-11 indicate specific polymer and surfactant concentrations. (b) The legend table lists the polymer and surfactant concentrations for the 11 dynamic surface tension curves, with the corresponding symbols for the plots in (a) and the corresponding numbers in (a), (c) and (d). The dynamic surface tension γ_d vs. the surface age τ is shown in (c), using the bubble pressure method. Curves 9-11 in (c) (5 cmc SDS) overlay with each other. (d) A bar chart showing the γ_d at $\tau \sim 10$ ms for curves 1-11, with the surface tension lowering $\Delta\gamma_d$ (γ_d at $\tau \sim 10$ ms - γ_d at $\tau \sim 4$ min). The error bars in all cases are determined as a standard deviation from an experimental error determined from 3 separate measurements.....58

Figure 3.3 The calculated Γ vs SDS concentration of mixed PEG-g-PVAc + SDS systems is shown. The Γ_{SDS} is shown in $\mu\text{mol m}^{-2}$ on the left axis and represented by the filled markers, and $\Gamma_{\text{PEG-g-PVAc}}$ is shown in mg m^{-2} on the right axis and represented by the empty markers. The dashed lines act as a guide to the eyes only.63

Figure 3.4 A summary of the thickness t , water volume fraction ϕ_{water} and polymer fraction $\phi_{\text{PEG-g-PVAc}}$ in a single-layer model used to fit the NR data of PEG-g-PVAc + SDS mixtures (O and \bullet for 0.2 and 2 cac polymer respectively). For comparison, the blue dashed lines represent the fitted values of 0.2 cac PEG-g-PVAc and 2 cac PEG-g-PVAc respectively. The data point with red outline represents the fitted value for 1.2 cmc pure SDS.65

Figure 3.5 Fitted NR data for 0.05 cmc SDS with 0.2 and 2 cac PEG-g-PVAc, with the fitted ρ profiles and schematic representation based on the fitted parameters. The data is colour coded as follows: red represents mixtures of PEG-g-PVAc and dSDS in D_2O , green represents mixtures of PEG-g-PVAc with hSDS in D_2O , blue represents mixtures of PEG-g-PVAc with dSDS in ACMW, and purple represents mixtures of PEG-g-PVAc with hSDS in ACMW. The error bars associated with the data points were determined from the data reduction, larger at higher Q values due to lower contrast between the solvent and sample. The solid lines show

the fitted curve, with the fitted parameters also shown, including thickness (t), solvent volume fraction (ϕ_{water}), and roughness of the layer (σ).68

Figure 3.6 Fitted NR data for 0.5 cmc SDS with 0.2 and 2 cac PEG-g-PVAc, with the fitted ρ profiles and schematic representation based on the fitted parameters. The data is colour coded as follows: red represents mixtures of PEG-g-PVAc and dSDS in D₂O, green represents mixtures of PEG-g-PVAc with hSDS in D₂O, blue represents mixtures of PEG-g-PVAc with dSDS in ACMW, and purple represents mixtures of PEG-g-PVAc with hSDS in ACMW. The error bars associated with the data points were determined from the data reduction, larger at higher Q values due to lower contrast between the solvent and sample. The solid lines show the fitted curve, with the fitted parameters also shown, including thickness (t), solvent volume fraction (ϕ_{water}), and roughness of the layer (σ).70

Figure 3.7 Fitted NR data for 5 cmc SDS with 0.2 and 2 cac PEG-g-PVAc, with the fitted ρ profiles and schematic representation based on the fitted parameters. The data is colour coded as follows: red represents mixtures of PEG-g-PVAc and dSDS in D₂O, green represents mixtures of PEG-g-PVAc with hSDS in D₂O, blue represents mixtures of PEG-g-PVAc with dSDS in ACMW, and purple represents mixtures of PEG-g-PVAc with hSDS in ACMW. The error bars associated with the data points were determined from the data reduction, larger at higher Q values due to lower contrast between the solvent and sample. The solid lines show the fitted curve, with the fitted parameters also shown, including thickness (t), solvent volume fraction (ϕ_{water}), and roughness of the layer (σ).72

Figure 3.8 A schematic representation of the polymer/surfactant adsorption behaviour at the air-water interface derived from the combination of dynamic surface tension and NR data. Top row: synergistic cooperative adsorption regime. Fully cooperative adsorption of the polymer/surfactant system at very low SDS concentration (0.05 cmc SDS + PEG-g-PVAc) at all timescales and as a fully mixed complex at the interface. Middle row: transition regime. SDS molecules adsorbed at the air-water interface first, followed by a secondary and much slower polymer adsorption towards the interface, forming a “hanging” polymer layer interacting mainly with the SDS headgroups at the interface, consistent with the data obtained for mixtures of 0.5 cmc SDS + PEG-g-PVAc. Bottom row: competitive adsorption regime: formation of SDS monolayer at the air-water interface followed by micellisation in the bulk and likely formation of polymer/SDS micelle complexes, consistent with data obtained for 5 cmc SDS + PEG-g-PVAc. The secondary adsorption of the polymer towards the interface can

be derived from the NR data fitting, as there is no influence of the polymer on the final surface tension data in the systems containing 5 cmc SDS.....74

Figure 3.9 Foaming data showing the: a) foam half-life time ($\tau_{FVS\ 50\%}$) which is a measure of foam stability, b) maximum foam volume ($V_{foam\ max}$) which is a measure of foamability, and c) initial average bubble radius ($R_{avg\ initial}$) showing the radius of the foam bubbles during the foam generation. The data in orange represents the pure SDS solutions at 3 concentrations, the data in blue represents data for the pure polymer at 2 concentrations. The mixed polymer/surfactant systems are shown in pale and dark purple for SDS with 0.2 cac PEG-g-PVAc and SDS with 2 cac PEG-g-PVAc respectively.....77

Figure 3.10 Macroscopic foaming behaviour data (overall foam volume) and foam bubble size recorded over a given period after foam generation are shown, comparing the pure 5 cmc SDS system (left column) to the mixed systems containing 5cmc SDS + 0.2 cac PEG-g-PVAc (middle column) and 5cmc SDS + 2 cac PEG-g-PVAc (right column). The bubble size is colour coded as follows: green is for smallest bubble radius, followed by blue, purple, pink and the largest bubbles are shown in white, with the scale bar shown representing 1 mm.....79

Figure 4.1 Molecular structures (with corresponding schematics) of PEG-g-PVAc co-polymer and the surfactants DTAB.....90

Figure 4.2 a) Equilibrium surface tension γ vs. surfactant or polymer concentration (in their respective cmc and cac) using the Wilhelmy plate method. Four sets of data are shown: pure DTAB (∇), pure polymer (\circ), and the polymer (0.2 \square and 2 cac \blacktriangle) mixed with DTAB at different concentrations. Data points labelled 1-11 indicate specific polymer and surfactant concentrations. (b) The legend table lists the polymer and surfactant concentrations for the 11 dynamic surface tension curves, with the corresponding symbols for the plots in (a) and the corresponding numbers in (a) and (c). The dynamic surface tension γ_d vs. the surface age τ is shown in (c), using the bubble pressure method. Curves 9-11 in (c) (5 cmc DTAB) overlay with each other. The error bars in all cases are determined as a standard deviation from an experimental error determined from 3 separate measurements.94

Figure 4.3 The calculated Γ vs DTAB concentration of mixed PEG-g-PVAc + DTAB systems is shown. The Γ_{DTAB} is shown in $\mu\text{mol m}^{-2}$ on the left axis and represented by the filled markers, and $\Gamma_{PEG-g-PVAc}$ is shown in mg m^{-2} on the right axis and represented by the empty markers. The dashed lines act as a guide to the eyes only.96

Figure 4.4 A summary of the thickness t , water volume fraction ϕ_{water} and polymer fraction $\phi_{\text{PEG-g-PVAc}}$ in a single-layer model used to fit the NR data of PEG-g-PVAc + DTAB mixtures (○ and ● for 0.2 and 2 cac polymer respectively). For comparison, the blue dashed lines represent the fitted values of 0.2cac PEG-g-PVAc and 2cac PEG-g-PVAc respectively. The data point with green outline represents the fitted value for 0.1 and 1.2 cmc pure DTAB.98

Figure 4.5 Fitted NR data to a 1-layer model for 0.05 cmc DTAB with 0.2 and 2 cac PEG-g-PVAc, with the fitted ρ profiles and schematic representation based on the fitted parameters. The data is colour coded as follows: red represents mixtures of PEG-g-PVAc and dDTAB in D₂O, green represents mixtures of PEG-g-PVAc with hDTAB in D₂O, blue represents mixtures of PEG-g-PVAc with dDTAB in ACMW, and purple represents mixtures of PEG-g-PVAc with hDTAB in ACMW. The error bars associated with the data points were determined from the data reduction, larger at higher Q values due to lower contrast between the solvent and sample. The solid lines show the fitted curve, with the fitted parameters also shown, including thickness (t), solvent volume fraction (ϕ_{water}), and roughness of the layer (σ). 100

Figure 4.6 Fitted NR data to a 2-layer model for 0.5 cmc DTAB with 0.2 and 2 cac PEG-g-PVAc, with the fitted ρ profiles and schematic representation based on the fitted parameters. The data is colour coded as follows: red represents mixtures of PEG-g-PVAc and dDTAB in D₂O, green represents mixtures of PEG-g-PVAc with hDTAB in D₂O, blue represents mixtures of PEG-g-PVAc with dDTAB in ACMW, and purple represents mixtures of PEG-g-PVAc with hDTAB in ACMW. The error bars associated with the data points were determined from the data reduction, larger at higher Q values due to lower contrast between the solvent and sample. The solid lines show the fitted curve, with the fitted parameters also shown, including thickness (t), solvent volume fraction (ϕ_{water}), and roughness of the layer (σ). 102

Figure 4.7 Fitted NR data to a 3-layer model for 5 cmc DTAB with 0.2 and 2 cac PEG-g-PVAc, with the fitted ρ profiles and schematic representation based on the fitted parameters. The data is colour coded as follows: red represents mixtures of PEG-g-PVAc and dDTAB in D₂O, green represents mixtures of PEG-g-PVAc with hDTAB in D₂O, blue represents mixtures of PEG-g-PVAc with dDTAB in ACMW, and purple represents mixtures of PEG-g-PVAc with hDTAB in ACMW. The error bars associated with the data points were determined from the data reduction, larger at higher Q values due to lower contrast between the solvent and sample. The solid lines show the fitted curve, with the fitted parameters also shown, including thickness (t), solvent volume fraction (ϕ_{water}), and roughness of the layer (σ). 103

Figure 4.8 Calculated ϕ_{water} , ϕ_{DTAB} and $\phi_{\text{PEG-g-PVAc}}$ for each layer in fitted mixtures of DTAB/PEG-g-PVAc. L1, L2 and L3 refer to Layer 1, 2, and 3 respectively in the fitting model, with L1 the top layer in the given model as indicated in the schematics in Figures 4.4-4.6. 105

Figure 4.9 Foaming data showing the: a) foam half-life time ($\tau_{\text{FVS } 50\%}$) which is a measure of foam stability; b) maximum foam volume ($V_{\text{foam max}}$) which is a measure of foamability; and c) initial average bubble radius ($R_{\text{avg initial}}$) showing the radius of the foam bubbles during the foam generation. The data in green represents the pure DTAB solutions at 3 concentrations, the data in blue represents data for the pure polymer at 2 concentrations. The mixed polymer/surfactant systems are shown in pale and dark purple for DTAB with 0.2 cac PEG-g-PVAc and DTAB with 2 cac PEG-g-PVAc respectively. 107

Figure 4.10 Macroscopic foaming behaviour data (overall foam volume) and foam bubble size recorded over given period after foam generation is shown, comparing the pure 5 cmc DTAB system (left column) to the mixed systems containing 5cmc DTAB + 0.2 cac PEG-g-PVAc (middle column) and 5cmc DTAB + 2 cac PEG-g-PVAc (right column). The bubble size is colour coded as follows: green is for smallest bubble radius, followed by blue, purple, pink and the largest bubbles are shown in white. 108

Figure 5.1 Molecular structures (with corresponding schematics) of PEG-g-PVAc co-polymer and the surfactants $C_{12}E_5$ 117

Figure 5.2 a) Equilibrium surface tension γ vs. surfactant or polymer concentration (in their respective cmc and cac) using the Wilhelmy plate method. Four sets of data are shown: pure $C_{12}E_5$ (∇), pure polymer (\circ), and the polymer (0.2 \square and 2 cac \blacktriangle) mixed with $C_{12}E_5$ at different concentrations. Data points labelled 1-11 indicate specific polymer and surfactant concentrations. (b) The legend table lists the polymer and surfactant concentrations for the 11 dynamic surface tension curves, with the corresponding symbols for the plots in (a) and the corresponding numbers in (a) and (c). The dynamic surface tension γ_d vs. the surface age τ is shown in (c), using the bubble pressure method. Curves 9-11 in (c) (5 cmc $C_{12}E_5$) overlay with each other. The error bars in all cases are determined as a standard deviation from an experimental error determined from 3 separate measurements. 120

Figure 5.3 The calculated Γ vs $C_{12}E_5$ concentration of mixed PEG-g-PVAc + $C_{12}E_5$ systems is shown. The $\Gamma_{C_{12}E_5}$ is shown in $\mu\text{mol m}^{-2}$ on the left axis and represented by the filled markers,

and $\Gamma_{\text{PEG-g-PVAc}}$ is shown in mg m^{-2} on the right axis and represented by the empty markers. The dashed lines act as a guide to the eyes only. 122

Figure 5.4 A summary of the thickness t , water volume fraction, ϕ_{water} , and polymer fraction $\phi_{\text{PEG-g-PVAc}}$ in a single-layer model used to fit the NR data of PEG-g-PVAc + C_{12}E_5 mixtures (\circ and \bullet for 0.2 and 2 cac polymer respectively). For comparison, the blue dashed lines represent the fitted values of 0.2cac PEG-g-PVAc and 2cac PEG-g-PVAc respectively. The data point with pale blue outline represents the fitted value for 1.2 cmc pure C_{12}E_5 123

Figure 5.5 Fitted NR data to a 1-layer model for 0.05 cmc C_{12}E_5 with 0.2 and 2 cac PEG-g-PVAc, with the fitted ρ profiles and schematic representation based on the fitted parameters. The data is colour coded as follows: red represents mixtures of PEG-g-PVAc and dC_{12}E_5 in D_2O , green represents mixtures of PEG-g-PVAc with hC_{12}E_5 in D_2O , blue represents mixtures of PEG-g-PVAc with dC_{12}E_5 in ACMW, and purple represents mixtures of PEG-g-PVAc with hC_{12}E_5 in ACMW. The error bars associated with the data points were determined from the data reduction, larger at higher Q values due to lower contrast between the solvent and sample. The solid lines show the fitted curve, with the fitted parameters also shown, including thickness (t), solvent volume fraction (ϕ_{water}), and roughness of the layer (σ). 126

Figure 5.6 Fitted NR data to a 2-layer model for 0.5 cmc C_{12}E_5 with 0.2 and 2 cac PEG-g-PVAc, with the fitted ρ profiles and schematic representation based on the fitted parameters. The data is colour coded as follows: red represents mixtures of PEG-g-PVAc and dC_{12}E_5 in D_2O , green represents mixtures of PEG-g-PVAc with hC_{12}E_5 in D_2O , blue represents mixtures of PEG-g-PVAc with dC_{12}E_5 in ACMW, and purple represents mixtures of PEG-g-PVAc with hC_{12}E_5 in ACMW. The error bars associated with the data points were determined from the data reduction, larger at higher Q values due to lower contrast between the solvent and sample. The solid lines show the fitted curve, with the fitted parameters also shown, including thickness (t), solvent volume fraction (ϕ_{water}), and roughness of the layer (σ). 127

Figure 5.7 Fitted NR data to a 3-layer model for 5 cmc C_{12}E_5 with 0.2 and 2 cac PEG-g-PVAc, with the fitted ρ profiles and schematic representation based on the fitted parameters. The data is colour coded as follows: red represents mixtures of PEG-g-PVAc and dC_{12}E_5 in D_2O , green represents mixtures of PEG-g-PVAc with hC_{12}E_5 in D_2O , blue represents mixtures of PEG-g-PVAc with dC_{12}E_5 in ACMW, and purple represents mixtures of PEG-g-PVAc with hC_{12}E_5 in ACMW. The error bars associated with the data points were determined from the data

reduction, larger at higher Q values due to lower contrast between the solvent and sample. The solid lines show the fitted curve, with the fitted parameters also shown, including thickness (t), solvent volume fraction (ϕ_{water}), and roughness of the layer (σ)..... 129

Figure 5.8 Foaming data showing the: a) foam half-life time ($\tau_{\text{FVS } 50\%}$) which is a measure of foam stability, b) maximum foam volume ($V_{\text{foam max}}$) which is a measure of foamability, and c) initial average bubble radius ($R_{\text{avg initial}}$) showing the radius of the foam bubbles during the foam generation. The data in pale blue represents the pure $C_{12}E_5$ solutions at 3 concentrations, the data in blue represents data for the pure polymer at 2 concentrations. The mixed polymer/surfactant systems are shown in pale and dark purple for $C_{12}E_5$ with 0.2 cac PEG-g-PVAc and $C_{12}E_5$ with 2 cac PEG-g-PVAc respectively. 131

Figure 5.9 Macroscopic foaming behaviour data (overall foam volume) and foam bubble size recorded over given period after foam generation is shown, comparing the pure 5 cmc $C_{12}E_5$ system (left column) to the mixed systems containing 5cmc $C_{12}E_5$ + 0.2 cac PEG-g-PVAc (middle column) and 5cmc $C_{12}E_5$ + 2 cac PEG-g-PVAc (right column). The bubble size is colour coded as follows: green is for smallest bubble radius, followed by blue, purple, pink and the largest bubbles are shown in white. 132

Figure 6.1 Molecular structures (with schematics) of SDS, DTAB, $C_{12}E_5$ and the two PEG-g-PVAc co-polymers: Polymer A and Polymer B. 141

Figure 6.2 Equilibrium γ data of polymer/surfactant mixtures vs surfactant or polymer concentration (in their respective cmc and cac). The polymer/surfactant mixtures are as follows: a) SDS and Polymer A, b) DTAB and Polymer A, c) $C_{12}E_5$ and Polymer A, d) SDS and Polymer B, e) DTAB and Polymer B, and f) $C_{12}E_5$ and Polymer B. The error bars were determined experimentally as a standard deviation from 3 separate measurements. 143

Figure 6.3 Fitted XRR data of pure PEG-g-PVAc polymers (Polymer A data shown in blue circles and Polymer B shown in purple diamonds) at two concentrations: 0.2 and 2 cac (empty and filled markers, respectively)..... 147

Figure 6.4 Fitted XRR data of pure SDS. Concentrations 0.05 cmc to 0.5 cmc SDS were fitted to a 1-layer model, with the concentrations 1.2 and 5 cmc SDS were fitted to a 2-layer model. 149

Figure 6.5 Fitted XRR data of SDS/polymer mixtures using a 1-layer model. The data is offset for clarity, with increasing SDS concentration. The mixtures of SDS/Polymer A are shown in circles and mixtures of SDS/Polymer B are shown in diamonds. In both cases, the lower polymer concentration (0.2 cac) is represented by empty markers, and 2 cac polymer concentration represented by filled markers. 150

Figure 6.6 Fitted XRR data of SDS/polymer mixtures using a 1-layer model for SDS/polymer mixtures containing: 0.05 cmc SDS (yellow), 2-layer model for 0.5 cmc SDS (blue) and 5 cmc SDS concentration (green). The data is offset for clarity, with increasing SDS concentration. The mixtures of SDS/Polymer A are shown in circles and mixtures of SDS/Polymer B are shown in diamonds. In both cases, the lower polymer concentration (0.2 cac) is represented by empty markers, and 2 cac polymer concentration represented by filled markers..... 152

Figure 6.7 Fitted XRR data of pure DTAB. 0.05 cmc DTAB was fitted to a 1-layer model, with the concentrations 0.1 to 5 cmc DTAB fitted to a 2-layer model 155

Figure 6.8 Fitted XRR data of DTAB/polymer mixtures using a 1-layer model. The data is offset for clarity, with increasing DTAB concentration. The mixtures of DTAB/Polymer A are shown in circles and mixtures of DTAB/Polymer B are shown in diamonds. In both cases, the lower polymer concentration (0.2 cac) is represented by empty markers, and 2 cac polymer concentration represented by filled markers. 157

Figure 6.9 Fitted XRR data of DTAB/polymer mixtures using a 1-layer model for DTAB/polymer mixtures containing: 0.05 cmc DTAB (yellow), 2-layer model for 0.5 cmc DTAB (blue) and 5 cmc DTAB concentration (green). The data is offset for clarity, with increasing DTAB concentration. The mixtures of DTAB/Polymer A are shown in circles and mixtures of DTAB/Polymer B are shown in diamonds. In both cases, the lower polymer concentration (0.2 cac) is represented by empty markers, and 2 cac polymer concentration represented by filled markers..... 159

Figure 6.10 Fitted XRR data of pure C₁₂E₅. All concentrations (0.05 to 5 cmc) were fitted to a 2-layer model. 161

Figure 6.11 Fitted XRR data of C₁₂E₅/polymer mixtures using a 1-layer model. The data is offset for clarity, with increasing C₁₂E₅ concentration. The mixtures of C₁₂E₅/Polymer A are shown in circles and mixtures of C₁₂E₅/Polymer B are shown in diamonds. In both cases, the

lower polymer concentration (0.2 cac) is represented by empty markers, and 2 cac polymer concentration represented by filled markers. 163

Figure 6.12 Fitted XRR data of C₁₂E₅/polymer mixtures using a 1-layer model for C₁₂E₅/polymer mixtures containing: 0.05 cmc C₁₂E₅ (yellow), 2-layer model for 0.5 cmc C₁₂E₅ (blue) and 5 cmc C₁₂E₅ concentration (green). The data is offset for clarity, with increasing C₁₂E₅ concentration. The mixtures of C₁₂E₅/Polymer A are shown in circles and mixtures of C₁₂E₅/Polymer B are shown in diamonds. In both cases, the lower polymer concentration (0.2 cac) is represented by empty markers, and 2 cac polymer concentration represented by filled markers. 165

Figure 7.1 Chemical structures of a) double tailed cationic surfactant DEEDMAC and b) SDS. Schematic representations of possible interactions and complex structures formation c) in the bulk and d) at interfaces. 176

Figure 7.2 a) example of thinly cleaved mica of thickness suitable for an SFA measurement, as observed by the purple colour. b) back-silvered mica glued onto two quartz cylindrical disks, used as top and bottom surfaces. 180

Figure 7.3 Back-silvered mica glued on quartz disks mounted on a) set of horizontal leaf springs in the boat and b) attached to the sectorized piezoelectric tube and a set of vertical springs. 181

Figure 7.4 An outline of sample vitrification and storage, as prepared for cryoTEM. 188

Figure 7.5 a) DLS and ζ -potential measurement correlated to a 2D sliced and a “3D” schematic representation of the bulk (b). With increasing SDS concentration, the size of the DEEDMAC vesicles increases steadily indicating SDS adsorption onto the vesicle surface. This is also confirmed by the surface charge reversal, implying the vesicle surface fully coated by the anionic SDS. At SDS concentrations above its cmc, we could speculate whole SDS micelles could adsorb onto the cationic vesicle surface, and also provide bridging between two or more vesicles. 192

Figure 7.6 The surface tension data of DEEDMAC vesicles (green), SDS (red) and their mixtures containing 0.05 and 5 mg mL⁻¹ DEEDMAC vesicle dispersion with increasing SDS concentration (blue and purple, respectively). The data point marked as 1 highlights the value

of pure 0.05 mg mL⁻¹ DEEDMAC, and data point marked as 2 shows the value of pure 5 mg mL⁻¹ DEEDMAC vesicle dispersion. The schematic representation in b) is a possible interfacial layer, with the charged headgroups and the interactions involved. 193

Figure 7.7 XRR data of DEEDMAC/SDS mixtures at the air-water interface, with layer t determined from the fringe spacing marked by dashed lines. 195

Figure 7.8 XRR curves for DEEDMAC with increasing SDS concentration, with t determined from fringe spacing. The * marks the mica half-Bragg peak. 197

Figure 7.9 Normalised force vs separation distance of two mica surfaces immersed in a solution containing 5 mg mL⁻¹ vesicle dispersion. The approach of the mica surfaces is represented by the circular data points, whereas the data measured during retraction of the surfaces is represented by triangles. The inset shows the log-normal plot of the normalised force vs separation, with fitted exponential decay to determine Debye length, κ^{-1} 199

Figure 7.10 Normalised force vs separation distance of two mica surfaces with adsorbed DEEDMAC bilayer immersed in a solution containing 0.5 cmc SDS. The approach of the mica surfaces is represented by the circular data points, whereas the data measured during retraction of the surfaces is represented by triangles. The inset shows the log-normal plot of the normalised force vs separation, with fitted exponential decay to determine Debye length, κ^{-1} 200

Figure 7.11 Normalised force vs separation distance of two mica surfaces with adsorbed DEEDMAC bilayer immersed in a solution containing 5 cmc SDS. The approach of the mica surfaces is represented by the circular data points, whereas the data measured during retraction of the surfaces is represented by triangles. The inset shows the log-normal plot of the normalised force vs separation, with fitted exponential decay to determine Debye length, κ^{-1} 201

Figure 7.12 A summary of normalised force vs separation distance of two mica surfaces with adsorbed DEEDMAC bilayer immersed in a solution of increasing SDS concentration. Only the data collected during approach of the mica surfaces is shown. 202

Figure 7.13 A summary of the log-normal plot of normalised force vs separation distance, with the data of DEEDMAC and SDS mixtures adsorbed to the mica surface fitted by an exponential decay to determine the Debye length, κ^{-1}204

Figure 7.14 Representation of Debye length, κ^{-1} (left axis) determined from exponential decay (line and circle data points) and the thickness, t ,(right axis) determined as half of the hard wall separation represented as bar charts.....205

Figure 7.15 Images of FECO corresponding to each system, with a possible schematic representations: bare mica in contact (grey), DEEDMAC bilayer formation (green), SDS adsorption below its cmc as a single layer (yellow), SDS adsorption above its cmc as micelles (red), SDS/DEEDMAC multilayer formation at 10 cmc SDS (purple), DEEDMAC vesicles trapped between the multilayers (green), and stable DEEDMAC/SDS multilayer preserved following rinsing with MilliQ (blue).206

Figure 7.16 Confocal images of a) 0.1 cmc SDS, b) 0.5 cmc SDS and c) 5 cmc SDS doped with fluorescein.....208

Figure 7.17 Negative stain TEM (a, b), cryoTEM (c, d) and confocal microscopy (e, f) of pure DEEDMAC vesicle dispersion. The Nile Blue doped DEEDMAC is represented by green colour.209

Figure 7.18 Negative stain TEM (a, b), cryoTEM (c, d) and confocal microscopy (e, f) of DEEDMAC vesicle dispersion and 0.1 cmc SDS. The Nile Blue doped DEEDMAC is represented by green colour, and fluorescein doped SDS by red.211

Figure 7.19 Negative stain TEM (a), cryoTEM (b, c, d) and confocal microscopy (e, f) of DEEDMAC vesicle dispersion and 0.5 cmc SDS. The Nile Blue doped DEEDMAC is represented by green colour, and fluorescein doped SDS by red.213

Figure 7.20 Negative stain TEM (a, b), cryoTEM (c, d) and confocal microscopy (e, f) of DEEDMAC vesicle dispersion and 5 cmc SDS. The Nile Blue doped DEEDMAC is represented by green colour, and fluorescein doped SDS by red.215

List of tables

Table 2.1 List of a) scattering lengths of the atoms and b) the scattering length densities of molecules relevant to the studied systems.	36
Table 3.1 The fitted parameters for the optimised multilayer models for mixtures of PEG-g-PVAc and SDS, as well as the pure systems. The superscripts for the fitted scattering length density (SLD) ρ values in the table correspond to the following polymer/surfactant volume fractions: ¹ 90% PEG-g-PVAc + 10% SDS, ² 74% PEG-g-PVAc + 26% SDS, ³ 71% PEG-g-PVAc + 29% SDS headgroup, ⁴ 97% PEG-g-PVAc + 3% SDS, ⁵ 95% PEG-g-PVAc + 5% SDS, ⁶ 63% PEG-g-PVAc + 37% SDS headgroup. The σ_{bkg} is the roughness between the water and the interfacial layers.	66
Table 3.2 The $V_{\text{foam max}}$, $\tau_{\text{FVS } 50\%}$ and $R_{\text{avg initial}}$ determined from foam measurements of PEG-g-PVAc mixtures with SDS.	76
Table 4.1 The fitted parameters for the optimised multilayer models for mixtures of PEG-g-PVAc and DTAB, as well as the pure systems. The superscripts for the fitted scattering length density (SLD) ρ values in the table correspond to the following polymer/surfactant volume fractions: ¹ 69% PEG-g-PVAc + 31% DTAB, ² 60% PEG-g-PVAc + 40% DTAB, ³ 61% PEG-g-PVAc + 39% DTAB headgroup, ⁴ 95% PEG-g-PVAc + 5% DTAB, ⁵ 97% PEG-g-PVAc + 3% DTAB, ⁶ 60% PEG-g-PVAc + 40% DTAB headgroup.	99
Table 4.2 The $V_{\text{foam max}}$, $\tau_{\text{FVS } 50\%}$ and $R_{\text{avg initial}}$ determined from foam measurements of PEG-g-PVAc mixtures with DTAB.	106
Table 5.1 The fitted parameters for the optimised multilayer models for mixtures of PEG-g-PVAc and C ₁₂ E ₅ , as well as the pure systems. The superscripts for the fitted scattering length density (SLD) ρ values in the table correspond to the following polymer/surfactant volume fractions: ¹ 75% PEG-g-PVAc + 25% C ₁₂ E ₅ , ² 60% PEG-g-PVAc + 40% C ₁₂ E ₅ , ³ 28% PEG-g-PVAc + 72% C ₁₂ E ₅ headgroup, ⁴ 52% PEG-g-PVAc + 48% C ₁₂ E ₅ , ⁵ 32% PEG-g-PVAc + 68% C ₁₂ E ₅ , ⁶ 97% PEG-g-PVAc + 3% C ₁₂ E ₅ , ⁷ 95% PEG-g-PVAc + 5% C ₁₂ E ₅ , ⁸ 18% PEG-g-PVAc + 82% C ₁₂ E ₅ headgroup and ⁹ 58% PEG-g-PVAc + 42% C ₁₂ E ₅ headgroup.	124

Table 5.2 The $V_{\text{foam max}}$, $\tau_{\text{FVS } 50\%}$ and $R_{\text{avg initial}}$ determined from foam measurements of PEG-g-PVAc mixtures with $C_{12}E_5$ 130

Table 6.1 XRR fitting parameters: thickness (t), scattering length density (σ), solvent volume fraction (ϕ_{water}) and roughness of the layer (σ) of the two PEG-g-PVAc polymers (Polymer A and Polymer B) determined from a 1-layer fit of XRR data..... 147

Table 6.2 XRR fitting parameters: thickness (t), scattering length density (σ), solvent volume fraction (ϕ_{water}) and roughness of the layer (σ) of pure DTAB determined from a 1-layer (at 0.05 cmc DTAB) and a 2-layer model (at concentrations 0.1 to 5 cmc) fit of XRR data. The superscripts for the fitted ρ values in the table correspond to the following headgroup/counterion associations: ¹ 50% counterion, ² 71% counterion associated with the surfactant headgroup. 100% counterion association is assumed when not stated otherwise. 149

Table 6.3 The fitting parameters: thickness (t), scattering length density (σ), solvent volume fraction (ϕ_{water}) and roughness of the layer (σ) of 1-layer model for mixtures of SDS/Polymers A and SDS/Polymer B. The superscripts for the fitted ρ values in the table correspond to the following polymer/surfactant volume fractions: ¹ 8% Polymer A + 92% SDS, ² 1% Polymer A + 99% SDS, ³ 1% Polymer A + 99% SDS, ⁴ 2% Polymer A + 98% SDS, ⁵ 0.5% Polymer A + 99.5% SDS, ⁶ 82% Polymer A + 18% SDS, ⁷ 0.5% Polymer A + 99.5% SDS, ⁸ 0.5% Polymer A + 99.5% SDS, ⁹ 1% Polymer A + 99% SDS, ¹⁰ 0% Polymer A + 100% SDS, and ¹¹ 9% Polymer B + 91% SDS, ¹² 12% Polymer B + 88% SDS, ¹³ 2% Polymer B + 98% SDS, ¹⁴ 0% Polymer B + 100% SDS, ¹⁵ 0.5% Polymer B + 99.5% SDS, ¹⁶ 13% Polymer B + 87% SDS, ¹⁷ 55% Polymer B + 45% SDS, ¹⁸ 1% Polymer B + 99% SDS, ¹⁹ 3% Polymer B + 97% SDS, ²⁰ 0.5% Polymer B + 99.5% SDS. 151

Table 6.4 The fitting parameters: thickness (t), scattering length density (σ), solvent volume fraction (ϕ_{water}) and roughness of the layer (σ) for the optimised multilayer models for mixtures of PEG-g-PVAc co-polymers (Polymer A and Polymer B) and SDS, as well as the pure systems. The superscripts for the fitted scattering length density (SLD) ρ values in the table correspond to the following polymer/surfactant volume fractions: ¹ 8% Polymer A + 92% SDS, ² 44% counterion associated with SDS headgroup, ³ 82% Polymer A + 18% SDS, ⁴ 90.4% counterion associated with SDS headgroup, and ⁵ 9% Polymer B + 91% SDS, ⁶ 77% counterion associated with SDS headgroup, ⁷ 13% Polymer B + 87% SDS, ⁸ 28% counterion associated with SDS headgroup. 153

Table 6.5 The fitting parameters: thickness (t), scattering length density (σ), solvent volume fraction (ϕ_{water}) and roughness of the layer (σ) of pure DTAB determined from a 1-layer (at 0.05 cmc DTAB) and a 2-layer model (at concentrations 0.1 to 5 cmc) fit of XRR data. The superscripts for the fitted ρ values in the table correspond to the following headgroup/counterion associations: ¹ 66% counterion, ² 95% counterion, ³ 93% counterion, ⁴ 90% counterion associated with the surfactant headgroup. 100% counterion association is assumed unless otherwise stated. 156

Table 6.6 The fitting parameters: thickness (t), scattering length density (σ), solvent volume fraction (ϕ_{water}) and roughness of the layer (σ) of 1-layer model for mixtures of DTAB/Polymers A and DTAB/Polymer B. The superscripts for the fitted scattering length density (SLD) ρ values in the table correspond to the following polymer/surfactant volume fractions: ¹ 97% Polymer A + 3% DTAB, ² 91% Polymer A + 9% DTAB, ³ 90% Polymer A + 10% DTAB, ⁴ 94% Polymer A + 6% DTAB, ⁵ 98% Polymer A + 2% DTAB, ⁶ 98% Polymer A + 2% DTAB, ⁷ 99.5% Polymer A + 0.5% DTAB, ⁸ 97% Polymer A + 3% DTAB, ⁹ 99% Polymer A + 1% DTAB, ¹⁰ 95% Polymer A + 5% DTAB, and ¹¹ 96% Polymer B + 4% DTAB, ¹² 93% Polymer B + 7% DTAB, ¹³ 97% Polymer B + 3% DTAB, ¹⁴ 97% Polymer B + 3% DTAB, ¹⁵ 96% Polymer B + 4% DTAB, ¹⁶ 97% Polymer B + 3% DTAB, ¹⁷ 98% Polymer B + 2% DTAB, ¹⁸ 88% Polymer B + 12% DTAB, ¹⁹ 96% Polymer B + 4% DTAB, ²⁰ 95% Polymer B + 5% DTAB. 158

Table 6.7 The fitted parameters: thickness (t), scattering length density (σ), solvent volume fraction (ϕ_{water}) and roughness of the layer (σ) for the optimised multilayer models for mixtures of PEG-g-PVAc co-polymers (Polymer A and Polymer B) and DTAB, as well as the pure systems. The superscripts for the fitted scattering length density (SLD) ρ values in the table correspond to the following polymer/surfactant volume fractions: ¹ 97% Polymer A + 3% DTAB, ² 82% counterion associated with DTAB headgroup, ³ 98% Polymer A + 2% DTAB, ⁴ 87% counterion associated with DTAB headgroup, and ⁵ 96% Polymer B + 4% DTAB, ⁶ 100% counterion associated with DTAB headgroup, ⁷ 97% Polymer B + 3% DTAB, ⁸ 33% counterion associated with DTAB headgroup. 160

Table 6.8 The fitted parameters: thickness (t), scattering length density (σ), solvent volume fraction (ϕ_{water}) and roughness of the layer (σ) of pure C₁₂E₅ determined from a 2-layer model (at concentrations 0.05 to 5 cmc) fit of XRR data. 162

Table 6.9 The fitting parameters: thickness (t), scattering length density (σ), solvent volume fraction (ϕ_{water}) and roughness of the layer (σ) of 1-layer model for mixtures of C₁₂E₅/Polymers A and C₁₂E₅/Polymer B. The superscripts for the fitted scattering length density (SLD) ρ values in the table correspond to the following polymer/surfactant volume fractions: ¹ 86% Polymer A + 14% C₁₂E₅, ² 97% Polymer A + 3% C₁₂E₅, ³ 93% Polymer A + 7% C₁₂E₅, ⁴ 85% Polymer A + 15% C₁₂E₅, ⁵ 91% Polymer A + 9% C₁₂E₅, ⁶ 99% Polymer A + 1% C₁₂E₅, ⁷ 98% Polymer A + 2% C₁₂E₅, ⁸ 99% Polymer A + 1% C₁₂E₅, ⁹ 88% Polymer A + 12% C₁₂E₅, ¹⁰ 78% Polymer A + 22% C₁₂E₅, and ¹¹ 99% Polymer B + 1% C₁₂E₅, ¹² 95% Polymer B + 5% C₁₂E₅, ¹³ 90% Polymer B + 10% C₁₂E₅, ¹⁴ 74% Polymer B + 26% C₁₂E₅, ¹⁵ 84% Polymer B + 16% C₁₂E₅, ¹⁶ 98% Polymer B + 2% C₁₂E₅, ¹⁷ 98% Polymer B + 2% C₁₂E₅, ¹⁸ 86% Polymer B + 14% C₁₂E₅, ¹⁹ 75% Polymer B + 25% C₁₂E₅, ²⁰ 92% Polymer B + 8% C₁₂E₅..... 164

Table 6.10 The fitting parameters: thickness (t), scattering length density (σ), solvent volume fraction (ϕ_{water}) and roughness of the layer (σ) for the optimised multilayer models for mixtures of PEG-g-PVAc co-polymers (Polymer A and Polymer B) and C₁₂E₅, as well as the pure systems. The superscripts for the fitted scattering length density (SLD) ρ values in the table correspond to the following polymer/surfactant volume fractions: ¹ 97% Polymer A + 3% C₁₂E₅, ² 99% Polymer A + 1% C₁₂E₅, and ³ 99% Polymer B + 1% C₁₂E₅, ⁴ 98% Polymer B + 2% C₁₂E₅..... 166

1 Introduction

Polymer/surfactant interactions and their co-assembly are introduced, with focus on the interfacial properties and structures at the air-water interface. The polymers and surfactants relevant to the project work are described, and their applications are discussed. Finally, an overview of foam behaviour and characteristics is provided, as well as introducing the concept of using the air-water interface as an analogous structure of foam bubbles.

1.1 Project Motivation

Foams are integral to many practical applications, including personal care products, dishwashing and laundry detergents. The current economical and ethical efforts in industry are focused on reducing the amount of active ingredients needed in such formulations, improved efficiency at lower temperatures, and thus reduced energy consumption, and biodegradability of the components.

It is well known that foam properties depend on the surfactants (or any stabilising agents including polymers) used [1]. However, there is no clear correlation between the macroscopic foaming properties and a chemical or physical property determined by a single experimental technique. Correlation of foam stability and foamability to surface tension measurements or thin film studies cannot be established universally [2, 3]. The interactions and internal ordering of molecules during foam formation and stabilisation is therefore of a high scientific interest [4]. Recent advances in surface-sensitive experimental techniques such as X-ray and neutron reflectivity have considerably advanced our understanding of polymer/surfactant interfacial structures and behaviour [5, 6]. The diffusion of surfactants from bulk of a liquid to the thin films stabilising foams can be likened to the adsorption of surfactants at a single air-water interface.

The structures and composition of polymer/surfactant mixtures were investigated at the air-water interface comprising of a neutral amphiphilic co-polymer consisting of polyethylene glycol backbone with polyvinyl acetate grafts (PEG-g-PVAc) and a set of three surfactants: anionic sodium dodecylsulfate (SDS), cationic dodecyltrimethylammonium bromide (DTAB) and non-ionic dodecylpentaethyleneglycol ether ($C_{12}E_5$). The adsorption behaviour of these

Chapter 1

mixtures was investigated by equilibrium and dynamic surface tension measurements, and the structure and composition of the adsorbed layers at the air-water interface were determined by X-ray and neutron reflectivity. Use of these complementary techniques allowed for a thorough investigation of the polymer/surfactant interactions present in these systems. The choice of three model surfactants enabled evaluation of the effects of surfactant headgroup charge and size on the polymer/surfactant interactions. Furthermore, the effect of polymer molecular architecture on the polymer/surfactant interfacial properties was investigated by variation of the length and number of hydrophobic PVAc grafts on the polymer, as well as its hydrophobicity. These PEG-*g*-PVAc co-polymers are currently used in a plethora of cleaning products, and while their bulk aggregation behaviour has been studied, our results at the air-water interface are unprecedented.

Additionally, complexation behaviour of oppositely charged mixed system comprised of anionic SDS and cationic double-tailed surfactant (DEEDMAC) forming vesicles was investigated. DEEDMAC is commercially important surfactant due to its high biodegradability and efficiency as a fabric softener. We have therefore studied the strongly adsorbing mixed surfactant system at the solid-liquid interface, with correlation drawn to its complexation in the bulk.

In summary, we have employed a combination of surface-sensitive techniques (predominantly X-ray and neutron reflectivity, surface tension measurements and surface force apparatus) to study interfacial properties of neutral polymer/surfactant and oppositely charged mixed surfactant systems.

The ultimate goal of the project is to gain an insight into the fundamental interactions of such mixed systems, as well as attempt to move closer towards establishing a link between molecular and macroscopic scale properties (*i.e.* structure of polymer/surfactant complexes at the air-water interface correlated to their foaming properties and the influence of surfactant and polymer characteristics on this complex behaviour), as well as linking interfacial and bulk complexation of strongly interacting surfactants and vesicles. Such a correlation will facilitate optimal design of these complexes at a molecular level, tailored to desired interfacial properties, which underpin their performance in a plethora of industrial applications.

1.2 Air-water interface

The air-water interface, or in general a gas-liquid interface, plays an important role in many applications, as well as furthering our fundamental knowledge of principles around us. There are many examples of this interface in our day-to-day life (such as washing up liquid, soaps, oil lubricants), different industrial uses (oil recovery, coatings, acoustics, colloid transport) [7], nature (spiders walking on water, insect and frogs protecting their eggs), art (painting and printing), and even enables us to breath as the lung alveoli (essentially small air sacks) exchange oxygen and carbon dioxide between the lungs and the bloodstream. The surface of the alveoli is protected by a layer of surfactants from fluid accumulation and collapse due to otherwise high surface tension and aid in the oxygen adsorption into the blood stream [8]. From a physical science point of view, an interface is formed when two or more different phases (*i.e.* solid, liquid or gas) meet, for example during a washing up process there is solid-liquid interface where the detergent meets the suds on a plate, a liquid-liquid interface inside the diluted detergent liquid containing solubilised oil particles in the aqueous bulk and a gas-liquid interface as the detergent is in contact with air and forms foam bubbles.

1.2.1 Surface tension and surfactant adsorption

Surface tension, γ , is the result of an imbalance between the intermolecular forces experienced by molecules in a bulk of a phase and at its interface. A schematic of the air-water interface is shown in Figure 1.1, where the water molecules at the surface are attracted towards the bulk of the solution as they lack “neighbours” above them, creating excess energy called the surface free energy. This makes the surface of the liquid contract and reduce the exposed surface area, creating an elastic membrane while lowering the surface free energy.

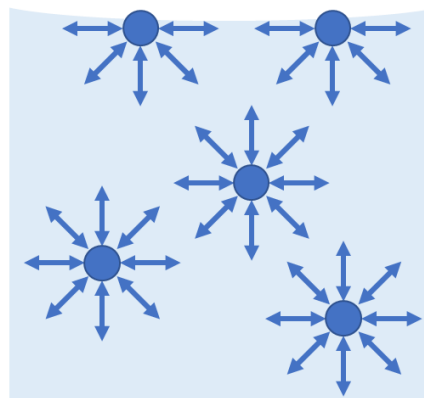


Figure 1.1 A schematic of the forces acting between water molecules in bulk and at the air-water interface. Due to the imbalance the molecules experience at the air-water interface, there is an overall pull downwards in attempt to minimise the surface area of the unfavourable interactions.

Chapter 1

Water has relatively high $\gamma \sim 72.8 \text{ mN m}^{-1}$ compared to other commonly used solvents (ethanol $\sim 22 \text{ mN m}^{-1}$) [9]. Surface active agents (surfactants) are used to lower the surface tension of aqueous solutions by adsorbing at the interface, forming a monolayer due to more thermodynamically favourable organisation and decreasing the surface free energy in doing so. This is a dynamic process, as the surfactants need to diffuse from the bulk towards the interface to form a complete monolayer and reach the equilibrium surface tension value over certain period of time, also known as the relaxation period [10]. The minimum, or limiting, surface tension and the adsorption dynamics were described to be depended on the surfactant structure, especially the characteristics of the hydrophobic tail and packing. The surface coverage at cmc concentration, φ_{cmc} , is another measure of the packing ability of surfactants. Recently, a correlation of high surface coverage value and limiting surface tension value, γ_{lim} , (*i.e.* the minimum surface tension value exhibited at and above the cmc concentration of surfactant) was found and used to evaluate the efficiency (term determined by the thermodynamics of the surfactant, meaning what is the concentration needed to reach γ_{lim}) and the effectiveness (what is the γ_{lim} achieved, a term related to the size of a surfactant) of different surfactants [11]. Working with mixed surfactant systems, γ_{lim} may be lowered more significantly compared to the systems comprised of the individual components due to different electrostatic attraction or screened repulsion, a phenomenon known as synergism [12]. Synergistic effects are very important in many applications, as majority of commercially and industrially used products contain more than one surface active agents, may that be oppositely charged surfactants, polymers, and additives such as salts.

1.2.2 Micellisation

Micellisation occurs in solutions above certain critical concentration, called a critical micellisation concentration (cmc). The cmc value is influenced by several factors, including the structure of the surfactant (the hydrophobic tail length and the hydrophilic head character), presence of counterions or salts in the solution, and the temperature [13]. With increasing concentration in a solution of amphiphilic molecules, such as surfactants and polymers, the molecules first exist in a dynamic equilibrium between single molecules in the solution and molecules adsorbing to the air-water interface, where the hydrophobic parts (such as hydrocarbon surfactant tails) are protruding into the air phase and the hydrophilic parts (such as surfactant headgroups) remain in the water phase just below the surface. When considering a simple case, further increasing the concentration of adsorbing species will lead to formation

of a complete interfacial monolayer, where no more molecules can adsorb at the interface. Aggregation occurs in the bulk to minimise the unfavourable interactions of hydrophobic moieties in the aqueous solvent; thus micelles are formed in the bulk, which are in dynamic equilibrium with the monolayer adsorbed at the interface. However, thermodynamics of the whole system should be considered as micellisation is not purely an interfacial phenomenon caused by the saturation of the interface. At certain concentration, the entropic gain from the free molecules existing in the bulk aqueous phase is overcome by the energetic loss due to the unfavourable interactions of the hydrophobic moieties with the aqueous solvent and the hydrophobic effect (*i.e.* the entropic gain of the free water molecules following micelle formation) [14]. At this concentration the cmc is reached, and aggregates/micelles form in the bulk phase to reach the minimum free energy of the system, while at dynamic equilibrium with monomers [15]. The cmc value can be measured by bulk techniques such as conductivity, viscosity, fluorescence and UV-vis spectroscopy, scattering (dynamic light scattering, small angle X-ray and neutron scattering) and NMR, as well as surface tension measurements at the air-water interface [16, 17]. The surface tension is lowered following surfactant adsorption to the interface, as the strong adhesion forces between water molecules are broken by the presence of higher interfacial concentration of the amphiphiles and the overall free energy of the system is lowered. Following formation of a complete monolayer, the surface tension is no longer lowered as the interfacial concentration (*i.e.* the surface excess) no longer increases.

For a mixed polymer/surfactant system there are a variety of options of bulk and interfacial structures formed, as well as both competitive adsorption or synergistic effect can be observed (Figure 1.2). For example, the surfactants or polymer may adsorb preferentially at the interface, the polymer may adsorb first and then be replaced by the surfactants or vice versa, or a layer of polymer/surfactant complexes may adsorb at the interface. Equally, the structures in the bulk can be formed by pure surfactant micelles and pure polymer micelles, or mixed micelles comprised of both surfactant and polymer, as well as a combination of all three scenarios. The ratio of these can also be varied, depending on the kinetics of the formation of the species, and the overall thermodynamics of the system.

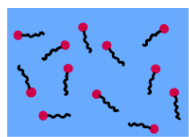
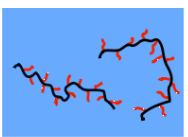
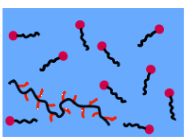
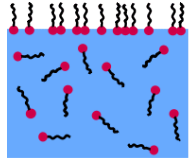
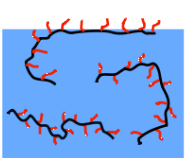
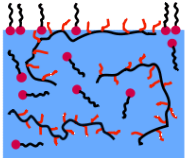
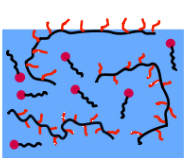
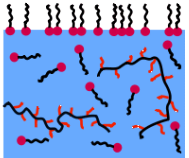
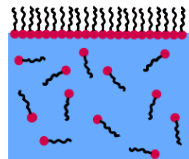
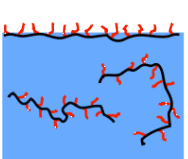
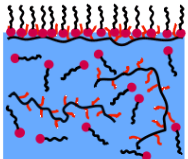
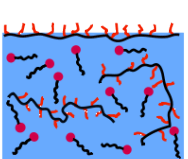
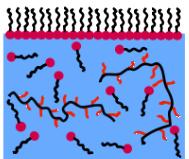
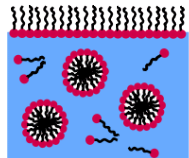
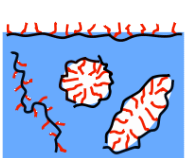
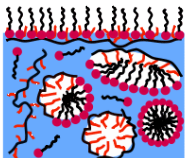
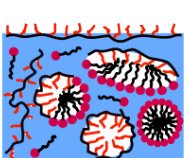
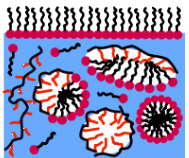
	surfactant only	polymer only	surfactant/polymer mixture		
below cmc monomers in bulk					
below cmc adsorption at interface					
at cmc complete monolayer at interface					
above cmc complete monolayer at interface, micelles in bulk					

Figure 1.2 Schematic drawing of different processes involved in micellisation of pure surfactant, pure polymer and surfactant/polymer mixed system.

1.3 Polymer/surfactant interactions

There is a large amount of work published on polymer/surfactant mixtures and their behaviour in solution and at interfaces [5, 18, 19]. It is not in the scope of this work to provide an exhaustive account of possible polymer/surfactant combinations, architectures, and applications of these mixed systems ubiquitous around us. Therefore, only a brief overview of the main categories of polymer/surfactant interactions is provided here, with a few examples for each category that are directly relevant to the studied systems. More specific overview of the polymer/surfactant or surfactant/surfactant interactions is provided in each chapter.

The inter-polymer and intra-polymer interactions, especially in the presence of surfactants, lead to in-plane association as well as out-of-plane organisation. Polymer/surfactant interfacial organisation is a crucial factor in determining the interfacial mechanical properties. The properties of polymer/surfactant mixtures at interfaces cannot be explained purely by electrostatic and hydrophobic interactions. There are more complex processes involved, such as complexation and synergistic effects, influencing the behaviour and properties of these mixtures. The main forces involved in polymer/surfactant interactions are the hydrophobic attractive forces (hydrocarbon surfactant tail and hydrophobic polymer region), electrostatic

repulsive forces (between the charged clusters of associated surfactant clusters), and the always present van der Waals attractions.

In general, polymer/surfactant mixtures can be divided into three main categories:

- a) equally charged, experiencing electrostatic repulsion and therefore weaker complexation
- b) neutral polymers with charged surfactants, with stronger hydrophobic interactions and electrostatic interactions should any partial charges arise
- c) oppositely charged systems, with strong electrostatic attractive forces in addition to hydrophobic interactions and therefore strong complexation.

Examples of neutral polymer/surfactant and oppositely charged complexes are given below, with a model surfactant SDS.

1.3.1 Neutral polymers

Neutral polymers are usually described as weakly interacting with charged surfactants. One of such examples, arguably the most well-known, is the interaction between polyethylene oxide (PEO or PEG) and SDS. Firstly, a formation of stoichiometric SDS complexes along the PEG polymeric strands (with SDS headgroup interacting with the PEG) was observed by Cabane *et al.* in the 1980s using NMR and neutron scattering techniques [20-22]. These complexes were spherical with ~ 20 Å radius (similar to a pure SDS micelle in size), with aggregation number ~ 38 (smaller than ~ 60 for a pure SDS micelle in water, possibly due to the PEG adsorption into the micelle palisade layer and increased micelle ionisation [23]). Increasing the SDS concentration in this case leads to formation of more spherical complexes along the PEG macromolecule unit until the polymer chain becomes saturated when the distance between two SDS complexes $< \sim 90$ Å, and the gain in free energy upon SDS binding is overcome by the higher electrostatic repulsion between two neighbouring micelles. Increasing the SDS concentration even further leads to an excess SDS concentrations and formation of free SDS micelles in addition to the PEG/SDS complexes. This behaviour has also been shown to be dependent on the ionic strength [24], where with increasing ionic strength the SDS micelle size increases, the radius of gyration of PEG decreases with increasing ionic strength, and the cac decreases. PEG/SDS complexation was also studied using surface tension measurements [25], and has been extended to studies of co-polymers, such as a comb co-polymer comprising a

methacrylate backbone and PEG grafts (MAA-PEG with 7, 11 and 20 monomer units). It was found that the electrostatic repulsion between the methacrylate backbone and the SDS molecules prevented any SDS/PEG complexation [26].

It is not surprising that the nature and strength of polymer/surfactant interactions is governed not only by the charge that the moieties carry but also their molecular architecture.

1.3.1.1 Polymer architecture

The self-assembly process of polymers can be controlled by their structural features, *e.g.* non-linear polymers containing branches, joints, and functionalised end groups which enable tuning of H-bonding and steric and static interactions, can be used to self-assemble into functional Langmuir-Blodgett (LB) films at the air-water interface [27]. The link between polymer molecular architecture, molecular weight and charge has been studied to certain extent, especially the differences between linear and branched polymers. For example, the interactions of SDS and linear *vs* branched PEI polymer were studied in aqueous solutions at different pH, with enhanced SDS adsorption observed in presence of the branched polymer compared to that of with linear PEI polymer [28].

NR studies performed on a graft co-polymer methylmethacrylate (MMA) backbone and varying content of PEG grafts spread at the air-water interface, with the PEG grafts extending to the water subphase [29]. The number of layers needed to describe the interfacial organisation of the graft co-polymer increases above 2 with increasing surface concentration of the co-polymer, as well as with increasing PEG grafts content. This dependency is overestimated by pure polymer brush theories (scaling or exact), and so highlights the graft co-polymer architecture as a separate family of functional co-polymers. Compared to this, a linear di-block MMA-PEO co-polymer spread at different surface pressures (2 to 10 mN m⁻¹) at the air-water interface can be described by a two-layer model with the PEO block in the water subphase [30]. This interfacial layer exhibits visco-elastic properties, dominated by the PEO block of the co-polymer, different to the behaviour of either of the pure homopolymers [31].

1.3.1.1.1 SDS with comb polymers

Comb co-polymers can be thought of as graft co-polymers with shorter side-chains of relatively low grafting density. The adsorption behaviour of neutral comb co-polymer (PEOMEMA backbone and PEG grafts) with SDS at the air-water interface was compared to the adsorption

behaviour of pure PEG of different MW with SDS. The study was conducted using surface tension and ellipsometry measurements [32]. The adsorption isotherm of SDS was almost identical in the systems containing high MW linear PEG and that of the comb PEOMEMA-PEG co-polymer. In the case of low MW PEG linear polymer with SDS, the polymer is replaced by SDS at the interface in greater extent compared to the high MW polymer/SDS mixtures. This can be explained by a high adsorption driving force for higher MW polymer, as well as additional amphiphilicity introduced in the structure of comb co-polymer.

1.3.2 Oppositely charged complexes

The interactions between oppositely charged polymers and surfactants involve an ion-exchange process (electrostatic attraction) and hydrophobic interactions, which induce restructuring of the system after charge neutralisation.

Linear and branched polymer/surfactant systems were studied in aqueous solutions of polyethylenimine (PEI) and SDS at different pH [28]. The SDS adsorption was reported to be enhanced with branched PEI compared to the linear PEI, with the most significant difference observed at pH 10 when the PEI polymer becomes essentially non-ionic and the steric interactions become significant.

Strong interactions were described between SDS and pseudo cationic polyvinylpyrrolidone (PVP), studied at different concentrations using NR and surface tension [33]. Below cac, the SDS adsorption at air-water interface is enhanced, which is an evidence of cooperative interaction. At higher concentrations, the SDS is slightly depleted from the interface and effectively substituted at the interface by a bound layer of PVP to the surfactant layer, again confirming strong SDS/PVP interactions.

Interactions of SDS with a comb co-polymer containing high charge density cationic backbone (quaternary ammonium methacryloxyethyl trimethylammonium chloride, METAC) with PEO methyl ether methacrylate (PEO₄₅MEMA) side chains were investigated at the silica-water interface by NR [34]. The organisation of interfacial polymer/surfactant layer is dependent on the ratio of charged part of the co-polymer (METAC) to the uncharged side chains. When 90% of the co-polymer is charged, there were four regimes of the interfacial behaviour observed, including charge-neutralisation of the polymer/surfactant complexes. When the ratio of the charged METAC segment is decreased to 75% of the co-polymer structure, the formation of

charge-neutral polymer/surfactant complexes is reduced. The SDS instead adsorbs as micelles/aggregates and interacts with the pre-existing layer of the comb co-polymer, causing the swelling of the PEO₄₅MEMA side chains from a mushroom to a brush-like regime.

In this work, systems containing neutral polymers with three different surfactants (anionic SDS, cationic DTAB and non-ionic C₁₂E₅) and a mixture of oppositely charged vesicle-forming surfactant and SDS are studied.

1.4 Foams

Foams are defined as dispersions of gas in a liquid or solid state [35], and are divided accordingly into liquid and solid foams (such as polyurethane foams or marshmallows). Liquid foams are further divided into capious (rich, dense and tight foam with small bubbles, for example shaving foam), billowing (large bubbles that may collapse easily), and lacy foams (lack richness and tightness, such as sea foam) [36-39]. Foams have a vast variety of applications [40], including but not limited to use in lightweight engineering materials [41], oil recovery, firefighting [42], packaging, food industry, pharmaceutical applications such as drug delivery [43], cosmetics and cleaning consumer products.

Pure liquids do not usually foam even though bubbles can be generated in the bulk. True foams are not formed due to the instability of the bubbles and the thin films stabilising them. An addition of a foaming agent is therefore required to produce stable foams by adsorbing at the interface providing stabilisation of the films, and, often lowering the surface tension too [44]. These agents can be of different shapes, such as simple amphiphilic surfactants [45], polymers [46], proteins [47] and solid nanoparticles [48]. The film stabilisation can be of steric (involving large polymers) or electrostatic (involving charge interactions and overlap of electrical double layers between the two surfaces of the foam films) characteristic. The electrostatic stabilisation is more long-ranged compared to the steric stabilisation, and therefore stabilises thick foam films rather than thin foam films [49]. Foams are often stabilised by a combination of two or more of such surface active species, as the combination of more than one species often provides improved foaming characteristics *via* synergistic effects, with the possibilities of tuning their specific interactions for a plethora of applications [40].

The mechanism of formation of close packed ordered crystalline structures in foams happens in a very short time scale and therefore cannot be guided solely by random kinetics. In addition, the interactions between bubbles in a foam system are of higher order than those observed for colloidal particles of comparable size. The observations of this internal ordering is therefore of a high scientific interest [4]. There are different length scales involved in foams (Figure 1.3), ranging from nanoscopic layers of single molecules adsorbed at the liquid-air interface and the thin films separating foam bubbles, through the microscopic channels and Plateau borders, all the way up to macroscopic foam bubbles encapsulating the dispersed gas phase [50].

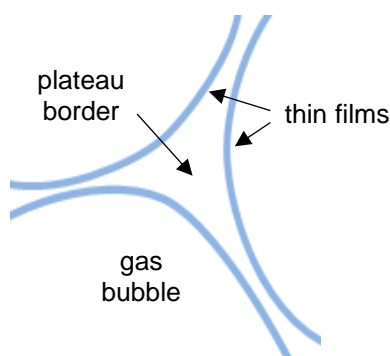


Figure 1.3 A schematic representation of the different length scales involved within a system of neighbouring foam bubbles.

To limit the complex multiple length scales behaviour of foams, isolated vertical films can be used as a method of simplification for studying mechanical properties of the interfaces [51]. If a study of the smaller length scale is desirable, such as in this work, a single air-water interface can be studied as an analogy of the thin film region stabilising individual foam bubbles (Figure 1.4).

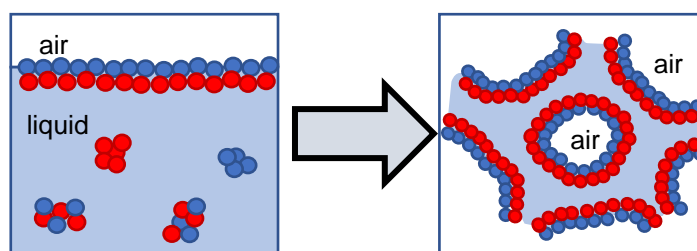


Figure 1.4 An analogy of the interfacial organisation of two surface active species at the air-water interface and when stabilising a foam bubble.

The two main properties of the foams are the foamability and the foam stability. The foamability is the ability of the solution to produce foam (*i.e.* the measure of the foam volume produced and the gas fraction) and is evaluated during the foam generation process. The foam stability is in contrast determined over time, as it is a measure of the foam lifetime [44]. In general, the foamability is considered to be better for solutions with lower viscosity and surface tension. In contrast, the foam stability is encouraged by higher viscosity and elasticity of the

solutions [52]. All foams are thermodynamically unstable and will eventually break down. The time it takes for foam destabilisation and breakdown can be increased by kinetically stabilising the foam, *e.g.* by slowing down the liquid drainage and limiting coalescence [53]. Extensive studies have been performed on the possible correlation of rheology [54], disjoining pressure [55] and single free-standing thin film stability [56], however no universally correct theory has yet been proposed. The disjoining pressure measurements can be linked to the kinetic stability of foams by influencing the liquid drainage [57]. Foams can further be stabilised by electrostatic or steric interactions in thin films [49], which are in turn governed by the molecular characteristics and interfacial structures involved. We therefore intend to link the interfacial structures of foam-stabilising polymer/surfactant mixtures to their foam behaviour [58], rather than just rheological properties and surface tension measurements. The interfacial structures and composition [59] can then be likened to the structures stabilising foam bubbles as each individual foam bubble is stabilised by two thin films at an air-water interface, separated by a channel of bulk liquid.

1.4.1.1 Techniques to study foam films

The effect of polyelectrolytes and polyelectrolyte/surfactant mixtures on the stability of foam films is the subject of many studies, highlighted in multiple reviews [60, 61]. Free-standing foam films are often used as analogues to macroscopic foams, and can be studied using thin film pressure balance (TFPB) [62], and scattering methods such as X-ray diffraction and small angle scattering [50]. While the thin film pressure balance is a productive method and information such as film thickness and disjoining pressure can be evaluated [63], no information of the film composition or structure can be gained. X-ray diffraction studies of thin black films have been reported in the early 1990s [64], with data analysis developed later [65]. The increase in hydrocarbon tail length of CTAB surfactant, from C₁₂TAB to C₁₄TAB was well correlated to the increase in foam film stability by TFPB [66] and the foam stability investigated by foam pressure drop technique [67]. However, the stability of thin films evaluated by TFPB does not always correlate exactly to the foam stability. The foam stability was found to be influenced by both the disjoining pressure and film elasticity. In some systems, such as polypropylene glycol, the surface forces (*i.e.* disjoining pressure measure) were found to be the major influencing factor, while in others (*e.g.* pentanol) it was the film elasticity [68].

1.4.1.2 *Interfacial rheology*

Foams have complex and unusual rheological behaviour (classified as Bingham plastics during flow and Kelvin solids under small deformation), low density, and high interfacial area, with characteristics of all three forms of matter [39, 69, 70]. Under small applied shear forces, the elastic behaviour is similar to solids. Under large applied shear forces, foams can flow and deform without breaking (they have a yield stress), similar to a liquid [70]. Foams behave like gas under pressure or temperature perturbations by changing their volume [39]. Film elasticity can be determined by measuring the surface dilatational rheology using an oscillating drop measurements [71, 72]. The correlation of interfacial rheology and foam films [73], macroscopic foam properties [74] and adsorption at air-water interface [75] have been discussed. The elastic and viscous moduli are determined from the change in γ (calculated from the profile of a pendant drop, using Young-Laplace fit) together with the change in the volume of the drop, which are plotted *vs* the time during the series of oscillations. The elastic and viscous moduli can be directly related to foam bubble stability. If the elastic modulus is small, and the viscous modulus is high, the foam bubble will burst if deformed. However, the major drawback of this technique is the inherent evaporation of water from the droplet surface, hence increasing sample concentration. The evaporation can be limited by enclosing the droplet in a receptacle containing few drops of the studied solution to ensure vapour saturation, yet the evaporation is still a limiting factor in precise measurements especially in systems containing low concentrations and slowly adsorbing species.

1.4.2 **Foam generation**

The foam generation proceeds in several stages (Figure 1.5). At first, a gas bubble is introduced to the bulk of the liquid. The surfactant molecules present in the bulk immediately align within the gas-liquid interface of the bubble. This structure then diffuses to the air-water interface, where, as the gas bubble rises from the liquid, an additional layer of surfactants is formed on the outside, forming lamella bilayer structure with a thin film of the liquid stabilised by surfactant molecules [36-38, 44]. This surfactant-stabilised structure is the building block of foams. The dominant effect during the initial stages of foam generation, controlling the volume of the foam, is believed to be the Marangoni effect (with the surface forces playing secondary role at low surfactant concentrations), which suppresses local thinning of the thin films [3]. In addition to surfactants, polymers can be used to increase viscosity which results in slower

drainage and so helps the bubble film to resist deformation. Impurities can provide additional surface plasticity.

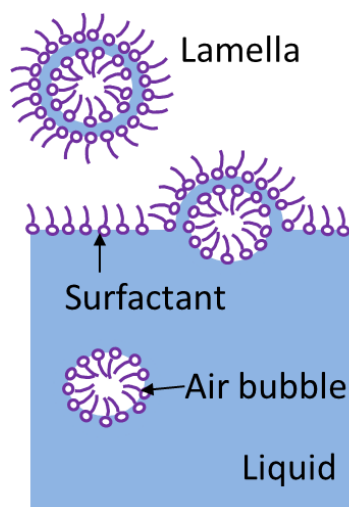


Figure 1.5 A representation of the formation of foam bubbles. The surfactants align at the air-water interface of a gas bubble as well as on the surface of the bulk liquid phase. A lamella structure stabilised by a layer of surfactants is then formed.

In certain cases foams aid detergency by incorporating oil in the lamellas between foam bubbles [76, 77]. Most often, foams aid in detergent effectiveness by clinging to the surface the foam has been applied to, which is especially useful when vertical surfaces are cleaned. Furthermore, foams or foaming agents are often parts of product formulations due to the consumer expectation and the misleading assumption that higher foamability means better detergency. In certain cases, such as in automatic dishwashers or laundry washing machines, foam production is unwanted and can lead to ineffective cleaning and malfunctions. Foam stability also plays role in detergency. In general, more stable foams require multiple rinsing which leads to water waste and consumer dissatisfaction. Higher foam stability is however preferred when suds are encapsulated within the foam lamella structures, as breakage of the foam would lead to redeposition of the suds and non-effective detergency.

1.4.3 Foam destabilisation

There are three main types of foam destabilisation, or destruction, mechanisms. The first of which is the drainage caused by the gravitational force and the surface tension gradients, forcing the liquid fractions of the foam to drain towards the liquid bulk and hence lowering the foam volume. The other two mechanisms of foam destabilisation are the Ostwald ripening or coarsening and the bubble coalescence (Figure 1.6). The coarsening is driven by the diffusion of gas across thin films from smaller to larger bubbles which causes the larger bubbles to grow, and the bubbles to deform into polyhedral structures. In comparison, the coalescence results in

a polydisperse system containing very large bubbles due to thinning and rupture of thin films separating individual bubbles [36-38].

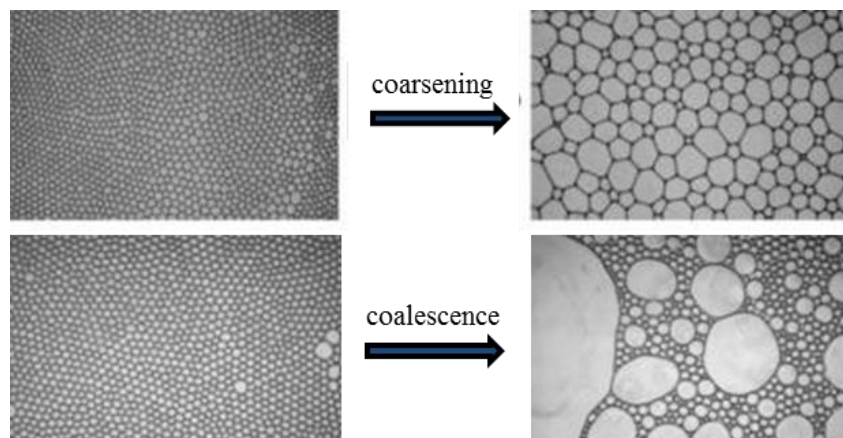


Figure 1.6 A representation of coarsening and coalescence destabilising processes within foam systems. Figure modified from [45].

The foam properties however depend on the surfactants used and the way of generating the foams itself [1]. The history of the sample can also play an important role when examining the interfacial properties. The interfacial adsorbed amount should not be determined solely based on observed surface tension values, as the foams are very often non-equilibrium systems with a possibility of exhibiting the cliff edge effect in surface tension [78]. When determining the foam stability (in other words, quantifying the destruction of the foam), the foam volume is measured as a function of time. Two well-defined regions of the foam decay were reported. At first, the foam volume decays rapidly over the first few seconds following foam formation (~10 s), followed by a much slower gradual decay which can last several hours for very stable foams. The foam stability and foamability are governed by different factors, and so a very stable foam may not be producing a large volume of the foam, and vice versa [3]. Regarding the foaming properties, it was shown in recent studies that the foamability and stability of the formed foam does not strictly correlate with neither the surface tension nor the surface elasticity [2, 3]. In addition, no real correlation between the thin film stability and foamability was yet established [51].

1.5 Polymers and surfactants studied

1.5.1 PEG and PVAc

Polyethylene glycol (PEG, or PEO) is a widely used polymer of ethylene oxide. It is used in various industrial applications, medicine and pharmaceuticals [79], drug delivery [80] often as a carrier of low molecular weight drugs, as a green reaction media [81], and a component of

many co-polymers. PEG is a non-toxic, biocompatible and FDA approved polymer, which can have a large range of molecular weights (routinely commercially available from 200 Da to ~100 kDa, even up to 8000 kDa in a powder form). PEG is biodegradable [82] and highly water soluble, both of these properties are highly desirable in formulations of consumer products such as cosmetics and detergents.

In addition to the use of pure PEG polymer, its complexes are often desirable in various industries. Conjugation of PEG and other chemical species, often biological molecules, is referred to as pegylation [83] and was first described in 1977 by Abuchowski [84, 85] and its effect on toxicity and immunogenicity was studied. Pegylation is often employed in the field of drug delivery [86], as PEG easily conjugates with biologically relevant molecules such as proteins and lipids [87, 88]. It is often used as one block of di- and tri-block copolymers, as well as side groups (or grafts) on polymeric backbones. It is less often used as the backbone, with a different polymer/monomer tethered onto it. This is therefore one of the novelties of the polymers described here, as both PEG-*g*-PVAc co-polymers contain a PEG backbone with tethered polyvinyl acetate (PVAc) grafts. Such architectures with hydrophilic backbone and hydrophobic side chains are not very usual yet are extremely useful as the polymer self-aggregates at low concentrations in water (~0.001-0.002 wt%, depending on the length and number of the PVAc grafts). Polyvinyl acetate (PVAc) is a polyvinyl ester, synthesised by free-radical polymerisation. PVAc is often used in graft copolymers, both as the backbone (PVAc-*g*-PLLA [89]) and as grafts (PAA-*g*-PVAc [90]). It can gain partial negative charge following hydrolysis [91]. The compatibility of PEG and PVAc polymers at the air-water interface was shown to depend upon the surface pressure, where the two polymers are compatible (PEG/PVAc attractive interactions) until the surface pressure exceeds the collapse surface pressure of PEG and the PEG/PVAc mixture then becomes independent of its composition [92].

1.5.2 PEG-*g*-PVAc co-polymers

Two neutral amphiphilic comb co-polymers comprising of PEG backbone and PVAc grafts were studied. Both polymers were synthesised using a radical initiator polymerisation on an industrial scale. The variation of the starting PEG chain MW and the ratio of PEG to PVAc, as well as temperature and other reaction conditions, leads to different length and grafting density of the PVAc side chains relative to the PEG backbone [93]. PEG-*g*-PVAc graft co-polymers can also be used as a precursor for synthesis of PEG-*g*-PVA (polyvinyl alcohol grafts) *via* the

PVAc graft hydrolysis. Such PEG-*g*-PVA co-polymers are then used as tablet coatings which can control release of the active ingredient [94].

PEG-*g*-PVAc co-polymers are patented for use as a greyness inhibitor for polyester and polyester/cotton blend fabrics [95] and included in formulations of laundry and dish-washing liquid [96] [97], mainly as a detergent additive to prevent soil redeposition [98, 99]. The comb co-polymer is efficient at solubilising soil and preventing its deposition onto fabrics after a wash cycle, working well in conditions other polymer architectures fail, specifically at higher water hardness level [100]. The polymers can also be used as a part of formulation used as a pre-wash treatment (so called 'pre-spotter') to remove hard-to clean soils (such as grass, blood, oil and other organic substances) without causing coloured fabrics to fade [101].

It is obvious these comb PEG-*g*-PVAc co-polymers are highly valuable to industry thanks to their superior cleaning properties; however, their interfacial properties and complexation with surfactants often found in product formulations have not been studied until now. The PEG-*g*-PVAc co-polymers used here were characterised using gas permeation chromatography (GPC, Appendix A) to gain indication of the M_n and the weight distribution (M_w/M_n). The ratios of PEG to PVAc was determined using NMR, with more insight into the structure, such as the grafting density and average length of the graft, provided by combination of ^1H NMR, ^{13}C NMR, and HCSQ NMR (Appendix B).

1.5.3 DEEDMAC vesicles

The system of oppositely charged surfactant mixture in this work contains SDS and a double tailed cationic surfactant DEEDMAC (diethyloxyester dimethylammonium chloride), which has been shown to form vesicles [102]. It was also shown before that SDS and DEEDMAC form complexes in aqueous solutions [103], yet the interfacial structures of such complexes have not been reported previously.

DEEDMAC is widely used in fabric softener formulations, owing to its fast biodegradability as well as adsorption properties onto textiles [104, 105]. The solid-liquid interface is therefore of immense relevance to the practical applications of the mixed DEEDMAC/SDS system and the interfacial structures (as well as bulk) are investigated.

1.6 Thesis outline

The aim of this thesis is to describe the interfacial behaviour of two neutral comb co-polymers and their interactions with surfactants at the air-water interface and its relevance to foaming behaviour, as well as complexation of charged cationic vesicles with an oppositely charged model surfactant.

Chapter 1 introduces polymer/surfactant interactions and the air-water interface.

Chapter 2 describes the main techniques used to probe the air-water interface: surface tension measurements, neutron and X-ray reflectivity.

Chapter 3 describes the interactions and interfacial structures and layer composition of SDS and PEG-*g*-PVAc co-polymer at the air-water interface, with correlation to their foaming behaviour. A transition from synergistic adsorption to competition with increasing SDS concentration was observed.

Chapter 4 compares the interfacial behaviour of cationic DTAB and the same PEG-*g*-PVAc co-polymer to the previous chapter. A distinct difference between the interfacial layer structure and composition was observed, dependent on the surfactant headgroup characteristics.

Chapter 5 finalises the comprehensive study of surfactant headgroup influence on interfacial layer structure and adsorption behaviour of polymer/surfactant mixtures by investigation of interactions between non-ionic C₁₂E₅ and PEG-*g*-PVAc co-polymer.

Chapter 6 focuses on the influence of polymer characteristics (of two PEG-*g*-PVAc co-polymers with varying length and number of PVAc grafts) and their influence on the interfacial properties of polymer/surfactant complexes investigated at the air-water interface.

Chapter 7 aims to study the interactions in a strongly interacting systems comprised of anionic SDS and vesicles formed by cationic surfactant DEEDMAC both in bulk and at interfaces.

Chapter 8 provides a summary of the results and highlights their relevance to the practical applications of the polymers and surfactants studied. Several possible areas for future work are suggested.

1.7 References

1. Eren, T., *Foam Characterization: Bubble Size and Texture Effect*. 2004, Middle East Technical University.
2. Kristen, N., et al., *No Charge Reversal at Foam Film Surfaces after Addition of Oppositely Charged Polyelectrolytes?* The Journal of Physical Chemistry B, 2009. **113**(23): p. 7986-7990.
3. Petkova, R., Tcholakova, S., and Denkov, N.D., *Foaming and Foam Stability for Mixed Polymer–Surfactant Solutions: Effects of Surfactant Type and Polymer Charge*. Langmuir, 2012. **28**(11): p. 4996-5009.
4. van der Net, A., et al., *The crystal structure of bubbles in the wet foam limit*. Soft Matter, 2006. **2**(2): p. 129-134.
5. Taylor, D.J.F., Thomas, R.K., and Penfold, J., *Polymer/surfactant interactions at the air/water interface*. Advances in Colloid and Interface Science, 2007. **132**(2).
6. Zhang, X.L., et al., *Adsorption of Polyelectrolyte/Surfactant Mixtures at the Air–Water Interface: Modified Poly(ethyleneimine) and Sodium Dodecyl Sulfate*. Langmuir, 2011. **27**(6): p. 2601-2612.
7. Markus, F. and Surachet, A., *Role of air - water interfaces in colloid transport in porous media: A review*. Water Resources Research, 2017. **53**(7): p. 5247-5275.
8. Olmeda, B., et al., *Pulmonary surfactant layers accelerate O₂ diffusion through the air-water interface*. Biochimica et Biophysica Acta (BBA) - Biomembranes, 2010. **1798**(6): p. 1281-1284.
9. Vazquez, G., Alvarez, E., and Navaza, J.M., *Surface Tension of Alcohol Water + Water from 20 to 50 .degree.C*. Journal of Chemical & Engineering Data, 1995. **40**(3): p. 611-614.
10. Eastoe, J. and Dalton, J.S., *Dynamic surface tension and adsorption mechanisms of surfactants at the air–water interface*. Advances in Colloid and Interface Science, 2000. **85**(2–3): p. 103-144.
11. Czajka, A., Hazell, G., and Eastoe, J., *Surfactants at the Design Limit*. Langmuir, 2015.
12. Högberg, I., et al., *The Interaction Parameter in Binary Surfactant Mixtures of a Chelating Surfactant and a Foaming Agent*, in *Trends in Colloid and Interface Science XXIV*, Starov, V. and Procházka, K., Editors. 2011, Springer Berlin Heidelberg. p. 17-20.
13. Fuchs-Godec, R., *The adsorption, CMC determination and corrosion inhibition of some N-alkyl quaternary ammonium salts on carbon steel surface in 2 M H₂SO₄*. Colloids and Surfaces A: Physicochemical and Engineering Aspects, 2006. **280**(1–3): p. 130-139.

Chapter 1

14. Maibaum, L., Dinner, A.R., and Chandler, D., *Micelle Formation and the Hydrophobic Effect*. The Journal of Physical Chemistry B, 2004. **108**(21): p. 6778-6781.
15. Hall, D.G., *Micellisation kinetics of ionic surfactants*. Journal of the Chemical Society, Faraday Transactions 2: Molecular and Chemical Physics, 1981. **77**(11): p. 1973-2006.
16. Zdziennicka, A., et al., *Critical micelle concentration of some surfactants and thermodynamic parameters of their micellization*. Fluid Phase Equilibria, 2012. **322-323**: p. 126-134.
17. Dominguez, A., et al., *Determination of Critical Micelle Concentration of Some Surfactants by Three Techniques*. Journal of Chemical Education, 1997. **74**(10): p. 1227.
18. Chang, C.-H. and Franses, E.I., *Adsorption dynamics of surfactants at the air/water interface: a critical review of mathematical models, data, and mechanisms*. Colloids and Surfaces A: Physicochemical and Engineering Aspects, 1995. **100**: p. 1-45.
19. Hansson, P. and Lindman, B., *Surfactant-polymer interactions*. Current Opinion in Colloid & Interface Science, 1996. **1**(5): p. 604-613.
20. Cabane, B. and Duplessix, R.J.J.P.F., *Organization of surfactant micelles adsorbed on a polymer molecule in water : a neutron scattering study*. 1982. **43**(10): p. 1529-1542.
21. Cabane, B. and Duplessix, R., *Neutron scattering study of water-soluble polymers adsorbed on surfactant micelles*. Colloids and Surfaces, 1985. **13**: p. 19-33.
22. Cabane, B. and Duplessix, R., *Decoration of semidilute polymer solutions with surfactant micelles*. Vol. 48. 1987.
23. Zana, R., Lianos, P., and Lang, J., *Fluorescence probe studies of the interactions between poly(oxyethylene) and surfactant micelles and microemulsion droplets in aqueous solutions*. The Journal of Physical Chemistry, 1985. **89**(1): p. 41-44.
24. Brown, W., Fundin, J., and Miguel, M.d.G., *Poly(ethylene oxide)-sodium dodecyl sulfate interactions studied using static and dynamic light scattering*. Macromolecules, 1992. **25**(26): p. 7192-7198.
25. Jones, M.N., *The interaction of sodium dodecyl sulfate with polyethylene oxide*. Journal of Colloid and Interface Science, 1967. **23**(1): p. 36-42.
26. Middleton, H., et al., *Interaction of Sodium Dodecyl Sulfate with Methacrylate-PEG Comb Copolymers*. Langmuir, 2005. **21**(11): p. 5174-5178.
27. Zhao, L. and Lin, Z., *Self-assembly of non-linear polymers at the air/water interface: the effect of molecular architecture*. Soft Matter, 2011. **7**(22): p. 10520-10535.
28. Wang, H., et al., *Binding of sodium dodecyl sulfate with linear and branched polyethyleneimines in aqueous solution at different pH values*. Langmuir, 2006. **22**(4): p. 1526-1533.

29. Peace, S.K., et al., *Organization of an Amphiphilic Graft Copolymer at the Air–Water Interface: A Neutron Reflectometry Study*. *Macromolecules*, 1998. **31**(4): p. 1261-1268.
30. Richards, R.W., Rochford, B.R., and Webster, J.R.P., *Organisation of an amphiphilic linear diblock copolymer at the air/water interface studied by neutron reflectometry*. *Faraday Discussions*, 1994. **98**(0): p. 263-281.
31. Richards, R.W., Rochford, B.R., and Taylor, M.R., *Surface Quasi-Elastic Light Scattering From Spread Monolayers of a Poly(methyl methacrylate)–Poly(ethylene oxide) Block Copolymer*. *Macromolecules*, 1996. **29**(6): p. 1980-1991.
32. Péron, N., et al., *Competitive Adsorption of Neutral Comb Polymers and Sodium Dodecyl Sulfate at the Air/Water Interface*. *The Journal of Physical Chemistry B*, 2008. **112**(25): p. 7410-7419.
33. Purcell, I.P., et al., *Adsorption of Sodium Dodecyl Sulfate at the Surface of Aqueous Solutions of Poly(vinylpyrrolidone) Studied by Neutron Reflection*. *Langmuir*, 1998. **14**(7): p. 1637-1645.
34. Moglianetti, M., et al., *Interaction of sodium dodecyl sulfate and high charge density comb polymers at the silica/water interface*. *Soft Matter*, 2009. **5**(19): p. 3646-3656.
35. Wilson, A.J., *Foams: Physics, Chemistry and Structure*. 1 ed. Springer Series in Applied Biology. 1989: Springer-Verlag London. 233.
36. Saadati, S., *Shaving Foam*, Department of Chemical Engineering University at Buffalo. Colloid & Surface Phenomena CE 527.
37. Piispanen, P.S., *Synthesis and Characterization of Surfactants Based on Natural Products*. 2002, Kungl Tekniska Hogskolan: Stockholm.
38. Hurcom, J., et al., *The interfacial structure of polymeric surfactant stabilised air-in-water foams*. *Soft Matter*, 2014. **10**(17): p. 3003-3008.
39. Weaire, D., *The rheology of foam*. *Current Opinion in Colloid & Interface Science*, 2008. **13**(3): p. 171-176.
40. Bureiko, A., et al., *Current applications of foams formed from mixed surfactant–polymer solutions*. *Advances in Colloid and Interface Science*, 2015. **222**: p. 670-677.
41. Lacroix, M., et al., *Silicon carbide foam composite containing cobalt as a highly selective and re-usable Fischer–Tropsch synthesis catalyst*. *Applied Catalysis A: General*, 2011. **397**(1–2): p. 62-72.
42. Hill, C. and Eastoe, J., *Foams: From nature to industry*. *Advances in Colloid and Interface Science*, 2017. **247**: p. 496-513.
43. Purdon, C., et al., *Foam Drug Delivery in Dermatology*. *American Journal of Drug Delivery*, 2003. **1**(1): p. 71-75.

44. Bureiko, A., et al., *Current applications of foams formed from mixed surfactant-polymer solutions*. Advances in Colloid and Interface Science, (0).
45. Denkov, N.D., et al., *The role of surfactant type and bubble surface mobility in foam rheology*. 2009. **5**(18): p. 3389-3408.
46. Alargova, R.G., et al., *Foam Superstabilization by Polymer Microrods*. Langmuir, 2004. **20**(24): p. 10371-10374.
47. Dickinson, E. and Izgi, E., *Foam stabilization by protein-polysaccharide complexes*. Colloids and Surfaces A: Physicochemical and Engineering Aspects, 1996. **113**(1): p. 191-201.
48. Binks, B.P. and Horozov, T.S.J.A.C.I.E., *Aqueous foams stabilized solely by silica nanoparticles*. 2005. **44**(24): p. 3722-3725.
49. Exerowa, D., et al., *Foam and wetting films: electrostatic and steric stabilization*. Advances in Colloid and Interface Science, 2003. **104**(1): p. 1-24.
50. Axelos, M.A.V. and Boué, F., *Foams As Viewed by Small-Angle Neutron Scattering*. Langmuir, 2003. **19**(17): p. 6598-6604.
51. Saulnier, L., et al., *Comparison between generations of foams and single vertical films - single and mixed surfactant systems*. Soft Matter, 2014. **10**(29): p. 5280-5288.
52. Bureiko, A., Trybala, A., Huang, J., Kovalchuk, N., Starov, V.M., *Effects of additives on the foaming properties of Aculyn 22 and Aculyn 33 polymeric solutions*. Colloids Surf. A, 2014(460): p. 265.
53. German, J.B., *Properties of stabilizing components in foams*. AIChE Symposium Series, 1990. **86**(277): p. 62-70.
54. Wasan, D.T., et al., *Foams, thin films and surface rheological properties*. Progress in Surface Science, 1992. **39**(2): p. 119-154.
55. Kristen, N., et al., *Foam Films from Oppositely Charged Polyelectrolyte/Surfactant Mixtures: Effect of Polyelectrolyte and Surfactant Hydrophobicity on Film Stability*. Langmuir, 2010. **26**(12): p. 9321-9327.
56. Klitzing, R.v. and Müller, H.-J., *Film stability control*. Current Opinion in Colloid & Interface Science, 2002. **7**(1): p. 42-49.
57. Lee, J., Nikolov, A., and Wasan, D., *Foam stability: The importance of film size and the micellar structuring phenomenon*. The Canadian Journal of Chemical Engineering, 2014. **92**.
58. Uhlig, M., et al., *New structural approach to rationalize the foam film stability of oppositely charged polyelectrolyte/surfactant mixtures*. Chemical Communications, 2020. **56**(6): p. 952-955.
59. Wilde, P.J., *Interfaces: their role in foam and emulsion behaviour*. Current Opinion in Colloid & Interface Science, 2000. **5**(3): p. 176-181.

60. Fauser, H. and von Klitzing, R., *Effect of polyelectrolytes on (de)stability of liquid foam films*. *Soft Matter*, 2014. **10**(36): p. 6903-6916.
61. Kristen, N. and von Klitzing, R., *Effect of polyelectrolyte/surfactant combinations on the stability of foam films*. *Soft Matter*, 2010. **6**(5): p. 849-861.
62. Stubenrauch, C. and Klitzing, R.v., *Disjoining pressure in thin liquid foam and emulsion films—new concepts and perspectives*. *Journal of Physics: Condensed Matter*, 2003. **15**(27): p. R1197.
63. Stubenrauch, C. and Klitzing, R.v., *Disjoining pressure in thin liquid foam and emulsion films—new concepts and perspectives*. *Journal of Physics: Condensed Matter*, 2003. **15**(27): p. R1197-R1232.
64. Platikanov, D., Graf, H., and Weiss, A., *X-ray scattering by black foam films*. *Colloid and Polymer Science*, 1990. **268**(8): p. 760-765.
65. Platikanov, D., et al., *X-ray scattering by black foam films: New data analysis*. 1993. **271**(1): p. 106-107.
66. Bergeron, V., *Disjoining pressures and film stability of alkyltrimethylammonium bromide foam films*. *Langmuir*, 1997. **13**(13): p. 3474-3482.
67. Stubenrauch, C. and Khristov, K., *Foams and foam films stabilized by C_nTAB: Influence of the chain length and of impurities*. *Journal of Colloid and Interface Science*, 2005. **286**(2): p. 710-718.
68. Wang, L. and Yoon, R.-H., *Effects of surface forces and film elasticity on foam stability*. *International Journal of Mineral Processing*, 2008. **85**(4): p. 101-110.
69. Cohen-Addad, S. and Höhler, R., *Rheology of foams and highly concentrated emulsions*. *Current Opinion in Colloid & Interface Science*, 2014. **19**(6): p. 536-548.
70. Höhler, R. and Cohen-Addad, S., *Rheology of liquid foam*. *Journal of Physics: Condensed Matter*, 2005. **17**(41): p. R1041.
71. Russev, S.C., et al., *Instrument and methods for surface dilatational rheology measurements*. 2008. **79**(10): p. 104102.
72. Thomsen, F., *Stretching exercises for drops*, in *KRUSS Application Report AR 246e*. 2005.
73. Santini, E., et al., *A surface rheological study of non-ionic surfactants at the water–air interface and the stability of the corresponding thin foam films*. *Colloids and Surfaces A: Physicochemical and Engineering Aspects*, 2007. **298**(1): p. 12-21.
74. Langevin, D., *Influence of interfacial rheology on foam and emulsion properties*. *Advances in Colloid and Interface Science*, 2000. **88**(1-2): p. 209-222.
75. Stubenrauch, C., et al., *Adsorption Behavior and Dilational Rheology of the Cationic Alkyl Trimethylammonium Bromides at the Water/Air Interface*. *The Journal of Physical Chemistry B*, 2005. **109**(4): p. 1505-1509.

Chapter 1

76. Stevenson, D.G., *The Role of Foam in Detergent Action*. Journal of the Society of Dyers and Colourists, 1952. **68**(2): p. 57-59.
77. Sonoda, J., Sakai, T., and Inomata, Y., *Liquid Oil That Flows in Spaces of Aqueous Foam without Defoaming*. The Journal of Physical Chemistry B, 2014. **118**(31): p. 9438-9444.
78. Campbell, R.A., et al., *New Perspective on the Cliff Edge Peak in the Surface Tension of Oppositely Charged Polyelectrolyte/Surfactant Mixtures*. The Journal of Physical Chemistry Letters, 2010. **1**(20): p. 3021-3026.
79. D'souza, A.A. and Shegokar, R., *Polyethylene glycol (PEG): a versatile polymer for pharmaceutical applications*. Expert Opinion on Drug Delivery, 2016. **13**(9): p. 1257-1275.
80. Knop, K., et al., *Poly(ethylene glycol) in Drug Delivery: Pros and Cons as Well as Potential Alternatives*. 2010. **49**(36): p. 6288-6308.
81. Chen, J., et al., *Polyethylene glycol and solutions of polyethylene glycol as green reaction media*. Green Chemistry, 2005. **7**(2): p. 64-82.
82. Zgola-Grzeskowiak, A., et al., *Comparison of biodegradation of poly(ethylene glycol)s and poly(propylene glycol)s*. Chemosphere, 2006. **64**(5): p. 803-809.
83. Bhadra, D., et al., *Pegnology: a review of PEG-ylated systems*. Die Pharmazie, 2002. **57**(1): p. 5-29.
84. Abuchowski, A., et al., *Alteration of immunological properties of bovine serum albumin by covalent attachment of polyethylene glycol*. J Biol Chem, 1977. **252**(11): p. 3578-3581.
85. Abuchowski, A., et al., *Effect of covalent attachment of polyethylene glycol on immunogenicity and circulating life of bovine liver catalase*. J Biol Chem, 1977. **252**(11): p. 3582-3586.
86. Veronese, F.M. and Pasut, G., *PEGylation, successful approach to drug delivery*. Drug Discovery Today, 2005. **10**(21): p. 1451-1458.
87. Zalipsky, S., *Chemistry of polyethylene glycol conjugates with biologically active molecules*. Advanced Drug Delivery Reviews, 1995. **16**(2): p. 157-182.
88. Bailon, P. and Berthold, W., *Polyethylene glycol-conjugated pharmaceutical proteins*. Pharmaceutical Science & Technology Today, 1998. **1**(8): p. 352-356.
89. Ding, N., et al., *Synthesis and Crystallization of Poly(vinyl acetate)-g-Poly(l-lactide) Graft Copolymer with Controllable Graft Density*. Industrial & Engineering Chemistry Research, 2013. **52**(36): p. 12897-12905.
90. Li, Y., et al., *Well-defined amphiphilic graft copolymer consisting of hydrophilic poly(acrylic acid) backbone and hydrophobic poly(vinyl acetate) side chains*. 2009. **47**(22): p. 6032-6043.

91. Karamyan, D.R., et al., *Kinetics of the Non-Catalysed Hydrolysis of Vinyl Acetate in an Aqueous Medium*. International Polymer Science and Technology, 2004. **31**(1): p. 49-51.
92. Kawaguchi, M. and Nishida, R., *Compatibility of polymer chains at the air/water interface*. Langmuir, 1990. **6**(2): p. 492-496.
93. Knecht, D., et al., *Multidimensional chromatographic techniques for hydrophilic copolymers: II. Analysis of poly(ethylene glycol)-poly(vinyl acetate) graft copolymers*. Journal of Chromatography A, 2006. **1130**(1): p. 43-53.
94. Gutzler, R., Smulders, M., and Lange, R.F.M., *The Role of Synthetic Pharmaceutical Polymer Excipients in Oral Dosage Forms – Poly(ethylene oxide)-graft-poly(vinyl alcohol) Copolymers in Tablet Coatings*. 2005. **225**(1): p. 81-94.
95. Kud, A., Trieselt, W., and Hartmann, H., *Use of graft polymers based on polyalkylene oxides as grayness inhibitors in the wash and aftertreatment of textile material containing synthetic fibers*. 1990: United States.
96. Schütz, T., et al., *Method of cleaning dishware*. 2009, The Procter and Gamble Company (One Procter & Gamble Plaza, Cincinnati, Ohio 45202, US).
97. Gopalkrishnan, S., et al., *Stable, aqueous concentrated liquid detergent compositions containing hydrophilic copolymers*. 1996, BASF Corporation (Mount Olive, NJ): United States.
98. Krinski, T.L. and Tran, T.H., *Method for improving the soil anti-redeposition properties of washing detergents and product*. 1992, Protein Technologies International, Inc. (St. Louis, MO): United States.
99. Gopalkrishnan, S., Guiney, K.M., and Sherman, J.V., *Modified polyacrylic acid polymers for anti-redeposition performance*. 1998, BASF Corporation (Mount Olive, NJ): United States.
100. Gopalkrishnan, S., et al., *Detergency boosting polymer blends as additives for laundry formulations*. 1998, BASF Corporation (Mount Olive, NJ): United States.
101. Sramek, J.A., *Low pH amphoteric fabric cleaning solution*. 2000, S. C. Johnson & Son, Inc. (Racine, WI): United States.
102. Basavaraj, M.G., et al., *Nanovesicle formation and microstructure in aqueous ditallowethylesterdimethylammonium chloride (DEEDMAC) solutions*. Journal of Colloid and Interface Science, 2014. **429**: p. 17-24.
103. Cocquyt, J., et al., *Interaction kinetics of anionic surfactants with cationic vesicles*. Colloids and Surfaces A: Physicochemical and Engineering Aspects, 2007. **298**(1): p. 22-26.
104. Giolando, S.T., et al., *Environmental fate and effects of DEEDMAC: A new rapidly biodegradable cationic surfactant for use in fabric softeners*. Chemosphere, 1995. **30**(6): p. 1067-1083.

Chapter 1

105. Kumar, A., et al., *Intact deposition of cationic vesicles on anionic cellulose fibers: Role of vesicle size, polydispersity, and substrate roughness studied via streaming potential measurements*. *Journal of Colloid and Interface Science*, 2016. **473**: p. 152-161.

2 Experimental methods

The air-water interface has been conventionally probed by surface tension (γ) measurements. With the development of synchrotron radiation, X-ray reflectivity (XRR) can be used to determine structural information of the interfacial layer. Neutron reflectivity (NR) further enables the composition, as well as the structure, to be determined via surface excess calculation. These three powerful techniques are described here.

2.1 Surface tension

2.1.1.1 Wilhelmy plate

The surface tension, γ , measured using the Wilhelmy plate method is related to the force (F) acting on the plate:

$$\gamma = \frac{F}{L \cos \theta}, \quad \text{Equation 2.1}$$

where L is the wetted length of the plate (*i.e.* the circumference of the plate to account for the total length where the sample is in contact with the plate), and θ is the contact angle between the plate and the liquid.

The platinum Wilhelmy plate was flamed before every measurement to ensure its cleanliness and surface activation (*i.e.* complete wetting hence θ is assumed to be 0°). F is then determined experimentally as a conversion of the change of mass detected by microbalance upon the plate contact with the liquid.

Long kinetic times can be studied using this instrument, until an equilibrium value is reached within a certain standard deviation (set to 0.01 mN m^{-1} between the last 5 measurements spaced 10 s apart). Using the K100 force tensiometer (Krüss GmbH) it is possible to set an automatic measurement series, during which a concentrated solution is gradually diluted with MilliQ and stirred between the measurements. The plate was not cleaned during the automatic acquisition mode between subsequent dilutions, which contributed to the measurement deviating from that of manually measured separate concentrations and was identified as the main fault of the

automatic measurement. The γ value determined straight after flaming (and therefore activating) was significantly higher than the one obtained using the automatic dilutions of the polymer solution (a difference of approximately 5 mN m^{-1}). This suggests there was some polymer adsorbed at the Wilhelmy plate throughout the measurement, hence lowering the apparent γ value. It was therefore concluded that this method should not be used with the polymer solutions, and all the measurements of polymers or polymer/surfactant mixtures were performed manually.

2.1.1.2 Surface excess

Surface excess (Γ) is the amount of adsorbed species at the interface per unit area. It is described as an excess as, strictly speaking, it is the difference in the concentration in a plane of the interface compared to an equivalent plane in the bulk of the liquid. To evaluate Γ , the Gibbs isotherm can be used to provide a quantitative description of the adsorption behaviour:

$$\Gamma = -\frac{1}{mRT} \left(\frac{\partial \gamma}{\partial \ln \frac{C}{C^0}} \right), \quad \text{Equation 2.2}$$

where m is the number of adsorbing species (1 for non-dissociating species and 2 for dissociating, *e.g.* ionic surfactants), R is the ideal gas constant, T is the temperature, γ is the surface tension, and C is the bulk molar concentration of surfactant and C^0 is 1 mol L^{-1} . The concentration can also be expressed as the bulk molar concentration C multiplied by activity coefficient f , which approaches 1 in dilute solutions. The Γ is inversely proportional to $\ln C$ due to the relationship between the chemical potential, μ , present in the system and the activity, a , of a surfactant takes form of [1]:

$$\mu = \mu^0 + RT \ln a. \quad \text{Equation 2.3}$$

Additionally, the area of a molecule adsorbed at the interface (or the headgroup in the case of simple surfactants) when a complete monolayer is formed can be calculated from Γ . This area referred to as the limiting molecular area, A_{cmc} , is therefore a measure of the packing ability of the surfactant (the lower the area per molecule the better the packing):

$$A_{cmc} = \frac{1}{\Gamma N_a}, \quad \text{Equation 2.4}$$

where N_a is the Avogadro constant.

The fact the surface excess is determined from the slope of the curve means there is an assumption that the surface excess is the same throughout the linear part of the surface tension curve (*i.e.* below the cmc). This is not necessarily physically true as the interfacial monolayer is not completely packed until the cmc is reached and the linear part of the surface tension curve does not account for this. Therefore another useful term is introduced to describe surfactant properties, and that is the surface coverage [2]. The surface coverage percentage can be determined from a plot of surface excess at given concentration *vs* the concentration, with the coverage reaching 100% above the cmc value of the surfactant. For this purpose, the surface excess is determined from the interfacial concentration of tritiated SDS and monitored by a flow-proportional counter [3]. The discrepancy between a direct measurement of the interfacial concentration at different bulk concentrations (*i.e.* surface excess) and the Gibbs determined surface excess calculated from a slope of the surface tension *vs* surfactant concentration explains a possible overestimation of certain molecular areas. Since the molecular area at the interface is inversely proportional to the surface excess, an underestimation of the surface excess from the slope of the linear part of the graph would lead to a higher than expected value for the molecular area. Calculations of the surface coverage at concentrations below SDS cmc suggest the interface is not saturated in part of the linear region, therefore the slope is expected to be lowered by this fact.

It is therefore highly desirable to determine the surface excess at various concentrations using other techniques, rather than purely surface tension data. Additionally, when it comes to mixtures of adsorbing species, such as polymer/surfactant complexes, it is not trivial to calculate Γ of the individual species from the Gibbs equation, especially for concentrations above cac [4]. Therefore, the reported surface excess data in this work was determined using neutron reflectivity at the air-water interface, described in detail later.

2.1.1.3 *Maximum bubble pressure*

Dynamic surface tension, γ_d , can be determined using the so-called maximum bubble pressure method [5, 6]. A glass capillary tip is immersed in a solution of studied liquid sample and a gas

bubble is formed at the tip of the capillary. The bubble curvature initially increases and at a critical point, corresponding to the bubble experiencing maximum pressure (p_{\max}), starts decreasing again.

The γ_d at time τ (measured between $\tau \sim 10$ ms - 4 min) is determined from the Young-Laplace equation (Equation 2.5, where p is the internal pressure of a spherical gas bubble, γ is surface tension and r is the radius of curvature), which when rearranged and taking into account the hydrostatic pressure due to capillary immersion (p_0) and the p_{\max} takes the form of Equation 2.6.

$$p = \frac{2\gamma}{r} \quad \text{Equation 2.5}$$

$$\gamma_d(\tau) = \frac{(p_{\max}(\tau) - p_0)r}{2}, \quad \text{Equation 2.6}$$

where r is the capillary radius which is determined experimentally from a calibration measurement of a liquid of known γ (usually MilliQ and/or other solvent).

Compared to the measurements performed using Wilhelmy plate method, much faster kinetics can be observed using the maximum bubble pressure tensiometer. Each new bubble formed at the tip of the capillary is a freshly formed interface and its $p_{\max}(\tau)$ is measured with only a few ms delay following the interface formation. This is especially valuable for samples with very fast surface adsorption, such as at high concentrations of surfactant solutions. This method enables us to differentiate between the behaviour of such systems, as well as their respective mixtures. However, we were unable to measure adsorption times higher than ~ 4 min, as the bubbles at the capillary tips become less stable in the liquid phase and often burst or migrate. The $p_{\max}(\tau)$ at each τ value was determined as an average of at least 10 bubbles kept at such τ and it is therefore not possible to evaluate samples with slow kinetics, such as low surfactant concentrations.

The two methods of γ determination are therefore deemed to be complementary to each other, as the small timescales of interfacial adsorptions can be investigated by the maximum bubble pressure method, while the slower adsorbing species, and the equilibrium γ , can be probed by the Wilhelmy plate method. The combination of the two techniques however does not provide

any information about the structural or compositional characteristics of the interface, and hence we employ X-ray and neutron reflectivity to elucidate the interfacial polymer/surfactant complex structures.

2.2 X-rays and neutrons

X-rays, sometimes referred to as Röntgen radiation in his honour, were first discovered by Röntgen in 1895 [7], who named them X-rays to signify their unknown nature at the time, and later received the first ever Nobel Prize in Physics for his discovery. It is now known that X-rays are high energy (range of 120 eV to 120 keV) electromagnetic waves with wavelengths (λ) corresponding to the distance between atoms of molecules and are hence well suited to study the structures of a range of materials from single crystals to nanoscale assemblies. A first example of employing X-ray to produce diffraction from crystals [8], followed by the discovery of crystal lattice structures specific to different materials (rock salt, calcite, zinc blends and iron pyrites) [9, 10]. The distance between atoms in crystal lattice (d), and thus the structure of studied material, can be determined using the Bragg equation from the known λ and incident angle (θ):

$$n\lambda = 2d \sin\theta . \quad \text{Equation 2.7}$$

Since the early 1900s, a lot of effort has been invested into perfecting the use of X-rays to study diffraction patterns of systems varying from simple single crystal structures to DNA double helix [11, 12], proteins [13] and large nanomolecules [14].

About 10 years after the discovery of X-rays, α -radiation was defined by Rutherford as a charged helium atom [15]. Chadwick then found out that bombardment of beryllium by α -radiation resulted in emitted penetrating radiation. This radiation was assigned to a particle with mass of 1 u and no charge, and so the neutron was discovered in 1932 [16]. Soon after, it was discovered that neutrons scattered following their collision with nitrogen nuclei in presence of nitrogen gas [17].

Following their discoveries and early studies, both X-rays and neutrons have found their use in medical applications such as imaging [18] and therapy [19, 20], as well as analytical techniques, such as small angle X-ray and neutron scattering (SAXS and SANS) [21, 22], grazing incidence small angle scattering (GI-SAXS and GI-SANS) [23, 24], X-ray

photoelectron spectrometry (XPS) [25] and X-ray and neutron reflectivity (XRR and NR) [26-29], which were used predominantly in this work.

2.2.1 X-Ray and neutron reflectivity

First XRR experiment was described in 1954 by Parrat, where total reflection of X-rays from a layer of evaporated copper on glass was studied [30]. Then, Parrat postulated the technique could be used to study surface properties which involve electron density variation with depth of the interfacial layer. NR is a relatively new technique, comparatively. It was first described in late 1980's by Felcher *et al.* as means to study superconductors and ferromagnets and their magnetic depth profiles [31]. This technique was quickly adopted by the soft matter scientists to study soft matter at interfaces, especially pioneered by the groups of Penfold and Thomas [32, 33]. Polymers and their mixtures are often subject of XRR and NR studies, pioneered by the group of Russell [34, 35].

2.2.1.1 X-ray synchrotron

The development of synchrotron facilities provides higher flux (or brightness) X-rays compared to bench-top X-ray tubes [36, 37]. In synchrotrons, electrons are produced with an electron gun, accelerated and transferred to the booster ring *via* linac (linear accelerator). The booster ring contains bending magnets which increase the electron energy up to 3 GeV. The accelerated electron beam then travels to the storage ring, where it passes through magnetic fields created by bending magnets, wigglers or undulators and loses energy in the form of X-rays. The emitted X-rays travel through the linear parts adjoined to the storage ring, otherwise known as beamlines. In this work, the I07 beamline at Diamond Light Source (a third generation synchrotron, UK) [38] was used for XRR data collection [39, 40].

2.2.1.2 Neutron generation

The NR data in this work was collected at two separate beamlines: FIGARO at Institut Laue-Langevin (ILL, France) and INTER at ISIS (UK). The two facilities employ different ways of neutron generation: ILL is a nuclear reactor source while ISIS uses spallation. In a nuclear reactor, neutrons are released following a fission chain reaction of uranium-235 in a cold reactor source [41]. In a spallation source [42, 43], accelerated negatively charged ion beam is passed through a thin layer of foil producing a proton, which is in turn accelerated in a synchrotron increasing its energy using bending magnets. The protons of sufficient energy then hit tungsten target and produce neutrons. The main difference in data obtained at the two

facilities is in the way the background is treated. The data from FIGARO beamline has some background subtraction included in the reduction and normalisation process, as the overall flux is much higher and so the background count is much higher too. The treatment of the INTER beamline data does not include any background subtraction, as the background intensity is generally smaller than that at ILL and can be fully accounted for during the fitting procedure.

2.2.1.3 General principles of reflectivity

During a reflectivity measurement, a sample of certain thickness, t , is placed on a clean substrate, in the case of studies performed at the air-water interface, the sample is poured into an adsorption trough, with the bulk liquid phase essentially acting as the substrate. An incoming monochromatic X-ray or neutron beam at a grazing incident angle, θ_i , is reflected from the surface (and each subsequent layer) at an angle θ_r with an intensity which is detected (Figure 2.1a). A scattering vector, Q , can be calculated from the incident angle, θ , and the wavelength of the incoming beam, λ :

$$Q = \frac{4\pi\sin\theta}{\lambda}. \quad \text{Equation 2.8}$$

When the reflectivity is plotted against the scattering vector, Q , oscillatory features called Kiessig fringes characteristic of thin adsorbed layers [44] are observed in case of ordered thin film layers. Reflectivity of multilayers with periodic spacing show similar XRR curve to crystalline matter, demonstrated by a series of sharp Bragg peaks [45] rather than Kiessig fringes. A plot of reflected intensity, R , vs Q (Figure 2.1) gives us information about the roughness, σ , and surface coverage, and arguably most importantly the thickness of the sample layer, t , can be calculated from the fringe spacing, ΔQ , using the Equation 2.9

$$t = \frac{2\pi}{\Delta Q}. \quad \text{Equation 2.9}$$

Specular reflectivity correlates to structures perpendicular to the plane of the interface, whereas off-specular reflectivity correlates to the structures parallel to the plane of the interface [46]. This means that thickness of an interfacial layer is probed by specular reflectivity, however this is insensitive to any spatial structuring along the interface. In this work, specular reflectivity

was used. Due to the large influence of surface σ on the shape of the reflectivity profile (Figure 2.1b), film t determination purely from fringe spacing is not an infallible method, and reflectivity data is therefore often fitted to a simulated curve based on a physical model described later, in section 2.2.3. The data is fitted to a scattering length density profile perpendicular to the surface.

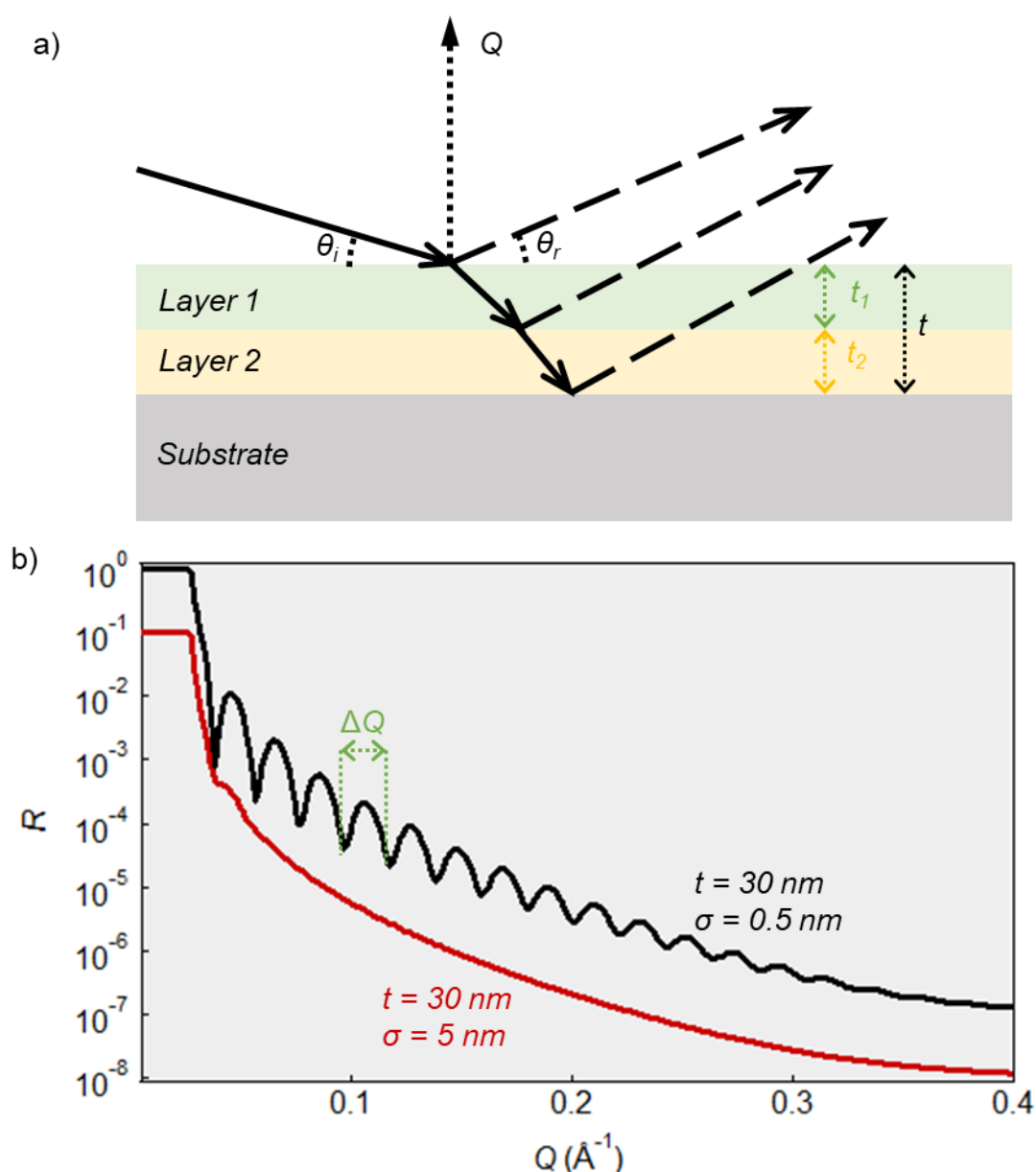


Figure 2.1 a) schematic representation of a reflectivity experiment setup, where the X-ray or neutron beam hits the interface at θ_i and is reflected from any structured layer at the interface. A simulated XRR curve of a 30 nm film adsorbed at interface is shown in b), as R plotted vs Q . In black are shown Kiessig fringes typical for ordered thin films. The influence of roughness, σ , on the shape of typical XRR curve is demonstrated by comparison to the simulated curve of 30 nm thick film with higher σ (5 nm, compared to 0.5 nm in black).

2.2.1.4 Scattering length density

The scattering length density (SLD), ρ , is the sum of scattering lengths per unit volume, V . The X-ray scattering length, f , scales directly with the number of electrons. However, the neutron scattering length (or coherence length, b), does not scale linearly with the atom size but rather with the number of neutrons and is therefore especially sensitive to different isotopes, best demonstrated by the difference in b value between H ($-3.739 \times 10^{-5} \text{ \AA}$) and D ($6.671 \times 10^{-5} \text{ \AA}$).

Due to the different scattering lengths associated with the same atom depending on the technique, we distinguish between the neutron scattering length density, ρ_N (Equation 2.10), and the X-ray scattering length density, ρ_X (Equation 2.11):

$$\rho_N = \frac{1}{V} \sum_i n_i b_i \quad \text{Equation 2.10}$$

and

$$\rho_X = \frac{1}{V} r_e \sum_i n_i f_{1i}, \quad \text{Equation 2.11}$$

where V is the volume of the molecule or molecular fragment in question, r_e is the Thomson scattering length $2.818 \times 10^{-5} \text{ \AA}$ (the classical radius of an electron) [47]. The values for scattering lengths of specific elements were taken from [48] and [49] and are presented along the calculated ρ values in Table 2.1 .

Table 2.1 List of a) scattering lengths of the atoms and b) the scattering length densities of molecules relevant to the studied systems.

a)	b (10^{-5} \AA)	f
C	6.646	6.00796
H	-3.739	0.99998
D	6.671	-
O	5.803	8.02360
N	9.36	7.01406
S	2.847	16.20291
Na	3.63	11.06797
Br	6.795	32.66480

b)	ρ_N (10^{-6} \AA^{-2})	ρ_X (10^{-6} \AA^{-2})
PEG-g-PVAc (Polymer A)	1.031	10.678
PEG-g-PVAc (Polymer B)	0.989	10.636
SDS headgroup	5.821	26.686 - 32.802
h-SDS	0.396	10.94
d-SDS	6.854	-
DTAB headgroup	0.184	8.881 - 14.133
DTAB	-0.233	9.517
d-DTAB	5.133	-
C ₁₂ E ₅ headgroup	0.652	10.434
C ₁₂ E ₅	0.129	9.098
d-C ₁₂ E ₅	3.841	-
C ₁₂ H ₂₅ tail	-0.39	7.773
C ₁₂ D ₂₅ tail	7.004	-
H ₂ O	-	9.414
D ₂ O	6.373	-
ACMW	0	-

2.2.2 XRR and NR experimental set-up

2.2.2.1 *Reflectivity at air-water interface*

The samples were poured into a Teflon trough, until a clear meniscus was observed above the level of the trough to ensure the reflectivity observed is coming from the sample rather than the trough itself. The samples were poured into a sample chamber with 4 up to 7 different positions (depending on the beamline). The lateral alignment of the sample contained in the adsorption trough in the horizontal plane of the beam was performed at the start of an experiment *via* optical method. The much larger length and width of the trough, and therefore the produced air-water interface, relative to the beam size ($\sim 5 \times 15$ cm trough size compared to few hundred μm beam size) allowed for a relatively relaxed requirements for such alignment procedure. The vertical alignment, however, was performed before each measurement, as to allow for any evaporation and differences between samples. During an XRR experiment, the height scan was performed using X-rays, and the beam was aligned to the centre of the sigmoidal decline of reflectivity (from a position where null beam intensity is detected due to a complete blockage of the beam by the trough and its metal holder, the sample is continually moved downwards so that the beam hits the sample and reflection is seen, until direct beam is detected when the beam is hitting air above the sample level). In an NR experiment, the sample height was determined by using a laser calibrated to a singular height alignment of the pure solvent.

2.2.2.2 *Reflectivity at solid-air and solid-liquid interface*

The sample alignment at solid-air or solid-liquid interface XRR involves precise alignment along the beam and in the horizontal plane of the beam, in addition to the above vertical alignment, using the ‘bending mica’ method in a custom build XRR liquid cell, described elsewhere [50, 51]. In summary, a cleaved piece of mica is fixed onto a steel stage of truncated cylinder geometry. The gentle bending of the mica provides a flat surface along the apex of the cylinder with radius of 7.5 cm. The reason for using mica instead of a flat Si wafer surface is the possibility of a direct comparison of measurements performed using the surface force apparatus (SFA) with the XRR data. Additionally, the charge density of mica is ~ 3 times larger than that of Si wafer [52], hence the adsorption of cationic species on the negatively charged mica surface would be more encouraged compared to Si surface.

2.2.2.3 Beamlines

2.2.2.3.1 I07 Beamline at Diamond Lights Source (DLS, UK)

XRR data at both air-water and solid-liquid interfaces was collected at the I07 beamline at Diamond Light Source (DLS, UK) [39]. The beam energy selection is enabled by using a double-crystal monochromator (DCM) with a set of two cryo-cooled Si(111) crystals, and a translation stage on the second one. The energy is changed by changing the Bragg angle, and the maximum flux at given energy is achieved by optimising the gap of the insertion device. The X-rays of selected energy (12.5 keV in this work) are then focused using a pair of mirrors, allowing control over the size of the beam, as well as acting as a low-pass filter. The schematic representation of the beamline is shown in Figure 2.2.

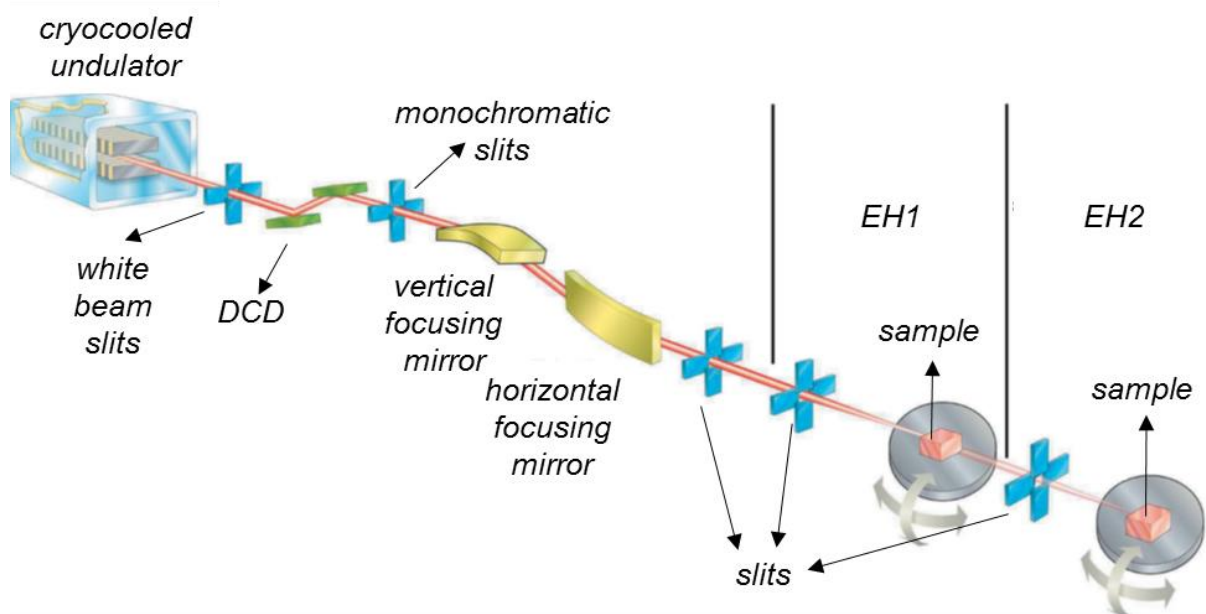


Figure 2.2 Outline of the I07 beamline. Figure taken from [39].

The size of the beam hitting the sample is controlled by the focusing mirrors as well as a set of slits. For our experiments, the beam size was approximately 120 μm vertical by 300 μm horizontal (full width at half-maximum, FWHM). A set of attenuators enables data collection from both low and high scattering regions of the sample surface without oversaturating the detector. The attenuators are a set of 12 UHV linear actuators with aluminium discs of varying thickness and molybdenum filters, with a final attenuator made of a thick lead disc to completely block the beam. The attenuators are used during a $\theta - 2\theta$ scan where the beam intensity drops with increasing θ angle and so attenuators are removed subsequently to collect a scan of the desired Q range with statistically significant intensity (where the detector count is >1000 at any Q value). Because of the use of different attenuators at different values over

the desired Q range, the data recorded for one sample needs to be “stitched” together afterwards. This is achieved by recording at least 3-5 data points at a high and low attenuation to obtain overlapping data points, for which the XRR data points for higher Q are then multiplied by the ratio of the two overlapping parts of the curve. The data is always normalised and plotted as an intensity in arbitrary units, therefore this data manipulation does not interfere with further data analysis.

It is possible to define two separate regions of interest (ROI) on the detector, one where the reflected beam hits the detector (ROI 1) and the second one (ROI 2) not in the path of the direct beam. It is then possible to subtract the overall intensity count from ROI 2 from the ROI 1, essentially allowing for background subtraction. This process is not 100% reliable, however it does limit the background contribution to minimum. However, this often also contributes to a loss of any faint Kiessig fringes in higher Q region, or even leads to an over-subtraction of data, and this background subtraction process was therefore omitted in the reported data. Instead, the reflectivity arising from the background was accounted for during the fitting procedure by fitting a non-zero value to the background contribution to the reflectivity curve.

When performing measurements at solid surfaces/interfaces, a hexapod is used to mount the sample and allows movement along its three axes (x , y and z), as well as rotations around each of these. In this case, the detector used is a Pilatus (an area detector Pilatus 100K, and a large-area detector Pilatus P2M are available). However, it is not possible to change the incident angle by rotation of the hexapod axis with air-water interfaces as the water level is governed by gravity and will not tilt. To overcome this limitation, a double crystal deflector (DCD) is used to deflect the X-rays and the reflected beam is tracked with diffractometer, while the sample remains stationary. This is achieved using two crystals, InSb(111) and InSb (220) and the rotation of the assembly of these crystals around the beam to change the incidence angle. The scattered X-rays are detected by the diffractometer detector rotations, either set up for XRR of grazing-incidence diffraction. This set-up has been used extensively in this work, as well as previously reported studies on thin films [53-55]. The beamline is capable of performing not only XRR measurements, but also surface X-ray diffraction (SXRD) [56], grazing-incidence small angle X-ray scattering (GISAXS) [57, 58], grazing-incidence wide-angle X-ray scattering (GIWAXS) [59], and coherent X-ray diffraction (CXD) for certain particle size [60]. It contains two experimental hutches (EH): EH1 which is used for XRR measurements,

amongst others, and EH2 to which the beam is delivered in vacuum flight tube and so allows studies of *in situ* grown samples in UHV using a large 2+3 diffractometer.

2.2.2.3.2 FIGARO Beamline at Institut Laue-Langevin (ILL, France)

The Fluid Interfaces Grazing Angles ReflectOmeter (FIGARO) is a horizontal neutron reflectometer at the ILL (Figure 2.3), developed to enable reflectometry measurements at liquid-air interface in addition to solid interfaces [61]. It is a high-flux time-of-flight reflectometer, where the neutron wavelength is controlled using frame overlap mirrors that act as a transmission filter and remove neutrons with λ above certain value, and a four-disc chopper assembly that controls the λ range of pulsed neutrons. Two Ni/Ti supermirrors act as deflectors and can be used to vary the angle of neutron beam approach relative to the interface studied from either below or above the interface horizon. The neutron beam then enters the collimation guide, where it is focused horizontally, followed by a set of four boron carbide collimation slits which define the beam size. The sample is mounted on an active anti-vibrational unit, and its position can be controlled by two flexible crossed goniometers, coarse and fine vertical translational stages, and a horizontal translational stage. Beam attenuator is used when the direct beam data is measured in order not to oversaturate the area detector.

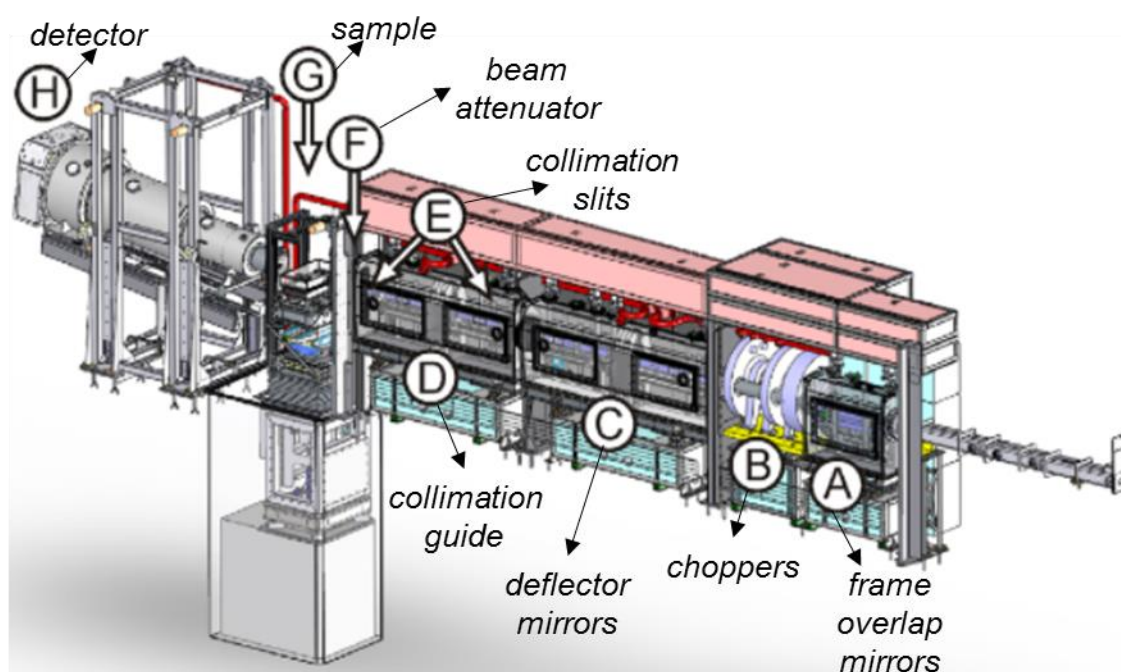


Figure 2.3 Schematic of the FIGARO beamline, highlighting the main components. Figure taken from [61].

2.2.2.3.3 INTER Beamline at ISIS (Didcot, UK)

The INTER beamline was the first beamline to measure neutron at the Target Station 2 (TS2) at ISIS (UK) [62, 63]. TS2 is a grooved composite moderator which provides a high flux of long-wavelength neutrons compared to the hydrogen moderator of TS1. A schematic representation of INTER is shown in Figure 2.4. The beam is guided to a set of choppers, of which the first one attenuates the spectrum of neutrons produced and the second chopper in the series defines neutron λ s (or the instrument bandwidth). The neutron beam is then directed through a set of frame-overlap mirrors and *via* fine collimation slits. As the instruments is optimised for use on liquid interfaces, a supermirror is used to direct the beam onto the sample, rather than employing sample rotation (as in beamlines optimised for solid interfaces). Just before the sample, a monitor is located to measure the incident wavelength distribution. Past the sample is again a series of slits and the low-background ^3He detector with adjustable sample-to-detector distance. The low background noise means that the background does not need to be subtracted from the data obtained at the INTER beamline.

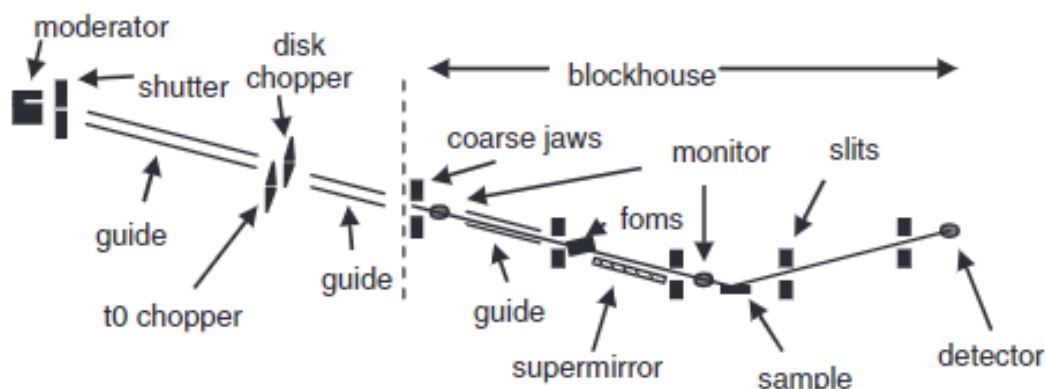


Figure 2.4 A schematic representation of the INTER beamline. Figure is taken from [63].

2.2.3 Data fitting

Before starting the fitting procedure, all possible scenarios of polymer/surfactant complexation and/or competition at the interface were considered. Based on γ data, and current knowledge, the surfactant was shown to be more surface active compared to the polymer and would therefore be expected to be found at the top layer of the interface, *i.e.* the surfactant hydrocarbon tails sticking into the air subphase and the headgroups with associated counterions solvated closer to the water subphase. However, at low concentration of a surfactant, the surface tension points towards synergistic effect and therefore we expect certain amount of complexation. We therefore must consider many possibilities for our fitting, each representing a slightly different physical model.

The first question is the number of layers we use to fit our samples. Each fitted layer is characterised by its own scattering length density, ρ , allowing us to determine the chemical composition of the layer, accounting for its physical characteristics with thickness, solvation and roughness determination. In general, the more layers there are included in our fitted model, the more information we have about the system. The main disadvantage of this approach is so-called over-fitting of the data, by assigning too many layers to a system where a smaller number of separate layers produces satisfactory fit.

In this study, we therefore start with fitting a 1-layer model only. This layer is assumed to be a homogeneously mixed surfactant/polymer complex at the interface. This model therefore does not distinguish the position of the species relative to the interface, however, is useful as an initial approach, as the overall thickness of the layer can be approximated in this way. Additionally, the data is fitted well using the 1-layer model at very low surfactant concentration, again pointing towards a complexation of polymer and surfactants at the interface.

At higher surfactant concentrations, at least 2-layer model must be used to fit the data. In a 2-layer model, surfactant is fitted as one layer and the polymer as the second layer. The position of these layers relative to the interface can be changed, and so the surface activity of the species can be determined relative to each other. The surfactant can also be separated into two distinguished layers, with the hydrocarbon tail as one layer and the head group (with counterions if present) as a second group. In this case, the fitting then consists of 3-layers, with a layer for the polymer being the third layer. Because we are dealing with air-water interface, we must account for the roughness of capillary waves at the water surface itself ($\sim 3 \text{ \AA}$) [64, 65], which increases relative to decreasing surface tension at higher surfactant concentrations [66]. We have therefore decided not to fit the graft polymers as two separate layers, as the grafts (or pendant PVAc groups) are only few \AA long and the roughness associated with the layer would have to be higher than the thickness. This is not trivial to convert into a physical model, and therefore we only use 1-layer to fit the polymer. It is of note to mention trial fitting with 2 layers for the polymer (separate PEG backbone layer and second layer for PVAc grafts) did not yield better fits (lower χ value) either way. In certain situations, the thickness of the surfactant head group is very similar to its roughness, however the ρ for the head groups varies hugely between the hydrocarbon tail and the head group and so the separate layer can still be

distinguished. Additionally, where the 3-layer model was used it is because it significantly improved the quality of the fit compared to a fit using single layer for the surfactant.

In the case of XRR, the charged surfactant headgroup has a much larger ρ compared to the hydrocarbon tail. A big portion of the contribution towards the ρ is from the associated counterion of the headgroup. In aqueous solutions, the counterion is likely to dissociate. This can be reflected in either higher solvation of the layer given to the head group, as well as change in the ρ for the given head group.

Multiple models were used to fit the data obtained for mixed polymer/surfactant systems:

- a) 1 completely mixed layer of polymer/surfactant complex, with the SLD calculated from ratio of the two components
- b) 2-layer model: top layer composed of the surfactant, with a separate layer for the polymer
- c) 2-layer model: top layer composed of surfactant hydrocarbon tail, with a mixed layer of surfactant headgroup and polymer beneath
- d) 2-layer model: top layer containing a mixture of surfactant tails and polymer, with surfactant headgroups beneath
- e) 2-layer model: top layer composed of polymer with layer of surfactant beneath
- f) 3-layer model: top layer composed of surfactant hydrocarbon chain, middle layer attributed to the surfactant headgroup, with the last layer occupied by the polymer

2.2.3.1 Neutron and X-ray practical comparison

There is an inherent difference between the NR and XRR data, as neutrons can penetrate deeper into materials compared to X-rays, *i.e.* NR “sees” the nuclei of atoms rather than the electron cloud probed by XRR. It is therefore not unreasonable to obtain fitted values of t , ρ and φ determined by the two techniques that do not match exactly.

In general, NR measurements take longer than XRR. Compared to ~ 30 min for 3 scans of XRR for one sample, the NR measurement is on the order of ~ 1 hr if the whole Q range accessible is measured, plus each system is measured in 4 different isotopic contrasts. The time needed for measurements is clearly a limiting factor in the accessibility of the NR measurements, but the advantages are numerous. As mentioned before, the isotopic labelling enables highlighting certain parts of molecules or mixed systems (in our case the hydrophobic tails of the

surfactants). Thanks to the multiple measurements of one system in different contrasts, the composition of the interface can be determined, both by co-fitting the curves but more importantly by direct calculation of the Γ of the two adsorbing species. Such Γ calculation is not possible from XRR data.

2.2.3.2 Surface excess determination from NR data

The Γ (the amount of species at the interface per unit area) can be estimated from surface tension measurement using the Gibbs isotherm (Equation 2.2). This method fails to account for mixed surfactant/polymer adsorption, especially above their cac [4, 67].

In this work we therefore calculate Γ from NR data obtained from samples in ACMW, using

$$\Gamma = \frac{\rho_N t}{N_A n_b}, \quad \text{Equation 2.12}$$

where ρ_N is the neutron scattering length density, t is the fitted thickness, N_A is the Avogadro constant, and n_b is the scattering length of the material.

Rearranging the above equation gives us:

$$\rho_N t = \Gamma (N_A n_b) \quad \text{Equation 2.13}$$

For a mixed polymer/surfactant system, the total surface excess, Γ , is equal to the sum of the surface excess of the polymer, Γ_{Pol} , and the surface excess of the surfactant, Γ_{h-surf} or Γ_{d-surf} . The above equation then takes form of [68]

$$\rho_{N(d-surf)} t_{d-surf} = \Gamma_{d-surf} (N_A n_{b(d-surf)}) + \Gamma_{Pol} (N_A n_{b(Pol)}) \quad \text{Equation 2.14}$$

And

$$\rho_{N(h-surf)} t_{h-surf} = \Gamma_{h-surf} (N_A n_{b(h-surf)}) + \Gamma_{Pol} (N_A n_{b(Pol)}) \quad \text{Equation 2.15}$$

From Equation 2.14 and Equation 2.15, the surface excess of polymer, Γ_{Pol} , can be determined as following:

$$\rho_{N(d-surf)}t_{d-surf} = \Gamma_{d-surf}(N_A n_{b(d-surf)}) + \Gamma_{Pol}(N_A n_{b(Pol)}) \quad \text{Equation 2.16}$$

$$\rho_{N(d-surf)}t_{d-surf} = N_A * (\Gamma_{d-surf}n_{b(d-surf)} + \Gamma_{Pol}n_{b(Pol)}) \quad \text{Equation 2.17}$$

$$\frac{\rho_{N(d-surf)}t_{d-surf}}{N_A} = \Gamma_{d-surf}n_{b(d-surf)} + \Gamma_{Pol}n_{b(Pol)} \quad \text{Equation 2.18}$$

$$\Gamma_{Pol}n_{b(Pol)} = \frac{\rho_{N(d-surf)}t_{d-surf}}{N_A} - \Gamma_{d-surf}n_{b(d-surf)} \quad \text{Equation 2.19}$$

Substituting the surface excess of polymer, Γ_{Pol} , back into the mixed system then gives us:

$$\rho_{N(h-surf)}t_{h-surf} = N_A * (\Gamma_{h-surf}n_{b(h-surf)} + \Gamma_{Pol}n_{b(Pol)}) \quad \text{Equation 2.20}$$

$$\rho_{N(h-surf)}t_{h-surf} = N_A * (\Gamma_{h-surf}n_{b(h-surf)} + \frac{\rho_{N(d-surf)}t_{d-surf}}{N_A} - \Gamma_{d-surf}n_{b(d-surf)}) \quad \text{Equation 2.21}$$

We assume that the surface excess of surfactant is independent on the deuteration, and $\Gamma_{h-surf} = \Gamma_{d-surf} = \Gamma_{surf}$. Therefore:

$$\rho_{N(h-surf)}t_{h-surf} = N_A * (\Gamma_{surf}n_{b(h-surf)} + \frac{\rho_{N(d-surf)}t_{d-surf}}{N_A} - \Gamma_{surf}n_{b(d-surf)}) \quad \text{Equation 2.22}$$

$$\text{Equation 2.23}$$

$$\frac{\rho_{N(h-surf)}t_{h-surf}}{N_A} = \Gamma_{surf}n_{b(h-surf)} + \frac{\rho_{N(d-surf)}t_{d-surf}}{N_A} - \Gamma_{surf}n_{b(d-surf)}$$

$$\frac{\rho_{N(h-surf)} t_{h-surf}}{N_A} = \Gamma_{surf} * (n_{b(h-surf)} - n_{b(d-surf)}) + \frac{\rho_{N(d-surf)} t_{d-surf}}{N_A} \quad \text{Equation 2.24}$$

$$\Gamma_{surf} * (n_{b(h-surf)} - n_{b(d-surf)}) = \frac{\rho_{N(h-surf)} t_{h-surf}}{N_A} - \frac{\rho_{N(d-surf)} t_{d-surf}}{N_A} \quad \text{Equation 2.25}$$

$$\Gamma_{surf} = \frac{\frac{\rho_{N(h-surf)} t_{h-surf}}{N_A} - \frac{\rho_{N(d-surf)} t_{d-surf}}{N_A}}{(n_{b(h-surf)} - n_{b(d-surf)})} \quad \text{Equation 2.26}$$

$$\Gamma_{surf} = \frac{\rho_{N(h-surf)} t_{h-surf} - \rho_{N(d-surf)} t_{d-surf}}{N_A * (n_{b(h-surf)} - n_{b(d-surf)})} \quad \text{Equation 2.27}$$

When calculating the surface excess of mixed polymer/surfactant systems, ρ of the system can be chosen arbitrarily (e.g. $\rho_{N(d-surf)}=3$, and $\rho_{N(h-surf)}=1.5$) within reason [68-70]. The reflectivity curve at low Q range for the specific concentration is then fitted using this value, and the fitted t is substituted into the above calculations. The rest of the parameters used are constants for a given system (N_A and n_b). The surface excess of the PEG-g-PVAc polymer is then determined using Equation 2.19 and the SDS surface excess is determined using Equation 2.27.

2.3 References

1. Eastoe, J., *Colloid Science Principles, Methods and Applications*. Second ed. 2010: Wiley.
2. Menger, F.M. and Rizvi, S.A.A., *Relationship between Surface Tension and Surface Coverage*. Langmuir, 2011. **27**(23): p. 13975-13977.
3. Nilsson, G., *The Adsorption of Tritiated Sodium Dodecyl Sulfate at the Solution Surface Measured with a Windowless, High Humidity Gas Flow Proportional Counter*. The Journal of Physical Chemistry, 1957. **61**(9): p. 1135-1142.
4. Péron, N., et al., *Competitive Adsorption of Neutral Comb Polymers and Sodium Dodecyl Sulfate at the Air/Water Interface*. The Journal of Physical Chemistry B, 2008. **112**(25): p. 7410-7419.
5. Fainerman, V.B., et al., *The measurement of dynamic surface tension by the maximum bubble pressure method*. 1994. **272**(6): p. 731-739.
6. Bendure, R.L., *Dynamic surface tension determination with the maximum bubble pressure method*. Journal of Colloid and Interface Science, 1971. **35**(2): p. 238-248.
7. Röntgen, W.K., *A New Form of Radiation*. Science, 1896. **3**(72): p. 726-729.

8. Laue, M., *Die Wellentheorie der Röntgenstrahlen*. Inaugural lecture, Zürich, 1912. **14**: p. 219-244.
9. Bragg, W.H. and Bragg, W.L., *The reflection of X-rays by crystals*. Proceedings of the Royal Society of London. Series A, Containing Papers of a Mathematical and Physical Character, 1913. **88**(605): p. 428-438.
10. Bragg, W.L. and Bragg, W.H., *The structure of some crystals as indicated by their diffraction of X-rays*. Proceedings of the Royal Society of London. Series A, Containing Papers of a Mathematical and Physical Character, 1913. **89**(610): p. 248-277.
11. Franklin, R.E. and Gosling, R.G.J.A.C., *The structure of sodium thymonucleate fibres. I. The influence of water content*. 1953. **6**(8-9): p. 673-677.
12. Watson, J.D. and Crick, F., *A structure for deoxyribose nucleic acid*. 1953.
13. Drenth, J., *Principles of protein X-ray crystallography*. 2007: Springer Science & Business Media.
14. Dass, A., et al., *Au133(SPh-tBu)52 Nanomolecules: X-ray Crystallography, Optical, Electrochemical, and Theoretical Analysis*. Journal of the American Chemical Society, 2015. **137**(14): p. 4610-4613.
15. Rutherford, E., et al., *XXI. The nature of the α particle from radioactive substances*. 1909. **17**(98): p. 281-286.
16. Chadwick, J., *The existence of a neutron*. Proceedings of the Royal Society of London. Series A, Containing Papers of a Mathematical and Physical Character, 1932. **136**(830): p. 692-708.
17. Feather, N. and Chadwick, J., *The collisions of neutrons with nitrogen nuclei*. Proceedings of the Royal Society of London. Series A, Containing Papers of a Mathematical and Physical Character, 1932. **136**(830): p. 709-727.
18. Johns, P.C. *Medical x-ray imaging with scattered photons*. in *Opto-Canada: SPIE Regional Meeting on Optoelectronics, Photonics, and Imaging*. 2017. International Society for Optics and Photonics.
19. Metcalfe, P., Kron, T., and Hoban, P., *The physics of radiotherapy x-rays and electrons*. 2012: Medical Physics Publ.
20. Soloway, A.H., et al., *The chemistry of neutron capture therapy*. 1998. **98**(4): p. 1515-1562.
21. Guinier, A., Fournet, G., and Yudowitch, K.L., *Small-angle scattering of X-rays*. 1955.
22. Feigin, L. and Svergun, D.I., *Structure analysis by small-angle X-ray and neutron scattering*. Vol. 1. 1987: Springer.
23. Levine, J.R., et al., *Grazing-incidence small-angle X-ray scattering: new tool for studying thin film growth*. 1989. **22**(6): p. 528-532.

24. Müller-Buschbaum, P.J.P.j., *Grazing incidence small-angle neutron scattering: challenges and possibilities*. 2013. **45**(1): p. 34.
25. Watts, J.F. and Wolstenholme, J., *An introduction to surface analysis by XPS and AES*. 2019: John Wiley & Sons.
26. Chason, E. and Mayer, T.M., *Thin film and surface characterization by specular X-ray reflectivity*. *Critical Reviews in Solid State and Materials Sciences*, 1997. **22**(1): p. 1-67.
27. Zabel, H., *X-ray and neutron reflectivity analysis of thin films and superlattices*. *Applied physics A*, 1994. **58**(3): p. 159-168.
28. Grundy, M., et al., *X-ray and neutron reflectivity from spread monolayers*. 1988. **159**(1-2): p. 43-52.
29. Daillant, J. and Gibaud, A., *X-ray and neutron reflectivity: principles and applications*. Vol. 770. 2008: Springer.
30. Parratt, L.G., *Surface Studies of Solids by Total Reflection of X-Rays*. *Physical Review*, 1954. **95**(2): p. 359-369.
31. Felcher, G.P., et al., *Polarized neutron reflectometer: A new instrument to measure magnetic depth profiles*. 1987. **58**(4): p. 609-619.
32. Penfold, J., Ward, R.C., and Williams, W.G., *A time-of-flight neutron reflectometer for surface and interfacial studies*. *Journal of Physics E: Scientific Instruments*, 1987. **20**(11): p. 1411.
33. Penfold, J. and Thomas, R.K., *The application of the specular reflection of neutrons to the study of surfaces and interfaces*. *Journal of Physics: Condensed Matter*, 1990. **2**(6): p. 1369-1412.
34. Russell, T.P., *X-ray and neutron reflectivity for the investigation of polymers*. *Materials Science Reports*, 1990. **5**(4): p. 171-271.
35. Russell, T.P., *On the reflectivity of polymers: Neutrons and X-rays*. *Physica B: Condensed Matter*, 1996. **221**(1): p. 267-283.
36. Wilson, E.J. *Fifty years of synchrotrons*. in *Proceedings of the 1996 European Particle Accelerator Conference (EPAC'96)*. 1996.
37. Winick, H., *Synchrotron radiation sources: a primer*. Vol. 1. 1995: World Scientific.
38. Christou, C., et al. *The Diamond Light Source Booster RF System*. in *EPAC*. 2006.
39. Nicklin, C., et al., *Diamond beamline I07: a beamline for surface and interface diffraction*. *J Synchrotron Radiat*, 2016. **23**(Pt 5): p. 1245-1253.
40. <https://www.diamond.ac.uk/Instruments/Structures-and-Surfaces/I07.html>. [cited 2019 September].

-
41. Ageron, P., *Cold neutron sources at ILL*. Nuclear Instruments and Methods in Physics Research Section A: Accelerators, Spectrometers, Detectors and Associated Equipment, 1989. **284**(1): p. 197-199.
 42. Klein, H. *Spallation neutron sources*. in *Proc. 1994 Linac Conf., Tsukuba*, p322. 1994.
 43. Gardner, I.S., *ISIS status report*. 1994, SCAN-9411012.
 44. Kiessig, H., *Untersuchungen zur Totalreflexion von Röntgenstrahlen*. Annalen der Physik, 1931. **402**(6): p. 715-768.
 45. DuMond, J. and Youtz, J.P., *An X - Ray Method of Determining Rates of Diffusion in the Solid State*. Journal of Applied Physics, 1940. **11**(5): p. 357-365.
 46. Charlton, T.R., et al., *Advances in Neutron Reflectometry at ISIS*. Neutron News, 2011. **22**(2): p. 15-18.
 47. <http://scienceworld.wolfram.com/physics/ElectronRadius.html>. [cited 2016 February].
 48. Sears, V.F., *Neutron scattering lengths and cross sections*. Neutron News, 1992. **3**(3).
 49. http://henke.lbl.gov/optical_constants/asf.html. [cited 2016 February].
 50. Briscoe, W.H., et al., *Applying grazing incidence X-ray reflectometry (XRR) to characterising nanofilms on mica*. Journal of Colloid and Interface Science, 2007. **306**(2): p. 459-463.
 51. Briscoe, W.H., et al., *Synchrotron XRR study of soft nanofilms at the mica-water interface*. Soft Matter, 2012. **8**(18): p. 5055-5068.
 52. Sironi, B., *Lipid Adsorption at Interfaces: A Synchrotron X-Ray Reflectivity Study*, in *School of Chemistry*. 2016, University of Bristol.
 53. Watkins, E.B., et al., *Equilibrium or Quenched: Fundamental Differences between Lipid Monolayers, Supported Bilayers, and Membranes*. ACS Nano, 2014. **8**(4): p. 3181-3191.
 54. Hemming, J.M., et al., *Environmental Pollutant Ozone Causes Damage to Lung Surfactant Protein B (SP-B)*. Biochemistry, 2015. **54**(33): p. 5185-5197.
 55. Clifton, L.A., et al., *The role of protein hydrophobicity in thionin–phospholipid interactions: a comparison of $\alpha 1$ and $\alpha 2$ -purothionin adsorbed anionic phospholipid monolayers*. Physical Chemistry Chemical Physics, 2012. **14**(39): p. 13569-13579.
 56. Howes, P.B., et al., *Silicon $\Sigma 13(5\ 0\ 1)$ grain boundary interface structure determined by bicrystal Bragg rod X-ray scattering*. Vol. 61. 2013. 5694-5701.
 57. Prehm, M., et al., *Axial-Bundle Phases – New Modes of 2D, 3D, and Helical Columnar Self-Assembly in Liquid Crystalline Phases of Bolaamphiphiles with Swallow Tail Lateral Chains*. Journal of the American Chemical Society, 2011. **133**(13): p. 4906-4916.

58. James Martin, D., et al., *Reversible restructuring of supported Au nanoparticles during butadiene hydrogenation revealed by operando GISAXS/GIWAXS*. Chem Commun (Camb), 2017. **53**(37): p. 5159-5162.
59. Agostinelli, T., et al., *Real-Time Investigation of Crystallization and Phase-Segregation Dynamics in P3HT:PCBM Solar Cells During Thermal Annealing*. 2011. **21**(9): p. 1701-1708.
60. Xiong, G., et al., *Atomic Diffusion within Individual Gold Nanocrystal*. Scientific Reports, 2014. **4**: p. 6765.
61. Campbell, R.A., Wacklin, H.P., and Sutton, I., *FIGARO: The new horizontal neutron reflectometer at the ILL*. The European Physical Journal Plus, 2011. **126**(107).
62. <https://www.isis.stfc.ac.uk/Pages/Inter-Timeline.aspx>. [cited 2019 August].
63. Webster, J., Holt, S., and Dalgliesh, R., *INTER the chemical interfaces reflectometer on target station 2 at ISIS*. Physica B: Condensed Matter, 2006. **385-386**: p. 1164-1166.
64. Braslau, A., et al., *Surface Roughness of Water Measured by X-Ray Reflectivity*. Physical Review Letters, 1985. **54**(2): p. 114-117.
65. Sinha, S.K., et al., *X-ray and neutron scattering from rough surfaces*. Physical Review B, 1988. **38**(4): p. 2297-2311.
66. Tikhonov, A.M., et al., *An X-ray Reflectivity Study of the Water-Docosane Interface*. The Journal of Physical Chemistry B, 2000. **104**(27): p. 6336-6339.
67. Péron, N., et al., *Competitive adsorption of sodium dodecyl sulfate and polyethylene oxide at the air/water interface*. Journal of Colloid and Interface Science, 2007. **313**(2): p. 389-397.
68. Braun, L., et al., *Polymers and surfactants at fluid interfaces studied with specular neutron reflectometry*. Advances in Colloid and Interface Science, 2017. **247**: p. 130-148.
69. Campbell, R.A., et al., *Polyelectrolyte/surfactant films spread from neutral aggregates*. Soft Matter, 2016. **12**(24): p. 5304-5312.
70. Campbell, R.A., *Recent advances in resolving kinetic and dynamic processes at the air/water interface using specular neutron reflectometry*. Current Opinion in Colloid & Interface Science, 2018. **37**: p. 49-60.

3 Synergy, competition, and the “hanging” polymer layer: Interactions between a neutral amphiphilic ‘tardigrade’ co-polymer with an anionic surfactant at the air-water interface

Understanding the structure of polymer/surfactant mixtures at the air-water interface is of fundamental importance and also of relevance to a variety of practical applications. Here, the complexation between a neutral ‘tardigrade’ comb co-polymer (consisting of a hydrophilic polyethylene glycol backbone with hydrophobic polyvinyl acetate grafts, PEG-g-PVAc) with an anionic surfactant (sodium dodecylsulfate, SDS) at the air-water interface has been studied. Neutron reflectivity (NR) complemented by surface tension measurements allowed elucidation of the interfacial composition and structure of these mixed systems, as well as providing physical insights into the polymer/surfactant interactions at the air-water interface. We observed a synergistic cooperative behaviour at low surfactant concentrations with a 1-2 nm mixed interfacial layer; a competitive adsorption behaviour at higher surfactant concentrations was observed where the polymer was depleted from the air-water interface, with an overall interfacial layer thickness ~1.6 nm independent of the polymer concentration. The weakly associated polymer layer “hanging” proximally to the interface, however, played a role in enhancing foam stability, thus was relevant to the detergency efficacy in such polymer/surfactant mixtures in industrial formulations.

3.1 Introduction

Polymer/surfactant interfacial organisation is important to many processes such as foaming [1-3], detergency [4], solubilisation [5], flotation [6], encapsulation [7], and lubrication [8], as well as applications such as personal care products [9], pharmaceuticals [10, 11], and oil industries [12]. Recent studies using surface-sensitive experimental techniques such as X-ray reflectivity (XRR) and neutron reflectivity (NR) have considerably advanced our understanding of the interfacial behaviour of polymer/surfactant mixtures [13-17]. NR is

particularly well suited for probing adsorbed surfactant layers at the air-water interface [13, 18-21]. In addition to the structure of the surfactant monolayer, the surface excess (or coverage), thickness, and the degree of solvation at the interface can also be determined [22].

Macromolecular architectures are crucial to polymer/surfactant interfacial interactions. For instance, association of polyelectrolytes with oppositely charged surfactants is understood to be driven by hydrophobic interactions at low degree of neutralisation (*i.e.* a relatively low surfactant concentration), and electrostatic attractions and entropic gains from liberated counterions at higher degrees of neutralisation (*i.e.* a higher surfactant concentration) [23, 24]. This balance can be influenced by changes in pH or variations of the polymer architecture (*e.g.* linear *vs* branched polymer) [25, 26], and leads to different polymer/surfactant micelle-like complexes (bottle-brush and spherical or worm-like micelles when hydrophobic interactions prevail; and electrostatic interactions enabling formation of lamellar complexes) [27].

Self-assembly and interactions between surfactants and a large number of neutral polymers (*i.e.* in the absence of the electrostatic driving force and utilising hydrogen bonding) in the bulk [28, 29] and at the air-water interface [13, 30] have also been studied. These neutral polymers can be linear or branched and form parts of rich architectures (such as, brush-like, dendritic, and star-shaped) that can be exploited in formulations and industrial applications. Different chemical groups can also be incorporated to generate graft co-polymer architectures, such as comb, bottle-brush and centipede [31, 32], with additional functionality (such as antimicrobial properties and friction modifiers) [33-35] and a range of self-assembled structures (such as bilayers, vesicles, micelles and nanogels) [36].

The polymer architecture of particular interest here can be described as a '*tardigrade*' comb co-polymer PEG-*g*-PVAc, with ~5-8 hydrophobic polyvinyl acetate (~13-19 PVAc monomer units) grafts along the hydrophilic polyethylene glycol (PEG) backbone (*i.e.* one graft every ~20 PEG monomer units). We termed the polymer *tardigrade* due to the superficial resemblance of its architecture to the morphology of the water-dwelling eight-legged segmented micro-animal (also known as "water bears"). The *tardigrade* polymer is surface active and self-aggregates in aqueous solution at concentrations above ~ 0.001 wt%. We refer to this concentration as a critical aggregation concentration, *cac*. The self-folding behaviour of chemically analogous PEG-*g*-PVAc co-polymer has been demonstrated before [37, 38]. The unique molecular architecture of this *tardigrade* polymer stems from the balance between the hydrophobic PVAc grafts and the hydrophilic PEG backbone, with both the number and the

length of the PVAc grafts important. If the grafting density is too high, the overall architecture of the polymer is analogous to a brush co-polymer and surfactant binding to such a non-ionic polymer would be significantly suppressed due to high steric repulsion [39]. On the other hand, if the grafting density is too low and the grafts are relatively long, the self-folding in the water would lead to a formation of single-chain nanoparticles [37] which can phase-separate at very high concentrations and in presence of surfactants [40]. There have been numerous patents highlighting the efficacy and widespread usage of similar graft co-polymers in consumer products [41-47], mainly as a detergent additive to prevent soil redeposition. The *comb* co-polymer is efficient at solubilising soil and preventing its deposition onto fabrics after a wash cycle, working well in conditions where other polymer architectures fail, specifically at higher water hardness levels. To our knowledge, the interfacial properties of the ‘*tardigrade*’ neutral co-polymer architecture are yet to be reported.

Despite a number of studies attempting to establish the correlation between foaming behaviour of polymer/surfactant mixtures and other physical properties (such as the interfacial surfactant layer structures [16, 48, 49] and charge [1, 2, 50], bubble stability determined by small angle neutron scattering [51, 52], disjoining pressure isotherms and the thin film stability [53, 54], and surface tension [55]), a complete understanding of foaming and foam stability facilitated by *comb* -polymer/surfactant complexes is yet to emerge [56].

In this study, we have used dynamic and equilibrium surface tension measurements and NR to study the compositional and structural characteristics of *comb*-polymer/surfactant mixtures at the air-water interface. Sodium dodecyl sulfate (SDS) was chosen as a model surfactant, as it is an analogue of anionic surfactants commonly used in detergent formulation [57]. Foaming behaviour of the *comb*-polymer/surfactant mixture was also evaluated to correlate with the surface tension and NR observations. The results, among the first on the interfacial structure containing the *comb* polymers, show both synergistic and competitive behaviour depending on the surfactant concentration. Such knowledge is relevant to fundamental understanding of the correlation between the *comb* architecture and its surface activity, and its efficacy in mediating detergency and foaming in industrial applications.

3.2 Methods

3.2.1 Materials

Both hydrogenous and deuterated sodium dodecylsulfate (h-SDS, $C_{12}H_{25}SO_4$, Sigma-Aldrich; d-SDS, $C_{12}D_{25}SO_4$, Sigma-Aldrich and ISIS Deuteration Facility) were recrystallised from ethanol (absolute >99.8%, Sigma-Aldrich). MilliQ water (Millipore, resistivity $18.2\text{ M}\Omega\text{ cm}$, <5 ppb organic matter) was used for solution preparation for surface tension measurements, as well as for the preparation of air contrast matched water (ACMW; $H_2O:D_2O$, 91.1:8.9 w:w). D_2O was supplied by Sigma-Aldrich (99.9%).

The amphiphilic *tardigrade comb* co-polymer (Figure 3.1) consisting of a PEG backbone and short PVAc grafts (Mn 15 kDa, PEG₁₃₆-g-PVAc₁₀₄ with the subscripts indicating the number of monomers; or PEG(6000)-g-PVAc(9000) with the corresponding segmental Mn indicated) was commercially available from BASF. It was freeze-dried and re-dissolved in H_2O , D_2O , or ACMW for sample preparation.

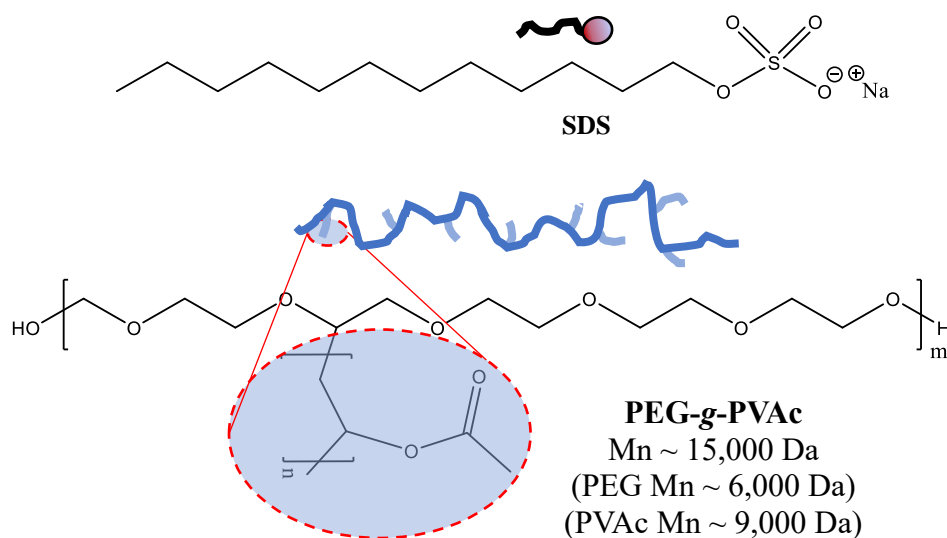


Figure 3.1 Molecular structures (with corresponding schematics) of SDS and PEG-g-PVAc co-polymer.

3.2.2 Surface tension measurements

The equilibrium surface tension (γ) data was collected at room temperature using the Wilhelmy plate method with a Krüss K100 force tensiometer (measurement stopped after standard deviation of last 5 data points recorded at 10 s intervals was $<0.01\text{ mN m}^{-1}$), and the dynamic

surface tension (γ_d) was collected using the Krüss BP100 bubble pressure tensiometer using a glass capillary. The platinum Wilhelmy plate was flamed before every measurement to ensure cleanliness and surface activation. The cleanliness of both the glass vessel and the platinum plate was confirmed by measuring γ of MilliQ water as $\gamma = 72.5 \pm 0.3 \text{ mN m}^{-1}$ prior to every measurement.

The bubble pressure was related to the surface tension according to the rearranged Young-Laplace equation:

$$\gamma_d(\tau) = \frac{(p_{max}(\tau) - p_0)r}{2} \quad (\text{Equation 3.1})$$

where $\gamma_d(\tau)$ is the dynamic surface tension at time τ (measured between $\tau \sim 10 \text{ ms} - 4 \text{ min}$), $p_{max}(\tau)$ is the maximum pressure experienced by the bubble at given τ , p_0 is the hydrostatic pressure due to capillary immersion, and r is the capillary radius.

3.2.3 Neutron reflectivity (NR)

The surface excess of adsorbed species is determined from fitting only the low Q range of the NR data obtained in ACMW, where the fitting is only sensitive to the product of t and ρ of the given layer and no other parameters. This approach was developed recently [16, 58, 59].

The structural information of the interface is elucidated from the fitting parameters of the interfacial layer: thickness (t), roughness (σ) and water volume fraction in the layer (ϕ_{water}) over the whole accessible Q range. Determination of the composition of interfacial structures (*i.e.* the volume fraction, ϕ) is based on fitting the reflectivity profile using calculated scattering length densities (SLDs, ρ) of the adsorbed species [60].

The NR data was obtained at the FIGARO beamline at Institut Laue-Langevin (ILL, Grenoble, France) [61] and at the INTER beamline at ISIS Neutron Source (STFC Rutherford Appleton Laboratory, Didcot, UK) [62]. Briefly, a neutron beam is detected by a time-of-flight detector, accessing a Q range of $\sim 0.005\text{-}0.25 \text{ \AA}^{-1}$ at FIGARO and $\sim 0.01\text{-}0.2 \text{ \AA}^{-1}$ at INTER by using neutrons with a range of wavelengths ($\lambda = 2 - 30 \text{ \AA}$ at FIGARO and $\lambda = 1.5 - 17 \text{ \AA}$ at INTER) at two different grazing incidence angles ($\theta = 0.62^\circ$ and 3.79° at FIGARO and $\theta = 0.80^\circ$ and 2.30° at INTER) at the air-water interface. Here Q is the momentum transfer perpendicular to the interface, $Q = \frac{4\pi \sin(\theta)}{\lambda}$. The obtained reflectivity profile can be plotted as reflectivity, $R(Q)$

vs. Q , or alternatively as $RQ^4(Q)$ vs. Q to highlight mild fringes by compensating the intrinsic $R(Q)$ decay with Q^{-4} . The background was subtracted from the data recorded at FIGARO thanks to use of the 2D detector but not from the data recorded at INTER.

The ρ of each species in the system is calculated as the sum of scattering lengths, n_b , of each atom in the molecule per unit volume. The n_b of ^1H and ^2H (or D) differ significantly from each other (n_b of $^1\text{H} = -3.739$ and n_b of $^2\text{H} = 6.671$), enabling the use of deuteration of certain molecules or their parts as a way of controlling the overall ρ of the material and its contrast to the surroundings. In this study, two media were used: D_2O and air contrast matched water (ACMW, *i.e.* $\rho = 0$ matched to that of air). The polymer was hydrogenous, whilst the surfactant hydrocarbon tail was either fully hydrogenous or deuterated. This deuterium labelling enabled us to collect data in 4 different isotopic contrasts for each polymer/surfactant mixed system (h-surfactant in ACMW, d-surfactant in ACMW, h-surfactant in D_2O , d-surfactant in D_2O , all with h-polymer). The four NR profiles for each sample (*i.e.* the four isotopic contrasts) were co-fitted with the same structural parameters, *i.e.* t , ρ , σ , and ϕ_{water} .

30 mL of the solution containing the polymer/surface mixture at a designated concentration was filled in a Teflon trough until a meniscus protruded above the trough to form an air-water interface, at which all NR measurements were made. The data was collected repeatedly over ~ 6 h to check and allow for sample equilibration. The data was reduced and calibrated against the reference measurements of pure ACMW and D_2O , and the direct beam. The surface excess was calculated from the data acquired in ACMW in the low Q range following the recent approach described in [16, 58]. The data fitting was performed using the Motofit package in IGOR Pro [63].

3.2.4 Surface excess calculation

Surface excess, Γ , is the amount of species at the interface per unit area (in $\mu\text{mol m}^{-2}$ in the case of SDS, and in mg m^{-2} in the case of PEG-*g*-PVAc). It is not trivial to calculate the surface excess of individual species in a polymer/surfactant mixture above the cac from the surface tension data [64, 65].

Γ of a single component layer can be determined from NR data in ACMW using:

$$\Gamma = \frac{\rho t}{N_A n_b} \quad (\text{Equation 3.2})$$

where ρ is the fitted SLD of the adsorbed species, t is the fitted thickness, N_a is Avogadro's constant, and n_b is the calculated scattering length of the adsorbed species in the layer.

It is also feasible to determine Γ of a two-component system, providing both components are available deuterated and their ρ can be also matched to that of ACMW. In such case, the Γ_{polymer} is determined from the mixture containing deuterated polymer and surfactant with its ρ matched to ACMW in ACMW [66]. However, when there is no deuterated polymer available, the low Q approach has to be applied. The Γ value of hydrogenous polymer is then determined by a low Q range data analysis from the mixtures with both hydrogenous and deuterated surfactant in ACMW, taking into account the volume fraction of each component in the layer. The derivation of equations used in the low Q approach is shown in Section 2.2.3.2 (Chapter 2). The $\Gamma_{\text{PEG-g-PVAc}}$ is shown in mg m^{-2} for clarity, due to the large size of the molecule and therefore a very small $\Gamma_{\text{PEG-g-PVAc}}$ value in $\mu\text{mol m}^{-2}$.

3.2.5 Foaming measurements

All foaming measurements were performed with a Krüss Dynamic Foam Analyser (DFA 100), using 60 mL of a solution in a glass column of 4 cm in diameter. The foam was generated by air flow through a sintered porous glass filter (pore size 40-100 μm , 3 cm in diameter) at a flow rate of 0.3 L min^{-1} for 12 s. The liquid, foam, and total height were detected using blue light illumination and a camera. The foamability was determined as the maximum foam volume (or height) reached after foam formation, whilst the foam stability was gauged by the half-life time (time at which the foam height decays to half of the maximum foam height). The camera was calibrated to determine the foam bubble size when foam was formed in the glass column with a prism, and the initial bubble radius was reported at the time of foam formation.

3.3 Results

3.3.1 Equilibrium and dynamic surface tension: From synergistic cooperative adsorption to SDS-Polymer competition

The equilibrium surface tension (γ) data of the pure polymer and SDS, as well as their mixtures, is shown in Figure 3.2a. The dynamic surface tension (γ_d) data using the bubble pressure method is shown as a function of time (τ , the age of the bubble generated at the tip of the

capillary) in Figure 3.2c. The data at such short time-scales offered insights on the kinetics of interfacial adsorption and diffusion in the system.

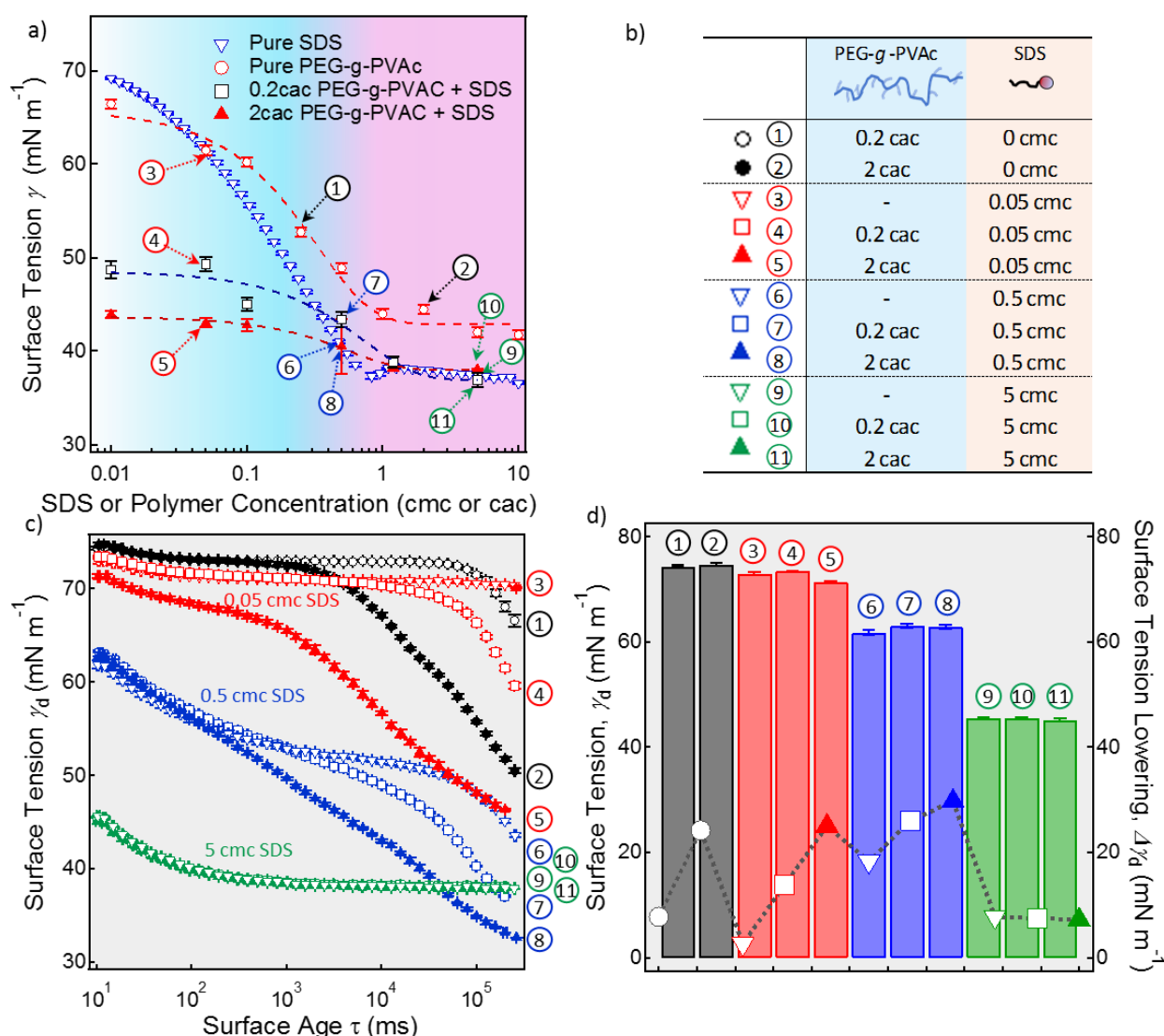


Figure 3.2. a) Equilibrium surface tension γ vs. surfactant or polymer concentration (in their respective cmc and cac determined experimentally) using the Wilhelmy plate method. Four sets of data are shown for pure SDS (∇), pure polymer (\circ), and the polymer (0.2 \square and 2 cac \blacktriangle) mixed with SDS at different concentrations. Data points labelled 1-11 indicate specific polymer and surfactant concentrations. (b) The legend table lists the polymer and surfactant concentrations for the 11 dynamic surface tension curves, with the corresponding symbols for the plots in (a) and the corresponding numbers in (a), (c) and (d). The dynamic surface tension γ_d vs. the surface age τ is shown in (c), using the bubble pressure method. Curves 9-11 in (c) (5 cmc SDS) overlay with each other. (d) A bar chart showing the γ_a at $\tau \sim 10$ ms for curves 1-11, with the surface tension lowering $\Delta\gamma_a$ (γ_a at $\tau \sim 10$ ms - γ_a at $\tau \sim 4$ min). The error bars in all cases are determined as a standard deviation from an experimental error determined from 3 separate measurements.

At low SDS concentrations ($< \sim 0.5$ cmc), for the polymer/surfactant mixtures at both 0.2 and 2 cac polymer concentrations (\square and \blacktriangle respectively in Figure 3.2a), there is a significant synergistic effect observed compared to pure SDS (∇), evident from the lowering in the

equilibrium surface tension by $\sim 13\text{-}18 \text{ mN m}^{-1}$ of the mixture. This is likely due to polymer/SDS cooperative adsorption to the interface, where the polymer could form loops and trains at the interface [67], as well as interacting with, and thus accommodating, the surfactant molecules. Compared to pure 0.2 cac polymer solution (\circ ; $\gamma \sim 55 \text{ mN m}^{-1}$), the synergy is also evident, with γ of the 0.2 cac-polymer/SDS mixture lower by $10\text{-}12 \text{ mN m}^{-1}$. For the 2 cac-polymer/SDS mixture, the synergistic effect is less pronounced, with γ lowering by only $\sim 1\text{-}2 \text{ mN m}^{-1}$ relative to the surface tension of the pure polymer above its cac ($\gamma \sim 44 \text{ mN m}^{-1}$). This suggests that the cooperative adsorption was much less pronounced in these mixtures, and it is likely the polymer adsorbed preferentially at the interface in these systems.

For the mixtures containing 0.2 and 2 cac polymer with 0.5 cmc SDS, a transition from the regime of cooperative to competitive adsorption behaviour was observed (*cf.* also the fitted thickness of the interfacial layer, Figure 3.4). The surface tension values for the mixtures are similar ($\gamma \sim 43.3 \pm 0.8 \text{ mN m}^{-1}$ for mixtures containing 0.2 cac PEG-*g*-PVAc and $\sim 40.5 \pm 2.9 \text{ mN m}^{-1}$ for mixtures containing 2 cac PEG-*g*-PVAc, from 5 separate measurements each) and fall between those of pure SDS ($\gamma \sim 40 \text{ mN m}^{-1}$) and pure polymer ($\gamma \sim 55$ and 44 mN m^{-1} for 0.2 and 2 cac, respectively). This suggests that the interface was largely occupied by the surfactant at the 0.5 cmc SDS concentration, which had been attributed to polymer partial desorption from the interface [68]; this led to a slight increase in the surface tension compared to that of pure SDS. In the case of 0.5 cmc-SDS mixtures with higher polymer concentration (2 cac PEG-*g*-PVAc), the surface tension values from 2 measurements showed a synergistic effect, whilst 3 other measurements pointed towards a competitive behaviour with less polymer adsorbing to the interface. The interfacial behaviour at this SDS concentration is therefore assumed to be the transition point between the cooperative polymer-surfactant adsorption and the competitive behaviour where SDS adsorbed preferentially to the interface compared to PEG-*g*-PVAc.

At higher SDS concentrations (1.2 cmc and 5 cmc), the γ values of the mixtures (~ 37 and 38 mN m^{-1} for 0.2 cac \square and 2 cac \blacktriangle polymer, respectively; Figure 2a) are very similar to that of the pure SDS solution ($\gamma \sim 37 \text{ mN m}^{-1}$). This indicates competitive adsorption between SDS and the polymer, with the polymer largely depleted and an SDS monolayer present at the interface. It is worth noting the presence of a minimum in the γ of pure SDS at concentrations around its cmc, which was likely caused by surface active impurities, such as dodecanol, present [69].

Such interfacial behaviour of transitioning from synergy to competition of the polymer/surfactant mixture has not been reported widely from previous observations. It has been more commonly observed that the addition of a polymer would typically increase γ , by essentially lowering the amount of SDS in the bulk solution from the surfactant cmc to its cac (critical aggregation concentration), hence leading to a lower corresponding adsorbed amount at the air-water interface [70]. In our case, any preferential adsorption of PEG-g-PVAc over SDS was not observed in the mixed system, even after a prolonged equilibration time (up to 48 h); neither was there evidence for adsorption of the depleted polymer to the interface with time.

This synergy-to-competition transition is also consistent with the dynamic surface tension data (γ_d as a function of time τ (surface age); Figure 3.2c). The onset of the lowering of γ_d is presumed to correspond to the adsorption of the polymer, surfactant and their mixture at the air (bubble)-water interface. Curve 1 in Figure 3.2c (○) for 0.2 cac PEG-g-PVAc shows relatively slow adsorption of the polymer, with γ_d lowering onsetting at $\tau \sim 1$ min after interface formation, and decreasing from ~ 75 mN m⁻¹ to ~ 68 mN m⁻¹ within ~ 4 min. The adsorption of 2 cac PEG-g-PVAc (Curve 2; ●) was much faster, onsetting at ~ 2 s and with a total γ_d lowering of ~ 24 mN m⁻¹, to ~ 50 mN m⁻¹, within the timeframe of the measurement.

Curves 3, 6 and 9 show the data for pure surfactant systems containing 0.05, 0.5 and 5 cmc SDS, respectively. There is no appreciable γ_d lowering in the case of 0.05 cmc SDS (Curve 3 ▽), with γ_d remaining at ~ 70 mN m⁻¹ throughout the measurement time (4 min). In the case of 0.5 cmc SDS (Curve 6 ▽), fast adsorption of the surfactant was observed at $\tau \sim 10$ ms ($\gamma_d \sim 62$ mN m⁻¹), with γ_d then lowering to ~ 44 mN m⁻¹ at $\tau \sim 4$ min. Even faster γ_d lowering and thus surfactant adsorption was observed in the case of 5 cmc SDS (Curve 9 ▽), with $\gamma_d \sim 46$ mN m⁻¹ already at $\tau \sim 10$ ms, which reached a plateau value of $\gamma_d \sim 38$ mN m⁻¹ rapidly at $\tau \sim 1$ s. These measurements are well aligned with reported literature, where synergistic effect similar to that described below was observed in SDS-zwitterionic surfactant mixed system [71, 72].

The strong synergistic effect at low SDS concentration (0.05 cmc) is evident from the difference in adsorption of polymer/surfactant mixtures (Curves 4 and 5: 0.2 cac PEG-g-PVAc + 0.05 cmc SDS, and 2 cac PEG-g-PVAc + 0.05 cmc SDS) compared to either of the pure systems (Curves 1, 2 and 3). Compared to pure 0.05 cmc SDS (Curve 3), the presence of PEG-g-PVAc at 0.2 cac (Curve 4) and 2 cac (Curve 5) led to both faster adsorption kinetics and a

greater reduction in the surface tension. This is evident from their similar initial $\gamma_d \sim 71\text{-}73 \text{ mN m}^{-1}$ at $\tau \sim 10 \text{ ms}$, a γ_d lowering at $\tau \sim 4 \text{ min}$ of $\Delta\gamma_d \sim 13$ and 24 mN m^{-1} , respectively (*i.e.* final $\gamma_d \sim 60$ and 46 mN m^{-1} for the mixtures containing 0.2 and 2 cac PEG-g-PVAc with 0.05 cmc SDS).

At 0.5 cmc SDS (Curves 6-8 in Figure 2c), the initial γ_d decay for both SDS-polymer mixtures (Curves 7,8) started from a similar value ($\gamma_d \sim 62 \text{ mN m}^{-1}$) and tracked that in pure SDS solution (Curve 5), attributed to fast SDS adsorption to the interface. Subsequent polymer adsorption to the interface further lowered surface tension. For the mixture containing 0.2 cac PEG-g-PVAc + 0.5 cmc SDS (Curve 7), γ_d begins to deviate from that of pure 0.5 cmc SDS at $\tau \sim 2 \text{ s}$ ($\gamma_d \sim 52 \text{ mN m}^{-1}$), and a further surface tension reduction $\sim 7 \text{ mN m}^{-1}$ was observed (*i.e.* at $\tau \sim 4 \text{ min}$, $\Delta\gamma_d \sim 26 \text{ mN m}^{-1}$ for the mixture, compared to $\Delta\gamma_d \sim 18 \text{ mN m}^{-1}$ in the case of pure 0.5 cmc SDS). Similar behaviour, with more pronounced secondary polymer adsorption, was observed in the case of 2 cac PEG-g-PVAc + 0.5 cmc SDS (Curve 8). The γ_d data starts differing from that of pure 0.5 cmc SDS at $\tau \sim 200 \text{ ms}$ ($\gamma_d \sim 54 \text{ mN m}^{-1}$). The final γ_d , at $\tau \sim 4 \text{ min}$ was $\gamma_d \sim 33 \text{ mN m}^{-1}$, which corresponds to an additional $\Delta\gamma_d$ relative to that of pure 0.5 cmc SDS (Curve 6) of $\Delta\gamma_d \sim 11 \text{ mN m}^{-1}$, and $\Delta\gamma_d \sim 4 \text{ mN m}^{-1}$ relative to that of 0.2 cac PEG-g-PVAc + 0.5 cmc SDS. This behaviour is interpreted to be due to the presence of a secondary “hanging” polymer layer adsorbing to an interface already partially covered by SDS molecules, likely *via* interacting with the SDS headgroups. This is also consistent with the NR data presented below (*cf.* Figure 3.6).

In the mixtures containing 5 cmc SDS (Curves 10, 11 in Figure 2b), the γ_d decay tracked closely that of a pure 5 cmc SDS (Curve 9) from $\tau \sim 10 \text{ ms}$ ($\gamma_d \sim 45 \text{ mN m}^{-1}$) and then throughout the measurement time (at $\tau \sim 4 \text{ min}$, $\gamma_d \sim 40 \text{ mN m}^{-1}$). This observation is consistent with competitive adsorption, where SDS rapidly forms a complete monolayer at the interface, with the polymer depleted from the interface and no further secondary polymer adsorption.

It is not straightforward to determine the surface excess of each of the adsorbing species within a mixture using the Gibbs isotherm from surface tension data, therefore the surface excess was determined from the NR data, which also yields the out-of-plane structure and composition of the interfacial layer. The equilibrium and dynamic surface tension data, however, offer qualitative insights of the polymer/surfactant adsorption behaviour and the transition from cooperative adsorption of SDS and the polymer at low SDS concentration to competitive adsorption at high SDS concentration.

3.3.2 NR results: Interfacial layer composition and structure

The composition of interfacial polymer/surfactant layer at the air-water interface was determined by the means of Γ calculation, in connection with t , σ , ρ and ϕ_{water} data fitting to obtain the structural information of the interfacial layer.

Γ of SDS and PEG-*g*-PVAc was determined by fitting the NR data using a 1-layer model at a restricted low Q range in 2 isotopic contrasts (h-SDS and d-SDS with h-PEG-*g*-PVAc) in ACMW. This approach, pioneered over the last few years on the FIGARO beamline and described in detail in [16, 58, 59], provides a more direct measure of the interfacial composition compared to a structural analysis, as it is independent of the model applied. We summarise Γ vs surfactant concentration in Figure 3.3. It shows that the amount of SDS at the interface is affected by the presence of the polymer only at SDS concentrations below its cmc value, with an increasing value from $\Gamma_{\text{SDS}} \sim 0.13 \mu\text{mol m}^{-2}$ to a plateau value of $\Gamma_{\text{SDS}} \sim 4.2 \mu\text{mol m}^{-2}$ at concentrations above the cmc of SDS. Correspondingly, $\Gamma_{\text{PEG-}g\text{-PVAc}}$ in the same mixtures decreases with the increasing SDS concentration, from $\Gamma_{\text{PEG-}g\text{-PVAc}} \sim 2.0 \text{ mg m}^{-2}$ to $\Gamma_{\text{PEG-}g\text{-PVAc}} \sim 0.02 \text{ mg m}^{-2}$, suggesting that the polymer is depleted from the interface by the surfactant. The relevant Γ_{SDS} and $\Gamma_{\text{PEG-}g\text{-PVAc}}$ values are later presented alongside the NR data fitting over the whole Q range in 4 isotopic contrasts.

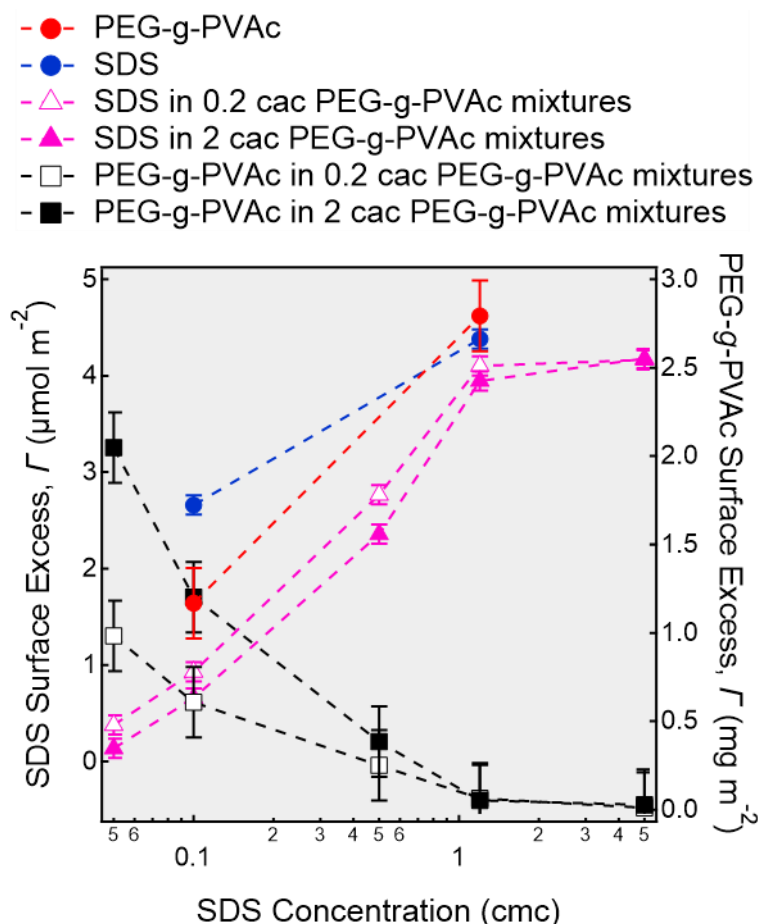


Figure 3.3 The calculated Γ vs SDS concentration of mixed PEG-g-PVAc + SDS systems is shown. The Γ_{SDS} is shown in $\mu\text{mol m}^{-2}$ on the left axis and represented by the filled markers, and $\Gamma_{\text{PEG-g-PVAc}}$ is shown in mg m^{-2} on the right axis and represented by the empty markers. The dashed lines act as a guide to the eyes only.

Figure C.1 (Appendix) shows NR data at the air-water interface in 2 isotopic contrasts (h-polymer in ACMW or D_2O) for the pure *comb* polymer at 0.2 and 2 cac, which can be well described by a homogenous 1-layer model of hydrated polymer, with the corresponding fitted scattering length density (SLD) ρ profiles also shown in Figure C.1 and the fitting parameters t , σ , and ϕ_{water} listed in Table 3.1. Consistent with the surface tension measurement, the NR data indicates that the surface activity of the *comb* polymer was due to the short hydrophobic PVAc grafts covering the air-water interface, although a single layer model could describe the data satisfactorily (without having to divide the interfacial layer into a PVAc layer and PEG layer), as the PVAc and PEG layers would be very thin separately. The interfacial polymer layer thickness increased from $t \sim 10.8 \text{ \AA}$ ($\Gamma_{\text{PEG-g-PVAc}} \sim 1.17 \text{ mg m}^{-2}$) at 0.2 cac to $t \sim 28.0 \text{ \AA}$ ($\Gamma_{\text{PEG-g-PVAc}} \sim 2.79 \text{ mg m}^{-2}$) at 2 cac.

The NR data and the fitted ρ profiles using a 1-layer model for SDS at 0.1 cmc and a 2-layer model for SDS at 1.2 cmc are shown in Figure C.2 in the Appendix, with two separate layers:

the hydrocarbon chain layer (its ρ depending on h- or d-surf used) and the headgroup layer (same ρ for both h- and d-surf). It has been shown that fitting of NR data of ionic surfactant above its cmc in multiple isotopic contrasts and over the accessible Q range requires the use of two separate layers [18]. However, this was not discussed in the case of a low surface coverage (*i.e.* low surfactant concentration, such as 0.1 cmc) in which case the low layer t indicates highly tilted molecules at the interface and so removes the need for separating the tails and headgroups in the fitting model. The fitting parameters listed in Table 3.1 show that the SDS layer thickness and coverage at the air-water interface increased (overall $t \sim 7.2 \text{ \AA}$, $\Gamma_{\text{SDS}} \sim 2.66 \text{ \mu mol m}^{-2}$ and $t \sim 11.9 \text{ \AA}$, $\Gamma_{\text{SDS}} \sim 4.38 \text{ \mu mol m}^{-2}$ for 0.1 and 1.2 cmc SDS respectively) with its bulk concentration, which is consistent with the literature [73].

For the polymer/surfactant mixtures, two approaches were taken to analyse the NR data over the whole accessible Q range. In the first trial approach, a single layer model was used to fit the NR data, with the layer composition calculated from the fitted ρ value to obtain the volume fraction of the polymer ($\phi_{\text{PEG-g-PVAc}}$) and the surfactant (ϕ_{SDS}). This approach gave an indicative overview of the general characteristics of the interface (Figure 3.4), such as a clear decrease of the $\phi_{\text{PEG-g-PVAc}}$ with increasing SDS concentration, confirming competitive adsorption behaviour at high SDS concentrations. The increase in the layer thickness relative to that of a pure SDS or polymer layer at 0.05 cmc SDS points towards cooperative adsorption at the interface at low SDS concentration. At 0.5 cmc SDS, the fitted interfacial layer thickness is smaller than that of a polymer or SDS monolayer ($t \sim 0.9 \text{ nm}$ in the mixtures of both 0.2 cac PEG-g-PVAc and 2 cac PEG-g-PVAc, compared to SDS monolayer $t \sim 1.1 \text{ nm}$). For both mixtures containing 5 cmc SDS, the interfacial layer is slightly thicker ($t \sim 1.2 \text{ nm}$). This appears consistent with a transition observed at 0.5 cmc SDS, from cooperative to competitive adsorption, as proposed based on surface tension data above. A previous study of oppositely charged PEI/SDS has reported similar synergy/competition behaviour – in that case, as a function of pH values [74] instead of SDS concentration. The fitted ϕ_{water} in the interfacial layer decreases with increasing SDS concentration (from $\phi_{\text{water}} \sim 22\%$ to $\phi_{\text{water}} \sim 1\%$), suggesting a more uniform and complete interfacial layer.

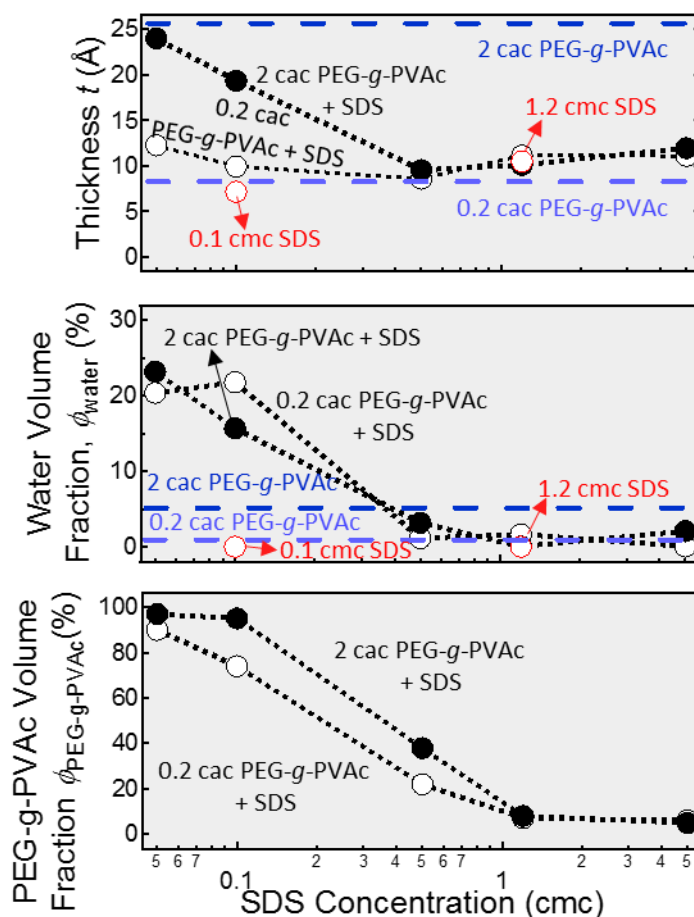


Figure 3.4 A summary of the thickness t , water volume fraction ϕ_{water} and polymer fraction $\phi_{\text{PEG-g-PVAc}}$ in a single-layer model used to fit the NR data of PEG-g-PVAc + SDS mixtures (\circ and \bullet for 0.2 and 2 cac polymer respectively). For comparison, the blue dashed lines represent the fitted values of 0.2 cac PEG-g-PVAc and 2 cac PEG-g-PVAc respectively. The data point with red outline represents the fitted value for 1.2 cmc pure SDS.

To gain more structural information, the NR data was further fitted using a *multilayer* model, where appropriate. A more detailed description of various different models used was discussed in the Methods section 2.2.3. Here, we present the models optimised to fit the data. In the *multilayer* model, an attempt was made to keep the σ values for separate layers constant, as this approach ensures conservation of mass in the fitted layer even though high roughness causes smearing of the ρ profile. However, this was not possible in our system, possibly due to the polymer loops increasing the σ of the layers around the PEG-g-PVAc. It was shown that highly asymmetrical σ values in a *multilayer* model cause unphysical σ profile with negative amount of material [18], therefore the σ variations within the layers were kept to minimal. The physicality of our fits was proved by the fact that in all cases the largest difference between σ values at different interfaces (so different layers) of the same model divided by the smallest t in the model was $<1/3$ (conservation of mass), and the ρ profile (although significantly smoothed) did not suggest negative amounts of adsorbed species at the interface.

For the mixtures of 0.05 cmc SDS with 0.2 and 2 cac polymer, the NR data (as $RQ^4(Q)$ vs. Q) and the fits with the corresponding fitted ρ profiles and schematic representations of the layer structure are shown in Figure 3.5; those for the mixtures with 0.5 and 5 cmc SDS are shown in Figure 3.6 and Figure 3.7, respectively. The NR data at other two mixtures with 0.1 and 1.2 cmc SDS are shown in Figure C.3 and C.4 in Appendix. All of the fitted parameters are listed in Table 3.1 below.

Table 3.1 The fitted parameters for the optimised multilayer models for mixtures of PEG-g-PVAc and SDS, as well as the pure systems. The superscripts for the fitted scattering length density (SLD) ρ values in the table correspond to the following polymer/surfactant volume fractions: ¹ 90% PEG-g-PVAc + 10% SDS, ² 74% PEG-g-PVAc + 26% SDS, ³ 71% PEG-g-PVAc + 29% SDS headgroup, ⁴ 97% PEG-g-PVAc + 3% SDS, ⁵ 95% PEG-g-PVAc + 5% SDS, ⁶ 63% PEG-g-PVAc + 37% SDS headgroup. The σ_{bkg} is the roughness between the water and the interfacial layers.

PEG-g-PVAc SDS		Layer 1					Layer 2				Layer 3				Bkg
<i>conc</i> (cac)	<i>conc</i> (cmc)	t_1 (Å)	$h-\rho_1$ (10^{-6}Å^{-2})	$d-\rho_1$ (10^{-6}Å^{-2})	$\varphi_{water-1}$ (%)	σ_1 (Å)	t_2 (Å)	ρ_2 (10^{-6}Å^{-2})	$\varphi_{water-2}$ (%)	σ_2 (Å)	t_3 (Å)	ρ_3 (10^{-6}Å^{-2})	$\varphi_{water-3}$ (%)	σ_3 (Å)	σ_{bkg} (Å)
0.2	0.05	12.3	0.968 ¹	1.613 ¹	20	3.6	-	-	-	-	-	-	-	-	2.6
0.2	0.1	10.0	0.866 ²	2.545 ²	22	5.0	-	-	-	-	-	-	-	-	3.1
0.2	0.5	5.8	-0.39	7.004	0	3.3	5.3	2.420 ³	47	2.8	-	-	-	-	4.2
0.2	1.2	8.7	-0.39	7.004	0	4.9	5.7	5.821	78	3.5	4.4	1.031	93	4.9	4.5
0.2	5	9.3	-0.39	7.004	0	4.0	3.9	5.821	66	5.0	3.2	1.031	82	4.0	4.0
2	0.05	24.0	1.012 ⁴	1.206 ⁴	23	7.6	-	-	-	-	-	-	-	-	2.9
2	0.1	19.4	0.999 ⁵	1.322 ⁵	16	6.6	-	-	-	-	-	-	-	-	4.3
2	0.5	4.9	-0.39	7.004	0	4.5	4.7	2.803 ⁶	44	4.1	-	-	-	-	4.2
2	1.2	8.3	-0.39	7.004	0	4.8	3.3	5.821	63	4.3	4.4	1.031	83	5.3	4.3
2	5	9.2	-0.39	7.004	0	5.0	3.2	5.821	58	5.7	2.7	1.031	92	5.0	5.4
0.2	-	10.8	1.031	-	12	3.9	-	-	-	-	-	-	-	-	3.2
2	-	28.0	1.031	-	19	3.6	-	-	-	-	-	-	-	-	5.2
-	0.1	7.2	0.396	6.854	0	3.2	-	-	-	-	-	-	-	-	3.0
-	1.2	9.0	-0.39	7.004	0	4.0	2.9	5.821	55	3.4	-	-	-	-	4.3

At low SDS concentrations (0.05 and 0.1 cmc), the NR data for the SDS/polymer mixtures is well described by a 1-layer model (the data plotted as R vs Q is shown in Figure C.5 and a comparison to a 2-layer model fitting is shown in Figure C.6 in the Appendix), with a mixed interfacial layer comprising mostly the polymer and the thickness of this layer was dependent on the polymer concentration ($t \sim 12.3 \text{Å}$ and $\sim 24.0 \text{Å}$ for 0.2 and 2 cac polymer, respectively). However, it is important to note that the data cannot be fitted with a pure polymer layer, suggesting that there was cooperative adsorption at the interface at low SDS concentrations. The corresponding schematic representation shows a uniformly mixed layer of surfactant and polymer at the interface (Figure 3.5), of thickness similar to that of a pure polymer layer. The fitted $\varphi_{\text{PEG-g-PVAc}}$ is higher in the mixed layer from the sample with 2 cac PEG-g-PVAc ($\varphi_{\text{PEG-g-PVAc}} \sim 97\%$ polymer, corresponding to $\Gamma_{\text{PEG-g-PVAc}} \sim 2.05 \text{ mg m}^{-2}$ and $\Gamma_{\text{SDS}} \sim 0.13 \text{ μmol m}^{-2}$, equivalent to $\Gamma_{\text{SDS}} \sim 0.04 \text{ mg m}^{-2}$), compared to that from 0.2 cac PEG-g-PVAc ($\varphi_{\text{PEG-g-PVAc}}$

~90% polymer, or $\Gamma_{\text{PEG-g-PVAc}} \sim 0.98 \text{ mg m}^{-2}$ and $\Gamma_{\text{SDS}} \sim 0.38 \text{ } \mu\text{mol m}^{-2}$, which is equivalent to $\Gamma_{\text{SDS}} \sim 0.11 \text{ mg m}^{-2}$, respectively), with the thickness and associated roughness almost twice the value ($t \sim 24.0 \text{ } \text{\AA}$ with $\sigma \sim 7.6 \text{ } \text{\AA}$ compared to $t \sim 12.3 \text{ } \text{\AA}$ with $\sigma \sim 3.6 \text{ } \text{\AA}$, respectively). This is consistent with cooperative adsorption at the interface, with a homogeneously mixed layer of SDS and the polymer, likely forming polymer loops and trains [67] associated with surfactant molecules. As the polymer itself contains hydrophobic regions and is intrinsically surface active, synergistic adsorption with SDS is conceivable, as reported before for other polymer/SDS complexes [75]. The polymer/surfactant distribution, however, could not be obtained from the single-layer model.

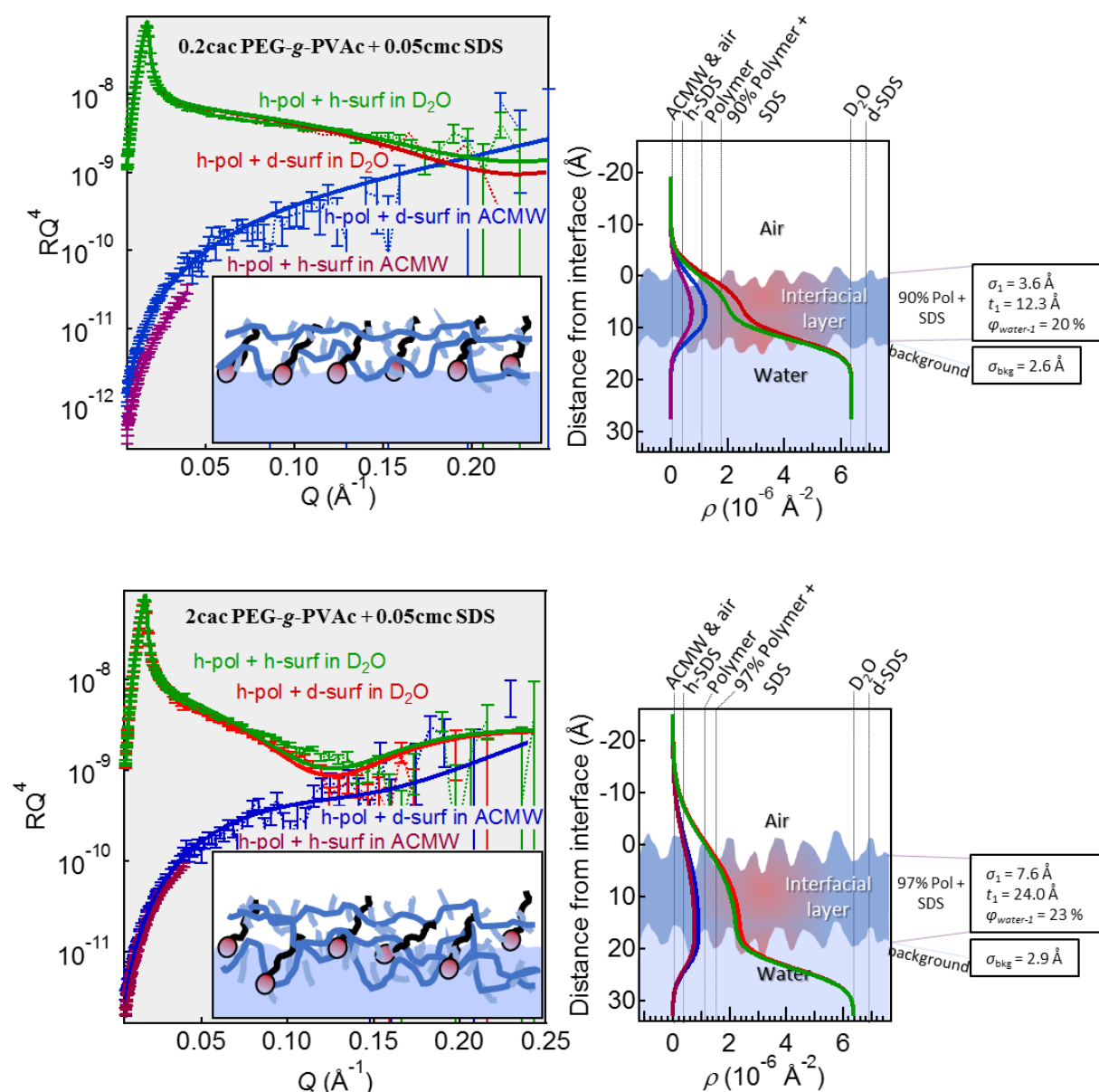


Figure 3.5 Fitted NR data for 0.05 cmc SDS with 0.2 and 2 cac PEG-g-PVAc, with the fitted ρ profiles and schematic representation based on the fitted parameters. The data is colour coded as follows: **red** represents mixtures of PEG-g-PVAc and dSDS in D_2O , **green** represents mixtures of PEG-g-PVAc with hSDS in D_2O , **blue** represents mixtures of PEG-g-PVAc with dSDS in ACMW, and **purple** represents mixtures of PEG-g-PVAc with hSDS in ACMW. The error bars associated with the data points were determined from the data reduction, larger at higher Q values due to lower contrast between the solvent and sample. The solid lines show the fitted curve, with the fitted parameters also shown, including thickness (t), solvent volume fraction (ϕ_{water}), and roughness of the layer (σ).

At intermediate concentration of SDS (0.5 cmc), the NR data was best fitted using a 2-layer model, with an upper layer at the air-water interface attributed to the surfactant hydrocarbon tails and a second underlying layer comprising a mixture of the SDS headgroups and the polymer (Figure 3.6). The headgroups are likely interacting with the PEG backbone, forming a tighter packed layer compared to a pure SDS layer [76]. For comparison, the fits using a 1-

layer model are also shown in Figure C.7. The much smaller fitted t_1 of the surfactant hydrocarbon tail layer ($t_1 \sim 4.9\text{-}5.8 \text{ \AA}$ depending on the polymer concentration, Table 3.1) compared to a pure monolayer of SDS ($t_1 \sim 9.0 \text{ \AA}$) suggests there is a tilted layer of SDS forming at the interface (with an average tilt angle ω of 50° in the case of 0.2 cac PEG-*g*-PVAc and 57° in the case of 2 cac PEG-*g*-PVAc with respect to the surface normal of pure 1.2 cmc SDS monolayer), with an underlying mixed polymer/SDS headgroup layer (*cf.* the schematic in figure insets).

The fitted t_2 of the polymer layer associated with SDS headgroups is relatively thin in both cases. Intriguingly, the headgroup/polymer layer thickness decreases with increased polymer concentration (from $t_2 \sim 5.3 \text{ \AA}$ to $t_2 \sim 4.7 \text{ \AA}$). Correspondingly, $\phi_{\text{PEG-}g\text{-PVAc}}$ in the layer decreases from $\sim 71 \%$ to $\sim 63 \%$. The adsorbed amount values at the interface are as follows: $\Gamma_{\text{PEG-}g\text{-PVAc}} \sim 0.25 \text{ mg m}^{-2}$ and $\Gamma_{\text{SDS}} \sim 2.77 \text{ \mu mol m}^{-2}$ (equivalent to $\Gamma_{\text{SDS}} \sim 0.80 \text{ mg m}^{-2}$) in the mixtures containing 0.2 cac PEG-*g*-PVAc, and $\Gamma_{\text{PEG-}g\text{-PVAc}} \sim 0.38 \text{ mg m}^{-2}$ and $\Gamma_{\text{SDS}} \sim 2.36 \text{ \mu mol m}^{-2}$ (equivalent to $\Gamma_{\text{SDS}} \sim 0.68 \text{ mg m}^{-2}$) in the mixtures containing 2 cac PEG-*g*-PVAc. This indicates preferential adsorption of the surfactant in the mixed layer at the lower polymer concentrations. Additionally, the SDS hydrocarbon tail thickness is also smaller in the mixture containing higher PEG-*g*-PVAc concentration, suggesting a more compact layer due to stronger interaction between the SDS and the polymer molecules at this concentration than at any other mixtures in the current series of measurements (0.05-5 cmc SDS and 0.2/2 cac PEG-*g*-PVAc).

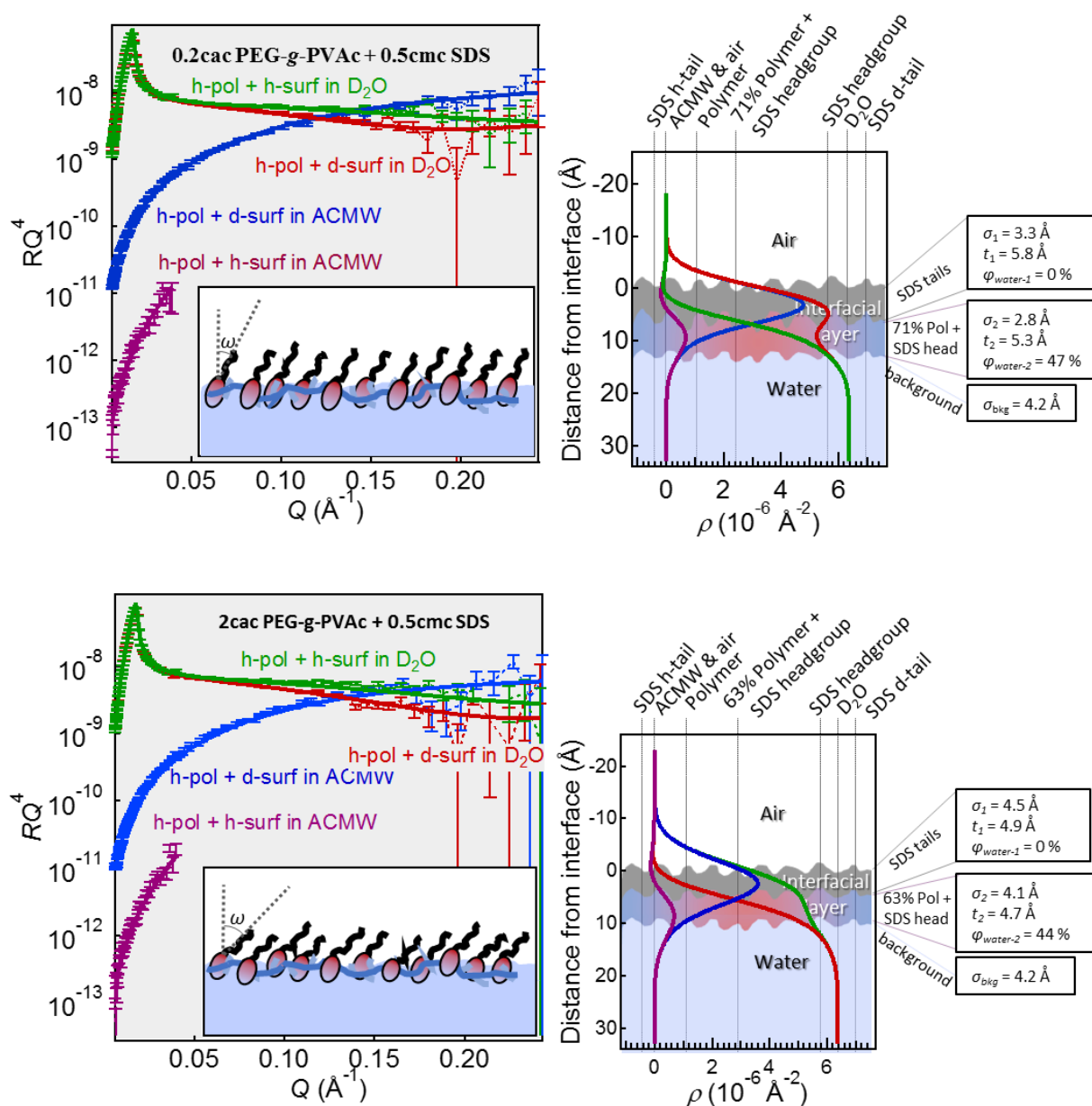


Figure 3.6 Fitted NR data for 0.5 cmc SDS with 0.2 and 2 cac PEG-g-PVAc, with the fitted ρ profiles and schematic representation based on the fitted parameters. The data is colour coded as follows: **red** represents mixtures of PEG-g-PVAc and dSDS in D_2O , **green** represents mixtures of PEG-g-PVAc with hSDS in D_2O , **blue** represents mixtures of PEG-g-PVAc with dSDS in ACMW, and **purple** represents mixtures of PEG-g-PVAc with hSDS in ACMW. The error bars associated with the data points were determined from the data reduction, larger at higher Q values due to lower contrast between the solvent and sample. The solid lines show the fitted curve, with the fitted parameters also shown, including thickness (t), solvent volume fraction (ϕ_{water}), and roughness of the layer (σ).

For mixtures with the SDS concentration above its cmc, a 3-layer model best describes the NR data: a SDS hydrocarbon tail layer at the air-water interface, an SDS headgroup layer, and an underlying PEG-g-PVAc layer (Figure 3.7). For comparison, the fits using a 1-layer model are also shown in Figure C.8. The thickness of the hydrocarbon tails ($t_1 \sim 9.2 \text{ \AA}$ in both cases) is similar to that of a pure SDS above its cmc (fitted $t_1 \sim 9.0 \text{ \AA}$, consistent with literature [18]), suggesting a complete SDS monolayer at the interface was formed (overall $\Gamma_{\text{SDS}} \sim 4.17 \text{ \mu mol m}^{-2}$). The fitted SDS headgroup layer thickness ($t_2 \sim 3.2\text{-}3.9 \text{ \AA}$) and ϕ_{water} agree with the literature values and theoretical calculations. The polymer layer beneath the SDS headgroups is very thin with a large interfacial roughness relative to its t ($t_3 \sim 3.2 \text{ \AA}$ with $\sigma_3 \sim 4.0 \text{ \AA}$ for SDS/0.2 cac PEG-g-PVAc, and $t_3 \sim 2.7 \text{ \AA}$ with $\sigma_3 \sim 4.1 \text{ \AA}$ for SDS/2 cac PEG-g-PVAc), which together with the high $\phi_{\text{water}} \sim 82\text{-}92\%$ suggests this layer is extremely inhomogeneous (low surface coverage and therefore very likely patchiness). This polymer layer is therefore likely to be stretching towards the bulk liquid sub-phase, and only have negligible effect on the γ (*cf.* Figure 3.2 and no visible $\Delta\gamma$ lowering compared to the pure SDS above its cmc). Such a behaviour suggests a strong competitive adsorption where the SDS forms a complete monolayer at the interface and the polymer is depleted from the interface with an extremely small amount associated with the interface, where the SDS headgroups can still interact with the solubilised polymer. This is reflected in the corresponding adsorbed amounts: $\Gamma_{\text{PEG-g-PVAc}} \sim 0.01 \text{ mg m}^{-2}$ in mixtures containing 0.2 cac PEG-g-PVAc, $\Gamma_{\text{PEG-g-PVAc}} \sim 0.03 \text{ mg m}^{-2}$ in mixtures containing 2 cac PEG-g-PVAc, and $\Gamma_{\text{SDS}} \sim 4.17 \text{ \mu mol m}^{-2}$ (equivalent to $\Gamma_{\text{SDS}} \sim 1.20 \text{ mg m}^{-2}$) independent of the polymer concentration.

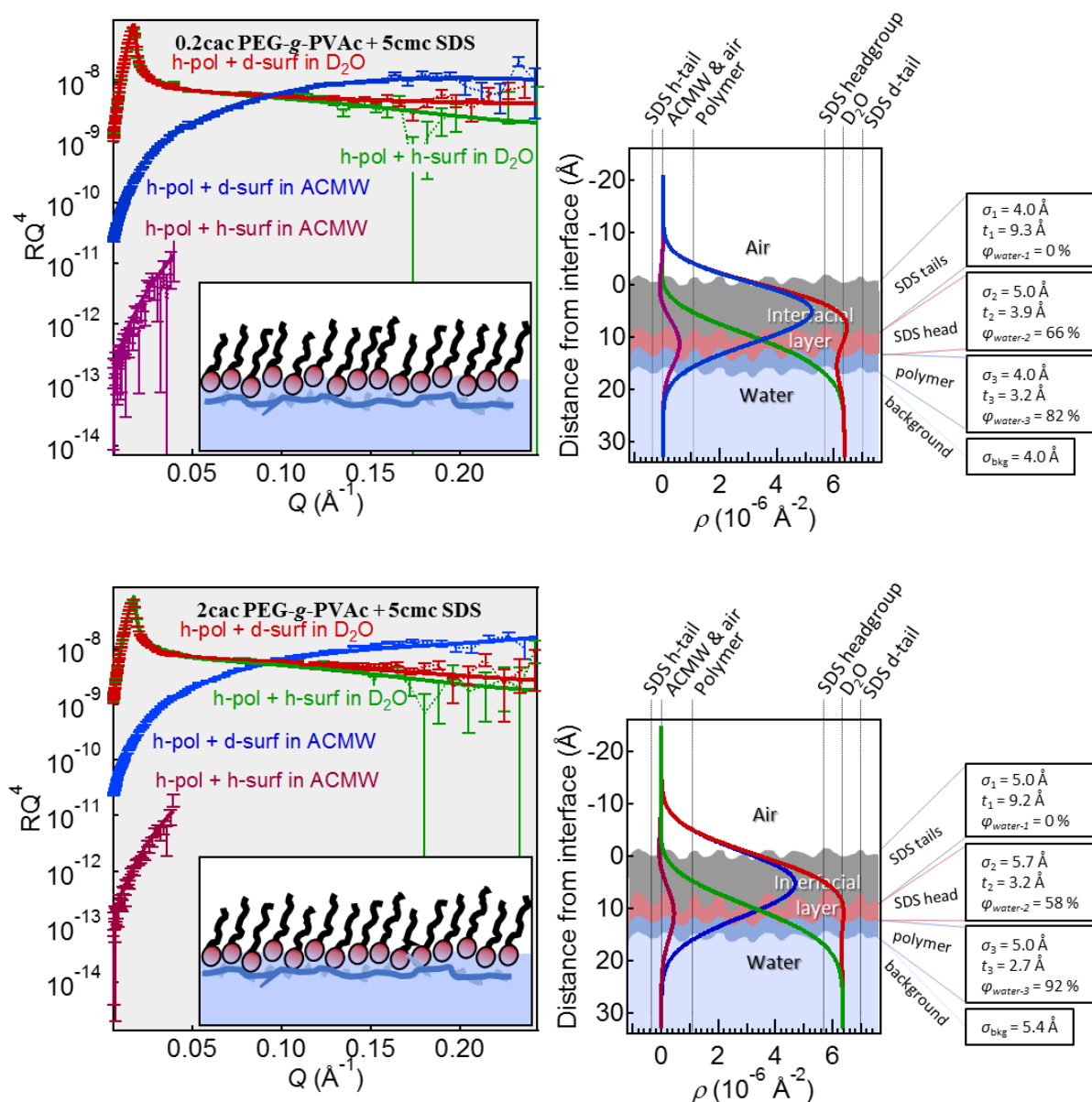


Figure 3.7 Fitted NR data for 5 cmc SDS with 0.2 and 2 cac PEG-g-PVAc, with the fitted ρ profiles and schematic representation based on the fitted parameters. The data is colour coded as follows: **red** represents mixtures of PEG-g-PVAc and dSDS in D₂O, **green** represents mixtures of PEG-g-PVAc with hSDS in D₂O, **blue** represents mixtures of PEG-g-PVAc with dSDS in ACMW, and **purple** represents mixtures of PEG-g-PVAc with hSDS in ACMW. The error bars associated with the data points were determined from the data reduction, larger at higher Q values due to lower contrast between the solvent and sample. The solid lines show the fitted curve, with the fitted parameters also shown, including thickness (t), solvent volume fraction (φ_{water}), and roughness of the layer (σ).

The trends observed from the calculated Γ data are consistent with the trends of the fitted t from the NR data, and the interfacial adsorption behaviour derived from the surface tension measurements. In general, over the range of samples examined, with increasing SDS concentration, t_1 and Γ_{SDS} increase and $\Gamma_{\text{PEG-g-PVAc}}$ (also $\phi_{\text{PEG-g-PVAc}}$ where relevant) and t_3 decrease progressively. That is, we have observed evidence for synergistic adsorption of SDS/PEG-g-PVAc mixtures at low SDS concentration, with a transition to competitive adsorption at the interface for mixtures at higher SDS concentrations (as schematically represented in Figure 3.8). At the SDS concentrations >0.5 cmc, the interfacial layer comprises predominantly of an SDS monolayer, with PEG-g-PVAc depleted from the interface.

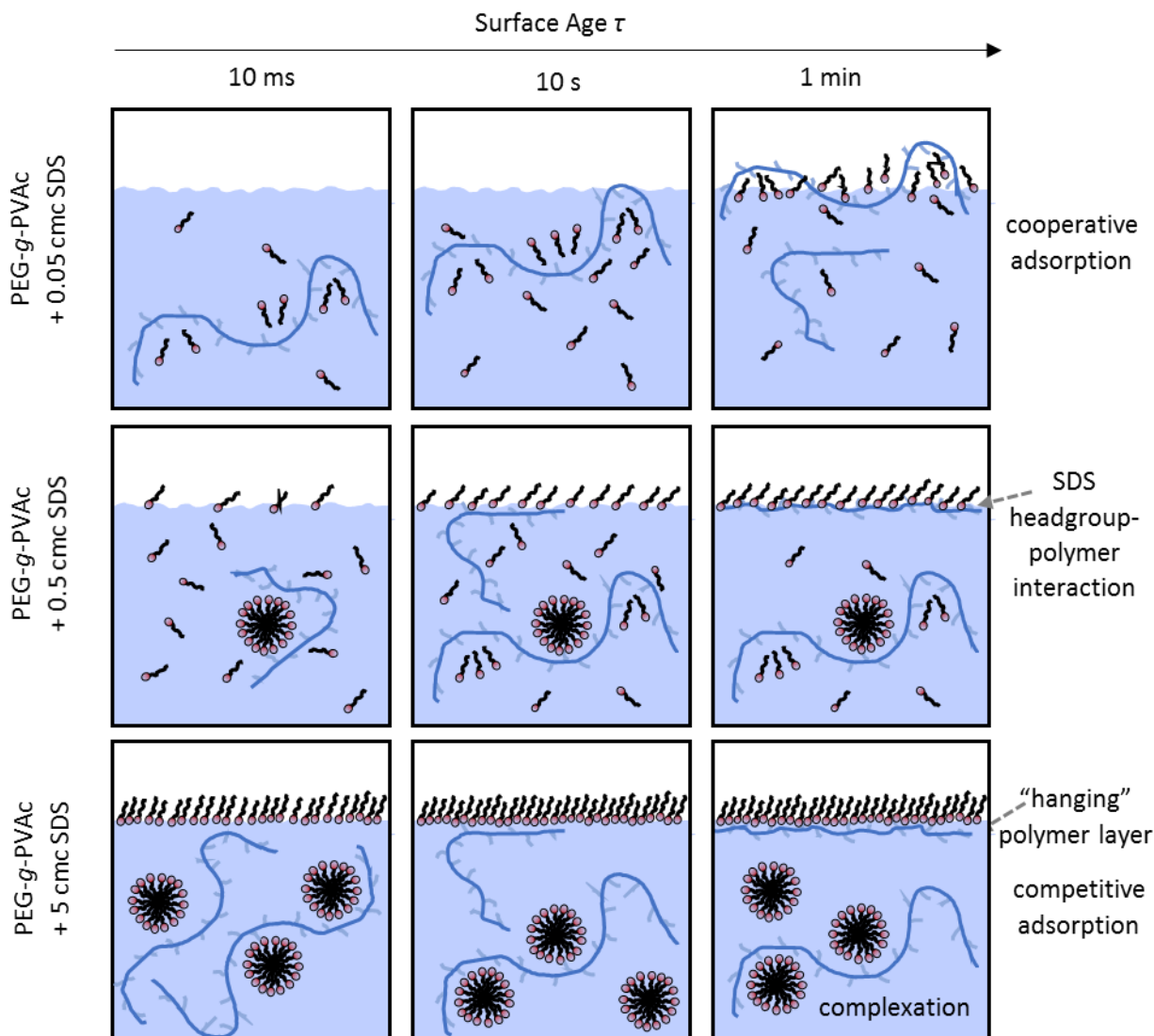


Figure 3.8 A schematic representation of the polymer/surfactant adsorption behaviour at the air-water interface derived from the combination of dynamic surface tension and NR data. Top row: synergistic cooperative adsorption regime. Fully cooperative adsorption of the polymer/surfactant system at very low SDS concentration (0.05 cmc SDS + PEG-g-PVAc) at all timescales and as a fully mixed complex at the interface. Middle row: transition regime. SDS molecules adsorbed at the air-water interface first, followed by a secondary and much slower polymer adsorption towards the interface, forming a "hanging" polymer layer interacting mainly with the SDS headgroups at the interface, consistent with the data obtained for mixtures of 0.5 cmc SDS + PEG-g-PVAc. Bottom row: competitive adsorption regime: formation of SDS monolayer at the air-water interface followed by micellisation in the bulk and likely formation of polymer/SDS micelle complexes, consistent with data obtained for 5 cmc SDS + PEG-g-PVAc. The secondary adsorption of the polymer towards the interface can be derived from the NR data fitting, as there is no influence of the polymer on the final surface tension data in the systems containing 5 cmc SDS.

3.3.3 Foaming behaviour of the polymer/surfactant mixtures: The “hanging” polymer layer affects the foamability and foam stability

The foam stability, measured as the time at which the foam volume has reduced to 50% of its initial value and denoted as $\tau_{FVS\ 50\%}$, is enhanced after the addition of PEG-*g*-PVAc compared to that of a pure SDS solution foam even at high surfactant concentration (Figure 3.9a, Table 3.2). The most pronounced $\tau_{FVS\ 50\%}$ enhancement is evident in the systems containing SDS concentrations below its cmc. In the pure system containing 0.05 cmc SDS, $\tau_{FVS\ 50\%} \sim 246$ s, compared to $\tau_{FVS\ 50\%} \sim 3555$ s in the system containing 2 cac PEG-*g*-PVAc + 0.05 cmc SDS showing synergistic behaviour in the polymer/surfactant foam stabilisation. The most pronounced foam stability enhancement was observed in systems containing 0.5 cmc SDS ($\tau_{FVS\ 50\%} \sim 3632$ s for 0.5 cmc SDS, $\tau_{FVS\ 50\%} \sim 10840$ s for 0.5 cmc SDS + 0.2 cac PEG-*g*-PVAc and $\tau_{FVS\ 50\%} \sim 11822$ s for 0.5 cmc SDS + 2 cac PEG-*g*-PVAc). At this concentration, we deduced a mixed SDS headgroup/polymer from NR fitting at the air-water interface (Figure 3.6). This interfacial layer will therefore be present in the foam bubbles, enhancing the foam stability *via* the presence of interacting polymer/headgroup layer.

The foamability (or the maximum foam volume produced, $V_{\text{foam max}}$, Figure 3.9b) is not significantly influenced by the addition of polymer to an SDS solution at higher SDS concentration with $V_{\text{foam max}} \sim 83$ mL in all systems containing SDS at 0.5 and 5 cmc, including the polymer/surfactant systems. Furthermore, it is only slightly influenced by the presence of polymer in the mixtures containing low concentration SDS, with $V_{\text{foam max}} \sim 78$ mL in 2 cac PEG-*g*-PVAc with 0.05 cmc SDS, compared to $V_{\text{foam max}} \sim 69$ mL in the pure 0.05 cmc SDS.

The initial bubble radius, $R_{\text{avg initial}}$ (Figure 3.9c), is essentially constant within the error margins of the measurements for the polymer/surfactant mixtures with the pure surfactant system. The bubble size of the pure polymer sample above its cmc value is larger ($R_{\text{avg initial}} \sim 180$ μm) than that of the mixed systems ($R_{\text{avg initial}} \sim 130$ μm for all the mixed systems studied), so we can conclude that SDS governs the bubble size at the initial stages of the foaming ($R_{\text{avg initial}} \sim 125$ -140 μm for SDS at 0.05-5 cmc).

Table 3.2 The $V_{\text{foam max}}$, $\tau_{\text{FVS } 50\%}$ and $R_{\text{avg initial}}$ determined from foam measurements of PEG-*g*-PVAc mixtures with SDS.

PEG- <i>g</i> - PVAc conc (cac)	SDS conc (cmc)	Foam half-life time, $\tau_{\text{FVS } 50\%}$ (s)	Maximum foam volume, $V_{\text{foam max}}$ (mL)	Initial average bubble radius, $R_{\text{avg initial}}$ (μm)
0.2	-	10.4 ± 8.3	11.7 ± 4.0	14.0 ± 0.5
2	-	121.7 ± 46.0	48.4 ± 6.8	180.7 ± 30.0
-	0.05	245.8 ± 134.3	69.3 ± 1.7	125.7 ± 11.6
0.2	0.05	66.4 ± 9.1	65.3 ± 5.1	129.7 ± 2.3
2	0.05	3555.0 ± 526.2	78.4 ± 0.8	134.0 ± 4.4
-	0.5	3632.4 ± 2215.0	84.0 ± 4.3	136.0 ± 5.6
0.2	0.5	10839.8 ± 1837.3	82.6 ± 5.0	128.0 ± 1.7
2	0.5	11821.9 ± 676.4	82.7 ± 1.8	130.0 ± 1.0
-	5	3538.0 ± 296.5	80.8 ± 1.4	141.3 ± 2.1
0.2	5	4863.7 ± 326.1	83.9 ± 3.6	129.7 ± 6.5
2	5	4633.0 ± 767.8	83.3 ± 0.8	125.7 ± 7.1

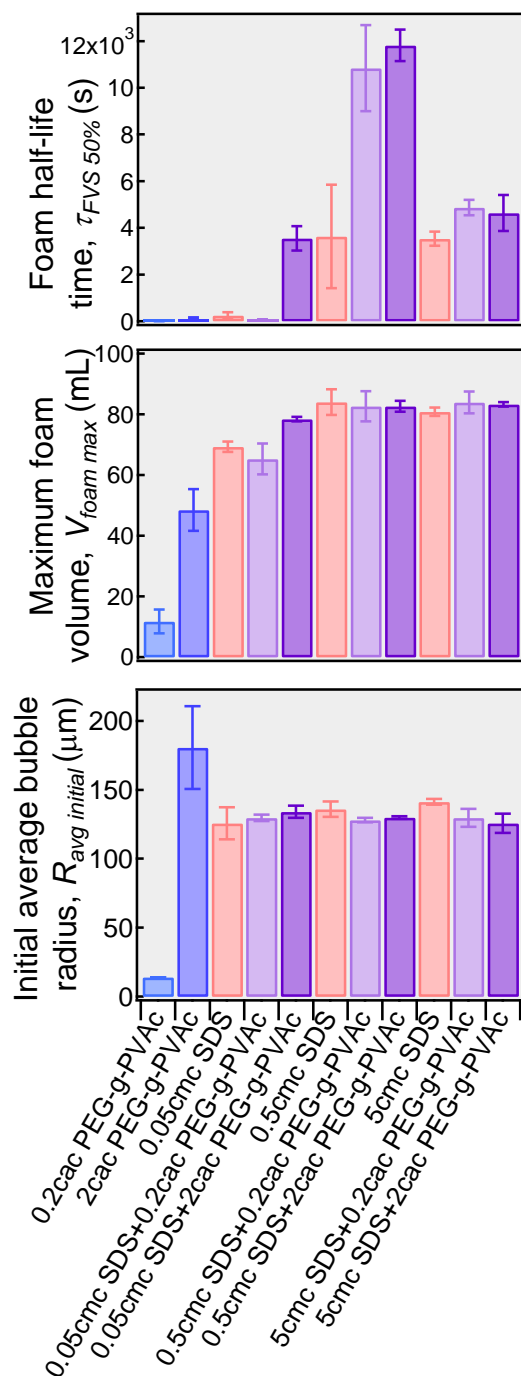


Figure 3.9 Foaming data showing the: a) foam half-life time ($\tau_{FVS 50\%}$) which is a measure of foam stability, b) maximum foam volume ($V_{foam max}$) which is a measure of foamability, and c) initial average bubble radius ($R_{avg initial}$) showing the radius of the foam bubbles during the foam generation. The data in orange represents the pure SDS solutions at 3 concentrations, the data in blue represents data for the pure polymer at 2 concentrations. The mixed polymer/surfactant systems are shown in pale and dark purple for SDS with 0.2 cac PEG-g-PVAc and SDS with 2 cac PEG-g-PVAc respectively.

The macroscopic foaming behaviour of PEG-g-PVAc/SDS mixtures containing 5 cmc SDS is shown in Figure 3.10. The surface tension data of this mixture suggests near complete polymer depletion from the interface, hence we would not expect a significant influence of the polymer presence on the foaming behaviour in mixtures containing high SDS concentration. However,

from the NR data fitting, we inferred the presence of a thin layer of the polymer ($t_3 \sim 0.3$ nm; *cf.* Figure 3.7) beneath the SDS monolayer. The slightly enhanced foam stability (Figure 3.9a) demonstrates the role of this polymer layer, even though it is depleted from the interface, highly solvated and inhomogeneous. The polymer is present at sufficiently low concentration so as to not significantly change the viscosity of the mixed polymer/surfactant liquid sample compared to that of a pure SDS solution and so does not influence the foam stability purely by increasing the viscosity. We attributed the increased foam stability to the presence of the “hanging” polymer layer interacting with the SDS at the air-water interfaces in the foam solution.

The foamability is relatively constant and not influenced by the addition of polymer to an SDS solution (Figure 3.9b), and so the polymer is thought to influence mainly the foam breakdown mechanism rather than foam formation. During the foam formation, the fast-adsorbing SDS molecules form thin film layers at the bubble interface which stabilise the foam during its generation. This effect can also be observed by comparing the bubble size at the initial stage of the foaming (Figure 3.9c), where the initial bubble size is governed by the SDS in the polymer/surfactant mixtures. The bubble size then varies with time during the foam destabilisation, with larger bubbles (on average) formed in the mixtures containing the polymer. The mixtures also exhibit a slightly more homogenous bubble size distribution (Figure 3.10). The enhanced foam stability is also shown visually in Figure 3.10 where the volume of foam present 1 hour after foam generation is larger for the polymer/surfactant mixtures than pure SDS.

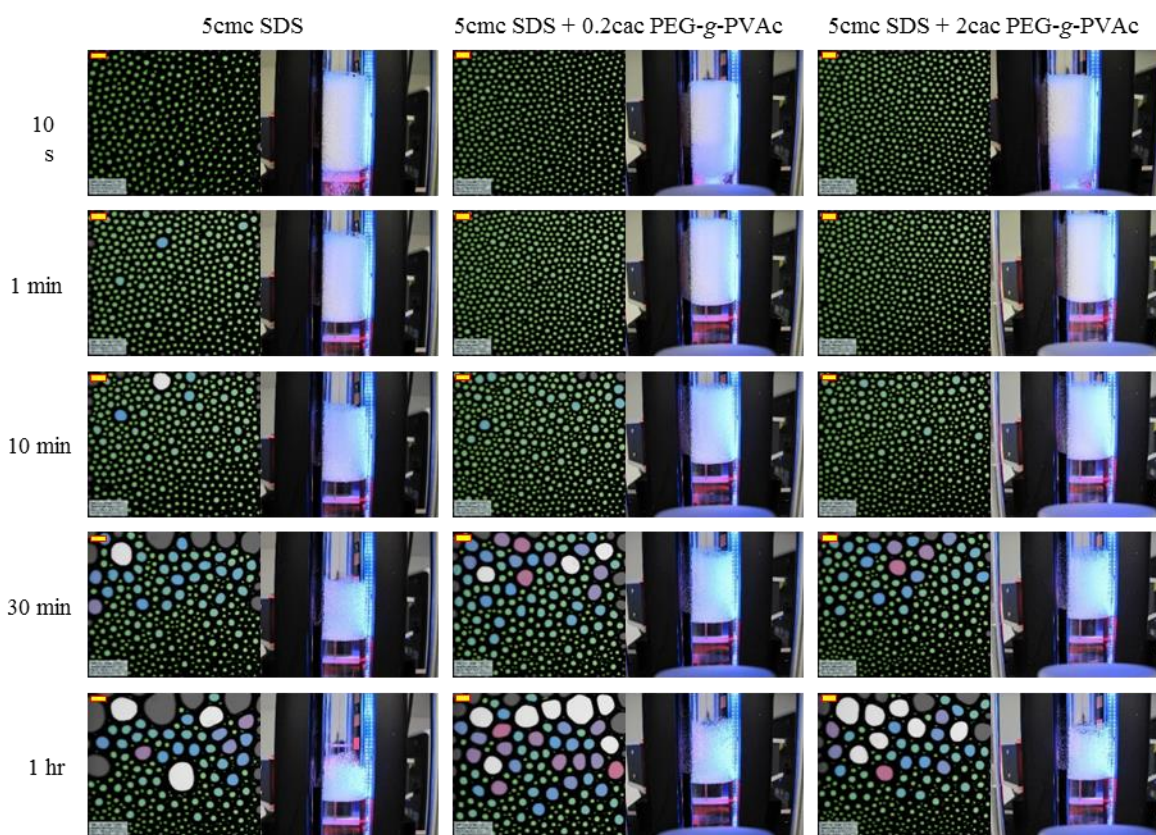


Figure 3.10 Macroscopic foaming behaviour data (overall foam volume) and foam bubble size recorded over a given period after foam generation are shown, comparing the pure 5 cmc SDS system (left column) to the mixed systems containing 5cmc SDS + 0.2 cac PEG-g-PVAc (middle column) and 5cmc SDS + 2 cac PEG-g-PVAc (right column). The bubble size is colour coded as follows: green is for smallest bubble radius, followed by blue, purple, pink and the largest bubbles are shown in white, with the scale bar shown representing 1 mm.

3.4 Conclusions

We have studied the interaction between a neutral ‘tardigrade’ co-polymer (consisting of a hydrophilic polyethylene glycol backbone with hydrophobic polyvinyl acetate grafts, PEG-g-PVAc) and an anionic surfactant (sodium dodecylsulfate, SDS) at the air-water interface. The polymer concentration in the mixture was 0.0002 wt% and 0.002 wt% (corresponding to 0.2 cac and 2 cac, respectively), whilst the SDS concentration was varied between 0.05 – 5 cmc. Contrast-matched neutron reflectivity (NR) complemented by surface tension measurements allowed elucidation of the interfacial composition and structure of these mixed systems, as well as providing physical insights into the polymer/surfactant interactions at the air-water interface. The foaming behaviour of these mixtures was also examined.

Surface tension measurements (Figure 3.2a) indicate a synergistic effect (cooperative adsorption) of the mixture at low surfactant concentration. At higher surfactant concentrations, the surface tension data points towards competitive adsorption with the polymer being depleted from the air-water interface, where the surface tension of the mixture had the same value as that of the pure SDS above its cmc.

Our observation of synergy at low surfactant concentration and the transition to competitive behaviour purely by increasing SDS concentration is not a commonly observed behaviour and has not been pointed out before, as such. Competitive behaviour of SDS with methacrylate-PEO comb co-polymers [64] and SDS with linear and branched PEO even before the cac [65] has been shown previously. In a system of SDS with PNIPAM, the polymer adsorption was not influenced before the cac, with depletion of the polymer from the air-water interface observed above cac [77]. We can conclude that both the molecular architecture (comb co-polymer of certain graft density and graft lengths) and the chemical characteristics of the co-polymer (hydrophilic PEO backbone with more hydrophobic PVAc grafts) play an important role in the interfacial behaviour and interactions with SDS.

Such a synergy-to-competition transition has also been observed from fitting the NR data of the mixtures at the air-water interface, which yielded structural and compositional information on the interfacial layer. There is a significant synergistic effect observed at low concentrations of SDS and PEG-*g*-PVAc, with a less pronounced synergy in the mixtures of the higher polymer concentration (0.002 wt%). The synergy-to-competition transition occurred at ~0.5 cmc SDS, where the interfacial behaviour changed from cooperative to competitive adsorption. The air-water interface was predominantly covered by an SDS monolayer, whilst PEG-*g*-PVAc interacted strongly with the SDS headgroups in the water subphase. The polymer was found depleted from the interface at SDS concentrations above its cmc, forming a thin, non-uniform layer “hanging” just underneath the SDS monolayer.

The implications of such structural and compositional characteristics of the interfacial layer for foaming behaviour of the polymer/surfactant mixture were also evaluated. Our preliminary foam behaviour measurements (on the foam half-life, height, and initial bubble size) show enhanced foam stability in the presence of PEG-*g*-PVAc polymer, as compared to pure SDS solutions, even when the polymer was depleted from the interface and did not contribute significantly to the surface activity (as gauged by the surface tension). This points to the subtle

and complex behaviour of foams, and the importance of the structural information in providing interpretation of the foaming efficacy of polymer/surfactant mixtures.

Our study thus highlights the importance of using a combination of different methods which can unravel structural and compositional details of polymer/surfactant mixtures at the air-water interface. Such information can complement classic surface tension measurements to gain insight into foam behaviour, important in understanding thin film stability and detergency efficacy of such polymer/surfactant mixtures widespread in industrial and personal care formulations. In addition to the polymer architecture, the chemical characteristics of the surfactant is also crucial to the structure and composition of the interfacial layer. We have also studied the mixture of the PEG-*g*-PVAc co-polymer with cationic C₁₂TAB and non-ionic C₁₂E₅ at the air-water interface, and the effect of the surfactant headgroup will be evaluated and its contribution towards the polymer/surfactant interactions (the effect on the synergy to competition transition) and the interfacial behaviour of such mixed layers discussed later.

3.5 References

1. Petkova, R., Tcholakova, S., and Denkov, N.D., *Foaming and Foam Stability for Mixed Polymer–Surfactant Solutions: Effects of Surfactant Type and Polymer Charge*. *Langmuir*, 2012. **28**(11): p. 4996-5009.
2. Mitrinova, Z., et al., *Role of interactions between cationic polymers and surfactants for foam properties*. *Colloids and Surfaces A: Physicochemical and Engineering Aspects*, 2016. **489**: p. 378-391.
3. Bureiko, A., et al., *Current applications of foams formed from mixed surfactant–polymer solutions*. *Advances in Colloid and Interface Science*, 2015. **222**: p. 670-677.
4. Goddard, E.D., *Polymer/surfactant interaction—Its relevance to detergent systems*. *Journal of the American Oil Chemists' Society*, 1994. **71**(1): p. 1-16.
5. Qi, S., et al., *Insights into the Role of Polymer-Surfactant Complexes in Drug Solubilisation/Stabilisation During Drug Release from Solid Dispersions*. *J Pharmaceutical Research*, 2013. **30**(1): p. 290-302.
6. Somasundaran, P. and Lee, L.T., *Polymer-Surfactant Interactions in Flotation of Quartz*. *Separation Science and Technology*, 1981. **16**(10): p. 1475-1490.
7. Sharipova, A.A., et al., *Polymer–surfactant complexes for microencapsulation of vitamin E and its release*. *Colloids and Surfaces B: Biointerfaces*, 2016. **137**: p. 152-157.

8. W. Sulek, M. and Jedynek, R., *The effect of the formation of polymer/surfactant complexes on selected tribological properties of their aqueous solutions*. Vol. 281. 2018. 117-122.
9. Somasundaran, P., et al., *Surfactants, polymers and their nanoparticles for personal care applications*. Vol. 27. 2005. 135-136.
10. Martani, R., Le Huede, E., and Dumas, J., *Controlled release pharmaceutical composition*. 1989, Google Patents.
11. Dakhara, S. and Anajwala, C.J.S.R.i.P., *Polyelectrolyte complex: A pharmaceutical review*. 2010. **1**(2): p. 121.
12. Canter, N.H., Robbins, M.L., and Baker, E.G., *Polymer-microemulsion complexes for the enhanced recovery of oil*. 1982, Google Patents.
13. Taylor, D.J.F., Thomas, R.K., and Penfold, J., *Polymer/surfactant interactions at the air/water interface*. *Advances in Colloid and Interface Science*, 2007. **132**(2).
14. Zhang, X.L., et al., *Adsorption of Polyelectrolyte/Surfactant Mixtures at the Air–Water Interface: Modified Poly(ethyleneimine) and Sodium Dodecyl Sulfate*. *Langmuir*, 2011. **27**(6): p. 2601-2612.
15. Narayanan, T., et al., *Recent applications of synchrotron radiation and neutrons in the study of soft matter*. *Crystallography Reviews*, 2017. **23**(3): p. 160-226.
16. Braun, L., et al., *Polymers and surfactants at fluid interfaces studied with specular neutron reflectometry*. *Advances in Colloid and Interface Science*, 2017. **247**: p. 130-148.
17. Skoda, M.W.A., *Recent developments in the application of X-ray and neutron reflectivity to soft-matter systems*. *Current Opinion in Colloid & Interface Science*, 2019. **42**: p. 41-54.
18. Campbell, R.A., et al., *Structure of surfactant and phospholipid monolayers at the air/water interface modeled from neutron reflectivity data*. *Journal of Colloid and Interface Science*, 2018. **531**: p. 98-108.
19. Lu, J., et al., *Adsorption of Dodecyl Sulfate Surfactants with Monovalent Metal Counterions at the Air-Water Interface Studied by Neutron Reflection and Surface Tension*. Vol. 158. 1993. 303-316.
20. Staples, E., et al., *The structure and composition of surfactant-polymer mixtures of sodium dodecyl sulphate, hexaethylene glycol monododecyl ether and poly-(dimethyldialyl ammonium chloride) adsorbed at the air-water interface*. *Journal of Physics: Condensed Matter*, 2000. **12**(28): p. 6023-6038.
21. Sebastiani, F., et al., *Nighttime oxidation of surfactants at the air–water interface: effects of chain length, head group and saturation*. *Atmos. Chem. Phys.*, 2018. **18**(5): p. 3249-3268.

-
22. Lu, J.R., Thomas, R.K., and Penfold, J., *Surfactant layers at the air/water interface: structure and composition*. *Advances in Colloid and Interface Science*, 2000. **84**(1–3): p. 143-304.
 23. Wang, C. and Tam, K.C., *Interaction between Polyelectrolyte and Oppositely Charged Surfactant: Effect of Charge Density*. *The Journal of Physical Chemistry B*, 2004. **108**(26): p. 8976-8982.
 24. Berret, J.-F., et al., *Electrostatic Self-Assembly of Oppositely Charged Copolymers and Surfactants: A Light, Neutron, and X-ray Scattering Study*. *Macromolecules*, 2004. **37**(13): p. 4922-4930.
 25. Penfold, J., et al., *Adsorption of Polyelectrolyte/Surfactant Mixtures at the Air–Solution Interface: Poly(ethyleneimine)/Sodium Dodecyl Sulfate†*. *Langmuir*, 2005. **21**(22): p. 10061-10073.
 26. Wang, H., et al., *Binding of Sodium Dodecyl Sulfate with Linear and Branched Polyethyleneimines in Aqueous Solution at Different pH Values*. *Langmuir*, 2006. **22**(4): p. 1526-1533.
 27. Khan, N. and Brettmann, B., *Intermolecular Interactions in Polyelectrolyte and Surfactant Complexes in Solution*. 2018. **11**(1): p. 51.
 28. Chen, H.-L., Ko, C.-C., and Lin, T.-L., *Self-Assembly in the Bulk Complexes of Poly(ethylene oxide) with Amphiphilic Dodecylbenzenesulfonic Acid*. *Langmuir*, 2002. **18**(14): p. 5619-5623.
 29. Azum, N., et al., *Thermodynamic aspects of polymer–surfactant interactions: Gemini (16-5-16)-PVP-water system*. *Arabian Journal of Chemistry*, 2016. **9**: p. S1660-S1664.
 30. Zhao, L. and Lin, Z., *Self-assembly of non-linear polymers at the air/water interface: the effect of molecular architecture*. *Soft Matter*, 2011. **7**(22): p. 10520-10535.
 31. Wang, W., et al., *Synthesis and Characterization of Comb and Centipede Multigraft Copolymers PnBA-g-PS with High Molecular Weight Using Miniemulsion Polymerization*. *Macromolecules*, 2014. **47**(21): p. 7284-7295.
 32. Gregory, A. and Stenzel, M.H., *Complex polymer architectures via RAFT polymerization: From fundamental process to extending the scope using click chemistry and nature's building blocks*. *Progress in Polymer Science*, 2012. **37**(1): p. 38-105.
 33. Ergene, C., Yasuhara, K., and Palermo, E.F., *Biomimetic antimicrobial polymers: recent advances in molecular design*. *Polymer Chemistry*, 2018. **9**(18): p. 2407-2427.
 34. Pettersson, T., et al., *Lubrication Properties of Bottle-Brush Polyelectrolytes: An AFM Study on the Effect of Side Chain and Charge Density*. *Langmuir*, 2008. **24**(7): p. 3336-3347.
 35. Banquy, X., et al., *Bioinspired Bottle-Brush Polymer Exhibits Low Friction and Amontons-like Behavior*. *Journal of the American Chemical Society*, 2014. **136**(17): p. 6199-6202.

36. Li, L., et al., *Self-assembly of random copolymers*. Chemical Communications, 2014. **50**(88): p. 13417-13432.
37. Bartolini, A., et al., *Poly(ethylene glycol)-graft-poly(vinyl acetate) single-chain nanoparticles for the encapsulation of small molecules*. Physical Chemistry Chemical Physics, 2017. **19**(6): p. 4553-4559.
38. Mamusa, M., et al., *Associative properties of poly(ethylene glycol)-poly(vinyl acetate) comb-like graft copolymers in water*. Nanoscale, 2019. **11**(14): p. 6635-6643.
39. Claesson, P.M., et al., *Bottle-brush polymers: Adsorption at surfaces and interactions with surfactants*. Advances in Colloid and Interface Science, 2010. **155**(1): p. 50-57.
40. Bartolini, A., et al., *Liquid-liquid Phase Separation of Polymeric Microdomains with Tunable Inner Morphology: Mechanistic Insights and Applications*. Journal of Colloid and Interface Science, 2019.
41. Gopalkrishnan, S., et al., *Detergency boosting polymer blends as additives for laundry formulations*. 1998, BASF Corporation (Mount Olive, NJ): United States.
42. Gopalkrishnan, S., Guiney, K.M., and Sherman, J.V., *Modified polyacrylic acid polymers for anti-redeposition performance*. 1998, BASF Corporation (Mount Olive, NJ): United States.
43. Gopalkrishnan, S., et al., *Stable, aqueous concentrated liquid detergent compositions containing hydrophilic copolymers*. 1996, BASF Corporation (Mount Olive, NJ): United States.
44. Krinski, T.L. and Tran, T.H., *Method for improving the soil anti-redeposition properties of washing detergents and product*. 1992, Protein Technologies International, Inc. (St. Louis, MO): United States.
45. Kud, A., Trieselt, W., and Hartmann, H., *Use of graft polymers based on polyalkylene oxides as grayness inhibitors in the wash and aftertreatment of textile material containing synthetic fibers*. 1990: United States.
46. Holland, R.J., York, A.V., and Ruppert, R.M., *Pre-treating textiles with dispersions of graft polymers based on polyalkylene oxides to impart soil release properties thereto*. 1991, BASF Corporation (Parsippany, NJ): United States.
47. Sramek, J.A., *Low pH amphoteric fabric cleaning solution*. 2000, S. C. Johnson & Son, Inc. (Racine, WI): United States.
48. Schulze-Zachau, F. and Braunschweig, B., *Structure of Polystyrenesulfonate/Surfactant Mixtures at Air-Water Interfaces and Their Role as Building Blocks for Macroscopic Foam*. Langmuir, 2017. **33**(14): p. 3499-3508.
49. Dickinson, E., et al., *A neutron reflectivity study of the adsorption of .beta.-casein at fluid interfaces*. Langmuir, 1993. **9**(1): p. 242-248.
50. Petkova, R., Tcholakova, S., and Denkov, N.D., *Role of polymer-surfactant interactions in foams: Effects of pH and surfactant head group for cationic*

-
- polyvinylamine and anionic surfactants*. Colloids and Surfaces A: Physicochemical and Engineering Aspects, 2013. **438**: p. 174-185.
51. Mansour, O., et al., *Assembly of small molecule surfactants at highly dynamic air-water interfaces*. Vol. 13. 2017.
 52. Mikhailovskaya, A., et al., *Probing foam with neutrons*. Vol. 247. 2017.
 53. Kristen-Hochrein, N., Schelero, N., and von Klitzing, R., *Effects of oppositely charged surfactants on the stability of foam films*. Colloids and Surfaces A: Physicochemical and Engineering Aspects, 2011. **382**(1–3): p. 165-173.
 54. Kristen, N., et al., *Foam Films from Oppositely Charged Polyelectrolyte/Surfactant Mixtures: Effect of Polyelectrolyte and Surfactant Hydrophobicity on Film Stability*. Langmuir, 2010. **26**(12): p. 9321-9327.
 55. Marinova, K.G., et al., *Physico-chemical factors controlling the foamability and foam stability of milk proteins: Sodium caseinate and whey protein concentrates*. Food Hydrocolloids, 2009. **23**(7): p. 1864-1876.
 56. Fauser, H. and von Klitzing, R., *Effect of polyelectrolytes on (de)stability of liquid foam films*. Soft Matter, 2014. **10**(36): p. 6903-6916.
 57. Sirisattha, S., et al., *Toxicity of anionic detergents determined by Saccharomyces cerevisiae microarray analysis*. Water Research, 2004. **38**(1): p. 61-70.
 58. Campbell, R.A., et al., *Polyelectrolyte/surfactant films spread from neutral aggregates*. Soft Matter, 2016. **12**(24): p. 5304-5312.
 59. Campbell, R.A., *Recent advances in resolving kinetic and dynamic processes at the air/water interface using specular neutron reflectometry*. Current Opinion in Colloid & Interface Science, 2018. **37**: p. 49-60.
 60. Li, Z.X., Dong, C.C., and Thomas, R.K., *Neutron Reflectivity Studies of the Surface Excess of Gemini Surfactants at the Air–Water Interface*. Langmuir, 1999. **15**(13): p. 4392-4396.
 61. Campbell, R.A., Wacklin, H.P., and Sutton, I., *FIGARO: The new horizontal neutron reflectometer at the ILL*. The European Physical Journal Plus, 2011. **126**(107).
 62. Webster, J., Holt, S., and Dalglish, R., *INTER the chemical interfaces reflectometer on target station 2 at ISIS*. Physica B: Condensed Matter, 2006. **385-386**: p. 1164-1166.
 63. Nelson, A., *Co-refinement of multiple-contrast neutron/X-ray reflectivity data using MOTOFIT*. 2006. **39**(2): p. 273-276.
 64. Péron, N., et al., *Competitive Adsorption of Neutral Comb Polymers and Sodium Dodecyl Sulfate at the Air/Water Interface*. The Journal of Physical Chemistry B, 2008. **112**(25): p. 7410-7419.
 65. Péron, N., et al., *Competitive adsorption of sodium dodecyl sulfate and polyethylene oxide at the air/water interface*. J. Colloid Interface Sci., 2007. **313**(2): p. 389-397.

-
66. Crowley, T.L., et al., *The application of neutron reflection to the study of layers adsorbed at liquid interfaces*. Colloids and Surfaces, 1991. **52**: p. 85-106.
 67. Millet, F., et al., *Adsorption of Hydrophobically Modified Poly(acrylic acid) Sodium Salt at the Air/Water Interface by Combined Surface Tension and X-ray Reflectivity Measurements*. Langmuir, 1999. **15**(6): p. 2112-2119.
 68. Darvas, M., Gilányi, T., and Jedlovsky, P., *Competitive Adsorption of Surfactants and Polymers at the Free Water Surface. A Computer Simulation Study of the Sodium Dodecyl Sulfate–Poly(ethylene oxide) System*. The Journal of Physical Chemistry B, 2011. **115**(5): p. 933-944.
 69. Miles, G.D. and Shedlovsky, L., *Minima in Surface Tension–Concentration Curves of Solutions of Sodium Alcohol Sulfates*. The Journal of Physical Chemistry, 1944. **48**(1): p. 57-62.
 70. Chari, K., Seo, Y.-S., and Satija, S., *Competitive Adsorption at the Air–Water Interface from a Self-Assembling Polymer-Surfactant Mixture*. The Journal of Physical Chemistry B, 2004. **108**(31): p. 11442-11446.
 71. López-Díaz, D., García-Mateos, I., and Velázquez, M.M., *Surface properties of mixed monolayers of sulfobetaines and ionic surfactants*. Journal of Colloid and Interface Science, 2006. **299**(2): p. 858-866.
 72. Christov, N.C., et al., *Maximum Bubble Pressure Method: Universal Surface Age and Transport Mechanisms in Surfactant Solutions*. Langmuir, 2006. **22**(18): p. 7528-7542.
 73. Purcell, I.P., et al., *Adsorption of SDS and PVP at the air/water interface*. Colloids and Surfaces A: Physicochemical and Engineering Aspects, 1995. **94**(2): p. 125-130.
 74. Penfold, J., et al., *Adsorption of Polymer/Surfactant Mixtures at the Air–Water Interface: Ethoxylated Poly(ethyleneimine) and Sodium Dodecyl Sulfate*. Langmuir, 2003. **19**(19): p. 7740-7745.
 75. Regismond, S.T.A., et al., *Polymer/Surfactant Complexes at the Air/Water Interface Detected by a Simple Measure of Surface Viscoelasticity*. Langmuir, 1997. **13**(21): p. 5558-5562.
 76. Cao, M. and Hai, M., *Investigation on the Interaction between Sodium Dodecyl Sulfate and Polyethylene Glycol by Electron Spin Resonance, Ultraviolet Spectrum, and Viscosity*. Journal of Chemical & Engineering Data, 2006. **51**(5): p. 1576-1581.
 77. Jean, B., Lee, L.-T., and Cabane, B., *Effects of Sodium Dodecyl Sulfate on the Adsorption of Poly(N-isopropylacrylamide) at the Air–Water Interface*. Langmuir, 1999. **15**(22): p. 7585-7590.

4 Interfacial structures and interactions of a neutral amphiphilic ‘tardigrade’ co-polymer with cationic surfactant at the air-water interface

Polymer/surfactant systems comprising neutral amphiphilic PEG-g-PVAc co-polymer (consisting of a hydrophilic polyethylene glycol backbone with hydrophobic polyvinyl acetate grafts) with cationic dodecyltrimethylammonium bromide (DTAB) were investigated at the air-water interface by a combination of dynamic and equilibrium surface tension, neutron reflectivity (NR), and preliminary foam behaviour tests. Surface tension and NR data fitting suggest that DTAB/PEG-g-PVAc is a moderately interacting polymer/surfactant system, with pronounced synergistic surface tension lowering and cooperative adsorption at the air-water interface at DTAB concentrations below its cmc. There was no significant influence on foaming behaviour observed in the DTAB/PEG-g-PVAc systems compared to the pure surfactant foams.

4.1 Introduction

Polymer/surfactant complexation at interfaces and in the bulk [1, 2] is important to many industrial applications such as foaming [3-5], detergency [6], solubilisation [7], flotation [8], encapsulation [9], lubrication [10], personal care products [11], pharmaceuticals [12, 13], and oil industries [14]. Neutron reflectivity (NR) has played a key role in understanding the polymer/surfactant layer structure (*i.e.* layer thickness, t , and roughness, σ), composition (surface excess of separate adsorbing species, Γ , and solvation, ϕ_{water}), and adsorption kinetics at the air-water interface [15-17]. The interplay of electrostatic and hydrophobic interactions drives such polymer/surfactant complexation [18], which sensitively depends on the surfactant and polymer architectures. For instance, the hydrophobic interactions are influenced by the surfactant hydrocarbon tail length, and the electrostatic interactions can be tuned by use of surfactants with different headgroups (charged or neutral) [19].

Here we are particularly interested in a neutral amphiphilic PEG-g-PVAc comb co-polymer consisting of a hydrophilic polyethylene glycol backbone with 5-8 hydrophobic polyvinyl acetate grafts (Figure 4.1), which we have termed the *tardigrade* polymer due to the superficial

resemblance of its architecture to the water bear [20]. This polymer has been widely used in industrial and personal care product formulations, *e.g.* as a detergent additive solubilising soil and preventing its redeposition on fabrics in laundry detergents [21, 22]; however, fundamental studies on its interfacial structure when complexed with surfactants - ubiquitous in these formulations – are few and far between. Previously, we studied the interactions of this tardigrade polymer with anionic SDS at the air-water interface. We observed a transition from synergistic adsorption of the mixture at the interface at low SDS concentrations to a competitive adsorption behaviour at higher SDS concentrations with the polymer depleted from the interface, forming a “hanging” layer beneath the SDS headgroup (Chapter 3). Despite its interfacial depletion, the thin hanging polymer layer contributed to the enhanced foam stability in the polymer/SDS mixtures.

The influence of the surfactant hydrocarbon tail architecture on the interfacial properties of polymer/surfactant complexes has been studied extensively [23-26]. In this study, we have kept the surfactant hydrocarbon tail same as SDS and studied the interactions of the same tardigrade comb co-polymer with a cationic dodecyltrimethylammonium bromide (DTAB). We thus focus on comparing the effect of the surfactant headgroup characteristics, *i.e.* charge and size, on the interfacial structures and composition of the polymer/surfactant complexes. Cationic DTAB (*vs.* anionic SDS) has been widely studied [24, 27-30], and is relevant to the application of the tardigrade polymer in question in detergency and laundry products, as cationic surfactants are often found in product formulations [31-34] where their formation of mixed micelles and interactions with other active agents are exploited.

The adsorption behaviour of cationic DTAB at the air-water interface in the presence of different polymers, *e.g.* polyacrylamide sulfonate (PAMPS), xanthan, and polystyrene sulfonate (PSS), has been reported before, and also compared with that of non-ionic C₁₂E₅ surfactant [35, 36]. In polymer/DTAB mixtures, synergistic surface tension (γ) reduction has been observed in the presence of the polymer and low concentration DTAB, with the extent of γ reduction depending on the polymer characteristics. However, this synergy is diminished and γ increases instead at higher DTAB concentration due to bulk complexation competing with the interfacial complexation.

More specifically relevant to the PEG-*g*-PVAc tardigrade co-polymer, interactions of DTAB with polymers bearing PEG or PVAc groups have also been reported previously, revealing complex interfacial complexation behaviours. The positive DTAB headgroup will interact with

negatively charged species, such as those of partially dissociated PVAc grafts forming OH⁻ groups [37, 38] *via* electrostatic attractive forces. Interactions between DTAB and a neutral PEG (Mn ~ 25 kDa and 100 kDa) and their adsorption at the air-water interface have been investigated before [39]. It was shown that, at low DTAB concentrations (<0.25 cmc), a PEG layer with a thickness $t \sim 34 \text{ \AA}$ was associated with the DTAB layer ($t \sim 18 \text{ \AA}$) at the air-water interface. As the DTAB concentration increased above 0.25 cmc, the surface excess (Γ_{DTAB}) increased and there was no PEG layer at the interface detected. In another study, PVA (polyvinyl alcohol)/CTAB (cetyltrimethylammonium bromide) mixture was reportedly forming a uniform film on a Si substrate, with no polymer-surfactant segregation observed [40]. From these studies, we would thus expect relatively strong interactions between the DTAB headgroup and the PVAc grafts of the PEG-*g*-PVAc tardigrade co-polymer. As such, in addition to its industrial relevance, DTAB also represents a simple model surfactant to evaluate the effect of headgroup interactions with the tardigrade polymer, which will complement our recent study on the interactions between SDS and the same polymer.

In this study, we have used dynamic (γ_d) and equilibrium (γ) surface tension measurements and NR to study interfacial adsorption of the PEG-*g*-PVAc tardigrade comb co-polymer with DTAB, examining the structure and composition of the polymer/surfactant mixtures at the air-water interface. The results show a transition from synergy to competition, similar to the polymer/SDS complex investigated previously. However, the onset surfactant concentration at which this transition occurred, and the extent of the competition, differed from the observations with the tardigrade/SDS mixture. Comparison of the foaming behaviour mediated by the polymer/DTAB and polymer/SDS mixtures showed that surfactant headgroup characteristics was crucial in determining the foamability and foam stability [3, 41].

4.2 Methods

4.2.1 Materials

Hydrogenous dodecyltrimethylammonium bromide (h-DTAB, $\text{C}_{12}\text{H}_{25}\text{N}(\text{CH}_3)_3\text{Br}$, Sigma-Aldrich) was recrystallised from 99:1 acetone:water (v:v). Deuterated dodecyltrimethylammonium bromide (d-DTAB, $\text{C}_{12}\text{D}_{25}\text{N}(\text{CH}_3)_3\text{Br}$, ISIS Deuteration Facility) was used as provided. MilliQ water (Millipore, resistivity 18.2 m Ω cm, total organic content <5 ppb) was used for solution preparation for surface tension measurements, as well as for the

preparation of air contrast matched water (ACMW; H₂O:D₂O, 91.1:8.9 w:w). D₂O was purchased from Sigma-Aldrich (99.9%).

The amphiphilic tardigrade comb co-polymer (Figure 4.1) consisting of a PEG backbone and 5-8 short PVAc grafts (M_n 15 kDa, PEG₁₃₆-g-PVAc₁₀₄ with the subscripts indicating the number of monomers; or PEG(6000)-g-PVAc(9000) with the corresponding segmental M_n indicated) was commercially available from BASF. It was freeze-dried and re-dissolved in H₂O, D₂O, or ACMW for sample preparation.

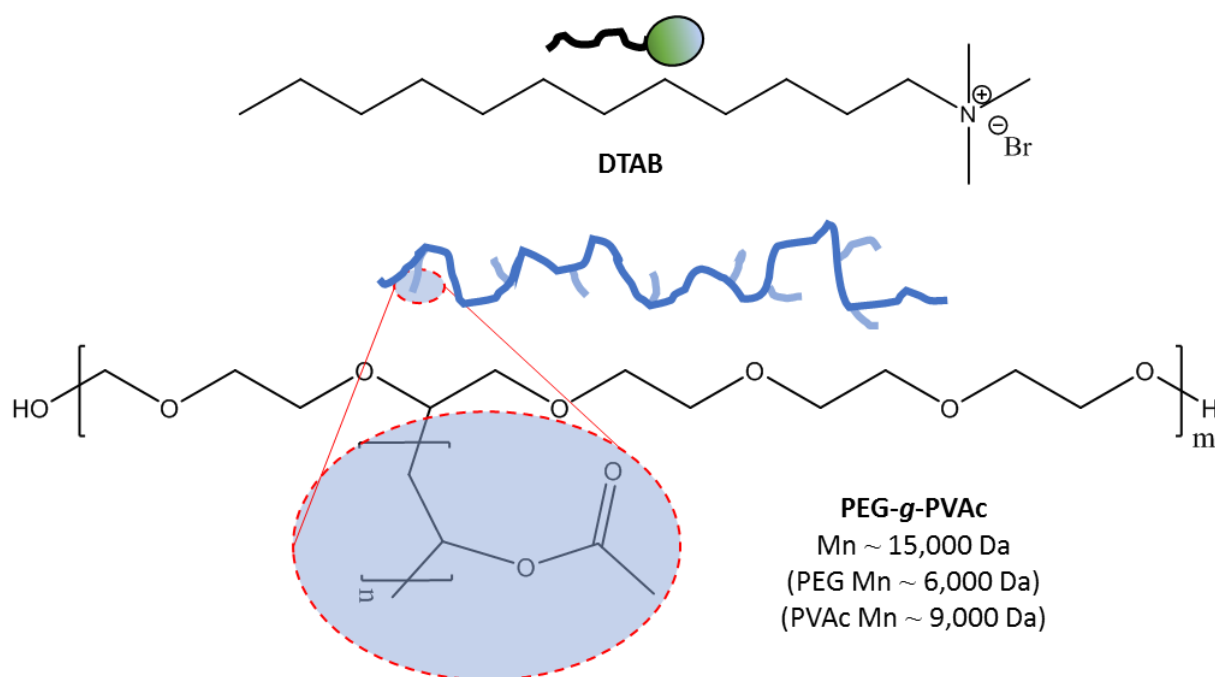


Figure 4.1 Molecular structures (with corresponding schematics) of PEG-g-PVAc co-polymer and the surfactants DTAB.

4.2.2 Surface tension measurements

A Krüss K100 force tensiometer was used to collect the equilibrium surface tension (γ) data using the Wilhelmy plate method at room temperature (with the measurement stopped after standard deviation of last 5 data points recorded at 10 s intervals was $<0.01 \text{ mN m}^{-1}$). The platinum Wilhelmy plate was flamed before every measurement to ensure cleanliness and surface activation. The dynamic surface tension (γ_d) data was collected using a Krüss BP100 bubble pressure tensiometer using a glass capillary. The cleanliness of both the glass vessel and the platinum plate was confirmed by measuring γ of MilliQ water as $\gamma = 72.5 \pm 0.3 \text{ mN m}^{-1}$ prior to every measurement. The bubble pressure was related to $\gamma_d(\tau)$ at time τ (measured between $\tau \sim 10 \text{ ms} - 4 \text{ min}$) according to the rearranged Young-Laplace equation, $\gamma_d(\tau) =$

$[(p_{max}(\tau) - p_0)r]/2$, where $p_{max}(\tau)$ is the maximum pressure experienced by the bubble at τ , p_0 is the hydrostatic pressure due to capillary immersion, and r is the capillary radius.

4.2.3 Neutron reflectivity (NR)

The NR data was obtained at the FIGARO beamline at Institut Laue-Langevin (ILL, Grenoble, France) [42] and at the INTER beamline at ISIS Neutron Source (STFC Rutherford Appleton Laboratory, Didcot, UK) [43]. Briefly, a neutron beam is detected by a time-of-flight detector, accessing a Q range of ~ 0.005 - 0.25 \AA^{-1} at FIGARO and ~ 0.01 - 0.2 \AA^{-1} at INTER by using neutrons with a range of wavelengths ($\lambda = 2 - 30 \text{ \AA}$ at FIGARO and $\lambda = 1.5 - 17 \text{ \AA}$ at INTER) at two different grazing incidence angles ($\theta = 0.62^\circ$ and 3.79° at FIGARO and $\theta = 0.80^\circ$ and 2.30° at INTER) at the air-water interface. Here $Q = \frac{4\pi \sin(\theta)}{\lambda}$ is the momentum transfer perpendicular to the interface. The obtained reflectivity profile can be plotted as reflectivity, $R(Q)$ vs. Q , or alternatively as $RQ^4(Q)$ vs. Q to highlight mild fringes in the high Q regime by compensating the intrinsic $R(Q)$ decay with Q^{-4} . The background was subtracted from the data recorded at FIGARO thanks to use of the 2D detector but not from the data recorded at INTER. NR measurements were made at the air-water interface formed by filling ~ 30 mL of the solution containing the polymer/surface mixture in a Teflon trough. The data for each NR curve was collected repeatedly over ~ 6 h to check and allow for sample equilibration.

The polymer was hydrogenous, whilst the surfactant hydrocarbon tail was either fully hydrogenous or deuterated. D_2O and air contrast matched water (ACMW, *i.e.* $\rho = 0$ matched to that of air) were used. This allowed NR data to be collected in 4 different isotopic contrasts for each polymer/surfactant mixed system, *i.e.* h-surfactant in ACMW, d-surfactant in ACMW, h-surfactant in D_2O , and d-surfactant in D_2O , all with the h-polymer. The four NR profiles obtained for each sample at the four isotopic contrasts were co-fitted with the same structural parameters of the interfacial layer, *i.e.* t , ρ , σ , and ϕ_{water} . The data was reduced and calibrated against the reference measurements of pure ACMW and D_2O , and the direct beam.

As described before [15, 16, 44], the surface excess of adsorbed species was determined from fitting the low Q range of the NR data obtained in ACMW, where the fitting was only sensitive to the product of t and ρ of the given layer. The structural information of the interfacial layer, *e.g.* thickness (t), roughness (σ) and water volume fraction in the layer (ϕ_{water}), layer was elucidated from the fitting parameters, using the Motofit package in IGOR Pro [45], of the interfacial layer over the whole accessible Q range in all 4 isotopic contrasts (h-surfactant and

d-surfactant with h-polymer) in ACMW and in D₂O. Determination of the composition of interfacial structures (*i.e.* the volume fraction, ϕ) is based on fitting the reflectivity profile using calculated scattering length densities (SLDs, ρ) of the adsorbed species [46]. First, a 1-layer model was used to fit the NR data to provide an overview of the polymer/surfactant interfacial behaviour, such as suggesting synergy or competition between the polymer and surfactant at the interface. Then, to gain more detailed structural information of the interface, the NR data was fitted using different multilayer models, as described in Methods section 2.2.3, to find the model that best described the data.

4.2.4 Foaming measurements

For the foaming measurements using a Krüss Dynamic Foam Analyser (DFA 100), the foam was generated by air flow, *via* a sintered porous glass filter (pore size 40-100 μm , 3 cm in diameter), through 60 mL solution in a glass column of 4 cm in diameter at a flow rate of 0.3 L min^{-1} for 12 s. The liquid, foam, and total height were detected using blue light illumination and a camera. The camera was calibrated to determine the foam bubble size. The foamability was evaluated from the maximum foam volume (or height) reached after foam generation, whilst the foam stability was gauged by the half-life time (time at which the foam height decays to half of the maximum foam height).

4.3 Results

4.3.1 Equilibrium and dynamic surface tension

The γ and γ_a vs. τ (the age of the bubble) data in Figure 4.2 shows two different interfacial behaviours in the polymer/surfactant mixtures containing low concentration DTAB ($< \sim 0.5$ cmc). In the mixtures containing 0.2 cac PEG-*g*-PVAc with < 0.5 cmc DTAB (\square data between points 4 and 7 in the figure), a synergistic effect is evident from a reduction in $\Delta\gamma \sim 5\text{-}10$ mN m^{-1} compared to pure PEG-*g*-PVAc ($\gamma \sim 55$ mN m^{-1} , Point 1 \circ). In the mixtures containing 2 cac PEG-*g*-PVAc with < 0.5 cmc DTAB (\blacktriangle data between points 5 and 8), the γ value ~ 43 mN m^{-1} is very similar to that of a pure PEG-*g*-PVAc at 2 cac (Point 2 \circ), with a minimal synergistic reduction of $\Delta\gamma \sim 1$ mN m^{-1} .

In mixtures containing 0.5 cmc DTAB and 0.2 cac PEG-*g*-PVAc (Point 7 \square), the γ value ~ 43 mN m^{-1} is higher than that of pure 0.5 cmc DTAB (Point 6 ∇ ; $\gamma \sim 40$ mN m^{-1}) and lower than

that of 0.2 cac PEG-*g*-PVAc (Point 1 ○; $\gamma \sim 55 \text{ mN m}^{-1}$). In mixtures containing 0.5 cmc DTAB and 2 cac PEG-*g*-PVAc (Point 8 ▲), the γ value $\sim 39 \text{ mN m}^{-1}$ (with a relatively large experimental error $\pm 4 \text{ mN m}^{-1}$ associated with the measurement) is closer to that of the pure DTAB at 0.5 cmc (Point 6 ▽; $\gamma \sim 40 \text{ mN m}^{-1}$), compared to 2 cac PEG-*g*-PVAc (Point 2 ○; $\gamma \sim 44 \text{ mN m}^{-1}$). This γ behaviour suggests that, at 0.5 cmc DTAB, there was a strong interaction between the polymer and surfactant in the bulk, suppressing the formation of a monolayer of either component with no additional synergistic adsorption observed. The carbonyl (ester) groups in the PVAc side chains could partially hydrolyse, resulting in negatively charged OH groups in the polymer structure [37, 38], providing additional attractive electrostatic interactions between the PEG-*g*-PVAc and the cationic DTAB.

At DTAB concentration around its cmc, a minimum in γ value was observed, indicative of a presence of impurities. Commonly present impurities in DTAB solutions include dodecanol [47], iodomethane [48] and/or alkylamines [49], depending on the chosen route of DTAB synthesis. Such impurities are surface active and therefore contribute to decrease of γ value compared to a monolayer of pure DTAB formed above its cmc. The effect of the impurity presence will later be discussed with reference to the interfacial layer structure fitted by NR.

In mixtures containing DTAB concentrations above its cmc (Points 10 □ and 11 ▲), $\gamma \sim 37 \text{ mN m}^{-1}$ is identical to the pure surfactant above its cmc (Point 9 ▽), suggesting the formation of a pure DTAB monolayer at the air-water interface, depleting the polymer from the interface immediately adjacent to air. However, the calculated Γ from NR data (*cf.* Figure 4.3) shows that a polymer layer was present proximal to the interface.

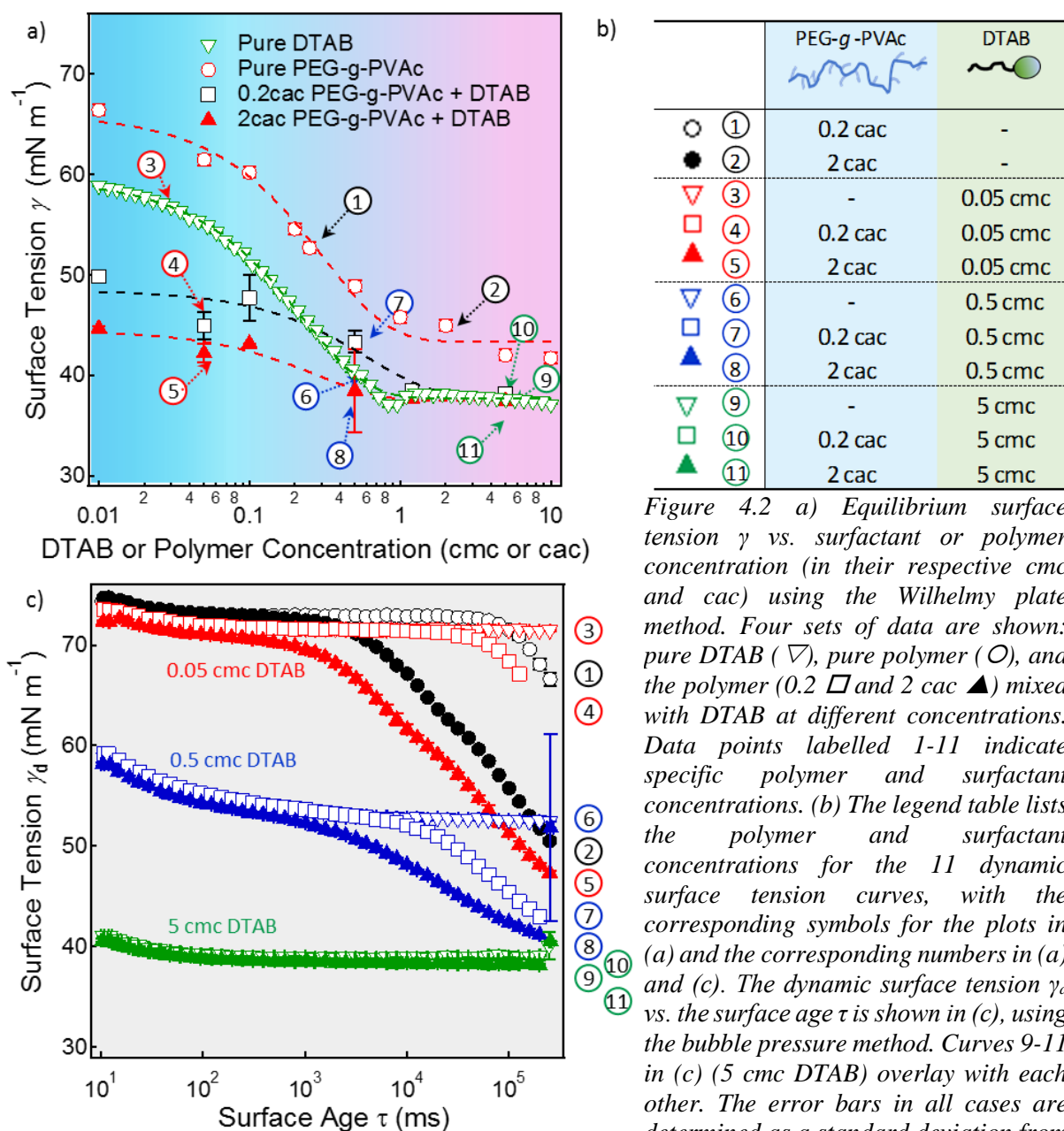


Figure 4.2 a) Equilibrium surface tension γ vs. surfactant or polymer concentration (in their respective cmc and cac) using the Wilhelmy plate method. Four sets of data are shown: pure DTAB (∇), pure polymer (\circ), and the polymer (0.2 \square and 2 cac \blacktriangle) mixed with DTAB at different concentrations. Data points labelled 1-11 indicate specific polymer and surfactant concentrations. (b) The legend table lists the polymer and surfactant concentrations for the 11 dynamic surface tension curves, with the corresponding symbols for the plots in (a) and the corresponding numbers in (a) and (c). The dynamic surface tension γ_d vs. the surface age τ is shown in (c), using the bubble pressure method. Curves 9-11 in (c) (5 cmc DTAB) overlay with each other. The error bars in all cases are determined as a standard deviation from an experimental error determined from 3 separate measurements.

The overall γ_d behaviour of polymer/surfactant mixtures containing DTAB (Figure 4.2c) was similar to the polymer/surfactant mixtures containing SDS. There was no appreciable γ_d lowering with time in the case of 0.05 cmc DTAB (Curve 3 ∇), with γ_d remaining at ~ 71 mN m^{-1} throughout the measurement time (~ 4 min, ~ 25 0000 ms). In the case of 0.5 cmc DTAB (Curve 6 ∇), $\gamma_d \sim 59$ mN m^{-1} at $\tau \sim 10$ ms, with a reduction of $\Delta\gamma_d \sim 7$ mN m^{-1} at $\tau \sim 4$ min reaching the final $\gamma_d \sim 52$ mN m^{-1} . In the case of 5 cmc DTAB (Curve 9 ∇), $\gamma_d \sim 40$ mN m^{-1} at $\tau \sim 10$ ms, with $\gamma_d \sim 39$ mN m^{-1} at $\tau \sim 4$ min.

There was a clear synergistic effect after $\tau \sim 4$ min in the mixture interfacial adsorption at DTAB concentrations below its cmc (Curves 4 \square , 5 \blacktriangle and 7 \square , 8 \blacktriangle), evident from γ_d of the mixtures reaching below that of either pure component. The interfacial adsorption process of the mixture could occur in two stages: the faster diffusing DTAB adsorbed to the interface first, and slower and progressive recruitment of polymer to the interface then led to γ_d decreasing with time, manifesting in the observed γ_d vs. τ trend in Figure 2c. The deviations of γ_d data for PEG-g-PVAc/DTAB only after certain time from the formation of the interface can be rationalised by considering the interfacial adsorption mechanism [50, 51]. At short time scale, the diffusion governs the interfacial adsorption, hence the faster diffusing DTAB is the major species contributing to the γ_d value at given τ . At longer τ , the adsorption barrier has to be overcome, and the behaviour is no longer diffusion controlled. Hence, the slower polymer adsorption can take place and contribute to the synergistic γ_d lowering. We labelled the time at which the polymer synergistic adsorption was first observed as τ_s . In polymer/surfactant mixtures containing 0.05 cmc DTAB + 0.2 cac PEG-g-PVAc (Curve 4 \square), synergy was observed after $\tau_s \sim 25$ s, with $\gamma_d \sim 67$ mN m⁻¹ at $\tau \sim 4$ min. In the mixtures of 0.05 cmc DTAB + 2 cac PEG-g-PVAc (Curve 5 \blacktriangle), the synergistic adsorption was observed after $\tau_s \sim 1$ s, with final $\gamma_d \sim 47$ mN m⁻¹ at $\tau \sim 4$ min and overall $\Delta\gamma_d \sim 25$ mN m⁻¹.

In the case of 0.2 cac PEG-g-PVAc + 0.5 cmc DTAB (Curve 7 \square), γ_d started deviating from that of pure surfactant at $\tau_s \sim 6$ s, with final $\gamma_d \sim 43$ mN m⁻¹ at $\tau \sim 4$ min. In the mixture containing 2 cac PEG-g-PVAc + 0.5 cmc DTAB (Curve 8 \blacktriangle), the synergistic adsorption started at $\tau_s \sim 1$ s with final $\gamma_d \sim 39$ mN m⁻¹ at $\tau \sim 4$ min.

At 5 cmc DTAB concentration, no significant synergy was observed in the presence of PEG-g-PVAc (Curves 10 \square and 11 \blacktriangle), and the γ_d data of the polymer/surfactant mixtures overlaps with that of the pure DTAB (Curve 9 ∇) within experimental errors, with $\gamma_d \sim 40$ mN m⁻¹ at $\tau \sim 100$ ms and $\gamma_d \sim 38$ mN m⁻¹ at $\tau \sim 4$ min.

4.3.2 Interfacial layer composition *via* surface excess evaluation from NR low Q data

As a control, the DTAB adsorbed amount at the air-water interface above its cmc was calculated from the 1-layer fitting of the NR data at low Q range (0.01 – 0.05 Å⁻¹) to be $\Gamma \sim 3.48$ μmol m⁻² which is in agreement with literature [24, 52]. Γ was also evaluated for DTAB/polymer mixtures as shown in Figure 4.3.

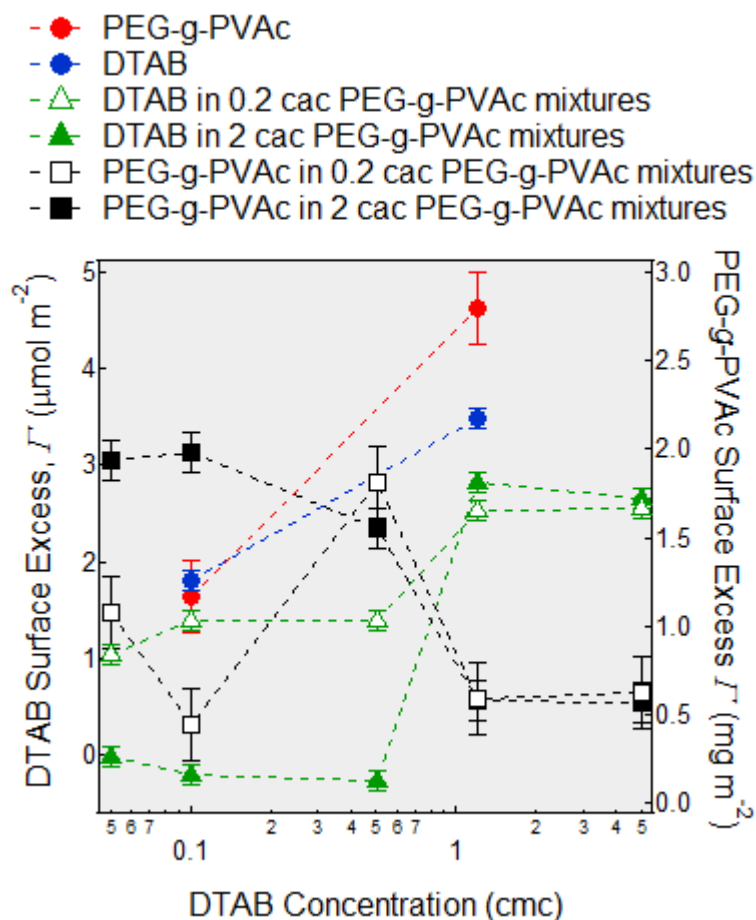


Figure 4.3 The calculated Γ vs DTAB concentration of mixed PEG-g-PVAc + DTAB systems is shown. The Γ_{DTAB} is shown in $\mu\text{mol m}^{-2}$ on the left axis and represented by the filled markers, and $\Gamma_{\text{PEG-g-PVAc}}$ is shown in mg m^{-2} on the right axis and represented by the empty markers. The dashed lines act as a guide to the eyes only.

Polymer adsorbance in the PEG-g-PVAc/DTAB mixtures decreased from $\Gamma_{\text{PEG-g-PVAc}} \sim 3.1 \text{ mg m}^{-2}$ at 0.1 DTAB cmc to $\Gamma_{\text{PEG-g-PVAc}} \sim 0.6 \text{ mg m}^{-2}$ at 5 cmc DTAB, again suggesting possible polymer depletion from the interface. Interestingly, the Γ_{DTAB} value in the mixtures did not reach that of a pure DTAB monolayer ($\Gamma_{\text{DTAB}} \sim 3.5 \mu\text{mol m}^{-2}$) even at the highest concentration studied ($\Gamma_{\text{DTAB}} \sim 2.6 \mu\text{mol m}^{-2}$ in 5 cmc DTAB with both polymer concentrations). This behaviour suggests strong interactions between DTAB and PEG-g-PVAc in the bulk, depleting the interface of both the polymer and the surfactant compared to their pure systems. This is unlike the clear competitive behaviour observed in the case of SDS, where only the polymer is depleted from the interface, forming a “hanging” polymer layer beneath the surfactant monolayer. Such polymer depletion has been reported in a PEO/C₁₄TAB mixture at high surfactant concentrations [53]. The presence of the PVAc grafts on the tardigrade PEG-g-PVAc co-polymer facilitated strong interactions with DTAB, giving rise to the synergistic behaviour observed in the current system. The interactions between the co-polymer/DTAB can also be confirmed by the consistently larger adsorbed amounts of DTAB in the mixtures containing

lower PEG-*g*-PVAc concentration (e.g. $\Gamma_{\text{DTAB}} \sim 1.4 \mu\text{mol m}^{-2}$ in 0.1 cmc DTAB + 0.2 cac PEG-*g*-PVAc and $\Gamma_{\text{DTAB}} \sim 0 \mu\text{mol m}^{-2}$ in 0.1 cmc DTAB + 2 cac PEG-*g*-PVAc). In comparison, the surfactant depletion at high polymer concentration was much less pronounced in the mixtures with SDS.

4.3.3 DTAB/PEG-*g*-PVAc interfacial layer structure from NR

Fitting the NR data with a 1-layer model (Figure 4.4) allowed us to survey the overall behaviour of the interfacial layer. In general, the thickness t of the mixed PEG-*g*-PVAc/DTAB layer at the interface decreased with increasing DTAB concentration. In the mixtures with lower DTAB concentrations (< 0.5 cmc) and 0.2 cac PEG-*g*-PVAc, the mixed interfacial layer was thicker ($t \sim 25 \text{ \AA}$) compared to the pure DTAB or pure PEG-*g*-PVAc (e.g. 0.1 cmc DTAB $t \sim 6 \text{ \AA}$, 0.2 cac PEG-*g*-PVAc $t \sim 11 \text{ \AA}$, respectively). Such synergistic increase in t relative to the pure systems, and $\phi_{\text{PEG-}g\text{-PVAc}} \sim 40\text{-}70\%$ (0.05 and 0.1 cmc DTAB + 0.2 cac PEG-*g*-PVAc mixtures), indicate relatively strong interactions between the PEG-*g*-PVAc and DTAB at the interface. ϕ_{water} was relatively high in the 0.1 cmc DTAB and 0.2 cac PEG-*g*-PVAc mixture ($\phi_{\text{water}} \sim 67\%$), reflecting the swelling of the hydrated interfacial layer.

For mixed interfacial layer of the solution containing lower concentration DTAB (< 0.5 cmc) and 2 cac PEG-*g*-PVAc, $t \sim 28 \text{ \AA}$ was equal to that of the pure polymer, with $\phi_{\text{water}} \sim 4 \%$ equal to that in the pure DTAB monolayer and lower than that of pure PEG-*g*-PVAc ($\phi_{\text{water}} \sim 12 \%$). The very high $\phi_{\text{PEG-}g\text{-PVAc}} \sim 95\text{-}97\%$ confirms that the interfacial layer predominantly comprised the polymer with a mixture of low DTAB concentrations and high PEG-*g*-PVAc concentration.

At DTAB concentration above its cmc, the thickness of the mixed interfacial layer was similar to that of a pure DTAB, i.e. $t \sim 14 \text{ \AA}$, yet containing $\phi_{\text{PEG-}g\text{-PVAc}} \sim 30\text{-}38\%$ depending on the polymer concentration which demonstrates presence of the polymer at the interface interacting with DTAB even at concentrations above its cmc.

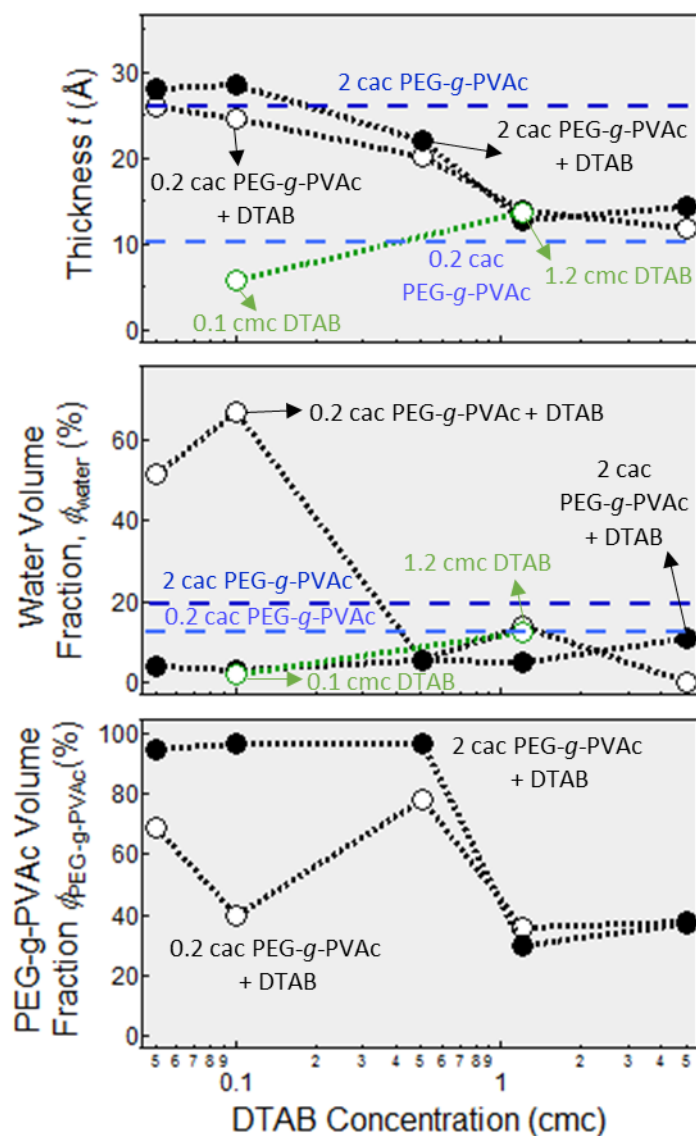


Figure 4.4 A summary of the thickness t , water volume fraction ϕ_{water} and polymer fraction $\phi_{\text{PEG-g-PVAc}}$ in a single-layer model used to fit the NR data of PEG-g-PVAc + DTAB mixtures (\circ and \bullet for 0.2 and 2 cac polymer respectively). For comparison, the blue dashed lines represent the fitted values of 0.2cac PEG-g-PVAc and 2cac PEG-g-PVAc respectively. The data point with green outline represents the fitted value for 0.1 and 1.2 cmc pure DTAB.

The pure DTAB layer was fitted using a 1-layer model at 0.1 cmc ($t \sim 5.7 \text{ \AA}$), and a 2-layer model at 1.2 cmc ($t_1 \sim 8.6 \text{ \AA}$ and $t_2 \sim 5.5 \text{ \AA}$) (Figure D.1 in Appendix). The Γ_{DTAB} value is consistent with literature ($\Gamma_{\text{DTAB}} \sim 3.48 \text{ \mu mol m}^{-2}$), as well as the overall layer t above its cmc ($t \sim 14 \text{ \AA}$) [54]. The fitted parameters are listed in Table 4.1, with clear indications of polymer/DTAB association in mixtures containing 0.05 and 0.1 cmc DTAB and polymer/DTAB competition at higher DTAB concentrations. This complements the calculated Γ of the components (*cf.* Figure 4.3). The fitted NR data is shown below in Figure 4.5, Figure 4.6, and Figure 4.7, and the fitted parameters are listed in Table 4.1.

Table 4.1 The fitted parameters for the optimised multilayer models for mixtures of PEG-g-PVAc and DTAB, as well as the pure systems. The superscripts for the fitted scattering length density (SLD) ρ values in the table correspond to the following polymer/surfactant volume fractions: ¹ 69% PEG-g-PVAc + 31% DTAB, ² 60% PEG-g-PVAc + 40% DTAB, ³ 61% PEG-g-PVAc + 39% DTAB headgroup, ⁴ 95% PEG-g-PVAc + 5% DTAB, ⁵ 97% PEG-g-PVAc + 3% DTAB, ⁶ 60% PEG-g-PVAc + 40% DTAB

PEG-g-PVAc DTAB		Layer 1					Layer 2					Layer 3				Bkg
conc (cac)	conc (cmc)	t_1 (\AA)	$h-\rho_1$ (10^{-6} \AA^{-2})	$d-\rho_1$ (10^{-6} \AA^{-2})	$\varphi_{\text{water-1}}$ (%)	σ_1 (\AA)	t_2 (\AA)	$h-\rho_1$ (10^{-6} \AA^{-2})	$d-\rho_1$ (10^{-6} \AA^{-2})	$\varphi_{\text{water-2}}$ (%)	σ_2 (\AA)	t_3 (\AA)	ρ_3 (10^{-6} \AA^{-2})	$\varphi_{\text{water-3}}$ (%)	σ_3 (\AA)	σ_{bkg} (\AA)
0.2	0.05	26.0	0.639 ¹	2.303 ¹	54	3.5	-	-	-	-	-	-	-	-	-	9.8
0.2	0.1	24.5	0.273 ²	3.492 ²	67	6.1	-	-	-	-	-	-	-	-	-	6.1
0.2	0.5	16.1	1.031	1.031	8	5.7	6.8	-0.233	5.133	27	5.7	-	-	-	-	3.9
0.2	1.2	5.5	-0.39	7.004	0	4.5	7.5	0.701 ³	0.701 ³	17	6.1	-	-	-	-	5.7
0.2	5	5.2	-0.39	7.004	0	3.3	3.1	0.184	0.184	36	3.1	5.4	1.031	26	5.5	3.5
2	0.05	28.1	0.968 ⁴	1.236 ⁴	4	5.1	-	-	-	-	-	-	-	-	-	11.7
2	0.1	28.5	0.993 ⁵	1.154 ⁵	3	9.4	-	-	-	-	-	-	-	-	-	11.1
2	0.5	20.4	1.031	1.031	10	5.8	14.4	-0.233	5.133	96	3.6	-	-	-	-	4.4
2	1.2	6.9	-0.39	7.004	0	5.7	5.6	0.692 ⁶	0.692 ⁶	58	5.8	-	-	-	-	4.0
2	5	6.0	-0.39	7.004	0	4.2	5.4	0.184	0.184	58	3.8	5.5	1.031	92	5.4	6.0
0.2	-	10.8	1.031	-	12	3.9	-	-	-	-	-	-	-	-	-	3.2
2	-	28.0	1.031	-	19	3.6	-	-	-	-	-	-	-	-	-	5.2
-	0.1	5.7	-0.233	5.133	2	5.4	-	-	-	-	-	-	-	-	-	3.6
-	1.2	8.6	-0.39	7.004	0	3.9	5.5	0.184	0.184	41	4.2	-	-	-	-	3.7

In polymer/surfactant mixtures with low (0.05 and 0.1 cmc) DTAB concentrations, the NR data was well fitted by a 1-layer model (Figure 4.5). t and $\varphi_{\text{PEG-g-PVAc}}$ were larger in the mixtures containing 2 cmc polymer ($\varphi_{\text{PEG-g-PVAc}} \sim 95\%$, $\Gamma_{\text{PEG-g-PVAc}} \sim 3.1 \text{ mg m}^{-2}$, at both 0.05 and 0.1 cmc DTAB concentrations) compared to 0.2 cmc polymer mixture ($\varphi_{\text{PEG-g-PVAc}} \sim 69\%$ and 40% , $\Gamma_{\text{PEG-g-PVAc}} \sim 1.0$ and 0.3 mg m^{-2} , at 0.05 and 0.1 cmc DTAB respectively). The layer ($t \sim 26 \text{ \AA}$ in 0.2 cmc PEG-g-PVAc + 0.05 cmc DTAB and $t \sim 25 \text{ \AA}$ in 0.2 cmc PEG-g-PVAc + 0.1 cmc DTAB) was larger than that of pure surfactant or pure polymer ($t \sim 6 \text{ \AA}$ in 0.1 cmc DTAB and $t \sim 11 \text{ \AA}$ nm in 0.2 cmc PEG-g-PVAc, respectively). This observation indicates a strong cooperative or synergistic adsorption at the interface in these systems. This increase in t was much less pronounced in the mixtures containing 2 cmc PEG-g-PVAc, where t of the mixed layer was marginally higher ($t \sim 28 \text{ \AA}$) than that of the pure polymer above its cmc ($t \sim 28 \text{ \AA}$). The large interfacial roughness σ value $\sim 11 \text{ \AA}$ also indicates an inhomogeneous layer.

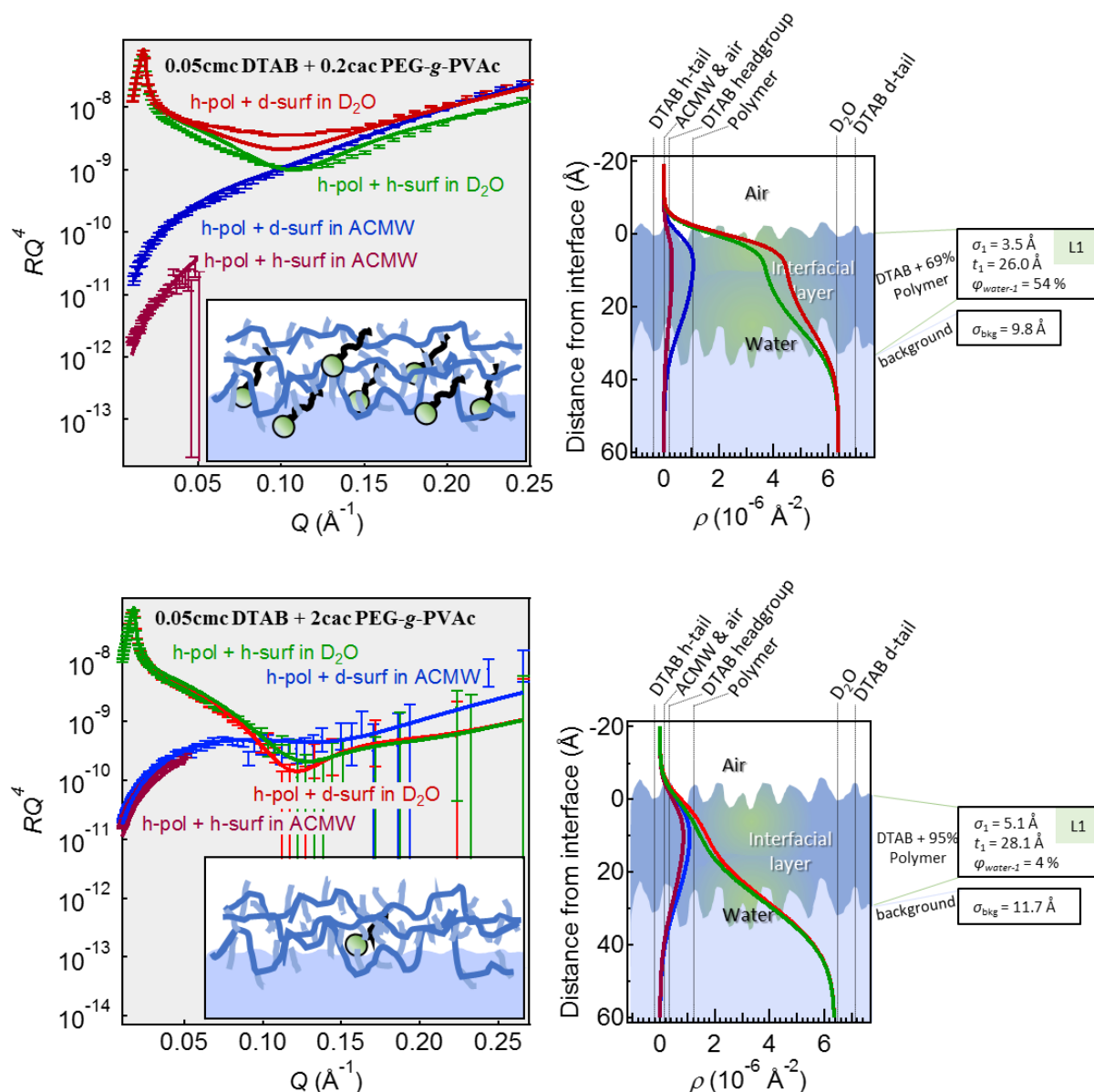


Figure 4.5 Fitted NR data to a 1-layer model for 0.05 cmc DTAB with 0.2 and 2 cac PEG-g-PVAc, with the fitted ρ profiles and schematic representation based on the fitted parameters. The data is colour coded as follows: **red** represents mixtures of PEG-g-PVAc and dDTAB in D₂O, **green** represents mixtures of PEG-g-PVAc with hDTAB in D₂O, **blue** represents mixtures of PEG-g-PVAc with dDTAB in ACMW, and **purple** represents mixtures of PEG-g-PVAc with hDTAB in ACMW. The error bars associated with the data points were determined from the data reduction, larger at higher Q values due to lower contrast between the solvent and sample. The solid lines show the fitted curve, with the fitted parameters also shown, including thickness (t), solvent volume fraction (ϕ_{water}), and roughness of the layer (σ).

At DTAB concentration of 0.5 cmc, the NR data was best fitted by a 2-layer model, with two separate layers for the polymer and the surfactant, of thickness t_1 and t_2 respectively (Figure 4.6). The polymer layer thickness was $t_1 \sim 16 \text{ \AA}$ and 20 \AA in the mixtures with 0.2 and 2 cac polymer, respectively; and $t_2 \sim 7 \text{ \AA}$ and 14 \AA , respectively. However, the DTAB layer was more hydrated in the 2 cac mixture, with $\phi_{\text{water}} \sim 96\%$. The Γ values in the mixtures (at 0.2 cac polymer: $\Gamma_{\text{PEG-g-PVAc}} \sim 1.8 \text{ mg m}^{-2}$ and $\Gamma_{\text{DTAB}} \sim 1.4 \text{ \mu mol m}^{-2}$; and at 2 cac polymer: $\Gamma_{\text{PEG-g-PVAc}}$

$\sim 2.3 \text{ mg m}^{-2}$ and $\Gamma_{\text{DTAB}} \sim 0 \text{ } \mu\text{mol m}^{-2}$ due to the high ϕ_{water}) are also indicative of synergistic adsorption and strong interactions between the polymer and DTAB, with only slight depletion of the polymer from the interface observed relative to the pure polymer system. Measurements involving ellipsometry at the air-water interface and Brewster angle microscopy (BAM) on a thinly spread layers using the Langmuir-Blodgett trough [53, 55, 56] could provide more details about the unexpected interfacial structures observed. Furthermore, a systematic study of the interfacial structure could be performed by surface tension measurements, as well as BAM, by first forming a pure polymer layer at the interface followed by addition of increasing DTAB concentration to the bulk of the system, and vice versa. Any restructuring observed during such addition could complement the NR data fitting presented here. Lastly, polymer/surfactant layers formed at the air-water interface are sensitive to the presence of any impurities at the interface. As previously discussed, the minimum in γ value (Figure 4.2) around the cmc of pure DTAB points towards likely presence of surface-active impurities in the sample, contributing to the peculiar structure observed here: especially the high solvation of the layer attributed to the surfactant.

For mixtures containing DTAB at concentration above its cmc, a 3-layer model best fitted the NR data at both polymer concentrations, with a relatively thick polymer layer (t_3) beneath a top layer of DTAB tails (t_1) and then a layer of DTAB headgroup (t_2) (Figure 4.7). The DTAB tail layer thickness ($t_1 \sim 5$ and $6 \text{ } \text{\AA}$ in mixtures containing 0.2 and 2 cac PEG-*g*-PVAc, respectively) was thinner compared to $t_1 \sim 9 \text{ } \text{\AA}$ of pure DTAB monolayer, attributed to the tail tilting at an angle $\omega \sim 46^\circ$ and 53° relative to normal. Consequently, the headgroups could not pack as efficiently as in a pure DTAB monolayer, leading to higher solvation/hydration ($t_2 \sim 3$ and $5 \text{ } \text{\AA}$ with $\phi_{\text{water}} \sim 36$ and 58% in mixtures containing 0.2 and 2 cac PEG-*g*-PVAc, compared to $t_2 \sim 6 \text{ } \text{\AA}$ and $\phi_{\text{water}} \sim 41\%$ of pure DTAB monolayer). The polymer layer thickness was $t_3 \sim 5 \text{ } \text{\AA}$ with $\phi_{\text{water}} \sim 26$ and 92% , with still relatively high $\Gamma_{\text{PEG-}g\text{-PVAc}} \sim 0.6 \text{ mg m}^{-2}$ and $\Gamma_{\text{DTAB}} \sim 2.5 \text{ } \mu\text{mol m}^{-2}$ at both 0.2 and 2 cac PEG-*g*-PVAc and 5 cmc DTAB. These results, along with Γ of the polymer/surfactant mixtures, suggest strong interactions between the surfactant headgroups and the polymer.

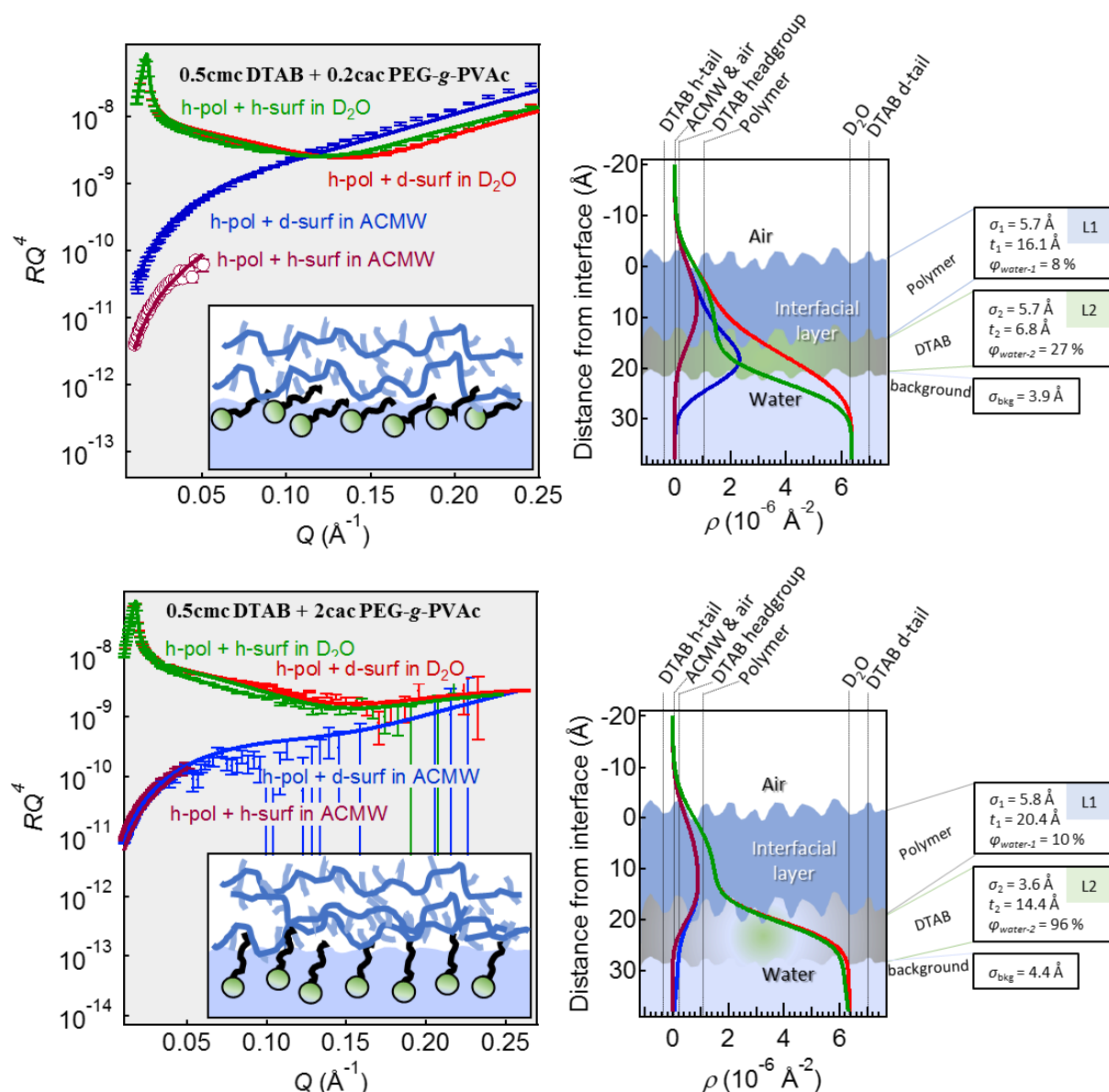


Figure 4.6 Fitted NR data to a 2-layer model for 0.5 cmc DTAB with 0.2 and 2 cac PEG-g-PVAc, with the fitted ρ profiles and schematic representation based on the fitted parameters. The data is colour coded as follows: *red* represents mixtures of PEG-g-PVAc and dDTAB in D_2O , *green* represents mixtures of PEG-g-PVAc with hDTAB in D_2O , *blue* represents mixtures of PEG-g-PVAc with dDTAB in ACMW, and *purple* represents mixtures of PEG-g-PVAc with hDTAB in ACMW. The error bars associated with the data points were determined from the data reduction, larger at higher Q values due to lower contrast between the solvent and sample. The solid lines show the fitted curve, with the fitted parameters also shown, including thickness (t), solvent volume fraction (ϕ_{water}), and roughness of the layer (σ).

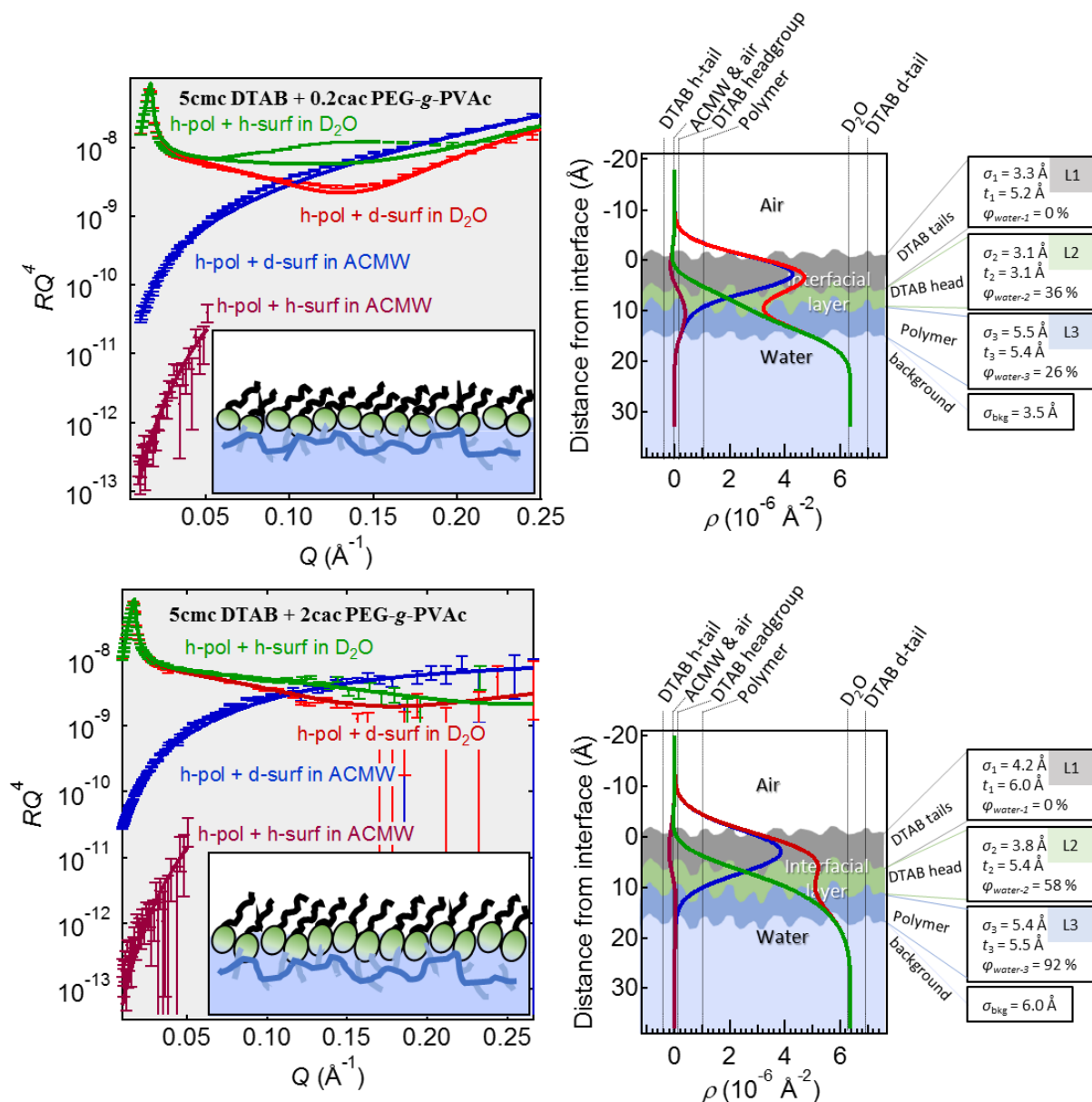


Figure 4.7 Fitted NR data to a 3-layer model for 5 cmc DTAB with 0.2 and 2 cac PEG-g-PVAc, with the fitted ρ profiles and schematic representation based on the fitted parameters. The data is colour coded as follows: red represents mixtures of PEG-g-PVAc and dDTAB in D_2O , green represents mixtures of PEG-g-PVAc with hDTAB in D_2O , blue represents mixtures of PEG-g-PVAc with dDTAB in ACMW, and purple represents mixtures of PEG-g-PVAc with hDTAB in ACMW. The error bars associated with the data points were determined from the data reduction, larger at higher Q values due to lower contrast between the solvent and sample. The solid lines show the fitted curve, with the fitted parameters also shown, including thickness (t), solvent volume fraction (ϕ_{water}), and roughness of the layer (σ).

It has been reported previously that, in a strongly interacting system containing DTAB and anionic polymer sodium poly(styrene sulfonate), NaPSS, a sizeable increase of the interfacial layer thickness was observed at DTAB concentrations around its cmc, up to $t \sim 60\text{-}90 \text{\AA}$ [26, 57]. It was explained by the formation of a sandwich structure at the interface composed of DTAB/NaPSS complexes underneath a DTAB monolayer at the interface. In DTAB/NaPSS

mixtures containing low surfactant concentration (~ 0.01 cmc), the layer thickness was $t \sim 20$ Å, indicating synergistic adsorption of the mixture to the interface. The same behaviour was observed in a system of DTAB and anionic sodium poly(acrylic acid), NaPAA, at 9.2 pH where NaPAA was more highly charged, compared to a 4.2 pH at which no significant increase in layer t was not observed at high DTAB concentration [58]. It was therefore concluded that the cooperative adsorption behaviour at low DTAB concentrations was dominated by hydrophobic forces, as it was present in both cases containing less and more highly charged polymers. The formation of the thick sandwich structure at the interface was attributed to the presence of electrostatic interactions between the DTAB and the anionic polymer.

Such a cooperative/synergistic behaviour at *low surfactant concentration* is consistent with our observations in a system containing DTAB and the tardigrade polymer, although no indication of the formation of a sandwich structure at the interface was observed (with $t < 20$ Å). We infer that the driving force was the hydrophobic interaction, with a small contribution from partially dissociated carbonyl group of the PVAc grafts on the polymer interacting *via* electrostatic interactions with the cationic DTAB headgroup. DTAB and PEG-*g*-PVAc could be considered as moderately interacting polymer/surfactant mixtures, as the interfacial behaviour lies intermediate between that of weakly interacting (equally charged) and strongly interacting (oppositely charged) mixed systems.

Finally, the calculated ϕ_{water} , ϕ_{DTAB} and $\phi_{\text{PEG-g-PVAc}}$ in the relevant layers of the fitting model are shown in Figure 4.8. The high $\phi_{\text{PEG-g-PVAc}}$ in DTAB/PEG-*g*-PVAc mixtures at DTAB concentrations below its cmc consistent with relatively strong interactions between DTAB and the polymer, and cooperative adsorption at the interface at these concentrations. Increasing the DTAB concentration to above its cmc led to decrease in $\phi_{\text{PEG-g-PVAc}}$ in the mixtures, indicative of competitive adsorption at the interface and partial depletion of the polymer.

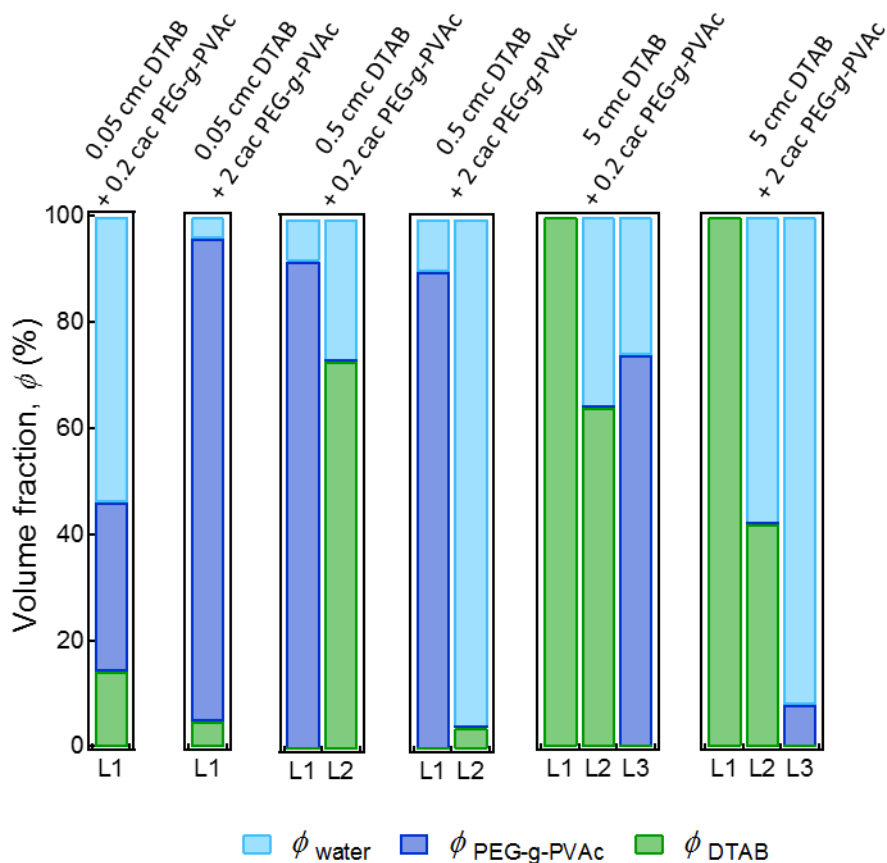


Figure 4.8 Calculated ϕ_{water} , ϕ_{DTAB} and $\phi_{\text{PEG-g-PVAc}}$ for each layer in fitted mixtures of DTAB/PEG-g-PVAc. L1, L2 and L3 refer to Layer 1, 2, and 3 respectively in the fitting model, with L1 the top layer in the given model as indicated in the schematics in Figures 4.4-4.6.

4.3.4 Foam behaviour of the polymer/surfactant mixtures

The results of the foaming behaviour of the PEG-g-PVAc/DTAB mixtures are presented in Table 4.2 and Figure 4.9. The foam stability gauged by its half-life ($\tau_{\text{FVS } 50\%}$) of all the PEG-g-PVAc/DTAB mixtures was within the experimental errors comparable to that of the relevant pure DTAB system. The foam volume ($V_{\text{foam max}}$) was marginally lowered in the presence of the polymer (maximum $\Delta V_{\text{foam max}} \sim 5 \text{ mL}$). The bubble size and size distribution of all PEG-g-PVAc/DTAB mixtures were within the experimental errors compared to the relevant pure DTAB bubble size (Figure 4.9).

There was no major influence of polymer presence on foamability ($\tau_{\text{FVS } 50\%}$), foam stability ($V_{\text{foam max}}$), or initial bubble size ($R_{\text{avg initial}}$) observed in the polymer/surfactant mixtures containing DTAB compared to the pure surfactant foams, even though we have seen synergistic γ lowering in the mixtures containing DTAB, as well as strong association of the

polymer/surfactant mixtures at the air-water interface observed from the NR data fitting. Compared to the PEG-*g*-PVAc/SDS mixtures, both $\tau_{FVS\ 50\%}$ and $V_{\text{foam max}}$ were lower in the DTAB mixtures. $R_{\text{avg initial}}$ was smaller than that of PEG-*g*-PVAc/SDS mixtures containing low surfactant concentration, but higher $R_{\text{avg initial}}$ was observed in PEG-*g*-PVAc/DTAB containing concentrations of 0.5 cmc and above of DTAB compared to mixtures with PEG-*g*-PVAc/SDS.

The macroscopic observation of foam behaviour of 5 cmc DTAB/PEG-*g*-PVAc mixtures is shown in Figure 4.10.

*Table 4.2 The $V_{\text{foam max}}$, $\tau_{FVS\ 50\%}$ and $R_{\text{avg initial}}$ determined from foam measurements of PEG-*g*-PVAc mixtures with DTAB.*

PEG- <i>g</i> -PVAc conc (cac)	DTAB conc (cmc)	Foam Half-life Time, $\tau_{FVS\ 50\%}$ (s)	Volume, $V_{\text{foam max}}$ (mL)	Initial Radius, $R_{\text{avg initial}}$ (μm)
0.2	-	10.4 \pm 8.3	11.7 \pm 4.0	14.0 \pm 0.5
2	-	121.7 \pm 46.0	48.4 \pm 6.8	180.7 \pm 30.0
-	0.05	16.8 \pm 0.7	30.1 \pm 1.1	14.7 \pm 2.1
0.2	0.05	23.3 \pm 5.9	29.4 \pm 5.0	33.7 \pm 15.5
2	0.05	9.4 \pm 13.4	18.5 \pm 5.8	84.7 \pm 32.0
-	0.5	399.0 \pm 507.4	111.8 \pm 4.7	279.3 \pm 13.6
0.2	0.5	742.0 \pm 321.1	70.3 \pm 1.2	222.3 \pm 41.9
2	0.5	435.8 \pm 90.1	73.8 \pm 5.6	266.7 \pm 20.8
-	5	1330.7 \pm 490.5	90.2 \pm 13.7	126.3 \pm 12.7
0.2	5	1064.6 \pm 212.2	86.9 \pm 0.8	116.3 \pm 2.1
2	5	1085.0 \pm 142.9	88.5 \pm 0.6	117.7 \pm 3.5

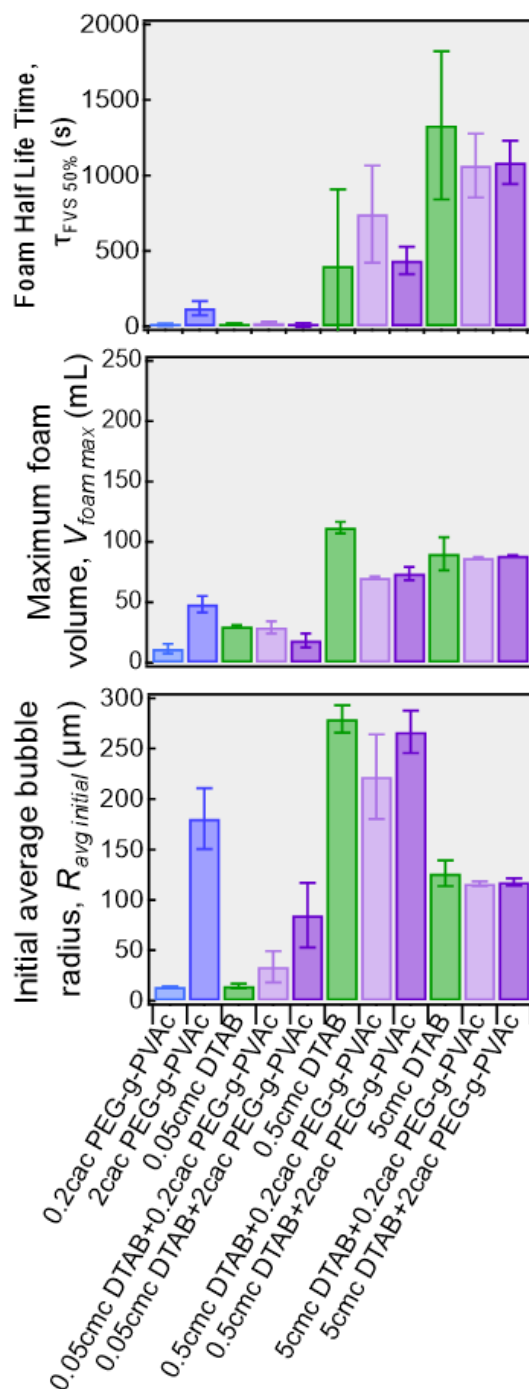


Figure 4.9 Foaming data showing the: a) foam half-life time ($\tau_{FVS\ 50\%}$) which is a measure of foam stability; b) maximum foam volume ($V_{foam\ max}$) which is a measure of foamability; and c) initial average bubble radius ($R_{avg\ initial}$) showing the radius of the foam bubbles during the foam generation. The data in green represents the pure DTAB solutions at 3 concentrations, the data in blue represents data for the pure polymer at 2 concentrations. The mixed polymer/surfactant systems are shown in pale and dark purple for DTAB with 0.2 cac PEG-g-PVAc and DTAB with 2 cac PEG-g-PVAc respectively.

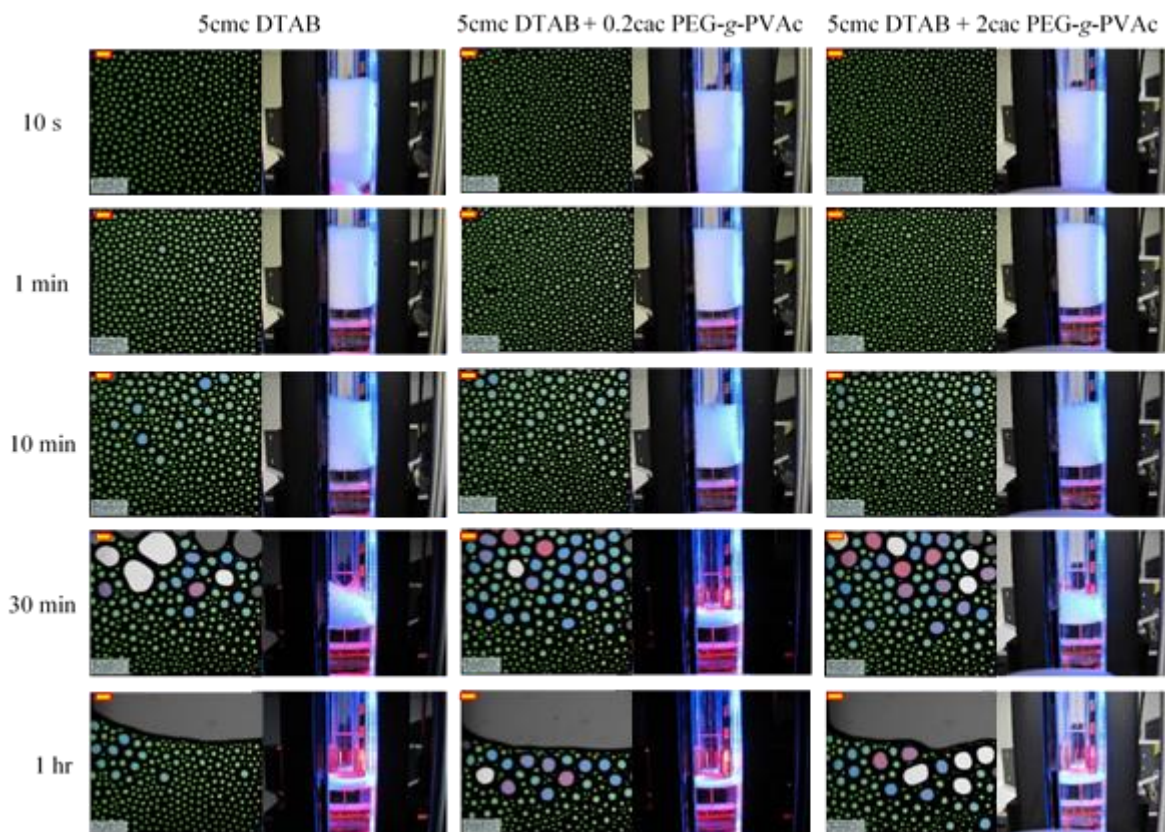


Figure 4.10 Macroscopic foaming behaviour data (overall foam volume) and foam bubble size recorded over given period after foam generation is shown, comparing the pure 5cmc DTAB system (left column) to the mixed systems containing 5cmc DTAB + 0.2 cac PEG-g-PVAc (middle column) and 5cmc DTAB + 2 cac PEG-g-PVAc (right column). The bubble size is colour coded as follows: green is for smallest bubble radius, followed by blue, purple, pink and the largest bubbles are shown in white.

4.4 Conclusions

We have studied the interactions between a neutral tardigrade co-polymer PEG-g-PVAc and cationic DTAB at the air-water interface. The composition and structure of the interfacial layer was determined from a combination of γ measurements and NR data fitting. The interfacial characterisation was then linked to the foam behaviour and compared to our previous study of the same polymer with anionic SDS.

The γ data showed pronounced synergistic adsorption in mixtures of PEG-g-PVAc/DTAB up to DTAB concentration ~ 0.5 cmc. Above this DTAB concentration, the γ value was similar to that of pure DTAB. This γ behaviour is comparable to that of PEG-g-PVAc/SDS.

Based on the NR data and Γ calculations, a clear difference can be seen in the behaviour of the PEG-g-PVAc/DTAB mixture compared to that of PEG-g-PVAc/SDS. At low concentration of DTAB, DTAB encouraged polymer surface adsorption. Even at a DTAB concentration above its cmc, there was a considerable amount of polymer present at the interface ($\Gamma \sim 0.6 \text{ mg m}^{-2}$). This behaviour could be rationalised by electrostatic interactions between partially dissociated PVAc groups in the polymer leading to a partial negative charge which can readily associate with the cationic DTAB, forming complexes both at the interface as well as in the bulk.

The interfacial and foaming behaviour observations we made here are interesting. From our NR data fitting, we would expect enhanced foam stability due to the presence of a polymer layer at the interface, buried underneath the surfactant monolayer, previously referred to as a “hanging” polymer layer in mixtures with SDS. There is a notable difference in the thickness t of this polymer layer: $t \sim 5 \text{ \AA}$ in the mixtures here containing DTAB, whereas in mixtures containing SDS, $t \sim 3 \text{ \AA}$ at high SDS concentrations. We speculate that it is the thickness of this hanging polymer layer that may influence the foam stability as well as the appearance (*i.e.* bubble size and bubble size distribution). SDS and DTAB both possess a $\text{C}_{12}\text{H}_{25}$ hydrocarbon tail; however, the SDS headgroup is anionic and relatively small, leading to the weak interactions between SDS and the polymer backbone. In the case of DTAB, the headgroup is cationic and can interact with the PVAc grafts of the polymer. The difference in the interfacial layer thickness, as well as γ and the foaming behaviour are therefore directly influenced by the surfactant headgroup characteristics. This finding has implications towards the practical applications of such polymer in detergents and personal care products, as controlled foamability and foam stability are important factors in customer satisfaction ratings. The different foaming behaviour of the PEG-g-PVAc co-polymer with different types of surfactants can therefore be exploited in product formulations, where depending on the surfactants present in the formulation, the polymer may act as both a slight defoamer (with DTAB; preferred in dishwasher detergents) or a foam enhancer (with SDS; preferred in hand dishwashing detergents).

4.5 References

1. Taylor, D.J.F., Thomas, R.K., and Penfold, J., *Polymer/surfactant interactions at the air/water interface*. Advances in Colloid and Interface Science, 2007. **132**(2).
2. Guzmán, E., et al., *Polymer–surfactant systems in bulk and at fluid interfaces*. Advances in Colloid and Interface Science, 2016. **233**: p. 38-64.
3. Petkova, R., Tcholakova, S., and Denkov, N.D., *Foaming and Foam Stability for Mixed Polymer–Surfactant Solutions: Effects of Surfactant Type and Polymer Charge*. Langmuir, 2012. **28**(11): p. 4996-5009.
4. Mitrinova, Z., et al., *Role of interactions between cationic polymers and surfactants for foam properties*. Colloids and Surfaces A: Physicochemical and Engineering Aspects, 2016. **489**: p. 378-391.
5. Bureiko, A., et al., *Current applications of foams formed from mixed surfactant–polymer solutions*. Advances in Colloid and Interface Science, 2015. **222**: p. 670-677.
6. Goddard, E.D., *Polymer/surfactant interaction—Its relevance to detergent systems*. Journal of the American Oil Chemists' Society, 1994. **71**(1): p. 1-16.
7. Qi, S., et al., *Insights into the Role of Polymer-Surfactant Complexes in Drug Solubilisation/Stabilisation During Drug Release from Solid Dispersions*. J Pharmaceutical Research, 2013. **30**(1): p. 290-302.
8. Somasundaran, P. and Lee, L.T., *Polymer-Surfactant Interactions in Flotation of Quartz*. Separation Science and Technology, 1981. **16**(10): p. 1475-1490.
9. Sharipova, A.A., et al., *Polymer–surfactant complexes for microencapsulation of vitamin E and its release*. Colloids and Surfaces B: Biointerfaces, 2016. **137**: p. 152-157.
10. W. Sulek, M. and Jedynek, R., *The effect of the formation of polymer/surfactant complexes on selected tribological properties of their aqueous solutions*. Vol. 281. 2018. 117-122.
11. Somasundaran, P., et al., *Surfactants, polymers and their nanoparticles for personal care applications*. Vol. 27. 2005. 135-136.
12. Martani, R., Le Huede, E., and Dumas, J., *Controlled release pharmaceutical composition*. 1989, Google Patents.
13. Dakhara, S. and Anajwala, C.J.S.R.i.P., *Polyelectrolyte complex: A pharmaceutical review*. 2010. **1**(2): p. 121.
14. Canter, N.H., Robbins, M.L., and Baker, E.G., *Polymer-microemulsion complexes for the enhanced recovery of oil*. 1982, Google Patents.

15. Braun, L., et al., *Polymers and surfactants at fluid interfaces studied with specular neutron reflectometry*. *Advances in Colloid and Interface Science*, 2017. **247**: p. 130-148.
16. Campbell, R.A., *Recent advances in resolving kinetic and dynamic processes at the air/water interface using specular neutron reflectometry*. *Current Opinion in Colloid & Interface Science*, 2018. **37**: p. 49-60.
17. Skoda, M.W.A., *Recent developments in the application of X-ray and neutron reflectivity to soft-matter systems*. *Current Opinion in Colloid & Interface Science*, 2019. **42**: p. 41-54.
18. Khan, N. and Brettmann, B., *Intermolecular Interactions in Polyelectrolyte and Surfactant Complexes in Solution*. 2018. **11**(1): p. 51.
19. Brackman, J.C. and Engberts, J.B.F.N., *The effect of surfactant headgroup charge on polymer—micelle interaction*. *Journal of Colloid and Interface Science*, 1989. **132**(1): p. 250-255.
20. Slastanova, A., et al., *Synergy, competition, and the “hanging” polymer layer: Interactions between a neutral amphiphilic ‘tardigrade’ co-polymer with an anionic surfactant at the air-water interface*. *Journal of Colloid and Interface Science*, 2019. **submitted**.
21. Krinski, T.L. and Tran, T.H., *Method for improving the soil anti-redeposition properties of washing detergents and product*. 1992, Protein Technologies International, Inc. (St. Louis, MO): United States.
22. Gopalkrishnan, S., Guiney, K.M., and Sherman, J.V., *Modified polyacrylic acid polymers for anti-redeposition performance*. 1998, BASF Corporation (Mount Olive, NJ): United States.
23. Bykov, A.G., et al., *Impact of surfactant chain length on dynamic surface properties of alkyltrimethylammonium bromide/polyacrylic acid solutions*. *Colloids and Surfaces A: Physicochemical and Engineering Aspects*, 2010. **354**(1): p. 382-389.
24. Lyttle, D.J., et al., *Structure of a Dodecyltrimethylammonium Bromide Layer at the Air/Water Interface Determined by Neutron Reflection: Comparison of the Monolayer Structure of Cationic Surfactants with Different Chain Lengths*. *Langmuir*, 1995. **11**(3): p. 1001-1008.
25. Monteux, C., et al., *Interfacial Microgels Formed by Oppositely Charged Polyelectrolytes and Surfactants. 1. Influence of Polyelectrolyte Molecular Weight*. *Langmuir*, 2004. **20**(13): p. 5358-5366.
26. Taylor, D.J.F., et al., *Adsorption of Oppositely Charged Polyelectrolyte/Surfactant Mixtures. Neutron Reflection from Alkyl Trimethylammonium Bromides and Sodium Poly(styrenesulfonate) at the Air/Water Interface: The Effect of Surfactant Chain Length*. *Langmuir*, 2003. **19**(9): p. 3712-3719.

27. Bergstrom, M. and Skov Pedersen, J., *Structure of pure SDS and DTAB micelles in brine determined by small-angle neutron scattering (SANS)*. Physical Chemistry Chemical Physics, 1999. **1**(18): p. 4437-4446.
28. Stubenrauch, C., et al., *Polymer/Surfactant Complexes at the Water/Air Interface: A Surface Tension and X-ray Reflectivity Study*. Langmuir, 2000. **16**(7): p. 3206-3213.
29. Vora, S., et al., *Mixed micelles of some anionic-anionic, cationic-cationic, and ionic-nonionic surfactants in aqueous media*. 1999. **2**(2): p. 213-221.
30. Lu, J.R., et al., *Structure of hydrocarbon chains in surfactant monolayers at the air/water interface: neutron reflection from dodecyl trimethylammonium bromide*. Journal of the Chemical Society, Faraday Transactions, 1996. **92**(3): p. 403-408.
31. Jadidi, N., Adib, B., and Malihi, F.B., *Synergism and Performance Optimization in Liquid Detergents Containing Binary Mixtures of Anionic–Nonionic, and Anionic–Cationic Surfactants*. 2013. **16**(1): p. 115-121.
32. Meyer, M. and Sepúlveda, L., *Counterion association in mixed micelles of cationic and nonionic detergents*. Journal of Colloid and Interface Science, 1984. **99**(2): p. 536-542.
33. Broze, G. and Bastin, D., *Non-aqueous liquid laundry detergents containing three surfactants including a polycarboxylic acid ester of a non-ionic*. 1984.
34. Hewitt, G., *Detergent compositions*. 1972.
35. Langevin, D., *Polyelectrolyte and surfactant mixed solutions. Behavior at surfaces and in thin films*. Advances in Colloid and Interface Science, 2001. **89–90**: p. 467-484.
36. Asnacios, A., Langevin, D., and Argillier, J.-F., *Complexation of Cationic Surfactant and Anionic Polymer at the Air–Water Interface*. Macromolecules, 1996. **29**(23): p. 7412-7417.
37. Wiliński, D., Łukowski, P., and Rokicki, G., *Application of fibres from recycled PET bottles for concrete reinforcement*. Vol. 1. 2016. 1-9.
38. Karamyan, D.R., et al., *Kinetics of the Non-Catalysed Hydrolysis of Vinyl Acetate in an Aqueous Medium*. International Polymer Science and Technology, 2004. **31**(1): p. 49-51.
39. Cooke, D.J., et al., *Interaction between Poly(ethylene oxide) and Monovalent Dodecyl Sulfates Studied by Neutron Reflection*. Langmuir, 1998. **14**(8): p. 1990-1995.
40. Briddick, A., et al., *Surfactant and Plasticizer Segregation in Thin Poly(vinyl alcohol) Films*. Langmuir, 2016. **32**(3): p. 864-872.
41. Kristen, N. and von Klitzing, R., *Effect of polyelectrolyte/surfactant combinations on the stability of foam films*. Soft Matter, 2010. **6**(5): p. 849-861.
42. Campbell, R.A., Wacklin, H.P., and Sutton, I., *FIGARO: The new horizontal neutron reflectometer at the ILL*. The European Physical Journal Plus, 2011. **126**(107).

-
43. Webster, J., Holt, S., and Dalglish, R., *INTER the chemical interfaces reflectometer on target station 2 at ISIS*. *Physica B: Condensed Matter*, 2006. **385-386**: p. 1164-1166.
 44. Campbell, R.A., et al., *Polyelectrolyte/surfactant films spread from neutral aggregates*. *Soft Matter*, 2016. **12**(24): p. 5304-5312.
 45. Nelson, A., *Co-refinement of multiple-contrast neutron/X-ray reflectivity data using MOTOFIT*. 2006. **39**(2): p. 273-276.
 46. Li, Z.X., Dong, C.C., and Thomas, R.K., *Neutron Reflectivity Studies of the Surface Excess of Gemini Surfactants at the Air–Water Interface*. *Langmuir*, 1999. **15**(13): p. 4392-4396.
 47. Carey, E. and Stubenrauch, C., *Properties of aqueous foams stabilized by dodecyltrimethylammonium bromide*. *Journal of Colloid and Interface Science*, 2009. **333**(2): p. 619-627.
 48. Smith, D.K., Miller, N.R., and Korgel, B.A., *Iodide in CTAB Prevents Gold Nanorod Formation*. *Langmuir*, 2009. **25**(16): p. 9518-9524.
 49. Maiti, S., et al., *Striking Improvement in Peroxidase Activity of Cytochrome c by Modulating Hydrophobicity of Surface-Functionalized Gold Nanoparticles within Cationic Reverse Micelles*. *Chemistry – A European Journal*, 2012. **18**(47): p. 15021-15030.
 50. Joos, P. and Rillaerts, E., *Theory on the determination of the dynamic surface tension with the drop volume and maximum bubble pressure methods*. *Journal of Colloid and Interface Science*, 1981. **79**(1): p. 96-100.
 51. Eastoe, J. and Dalton, J.S., *Dynamic surface tension and adsorption mechanisms of surfactants at the air–water interface*. *Advances in Colloid and Interface Science*, 2000. **85**(2–3): p. 103-144.
 52. Eastoe, J., et al., *Adsorption of Ionic Surfactants at the Air–Solution Interface*. *Langmuir*, 2000. **16**(10): p. 4511-4518.
 53. Angus-Smyth, A., Campbell, R.A., and Bain, C.D., *Dynamic Adsorption of Weakly Interacting Polymer/Surfactant Mixtures at the Air/Water Interface*. *Langmuir*, 2012. **28**(34): p. 12479-12492.
 54. Campbell, R.A., et al., *Structure of surfactant and phospholipid monolayers at the air/water interface modeled from neutron reflectivity data*. *Journal of Colloid and Interface Science*, 2018. **531**: p. 98-108.
 55. Mann, E., et al., *Mixed polymer - surfactant layers at the air - water interface*. *Berichte der Bunsengesellschaft für physikalische Chemie*, 1994. **98**(3): p. 519-520.
 56. Mann, E., et al., *Polymer-surfactant films at the air-water interface. 1. Surface pressure, ellipsometry, and microscopic studies*. *Macromolecules*, 1993. **26**(25): p. 7037-7045.

57. Taylor, D.J.F., Thomas, R.K., and Penfold, J., *The Adsorption of Oppositely Charged Polyelectrolyte/Surfactant Mixtures: Neutron Reflection from Dodecyl Trimethylammonium Bromide and Sodium Poly(styrene sulfonate) at the Air/Water Interface*. *Langmuir*, 2002. **18**(12): p. 4748-4757.
58. Zhang, J., Thomas, R.K., and Penfold, J., *Interaction of oppositely charged polyelectrolyte–ionic surfactant mixtures: adsorption of sodium poly(acrylic acid)–dodecyl trimethyl ammonium bromide mixtures at the air–water interface*. *Soft Matter*, 2005. **1**(4): p. 310-318.

5 Interfacial structures and interactions of a neutral amphiphilic ‘tardigrade’ co-polymer with non-ionic surfactant at the air-water interface

Polymer/surfactant systems comprising of neutral amphiphilic PEG-g-PVAc co-polymer with a non-ionic dodecylpentaethyleneglycol ether ($C_{12}E_5$) were investigated at the air-water interface by a combination of dynamic and equilibrium surface tension, neutron reflectivity (NR) and preliminary foam behaviour tests. The choice of the surfactant used is relevant to the applications of this PEG-g-PVAc co-polymer in detergents and aims to finalise the investigation of the influence of the surfactant headgroup characteristics on the polymer/surfactant interfacial behaviour. Competitive adsorption behaviour in $C_{12}E_5$ /PEG-g-PVAc system at surfactant concentration above ~ 0.1 cmc $C_{12}E_5$ was observed, with polymer depletion from the interface and forming a “hanging” layer underneath the $C_{12}E_5$ monolayer at the interface. Finally, a small suppression of foam stability was observed in the $C_{12}E_5$ /PEG-g-PVAc systems, confirming the importance of the surfactant headgroup characteristics in the polymer/surfactant behaviour at the air-water interface.

5.1 Introduction

Here, the study of composition and interactions of the tardigrade comb co-polymer with a non-ionic dodecylpentaethyleneglycol ether ($C_{12}E_5$) is presented. The non-ionic surfactant chosen has been widely studied [1-5] and possesses the same hydrocarbon tail as SDS and DTAB described previously, therefore the effect of the surfactant headgroup charge and size on the interfacial behaviour can be evaluated from this series of interfacial studies. Additionally, non-ionic surfactants are often found in cleaning product formulations [6-9], highlighting further relevance of this study to the practical application of the PEG-g-PVAc polymer in laundry and detergent products.

Different adsorption behaviours of non-ionic $C_{12}E_5$ and a charged cationic DTAB at the air-water interface in the presence of different polymers have been reported before [10]. In the case of $C_{12}E_5$, no appreciable synergistic adsorption was observed in the presence of

polyacrylamide sulfonate (PAMPS), xanthan and other polymers [11]. Polystyrene sulfonate (PSS) addition to C₁₂E₅ solution induced an increase in the surface tension, most likely due to complexation in the bulk competing with the interfacial complexation.

Interactions of C₁₂E₅ with polymers bearing PEG or PVAc groups have been reported previously. It has been shown that the C₁₂E₅ headgroup (essentially an extremely short PEG) bound to the PEG polymer *via* hydrophobic interactions [2]. Surface segregation in PVA (polyvinyl alcohol) films was observed when C₁₂E₅ was present in the film, compared to a uniform film with CTAB (cetyltrimethylammonium bromide) [12]. Based on this knowledge, we would expect relatively strong interactions between the C₁₂E₅ headgroup and the PEG backbone of the PEG-*g*-PVAc tardigrade co-polymer. In general, the C₁₂E₅ molecule is bigger and can therefore interact *via* stronger hydrophobic forces compared to other model surfactants such as SDS and DTAB, all with the C₁₂H₂₅ tail. Therefore, in addition to their industrial relevance, C₁₂E₅ also represents a simple model system to evaluate the effect of headgroup interactions with the tardigrade polymer, complementing studies on the interactions between the same polymer and SDS (Chapter 3) and DTAB (Chapter 4).

In this study, we have used dynamic (γ_d) and equilibrium (γ) surface tension measurements and neutron reflectivity (NR) to study the interfacial adsorption of PEG-*g*-PVAc polymer with C₁₂E₅, and the structure (layer thickness, t , and roughness, σ) and composition (surface excess of separate adsorbing species, Γ , and solvation, ϕ_{water}) of the polymer/surfactant mixtures at the air-water interface [13-15]. The results show a transition from synergy to competition, similar to the polymer/SDS complex investigated previously. However, the onset surfactant concentration at which this transition happened, and the extent of the competition, was dependent on the surfactant used. A comparison is made of the foaming behaviour mediated by these polymer/surfactant mixtures, where again the characteristics of the surfactant was crucial in determining the foamability and foam stability of such polymer/surfactant mixtures [16, 17]. It is important to note that the cmc value of the three surfactants compared differs as following: cmc of SDS $\sim 8.2 \text{ mmol L}^{-1}$, DTAB $\sim 14 \text{ mmol L}^{-1}$ and C₁₂E₅ $\sim 0.7 \text{ mmol L}^{-1}$. The results of polymer/surfactant mixtures here are presented in their relevant cmc values and do not take the surfactant efficiency or specific amount into account.

5.2 Methods

5.2.1 Materials

Both hydrogenous and deuterated dodecyl pentaethylene glycol ether (h- $C_{12}E_5$, $C_{12}H_{25}(C_2H_4O)_5OH$, Sigma-Aldrich; d- $C_{12}E_5$, $C_{12}D_{25}(C_2H_4O)_5OH$, ISIS Deuteration Facility) were used as delivered. MilliQ water (Millipore, resistivity 18.2 m Ω cm, <5 ppb organic matter) was used for solution preparation for surface tension measurements, as well as for the preparation of air contrast matched water (ACMW; $H_2O:D_2O$, 91.1:8.9 w:w). D_2O was supplied by Sigma-Aldrich (99.9%).

The amphiphilic *tardigrade comb* co-polymer (Figure 5.1) consisting of a PEG backbone and short PVAc grafts (Mn 15 kDa, PEG₁₃₆-g-PVAc₁₀₄ with the subscripts indicating the number of monomers; or PEG(6000)-g-PVAc(9000) with the corresponding segmental Mn indicated) was commercially available from BASF. It was freeze-dried and re-dissolved in H_2O , D_2O , or ACMW for sample preparation.

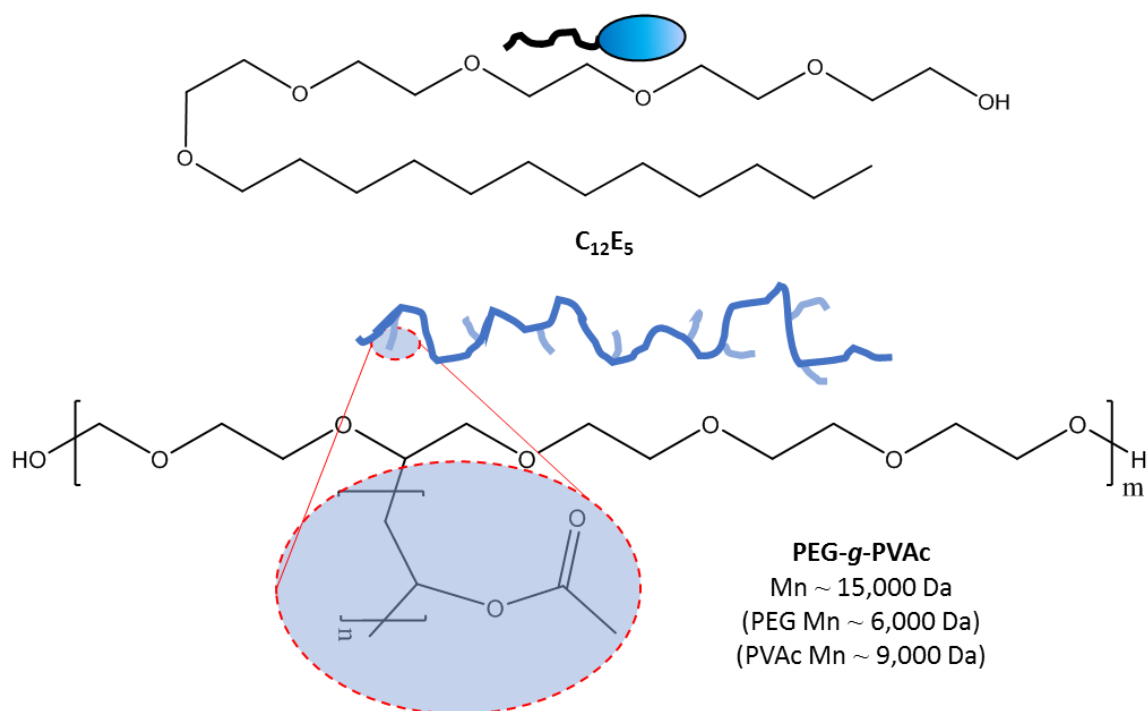


Figure 5.1 Molecular structures (with corresponding schematics) of PEG-g-PVAc co-polymer and the surfactants $C_{12}E_5$.

5.2.2 Surface tension measurements

The equilibrium (γ) and dynamic (γ_d) surface tension data was collected on a force tensiometer (K100, Krüss GmbH) and a bubble pressure tensiometer (BP100, Krüss GmbH), as described previously. Same settings were used as previously, *i.e.* γ measurement was performed using the Wilhelmy plate method and data collection was stopped after the standard deviation between the last 5 data points $< 0.01 \text{ mN m}^{-1}$ at which point equilibration was assumed. The γ_d was determined from the bubble pressure experienced at different surface age, τ , (measured between $\tau \sim 10 \text{ ms}$ and 4 min).

5.2.3 Neutron reflectivity (NR)

The NR data at the air-water interface, in Teflon adsorption troughs, was obtained at the FIGARO beamline at Institut Laue-Langevin (ILL, Grenoble, France) [18]. The same set-up as described previously was used, with a time-of-flight detector, accessing a Q range of $\sim 0.005\text{-}0.25 \text{ \AA}^{-1}$ (neutrons wavelengths range: $\lambda \sim 2 - 30 \text{ \AA}$) at two different grazing incidence angles ($\theta = 0.62^\circ$ and 3.79°). The obtained reflectivity profiles were plotted as $RQ^4(Q)$ vs. Q (the momentum transfer perpendicular to the interface). The background was subtracted from the data and the data was reduced and calibrated according to the direct beam and D₂O and ACMW data, using COSMOS software package [19].

As previously, NR data of polymer/surfactant mixtures was collected at 4 different isotopic contrasts: h-surfactant in ACMW, d-surfactant in ACMW, h-surfactant in D₂O, and d-surfactant in D₂O, all with the h-polymer. In this case, h-surfactant stands for fully hydrogenous C₁₂E₅, while d-surfactant stands for deuterated C₁₂D₂₅- hydrocarbon tail and hydrogenous surfactant headgroup ((C₂H₄O)₅OH).

The compositional information of the interfacial structures was obtained from a 1-layer data fitting model at low Q range to determine the surface excess Γ , of the adsorbed polymer and surfactant [13, 14, 20]. The NR data over the whole accessible Q range was then fitted using 1-layer and multilayer-models, to elucidate the structural information, such as thickness (t), roughness (σ) and water volume fraction in the layer (ϕ_{water}). The volume fraction of polymer or surfactant in a mixed layer was determined from the fitted ρ of said layer [21]. All the data fitting was performed using the Motofit package in IGOR Pro [22].

5.2.4 Foaming measurements

Foams were generated by air flow through a sintered porous glass filter (pore size 40-100 μm , 3 cm in diameter) at a flow rate of 0.3 L min^{-1} for 12 s, as previously. The foamability (maximum foam volume), foam stability (half-life of the maximum foam height) and initial bubble size were determined using a dynamic foam analyser (DFA 100, Krüss GmbH).

5.3 Results

5.3.1 Equilibrium and dynamic surface tension measurements

The γ data of the pure polymer and C_{12}E_5 , as well as their mixtures, is shown in Figure 5.2a, with the γ_d data shown in Figure 5.2c. In the polymer/surfactant mixtures containing low C_{12}E_5 concentrations ($< \sim 0.1$ cmc C_{12}E_5), there are two separate interfacial behaviours observed. In the mixtures containing 0.2 cac PEG-*g*-PVAc and < 0.1 cmc C_{12}E_5 (data around point 4 \square), there is a small synergistic effect ($\Delta\gamma \sim 5\text{-}10$ mN m^{-1} compared to pure PEG-*g*-PVAc $\gamma \sim 55$ mN m^{-1} , Point 1 \circ). In the mixtures containing 2 cac PEG-*g*-PVAc and ≤ 0.1 cmc C_{12}E_5 (Point 5 \blacktriangle), the γ value ~ 44 mN m^{-1} is very similar to that of a pure PEG-*g*-PVAc at 2 cac (Point 2 \circ). In mixtures containing 0.5 cmc C_{12}E_5 , and both 0.2 and 2 cac PEG-*g*-PVAc (Points 7 \square and 8 \blacktriangle) the γ value ~ 39 mN m^{-1} is higher than that of pure 0.5 cmc C_{12}E_5 (Point 6 ∇) $\gamma \sim 35$ mN m^{-1} and lower than that of PEG-*g*-PVAc $\gamma \sim 55$ and 44 mN m^{-1} at 0.2 cac (Point 1 \circ) and 2 cac (Point 2 \circ) concentrations, respectively. This adsorption behaviour is suggesting interactions of C_{12}E_5 and PEG-*g*-PVAc, likely between the headgroup and the PEG backbone [2], possibly forming polymer/surfactant complexes in the bulk solution and partially depleting the interface of the surfactant. At concentrations containing ≥ 1.2 cmc C_{12}E_5 , for mixtures with both 0.2 and 2 cac PEG-*g*-PVAc (Points 10 \square and 11 \blacktriangle) the γ data overlaps with the values of pure C_{12}E_5 (Point 9 ∇). This behaviour points toward competitive adsorption at the interface, where the polymer is depleted from the interface and C_{12}E_5 becomes the dominant adsorbing species.

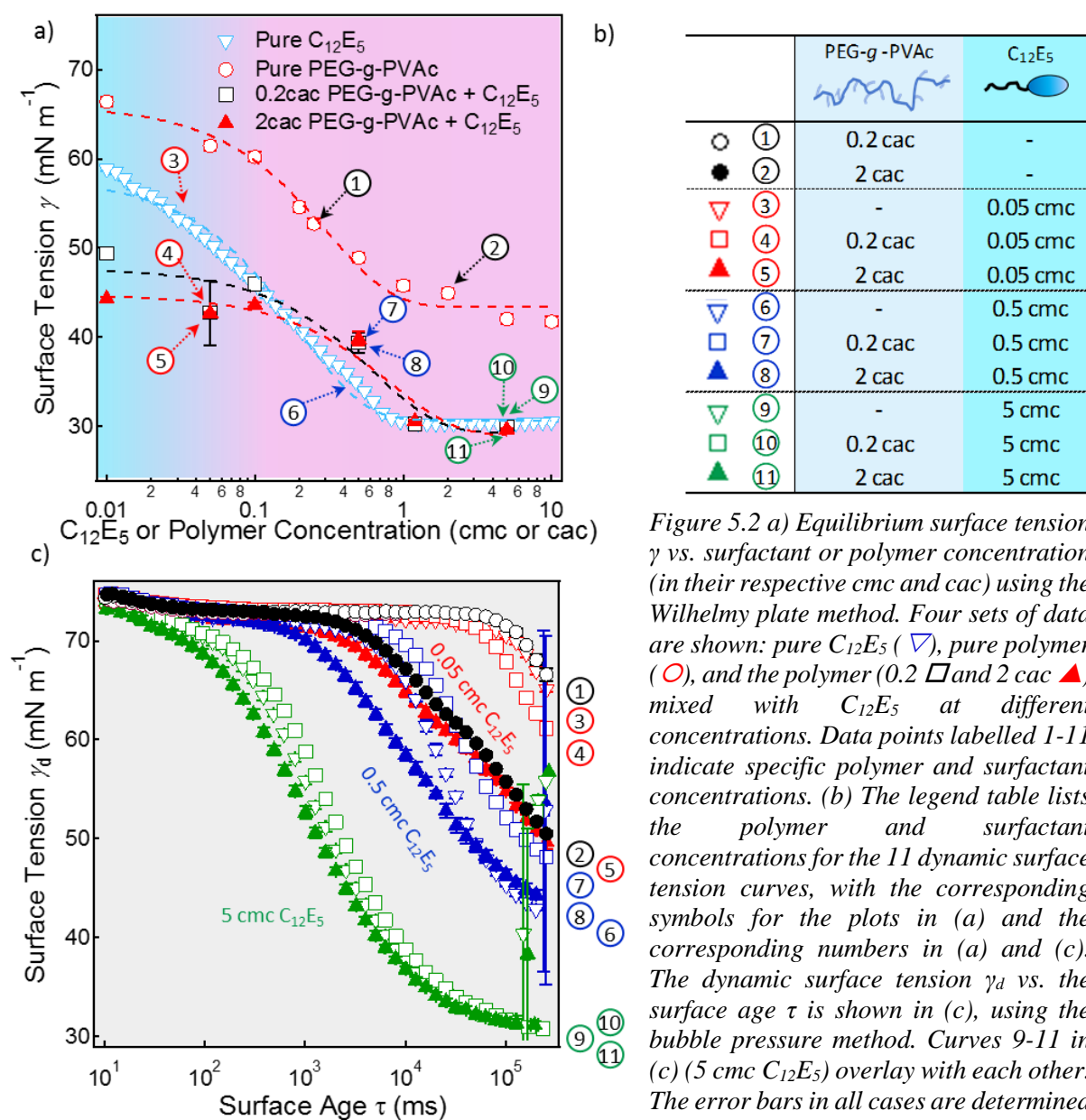


Figure 5.2 a) Equilibrium surface tension γ vs. surfactant or polymer concentration (in their respective cmc and cac) using the Wilhelmy plate method. Four sets of data are shown: pure C₁₂E₅ (∇), pure polymer (\circ), and the polymer (0.2 \square and 2 cac \blacktriangle) mixed with C₁₂E₅ at different concentrations. Data points labelled 1-11 indicate specific polymer and surfactant concentrations. (b) The legend table lists the polymer and surfactant concentrations for the 11 dynamic surface tension curves, with the corresponding symbols for the plots in (a) and the corresponding numbers in (a) and (c). The dynamic surface tension γ_d vs. the surface age τ is shown in (c), using the bubble pressure method. Curves 9-11 in (c) (5 cmc C₁₂E₅) overlay with each other. The error bars in all cases are determined as a standard deviation from an experimental error determined from 3 separate measurements.

The dynamic surface tension (γ_d) of the polymer/surfactant mixtures containing C₁₂E₅ (Figure 5.2c) shows very different adsorption behaviour compared to the mixtures containing either DTAB or SDS, discussed in previous chapters. The main difference is that, at small τ , γ_d tracks that of water or a slowly adsorbing species at $\tau \sim 100$ ms, $\gamma_d \sim 70$ -74 mN m⁻¹ in all studied concentrations. At such short τ the adsorption of surface active species is diffusion controlled and so this behaviour could be explained by the relatively large C₁₂E₅ molecular volume, therefore with slower diffusion by approximately an order of magnitude compared to DTAB and SDS: the diffusion coefficients of surfactants just above their cmc were reported as $\sim 2 \times 10^{-6}$ cm² s⁻¹ in SDS [23], $\sim 1 \times 10^{-6}$ cm² s⁻¹ in DTAB [24], and $\sim 2 \times 10^{-7}$ cm² s⁻¹ in C₁₂E₅ [2]). The

γ_d lowering starts at $\tau \sim 1$ min in the case of 0.05 cmc $C_{12}E_5$ (Curve 3), with the final $\gamma_d \sim 65$ $mN\ m^{-1}$ at $\tau \sim 4$ min. Up to $\tau_s \sim 50$ s, the γ_d of 0.2 cac PEG-*g*-PVAc and 0.05 cmc $C_{12}E_5$ mixture (Curve 4) follows that of pure surfactant. However, after this τ_s , γ_d of the mixture starts to deviate from that of pure surfactant to reach $\gamma_d \sim 61$ $mN\ m^{-1}$ at $\tau \sim 4$ min compared to $\gamma_d \sim 65$ $mN\ m^{-1}$ at of the pure 0.05 cmc $C_{12}E_5$ (Curve 3). γ_d of 2 cac PEG-*g*-PVAc + 0.05 cmc $C_{12}E_5$ (Curve 5) starts deviating from that of the pure 0.05 cmc $C_{12}E_5$ at $\tau_s \sim 1$ s, and reaches $\gamma_d \sim 50$ $mN\ m^{-1}$ at $\tau \sim 4$ min. However, this γ_d behaviour matches that of the pure 2 cac PEG-*g*-PVAc (Curve 2). It is thus not clear that one could speak of synergistic adsorption at this concentration in this short adsorption time.

In the case of 0.5 cmc $C_{12}E_5$ (Curve 6), the γ_d lowering starts at $\tau \sim 4$ s, with $\gamma_d \sim 43$ $mN\ m^{-1}$ at $\tau \sim 4$ min. There is a hint of synergistic adsorption at short adsorption time in the mixtures containing 2 cac PEG-*g*-PVAc + 0.5 cmc $C_{12}E_5$ (Curve 8), where $\gamma_d \sim 65$ $mN\ m^{-1}$ at $\tau \sim 10$ s in the case of pure 0.5 cmc $C_{12}E_5$ solution. However, γ_d is lowered to ~ 58 $mN\ m^{-1}$ at $\tau \sim 10$ s in the case of 2 cac PEG-*g*-PVAc + 0.5 cmc $C_{12}E_5$ mixture. Intriguingly, γ_d of 0.2 cac PEG-*g*-PVAc + 0.5 cmc $C_{12}E_5$ mixture is ~ 70 $mN\ m^{-1}$ at $\tau \sim 10$ s, which is higher than either the pure surfactant or the mixture containing higher polymer concentration. This slight anomaly, also observed in γ data, is still evident at the end of the measurement, where $\gamma_d \sim 48$ $mN\ m^{-1}$ at $\tau \sim 4$ min in the system containing 0.2 cac PEG-*g*-PVAc + 0.5 cmc $C_{12}E_5$, compared to $\gamma_d \sim 44$ $mN\ m^{-1}$ in both the system containing pure 0.5 cmc $C_{12}E_5$ and the mixture containing 2 cac PEG-*g*-PVAc + 0.5 cmc $C_{12}E_5$. A possible explanation for this behaviour is presence of relatively strong interactions between the polymer and $C_{12}E_5$ in the bulk, also postulated from the NR data fitting, shown in Figure 5.6.

At the highest $C_{12}E_5$ concentration studied (5 cmc, Curve 9), γ_d lowering starts at $\tau \sim 100$ ms, with $\gamma_d \sim 30$ $mN\ m^{-1}$ at $\tau \sim 4$ min. In the polymer/surfactant mixtures containing 5 cmc $C_{12}E_5$, γ_d follows that of pure surfactant, where γ_d value starts to significantly decrease at $\tau \sim 200$ ms and reaches a plateau at $\tau \sim 100$ s and $\gamma_d \sim 32$ $mN\ m^{-1}$. This suggests no strong interactions between $C_{12}E_5$ and PEG-*g*-PVAc are present at this concentration.

In general, γ data differs significantly from the mixtures of SDS or DTAB with the same PEG-*g*-PVAc polymer, with the transition of synergistic adsorption to the competitive behaviour observed at much lower concentrations (~ 0.1 cmc $C_{12}E_5$, ~ 0.5 cmc DTAB and SDS) consistent with higher $C_{12}E_5$ efficiency manifested by much lower cmc value of the pure surfactant, and

a slower interfacial adsorption observed from γ_d data, which is attributed to the slower diffusion of $C_{12}E_5$ compared to SDS and DTAB.

5.3.2 Neutron reflectivity results

5.3.2.1 Interfacial layer composition via surface excess evaluation

The surface excess, Γ , of $C_{12}E_5$ above its cmc was calculated from the NR data to be $\Gamma \sim 3.70 \mu\text{mol m}^{-2}$, which is in agreement with literature [3, 4]. The Γ of $C_{12}E_5$ /polymer mixtures is shown in Figure 5.3.

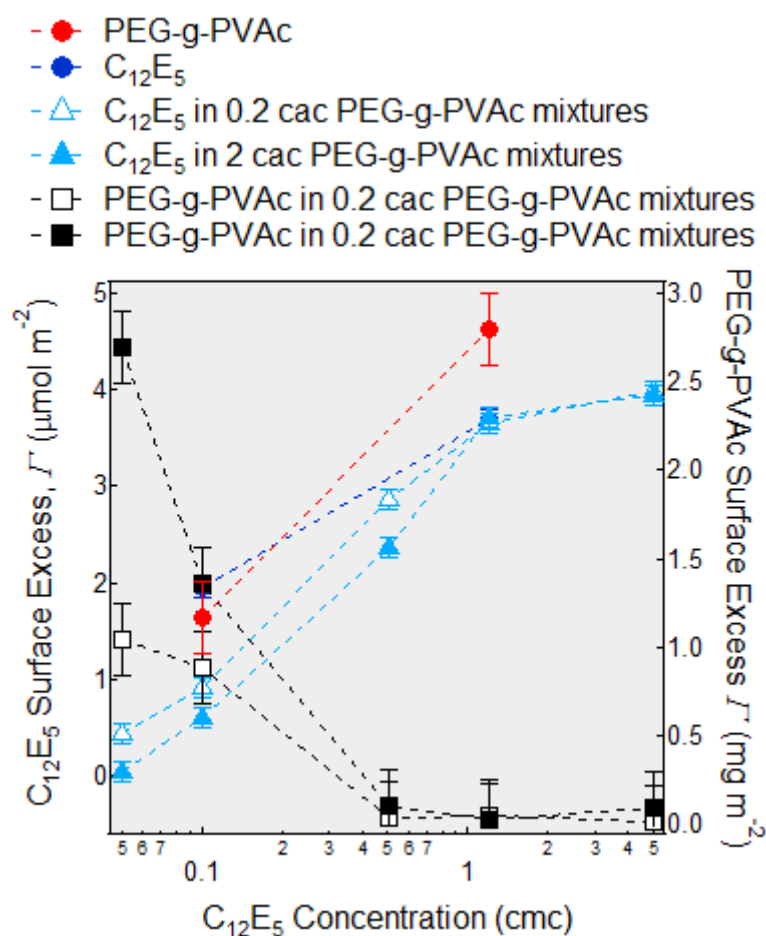


Figure 5.3 The calculated Γ vs $C_{12}E_5$ concentration of mixed PEG-g-PVAc + $C_{12}E_5$ systems is shown. The $\Gamma_{C_{12}E_5}$ is shown in $\mu\text{mol m}^{-2}$ on the left axis and represented by the filled markers, and $\Gamma_{\text{PEG-g-PVAc}}$ is shown in mg m^{-2} on the right axis and represented by the empty markers. The dashed lines act as a guide to the eyes only.

Unlike in the case of DTAB/PEG-g-PVAc, there was clear competitive behaviour observed in polymer mixtures containing > 0.1 cmc $C_{12}E_5$ (compared to > 0.5 cmc SDS). Based on the Γ data, there was very small amount of PEG-g-PVAc at the interface at 0.5 cmc $C_{12}E_5$ and above ($\Gamma_{\text{PEG-g-PVAc}}$ plateau $< 0.1 \text{ mg m}^{-2}$). Interestingly, there was an influence of the polymer presence on the $\Gamma_{C_{12}E_5}$ in concentrations < 0.5 cmc, as there were consistently larger amounts of $C_{12}E_5$

in the mixtures containing lower PEG-*g*-PVAc concentration (e.g. $\Gamma_{C_{12}E_5} \sim 0.9 \mu\text{mol m}^{-2}$ in 0.1 cmc $C_{12}E_5$ + 0.2 cac PEG-*g*-PVAc and $\Gamma_{C_{12}E_5} \sim 0.6 \mu\text{mol m}^{-2}$ in 0.1 cmc $C_{12}E_5$ + 2 cac PEG-*g*-PVAc, compared to $\Gamma_{C_{12}E_5} \sim 1.2 \mu\text{mol m}^{-2}$ in pure 0.1 cmc $C_{12}E_5$). This behaviour therefore indicated some interactions between the polymer and $C_{12}E_5$ at these concentrations, as well as previously described synergistic γ lowering.

5.3.2.2 $C_{12}E_5$ /PEG-*g*-PVAc interfacial layer structure (NR data fitting)

The NR data fitted using a single-layer model is shown in Figure 5.4. At $C_{12}E_5$ concentrations <0.5 cmc, the thickness of the polymer/surfactant mixtures with 0.2 cmc PEG-*g*-PVAc was higher ($t \sim 15 \text{ \AA}$) than that of pure $C_{12}E_5$ ($t \sim 10 \text{ \AA}$) or polymer ($t \sim 11 \text{ \AA}$). In the polymer/surfactant mixtures with 2 cac PEG-*g*-PVAc, $t \sim 2.3 \text{ nm}$ was between that of pure $C_{12}E_5$ ($t \sim 10 \text{ \AA}$) or polymer ($t \sim 28 \text{ \AA}$). At $C_{12}E_5$ concentrations >0.5 cmc, t of polymer/surfactant mixtures ($t \sim 22 \text{ \AA}$) was equal to that of pure $C_{12}E_5$ above its cmc.

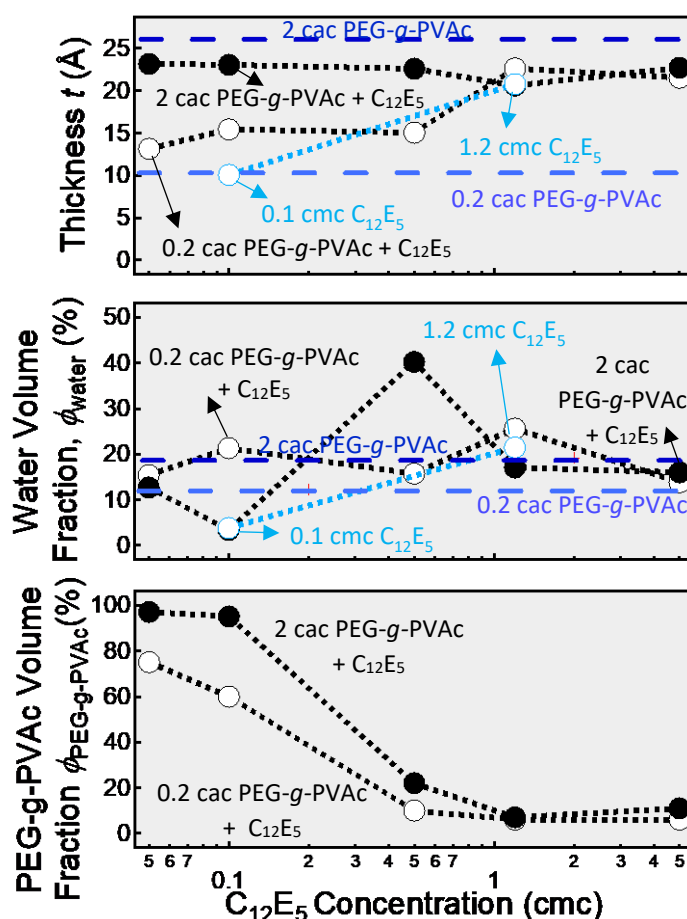


Figure 5.4 A summary of the thickness t , water volume fraction, ϕ_{water} , and polymer fraction $\phi_{\text{PEG-g-PVAc}}$ in a single-layer model used to fit the NR data of PEG-*g*-PVAc + $C_{12}E_5$ mixtures (\circ and \bullet for 0.2 and 2 cac polymer respectively). For comparison, the blue dashed lines represent the fitted values of 0.2 cac PEG-*g*-PVAc and 2 cac PEG-*g*-PVAc respectively. The data point with pale blue outline represents the fitted value for 1.2 cmc pure $C_{12}E_5$.

The ϕ_{water} in all the mixtures studied was between $\phi_{water} \sim 3$ -20%, apart from in the mixture of 0.5 cmc $C_{12}E_5$ + 2 cac PEG-g-PVAc the $\phi_{water} \sim 40\%$. There was a clear decrease in $\phi_{PEG-g-PVAc}$ observed with increasing $C_{12}E_5$ concentration, suggesting polymer depletion at the interface and competitive adsorption at $C_{12}E_5$ concentrations > 0.1 cmc.

Next, multi-layer fitting models were used to deduce the interfacial structure and organisation of $C_{12}E_5$ /PEG-g-PVAc mixtures where relevant (Table 5.1). The pure $C_{12}E_5$ layer was fitted using a 1-layer model at 0.1 cmc ($t \sim 10.1$ Å), and a 2-layer model at 1.2 cmc ($t_1 \sim 8.2$ Å and $t_2 \sim 9.1$ Å) (Figure E.1 in Appendix). At low $C_{12}E_5$ concentrations (0.05 and 0.1 cmc) a single layer model was used. At higher $C_{12}E_5$ concentrations (0.5 and 5 cmc) a 2-layer model was used accounting for a separate $C_{12}E_5$ tail layer and a mixed $C_{12}E_5$ headgroup/polymer layer, with a 3-layer model used in the case of 5 cmc $C_{12}E_5$ + 2 cmc PEG-g-PVAc mixture.

Table 5.1 The fitted parameters for the optimised multilayer models for mixtures of PEG-g-PVAc and $C_{12}E_5$, as well as the pure systems. The superscripts for the fitted scattering length density (SLD) ρ values in the table correspond to the following polymer/surfactant volume fractions: ¹ 75% PEG-g-PVAc + 25% $C_{12}E_5$, ² 60% PEG-g-PVAc + 40% $C_{12}E_5$, ³ 28% PEG-g-PVAc + 72% $C_{12}E_5$ headgroup, ⁴ 52% PEG-g-PVAc + 48% $C_{12}E_5$, ⁵ 32% PEG-g-PVAc + 68% $C_{12}E_5$, ⁶ 97% PEG-g-PVAc + 3% $C_{12}E_5$, ⁷ 95% PEG-g-PVAc + 5% $C_{12}E_5$, ⁸ 18% PEG-g-PVAc + 82% $C_{12}E_5$ headgroup and ⁹ 58% PEG-g-PVAc + 42% $C_{12}E_5$ headgroup.

PEG-g-PVAc $C_{12}E_5$		Layer 1					Layer 2				Layer 3				Bkg
conc (cac)	conc (cmc)	t_1 (Å)	$h-\rho_1$ (10^{-6} Å^{-2})	$d-\rho_1$ (10^{-6} Å^{-2})	$\phi_{water-1}$ (%)	σ_1 (Å)	t_2 (Å)	ρ_2 (10^{-6} Å^{-2})	$\phi_{water-2}$ (%)	σ_2 (Å)	t_3 (Å)	ρ_3 (10^{-6} Å^{-2})	$\phi_{water-3}$ (%)	σ_3 (Å)	σ_{bkg} (Å)
0.2	0.05	13.1	0.806 ¹	1.734 ¹	15	5.2	-	-	-	-	-	-	-	-	5.4
0.2	0.1	15.4	0.670 ²	2.155 ²	21	5.1	-	-	-	-	-	-	-	-	4.3
0.2	0.5	6.2	-0.39	7.004	0	5.6	7.9	0.758 ³	35	4.1	-	-	-	-	4.5
0.2	1.2	7.7	-0.39	7.004	0	5.3	9.6	0.849 ⁴	35	4.3	-	-	-	-	3.5
0.2	5	8.5	-0.39	7.004	0	5.3	9.1	0.773 ⁵	34	4.7	-	-	-	-	4.5
2	0.05	23.1	1.004 ⁶	1.115 ⁶	13	2.4	-	-	-	-	-	-	-	-	8.1
2	0.1	23.0	0.986 ⁷	1.172 ⁷	3	3.4	-	-	-	-	-	-	-	-	9.7
2	0.5	5.2	-0.39	7.004	0	5.6	10.1	0.720 ⁸	18	5.0	-	-	-	-	4.1
2	1.2	7.8	-0.39	7.004	0	5.7	9.8	0.872 ⁹	44	3.8	-	-	-	-	3.3
2	5	8.1	-0.39	7.004	0	3.4	8.3	0.652	4	5.8	5.4	1.031	84	4.1	5.0
0.2	-	10.8	1.031	-	12	3.9	-	-	-	-	-	-	-	-	3.2
2	-	28.0	1.031	-	19	3.6	-	-	-	-	-	-	-	-	5.2
-	0.1	10.1	0.129	3.841	4	6.9	-	-	-	-	-	-	-	-	3.7
-	1.2	8.2	-0.39	7.004	0	3.5	9.1	0.652	20	4.6	-	-	-	-	4.7

In polymer/surfactant mixtures at low $C_{12}E_5$ concentrations (0.05 and 0.1 cmc), the NR data was well fitted by a 1-layer model (Figure 5.5). The characteristics of the interfacial layer were largely governed by the polymer concentration, both the t and $\phi_{PEG-g-PVAc}$ increased in the mixtures containing 2 cmc polymer ($\phi_{PEG-g-PVAc} > 95\%$, corresponding to $\Gamma_{PEG-g-PVAc} \sim 2.6$ and 1.4 mg m^{-2} and $\Gamma_{C_{12}E_5} \sim 0.04$ and $0.6 \text{ } \mu\text{mol m}^{-2}$) compared to 0.2 cmc polymer ($\phi_{PEG-g-PVAc} \sim$

75% and 60%, corresponding to $\Gamma_{\text{PEG-g-PVAc}} \sim 1.0$ and 0.9 mg m^{-2} and $\Gamma_{\text{C}_{12}\text{E}_5} \sim 0.4$ and $0.9 \text{ } \mu\text{mol m}^{-2}$). In the mixtures containing 0.2 cmc PEG-g-PVAc, the t of the layer ($t \sim 13$ and $t \sim 15 \text{ \AA}$ in 0.2 cmc PEG-g-PVAc + 0.05 cmc C_{12}E_5 and 0.2 cmc PEG-g-PVAc + 0.1 cmc C_{12}E_5 , respectively) was larger than that of pure surfactant or pure polymer ($t \sim 10 \text{ \AA}$ in both 0.1 cmc C_{12}E_5 and 0.2 cmc PEG-g-PVAc). This observation indicates a slight cooperative adsorption at the interface in these systems. This synergistic increase in the layer t was however not observed in the mixtures containing 2 cmc PEG-g-PVAc, where the t of the mixed layer was lower ($t \sim 23 \text{ \AA}$) than that of the pure polymer above its cmc ($t \sim 28 \text{ \AA}$). Such behaviour at low C_{12}E_5 concentrations can be attributed to interactions between the surfactant and polymer, especially the PEG backbone and C_{12}E_5 headgroup, similar to a PEG/ C_{12}E_5 microemulsion studied using small angle X-ray scattering and dynamic light scattering where strong interactions were observed in the polymer/surfactant system with no increase in droplet size at higher PEG concentrations [25].

Increasing the C_{12}E_5 concentrations to 0.5 cmc, the NR data was best fitted by a 2-layer model, with a separate layer for the surfactant hydrophobic tails and a second layer consisting of mixed surfactant headgroup and the polymer (Figure 5.6). The t_1 of the surfactant tail layer decreased slightly in the mixtures containing higher polymer concentration ($t_1 \sim 6 \text{ \AA}$ and 5 \AA , respectively), indicating a more tilted tail layer and likely stronger interactions with the polymer in the bulk. C_{12}E_5 was shown to adsorb at the air-water interface as tilted and highly entangled molecules, also accounting for the shorter fitted t_1 compared to SDS [1]. The t_2 of the second layer increased with increasing polymer concentration, with $t_2 \sim 8 \text{ \AA}$ and 10 \AA , respectively. Surprisingly, the $\phi_{\text{PEG-g-PVAc}}$ decreased with increasing PEG-g-PVAc bulk concentration ($\phi_{\text{PEG-g-PVAc}} \sim 28\%$, corresponding to $\Gamma_{\text{PEG-g-PVAc}} \sim 0.03 \text{ mg m}^{-2}$ and $\Gamma_{\text{C}_{12}\text{E}_5} \sim 2.9 \text{ } \mu\text{mol m}^{-2}$ in the mixture containing 0.2 cmc PEG-g-PVAc, and $\phi_{\text{PEG-g-PVAc}} \sim 18\%$, corresponding to $\Gamma_{\text{PEG-g-PVAc}} < 0.1 \text{ mg m}^{-2}$ and $\Gamma_{\text{C}_{12}\text{E}_5} \sim 2.4 \text{ } \mu\text{mol m}^{-2}$ in mixture containing 2 cmc PEG-g-PVAc). This $\phi_{\text{PEG-g-PVAc}}$ decrease with increasing polymer concentration could indicate stronger interactions between the surfactant and polymer in the bulk, rather than at the interface. The characteristics of the interfacial layer at this concentration were largely governed by the surfactant concentration, with the polymer depleted from the interface towards the bulk as indicated by decreasing $\Gamma_{\text{PEG-g-PVAc}}$ values to $< 0.1 \text{ mg m}^{-2}$, which is a clear shift in the interfacial behaviour from the lower surfactant concentrations. This $\text{C}_{12}\text{E}_5/\text{PEG-g-PVAc}$ interactions at the interface, however small, accounted for the small γ increase compared to pure C_{12}E_5 at this concentration (Figure 5.2a).

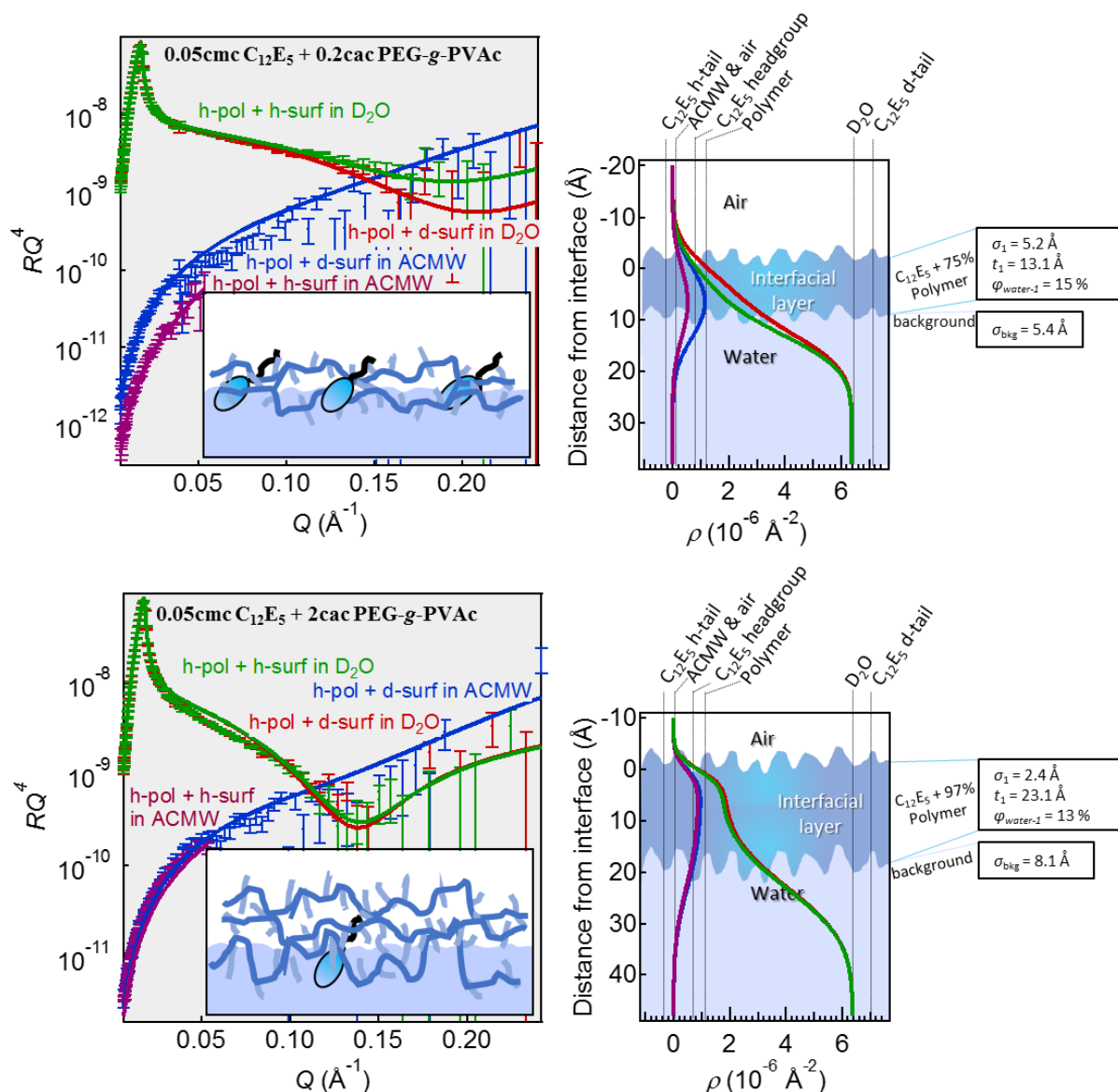


Figure 5.5 Fitted NR data to a 1-layer model for 0.05 cmc C₁₂E₅ with 0.2 and 2 cac PEG-g-PVAc, with the fitted ρ profiles and schematic representation based on the fitted parameters. The data is colour coded as follows: **red** represents mixtures of PEG-g-PVAc and dC₁₂E₅ in D₂O, **green** represents mixtures of PEG-g-PVAc with hC₁₂E₅ in D₂O, **blue** represents mixtures of PEG-g-PVAc with dC₁₂E₅ in ACMW, and **purple** represents mixtures of PEG-g-PVAc with hC₁₂E₅ in ACMW. The error bars associated with the data points were determined from the data reduction, larger at higher Q values due to lower contrast between the solvent and sample. The solid lines show the fitted curve, with the fitted parameters also shown, including thickness (t), solvent volume fraction (ϕ_{water}), and roughness of the layer (σ).

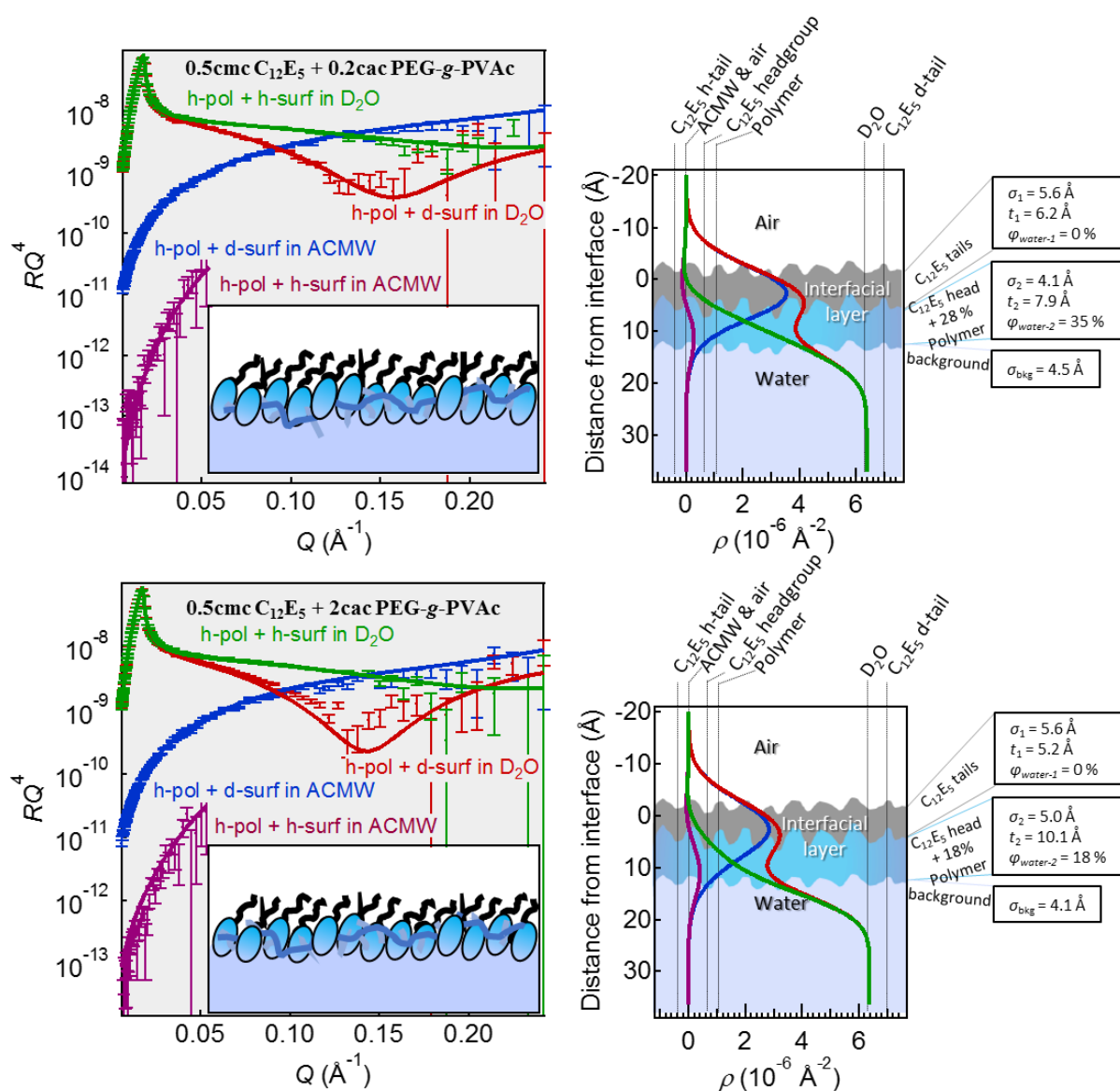


Figure 5.6 Fitted NR data to a 2-layer model for 0.5 cmc $C_{12}E_5$ with 0.2 and 2 cac PEG-g-PVAc, with the fitted ρ profiles and schematic representation based on the fitted parameters. The data is colour coded as follows: **red** represents mixtures of PEG-g-PVAc and $dC_{12}E_5$ in D_2O , **green** represents mixtures of PEG-g-PVAc with $hC_{12}E_5$ in D_2O , **blue** represents mixtures of PEG-g-PVAc with $dC_{12}E_5$ in ACMW, and **purple** represents mixtures of PEG-g-PVAc with $hC_{12}E_5$ in ACMW. The error bars associated with the data points were determined from the data reduction, larger at higher Q values due to lower contrast between the solvent and sample. The solid lines show the fitted curve, with the fitted parameters also shown, including thickness (t), solvent volume fraction (ϕ_{water}), and roughness of the layer (σ).

In the systems containing 5 cmc C₁₂E₅, the best model to fit the NR data depended on the PEG-*g*-PVAc concentration, where a 2-layer described above was used to fit the 5 cmc C₁₂E₅ + 0.2 cac PEG-*g*-PVAc and a 3-layer model was used to fit the 5 cmc C₁₂E₅ + 2 cac PEG-*g*-PVAc, accounting for separate layers for C₁₂E₅ hydrocarbon tails, headgroup, and the polymer (Figure 5.7).

In both cases, the thickness of the hydrocarbon tails ($t_1 \sim 8\text{-}9 \text{ \AA}$ in both cases) is similar to that of a pure C₁₂E₅ above its cmc (fitted $t_1 \sim 8 \text{ \AA}$), suggesting a complete C₁₂E₅ monolayer at the interface was formed. In mixture containing 0.2 cac PEG-*g*-PVAc, the $t_2 \sim 9 \text{ \AA}$ and $\phi_{\text{PEG-}g\text{-PVAc}} \sim 32\%$ does not correspond to the calculated Γ value, where $\Gamma_{\text{PEG-}g\text{-PVAc}} \sim 0.1 \text{ mg m}^{-2}$ and $\Gamma_{\text{C}_{12}\text{E}_5} \sim 4.0 \text{ \mu mol m}^{-2}$. In mixture containing 2 cac PEG-*g*-PVAc, $t_2 \sim 8 \text{ \AA}$ and $t_3 \sim 5 \text{ \AA}$, indicative of a C₁₂E₅ monolayer stretching above a layer of PEG-*g*-PVAc. The calculated Γ values ($\Gamma_{\text{PEG-}g\text{-PVAc}} < 0.01 \text{ mg m}^{-2}$ and $\Gamma_{\text{C}_{12}\text{E}_5} \sim 4.0 \text{ \mu mol m}^{-2}$) again did not mirror this behaviour. We therefore propose there is a relatively strong interactions between the polymer and C₁₂E₅ in the bulk, furthermore depleting the polymer from the top layer of the interface to form a much thicker polymer “hanging” layer underneath, compared to that of mixtures containing SDS at the same concentration, comparable in $t \sim 5 \text{ \AA}$ to the mixtures containing DTAB.

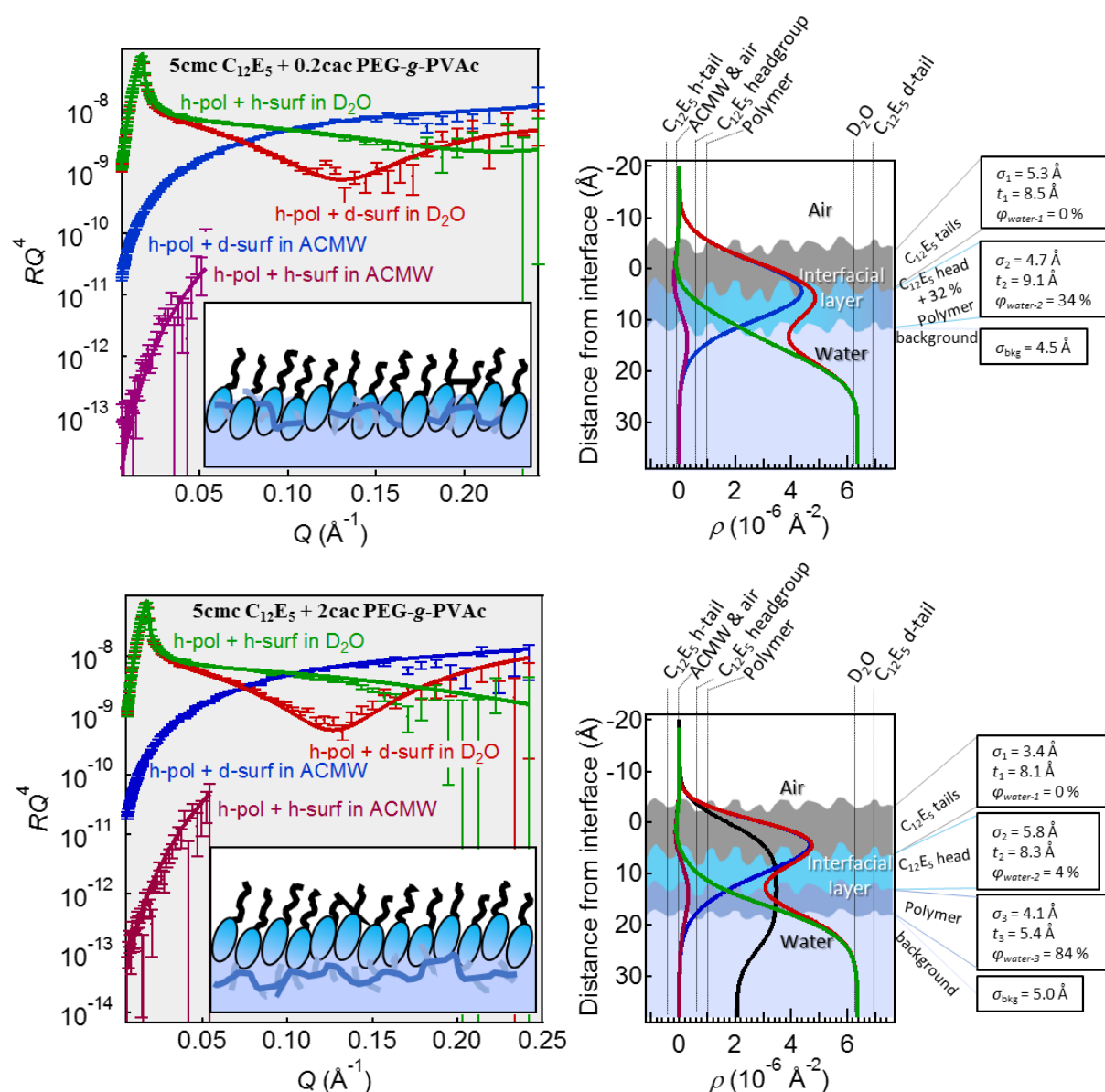


Figure 5.7 Fitted NR data to a 3-layer model for 5 cmc $C_{12}E_5$ with 0.2 and 2 cac PEG-g-PVAc, with the fitted ρ profiles and schematic representation based on the fitted parameters. The data is colour coded as follows: red represents mixtures of PEG-g-PVAc and $dC_{12}E_5$ in D_2O , green represents mixtures of PEG-g-PVAc with $hC_{12}E_5$ in D_2O , blue represents mixtures of PEG-g-PVAc with $dC_{12}E_5$ in ACMW, and purple represents mixtures of PEG-g-PVAc with $hC_{12}E_5$ in ACMW. The error bars associated with the data points were determined from the data reduction, larger at higher Q values due to lower contrast between the solvent and sample. The solid lines show the fitted curve, with the fitted parameters also shown, including thickness (t), solvent volume fraction (ϕ_{water}), and roughness of the layer (σ).

5.3.3 Foaming behaviour of the polymer/surfactant mixtures

The foam stability and foamability ($\tau_{FVS\ 50\%}$ and $V_{foam\ max}$) of PEG-*g*-PVAc/ $C_{12}E_5$ mixtures are presented in Table 5.2 and Figure 5.8. The foam stability ($\tau_{FVS\ 50\%}$) was somewhat increased by the presence of the polymer in mixtures containing 0.05 cmc $C_{12}E_5$ compared to the pure surfactant ($\tau_{FVS\ 50\%} \sim 13$ s for pure 0.05 cmc $C_{12}E_5$, $\tau_{FVS\ 50\%} \sim 16$ s and 20 s in the mixtures containing 0.2 cac and 2 cac PEG-*g*-PVAc, respectively). In the polymer/surfactant mixtures containing higher $C_{12}E_5$ concentration, the $\tau_{FVS\ 50\%}$ was actually lowered in the presence of the polymer ($\tau_{FVS\ 50\%} \sim 402$ s for pure 0.5 cmc $C_{12}E_5$, $\tau_{FVS\ 50\%} \sim 119$ s and 187 s in the mixtures containing 0.2 cac and 2 cac PEG-*g*-PVAc, respectively; and $\tau_{FVS\ 50\%} \sim 1121$ s for pure 5 cmc $C_{12}E_5$, $\tau_{FVS\ 50\%} \sim 836$ s and 780 s in the mixtures containing 0.2 cac and 2 cac PEG-*g*-PVAc, respectively) (Figure 5.8).

The foamability, or the maximum foam volume $V_{foam\ max}$, of 0.05 $C_{12}E_5$ + 2 cac PEG-*g*-PVAc was increased ($V_{foam\ max} \sim 39$ mL) compared to pure $C_{12}E_5$ ($V_{foam\ max} \sim 9$ mL) but was below that of pure 2 cac PEG-*g*-PVAc ($V_{foam\ max} \sim 48$ mL). The $V_{foam\ max}$ in the other polymer/surfactant mixtures was within the experimental errors compared to the relevant pure $C_{12}E_5$ foamability.

Table 5.2 The $V_{foam\ max}$, $\tau_{FVS\ 50\%}$ and $R_{avg\ initial}$ determined from foam measurements of PEG-*g*-PVAc mixtures with $C_{12}E_5$.

PEG- <i>g</i> -PVAc conc (cac)	$C_{12}E_5$ conc (cmc)	Foam Half-life Time, $\tau_{FVS\ 50\%}$ (s)	Volume, $V_{foam\ max}$ (mL)	Initial Radius, $R_{avg\ initial}$ (μ m)
0.2	-	10.4 ± 8.3	11.7 ± 4.0	14.0 ± 0.5
2	-	121.7 ± 46.0	48.4 ± 6.8	180.7 ± 30.0
-	0.05	13.5 ± 2.9	9.4 ± 1.8	13.3 ± 0.6
0.2	0.05	15.6 ± 1.4	10.9 ± 0.2	15.7 ± 2.1
2	0.05	20.0 ± 1.8	39.1 ± 2.3	56.3 ± 7.6
-	0.5	402.0 ± 115.3	61.1 ± 3.2	42.7 ± 10.8
0.2	0.5	119.1 ± 109.0	52.7 ± 5.0	27.3 ± 7.4
2	0.5	187.3 ± 94.5	60.1 ± 2.7	45.3 ± 15.7
-	5	1121.3 ± 301.1	72.1 ± 1.4	142.0 ± 20.2
0.2	5	836.4 ± 125.5	72.7 ± 0.7	190.7 ± 20.0
2	5	779.7 ± 28.0	72.8 ± 0	156.3 ± 20.8

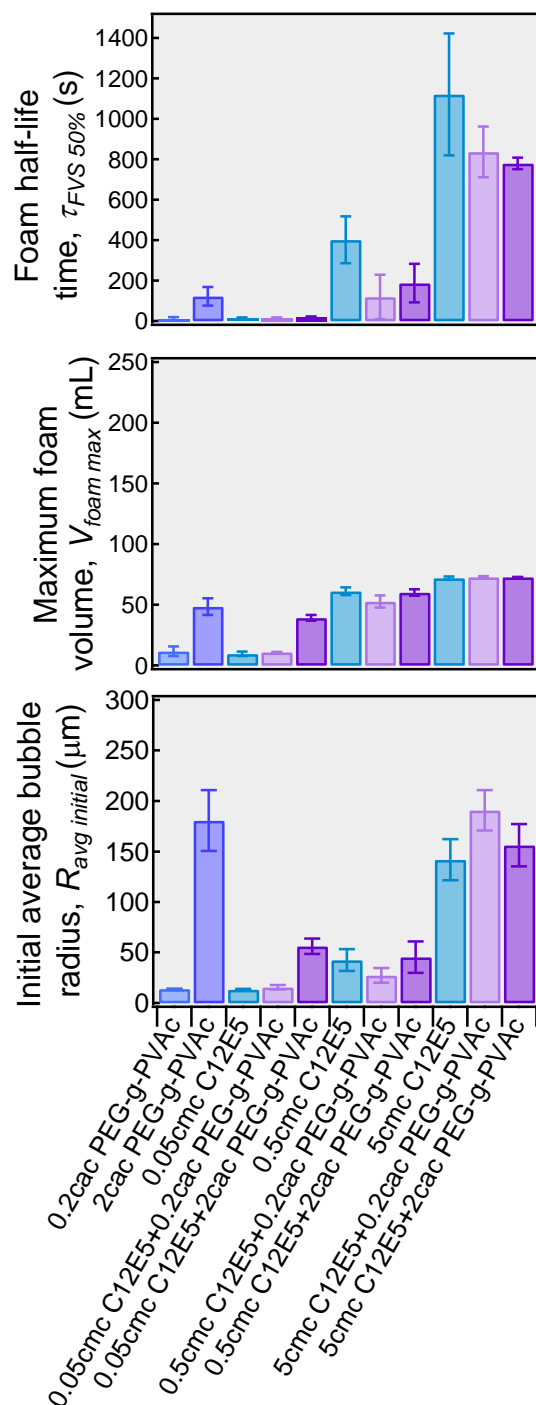


Figure 5.8 Foaming data showing the: a) foam half-life time ($\tau_{FVS\ 50\%}$) which is a measure of foam stability, b) maximum foam volume ($V_{foam\ max}$) which is a measure of foamability, and c) initial average bubble radius ($R_{avg\ initial}$) showing the radius of the foam bubbles during the foam generation. The data in pale blue represents the pure $C_{12}E_5$ solutions at 3 concentrations, the data in blue represents data for the pure polymer at 2 concentrations. The mixed polymer/surfactant systems are shown in pale and dark purple for $C_{12}E_5$ with 0.2 cac PEG-g-PVAc and $C_{12}E_5$ with 2 cac PEG-g-PVAc respectively.

The macroscopic foaming behaviour and bubble size distribution are shown in Figure 5.9. There was no major increase in foamability or foam stability observed in the polymer/surfactant mixtures containing $C_{12}E_5$. The bubble size was slightly larger in the systems containing PEG-g-PVAc, however there was a large bubble size distribution in all of the studied systems. From the NR data fitting, we did not observe any synergistic t increase of the interfacial layer relative to the pure $C_{12}E_5$ or PEG-g-PVAc, however there was an evidence of polymer layer associated with the surfactant at the interface. We did not observe any significant influence of this relatively thick polymer “hanging” layer on the foaming behaviour, similar to DTAB/polymer mixtures.

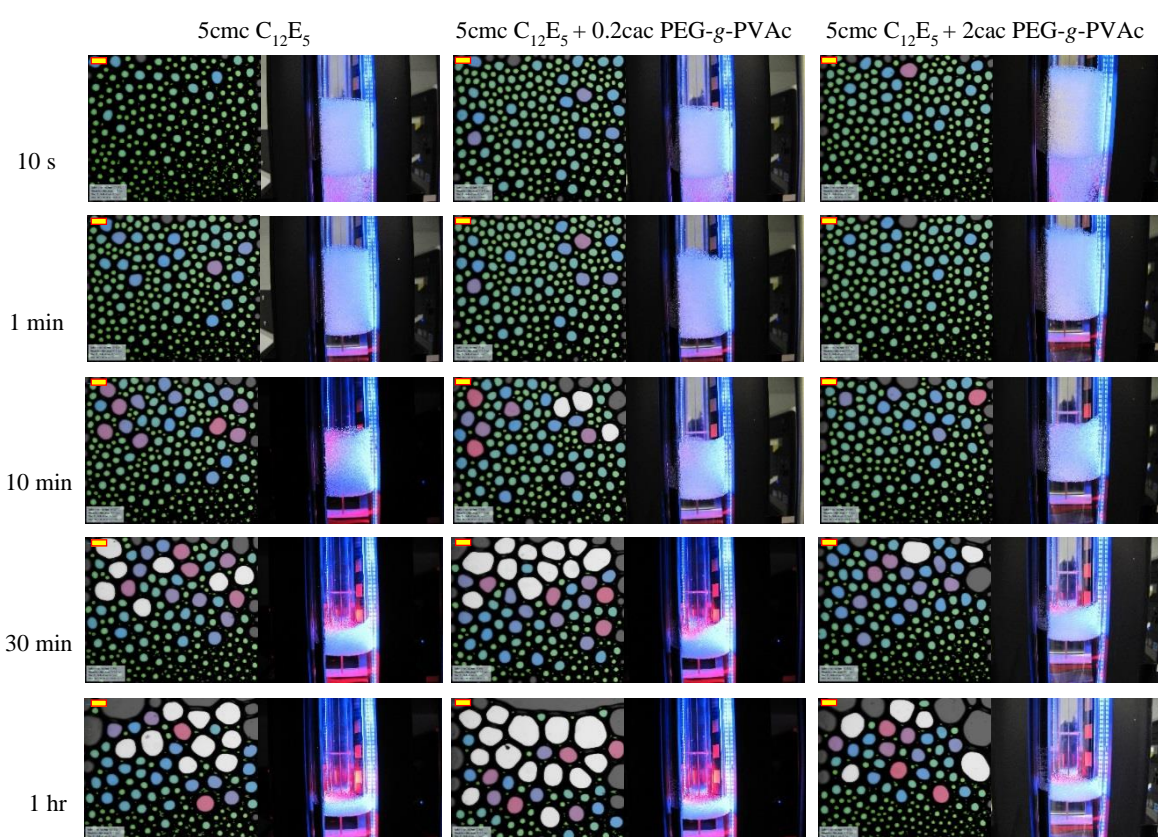


Figure 5.9 Macroscopic foaming behaviour data (overall foam volume) and foam bubble size recorded over given period after foam generation is shown, comparing the pure 5 cmc $C_{12}E_5$ system (left column) to the mixed systems containing 5 cmc $C_{12}E_5 + 0.2$ cac PEG-g-PVAc (middle column) and 5 cmc $C_{12}E_5 + 2$ cac PEG-g-PVAc (right column). The bubble size is colour coded as follows: green is for smallest bubble radius, followed by blue, purple, pink and the largest bubbles are shown in white.

5.4 Conclusions

The composition and structure PEG-*g*-PVAc/ C₁₂E₅ interfacial layer was determined from a combination of γ measurements and NR data fitting. The interfacial characterisation was then linked to the foam behaviour and compared to our previous study of the same polymer with anionic SDS and cationic DTAB, hence finalising a series of investigations into the effect of surfactant headgroup characteristics (*i.e.* charge and size).

The synergistic γ lowering at low surfactant concentrations was much less pronounced in PEG-*g*-PVAc/C₁₂E₅ mixtures compared to PEG-*g*-PVAc/DTAB and PEG-*g*-PVAc/SDS mixtures, with the transition from synergy to competition observed at much lower concentrations (~ 0.1 cmc C₁₂E₅, compared to ~ 0.5 cmc DTAB and SDS).

Based on the reflectivity data and Γ calculations, a clear competitive adsorption behaviour was observed in the PEG-*g*-PVAc/C₁₂E₅ mixtures, with the polymer depleted from the interface at higher C₁₂E₅ concentrations. The polymer then forms a layer underneath the C₁₂E₅, where the head groups of C₁₂E₅ can interact with the polymer PEG backbone. Compared to our data obtained for SDS/PEG-*g*-PVAc complex, the non-ionic C₁₂E₅ appears to be more effective at depleting the interface of the polymer, with the onset of this competitive adsorption observed at concentrations ~ 0.1 cmc C₁₂E₅, compared to $>\sim 0.5$ cmc SDS or DTAB required for polymer depletion from the interface. As mentioned previously, the cmc value of C₁₂E₅ is lower on the order of magnitude compared to SDS and DTAB, furthermore manifesting higher efficiency of pure C₁₂E₅. Additionally, the t of the “hanging” polymer layer in the PEG-*g*-PVAc/C₁₂E₅ mixture was very similar to that of PEG-*g*-PVAc/DTAB mixture at surfactant concentrations above their cmc. However, Γ of this polymer layer was determined as < 0.1 mg m⁻² in mixtures containing C₁₂E₅, compared to ~ 0.6 mg m⁻² in mixtures with DTAB, consistent with the strong competitive adsorption behaviour.

The foaming behaviour of PEG-*g*-PVAc/C₁₂E₅ remained largely unchanged from that of the pure systems. Some decrease in the foam stability at higher surfactant concentrations was observed, unlike in the mixed systems of PEG-*g*-PVAc/SDS where foam stability was increased in the presence of polymer, and no significant effect of the polymer presence on foam stability of the PEG-*g*-PVAc/DTAB mixtures. We previously postulated it may be the difference in the polymer layer t responsible for the different foaming behaviours in these polymer/surfactant interactions. This hypothesis remains valid, as both the C₁₂E₅ and SDS

headgroups interact with the PEG backbone of the surfactant, and therefore the main difference between the interfacial layer characteristics of the polymer/surfactant mixtures was the polymer layer thickness.

Overall, a direct influence of surfactant headgroup charge and size was observed on the interfacial layer composition and structure, as determined by γ measurements and NR data fitting, and foaming characteristics of the neutral PEG-g-PVAc/surfactant mixtures. These observations are relevant to the practical applications of the polymer, mainly in detergent product formulations.

5.5 References

1. Cuny, V., et al., *Structural properties and dynamics of C12E5 molecules adsorbed at water/air interfaces: A molecular dynamic study*. Colloids and Surfaces A: Physicochemical and Engineering Aspects, 2008. **323**(1): p. 180-191.
2. López-Esparza, R., et al., *Interaction between poly(ethylene glycol) and two surfactants investigated by diffusion coefficient measurements*. Journal of Colloid and Interface Science, 2006. **300**(1): p. 105-110.
3. Green, R.J., et al., *Competitive adsorption of lysozyme and C12E5 at the air/liquid interface*. Physical Chemistry Chemical Physics, 2000. **2**(22): p. 5222-5229.
4. Binks, B.P., et al., *Equilibrium and Dynamic Adsorption of C12E5 at the Air–Water Surface Investigated Using Ellipsometry and Tensiometry*. Langmuir, 2000. **16**(23): p. 8926-8931.
5. Feitosa, E., Brown, W., and Hansson, P., *Interactions between the Non-ionic Surfactant C12E5 and Poly(ethylene oxide) Studied Using Dynamic Light Scattering and Fluorescence Quenching*. Vol. 29. 1996. 2169-2178.
6. Jadidi, N., Adib, B., and Malihi, F.B., *Synergism and Performance Optimization in Liquid Detergents Containing Binary Mixtures of Anionic–Nonionic, and Anionic–Cationic Surfactants*. 2013. **16**(1): p. 115-121.
7. Meyer, M. and Sepúlveda, L., *Counterion association in mixed micelles of cationic and nonionic detergents*. Journal of Colloid and Interface Science, 1984. **99**(2): p. 536-542.
8. Broze, G. and Bastin, D., *Non-aqueous liquid laundry detergents containing three surfactants including a polycarboxylic acid ester of a non-ionic*. 1984.
9. Hewitt, G., *Detergent compositions*. 1972.
10. Langevin, D., *Polyelectrolyte and surfactant mixed solutions. Behavior at surfaces and in thin films*. Advances in Colloid and Interface Science, 2001. **89–90**: p. 467-484.

11. Asnacios, A., Langevin, D., and Argillier, J.-F., *Complexation of Cationic Surfactant and Anionic Polymer at the Air–Water Interface*. *Macromolecules*, 1996. **29**(23): p. 7412-7417.
12. Briddick, A., et al., *Surfactant and Plasticizer Segregation in Thin Poly(vinyl alcohol) Films*. *Langmuir*, 2016. **32**(3): p. 864-872.
13. Braun, L., et al., *Polymers and surfactants at fluid interfaces studied with specular neutron reflectometry*. *Advances in Colloid and Interface Science*, 2017. **247**: p. 130-148.
14. Campbell, R.A., *Recent advances in resolving kinetic and dynamic processes at the air/water interface using specular neutron reflectometry*. *Current Opinion in Colloid & Interface Science*, 2018. **37**: p. 49-60.
15. Skoda, M.W.A., *Recent developments in the application of X-ray and neutron reflectivity to soft-matter systems*. *Current Opinion in Colloid & Interface Science*, 2019. **42**: p. 41-54.
16. Kristen, N. and von Klitzing, R., *Effect of polyelectrolyte/surfactant combinations on the stability of foam films*. *Soft Matter*, 2010. **6**(5): p. 849-861.
17. Petkova, R., Tcholakova, S., and Denkov, N.D., *Foaming and Foam Stability for Mixed Polymer–Surfactant Solutions: Effects of Surfactant Type and Polymer Charge*. *Langmuir*, 2012. **28**(11): p. 4996-5009.
18. Campbell, R.A., Wacklin, H.P., and Sutton, I., *FIGARO: The new horizontal neutron reflectometer at the ILL*. *The European Physical Journal Plus*, 2011. **126**(107).
19. Gutfreund, P., et al., *Towards generalized data reduction on a chopper-based time-of-flight neutron reflectometer*. 2018. **51**(3).
20. Campbell, R.A., et al., *Polyelectrolyte/surfactant films spread from neutral aggregates*. *Soft Matter*, 2016. **12**(24): p. 5304-5312.
21. Li, Z.X., Dong, C.C., and Thomas, R.K., *Neutron Reflectivity Studies of the Surface Excess of Gemini Surfactants at the Air–Water Interface*. *Langmuir*, 1999. **15**(13): p. 4392-4396.
22. Nelson, A., *Co-refinement of multiple-contrast neutron/X-ray reflectivity data using MOTOFIT*. 2006. **39**(2): p. 273-276.
23. Weinheimer, R.M., Evans, D.F., and Cussler, E.L., *Diffusion in surfactant solutions*. *Journal of Colloid and Interface Science*, 1981. **80**(2): p. 357-368.
24. Tominaga, T. and Nishinaka, M., *Tracer diffusion of ionic micelles: effects of size and interactions*. *Journal of the Chemical Society, Faraday Transactions*, 1993. **89**(18): p. 3459-3464.
25. Sharifi, S. and Amirkhani, M., *Light Scattering Study of Mixture of Polyethylene Glycol with C 12 E 5 Microemulsion*. *Soft Nanoscience Letters*, 2011. **01**: p. 76-80.

6 Effect of polymer architecture on the interfacial structures and interactions between neutral amphiphilic comb co-polymers and surfactants at the air-water interface: XRR study

The interfacial adsorption behaviour and structure of complexes of three surfactants and two polymers were studied by the means of equilibrium surface tension measurements and XRR at the air-water interface. The three surfactants possessed the same hydrophobic tail and varied in the headgroup characteristics: anionic SDS, cationic DTAB and non-ionic C₁₂E₅. The two studied PEG-g-PVAc co-polymers both consisted of a PEG backbone and PVAc grafts but varied in the PEG backbone size, the average length of the PVAc grafts and the overall hydrophilic/hydrophobic ratio of the molecule. A clear effect of the polymer structure was observed in both the interfacial adsorption behaviour (demonstrated by γ data) and the interfacial structure and composition at the air-water interface (determined by XRR).

6.1 Introduction

6.1.1 Polymer/surfactant interactions

As described in previous chapters in more detail, the surfactants chosen are well studied both at the air-water interface and in bulk. Their interactions with various polymers have also been reported in literature [1-3] and introduced in previous chapters. Overall, we would expect interactions between DTAB and the PVAc grafts of the polymers *via* electrostatic attractive forces [4, 5], C₁₂E₅ headgroup interacting *via* hydrophobic interactions with the PEG backbone of the polymers [3, 6], and primarily hydrophobic interactions, with some electrostatic contribution, between SDS and the PEG backbone (SDS complexation with PEG, and PEG containing co-polymers, are one of the most well-studied polymer/surfactant systems known) [7-10]. In addition to the effect of surfactant headgroup characteristics, the effect of the polymer architecture [11, 12] (especially the hydrophilic/hydrophobic ratio and the graft length) on the polymer/surfactant interactions at the air-water interface is investigated in this

chapter. The polymer architecture role has been reported in many studies on, *e.g.* star [13, 14], comb [15-17], hyperbranched or dendritic [18-20] polymers, and flexible or globular proteins [21], among others. The two co-polymers studied here both belong to the family of comb co-polymers with hydrophilic PEG backbone and hydrophobic PVAc grafts (PEG-*g*-PVAc) and are referred to as Polymer A (whose interactions with SDS, DTAB and C₁₂E₅ were described in the previous chapters) and Polymer B in this chapter for clarity.

6.1.2 Polymer molecular structure (*i.e.* Polymer A vs Polymer B)

If Polymer A was described as a *tardigrade* with its ~ 8 relatively short grafts resembling the 8-legged water bear, Polymer B could be likened to the sea animal *scotoplane*, which is larger than a tardigrade and possesses ~ 10 legs (approximately same as the number of grafts in Polymer B).

6.1.2.1 Importance of the hydrophilic/hydrophobic ratio

The molecular weight of the hydrophobic PVAc grafts is approximately the same in the two polymers: specifically $M_{nPVAc} \sim 9$ kDa in Polymer A and $M_{nPVAc} \sim 8.5$ kDa in Polymer B. However, there is a difference in the Mn of the hydrophilic PEG backbone ($M_{nPEG} \sim 6$ kDa in Polymer A and $M_{nPEG} \sim 7.5$ kDa in Polymer B), which means the hydrophilic/hydrophobic ratios of the polymers, known as the hydrophilic-lipophilic balance (HLB) [22-24] are different. The ratio of the more hydrophilic PEG to the more hydrophobic PVAc grafts for the two polymers calculated from the average Mn is ~ 0.68 and 0.88 for Polymer A and Polymer B, respectively. The HLB determined using the Griffin's method (value between 0 for completely hydrophobic/lipophilic species and 20 signifying a completely hydrophilic species) [25] was calculated as ~ 8 for Polymer A and ~ 9.4 for Polymer B. The higher hydrophilicity of Polymer B is consistent with higher cac compared to the more hydrophobic Polymer A ($ca_{CPolymer B} \sim 0.002$ wt% and $ca_{CPolymer A} \sim 0.001$ wt%).

6.1.2.2 Grafts length and grafting density

Apart from the HLB difference, there is a difference in the PVAc graft length (~ 13 to 19 PVAc monomer units in Polymer A graft and ~ 9 to 16 PVAc monomer units in Polymer B graft) and the number of grafts (~ 6 to 9 PVAc grafts per backbone in Polymer A and ~ 8 to 10 PVAc grafts per backbone in Polymer B) between the two polymers. Even though the polymers

possess different number of grafts, the grafting density is relatively unchanged, due to the longer PEG backbone in Polymer B (graft every ~ 15 to 21 PEG units in Polymer A and every ~ 16 to 20 PEG units in Polymer B).

The different graft length and number of grafts, as well as the hydrophilic/hydrophobic ratio, will play an important part in polymer/surfactant interactions. Different patterns were formed following an interaction of surfactant and grafted polymer onto a surface with different grafting densities (forming a polymer brush), from lamellae *via* oblong and round pores to homogeneous brush with increasing grafting density [26]. The influence of the chain length and grafting density on the interfacial behaviour and interactions between polymers and surfactants or proteins has been widely reported in the case of polymer brushes. For example, the hydrolysis rate of PDMA (poly-*N,N*-dimethylacrylamide) brushes grafted on a solid substrate increased with higher grafting density and chain length [27]. Densely grafted PEO brushes onto a solid surface prevented adsorption of proteins (bovine serum albumin and human plasma proteins) to the surface; however, at the lower grafting density the protein adsorption was enhanced by increasing the length of the brush [28].

6.1.3 XRR and NR: A brief comparison

Comparisons between XRR and NR have been discussed before in some detail [29, 30]. XRR data collection is much faster, with only ~ 15 min per sample scan needed for our systems due to the higher photon flux provided by synchrotron facilities, compared to ~ 1 hr per sample needed for each contrast used in NR (so overall ~ 4 hours needed for one concentration mixture of a polymer/surfactant system). The XRR data is also collected over a larger Q range, allowing for observation of Kiessig fringes at higher Q values (up to $Q \sim 0.8 \text{ \AA}^{-1}$ in XRR compared to $Q \sim 0.25 \text{ \AA}^{-1}$ in NR data), therefore smaller thicknesses. The main disadvantage of XRR compared to NR however stems for the lack of isotopic contrast variations, as it is not possible to determine the surface excess, Γ , of the adsorbed species (therefore a direct measure of layer composition) [31] and the XRR data fitting can be less reliable especially if the ρ contrast between two species of interest is not sufficient (be that between the surfactant/polymer and the solvent, or between the surfactant and the polymer). The NR data can be co-fitted using the same model and fitting parameters in multiple isotopic contrasts for one specific system [32], as well as the ρ can be varied to provide enhanced contrast between different species of interest, such as polymer/surfactant mixtures. No such control of ρ is possible when dealing with XRR.

The two techniques are therefore deemed complementary to each other [33-35], as somewhat different information can be obtained from each technique [36, 37].

6.2 Methods

6.2.1 Materials

The two polymers, Polymer A ($M_n \sim 15$ kDa, PEG(6000)-g-PVAc(9000) with the corresponding segmental M_n indicated) and Polymer B ($M_n \sim 16$ kDa, PEG(7500)-g-PVAc(8500)), can both be described as PEG-g-PVAc co-polymers consisting of a PEG backbone and PVAc grafts. The average graft length and grafting density also differ slightly in the two polymers (Figure 6.1), with longer grafts on average in Polymer A (~ 13 to 19 PVAc monomer units) compared to Polymer B (~ 9 to 16 PVAc monomer units) and a similar grafting density: ~ 6 to 9 PVAc grafts per backbone which corresponds to a PVAc graft every ~ 16 -21 PEG monomer units in Polymer A; and ~ 8 to 10 PVAc grafts per backbone corresponding to a PVAc graft every ~ 16 -20 PEG monomer units in Polymer B. The polymers were freeze-dried and re-dissolved in water.

Sodium dodecyl sulfate (h-SDS, $C_{12}H_{25}SO_4$, Sigma-Aldrich) was recrystallised from ethanol. Dodecyltrimethylammonium bromide (DTAB, $C_{12}H_{25}N(CH_3)_3Br$, Sigma-Aldrich) was recrystallised from acetone:water (99:1 v:v). Dodecyl pentaethylene glycol ether ($C_{12}E_5$, $C_{12}H_{25}(C_2H_4O)_5OH$, Sigma-Aldrich) was used as received. The three surfactants used possess identical hydrocarbon tail ($C_{12}H_{25}$) but vary in the size and charge of the headgroup.

MilliQ water (Millipore, resistivity 18.2 $m\Omega$ cm, total organic content <5 ppb) was used for sample preparation and control measurements.

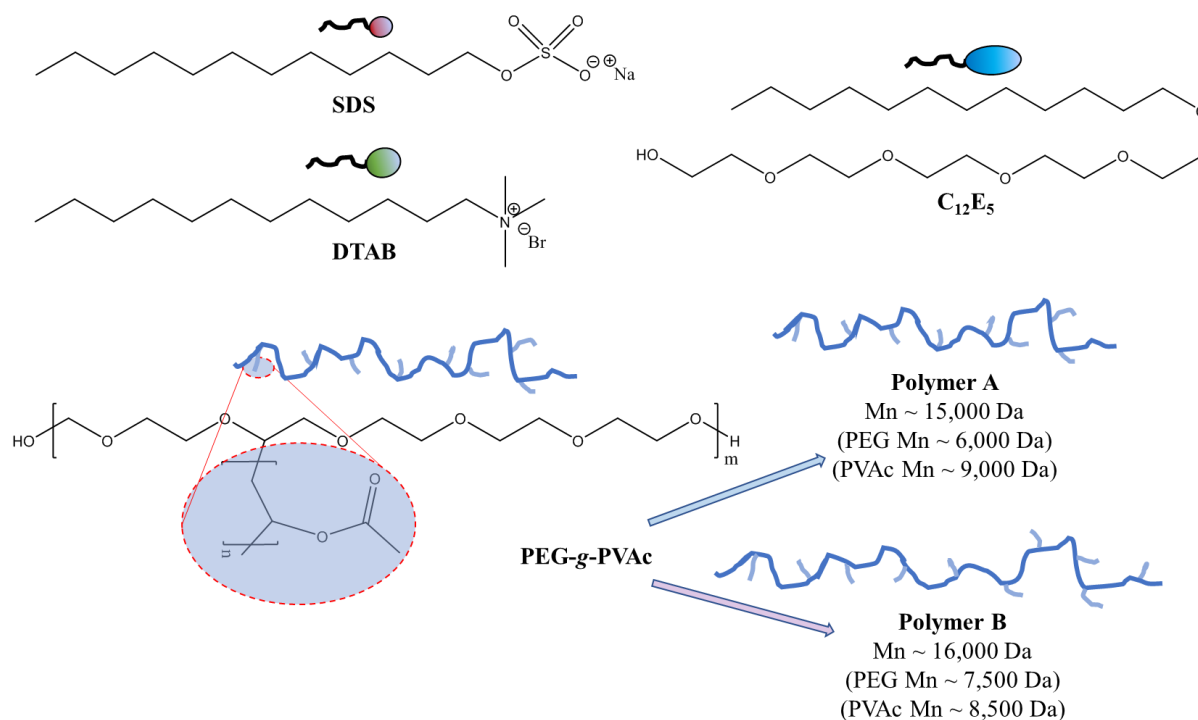


Figure 6.1 Molecular structures (with schematics) of SDS, DTAB, C₁₂E₅ and the two PEG-g-PVAc copolymers: Polymer A and Polymer B.

6.2.2 Surface tension

Equilibrium surface tension (γ) data was collected using the Wilhelmy plate method on a force tensiometer (K100, Krüss) at RT. The γ was measured over time to allow for interface equilibration. Each measurement was stopped automatically after the standard deviation of the last 5 points (recorded at 10 s intervals) was $< 0.01 \text{ mN m}^{-1}$. The platinum Wilhelmy plate was flamed before each measurement to ensure the Pt surface activation (therefore the contact angle between the plate and the liquid $\sim 0^\circ$). The surface tension data of Polymer B was collected in collaboration with a final year BSc student, Mr Dong Kuk Kim, and was presented in his thesis [38].

6.2.3 X-ray reflectivity (XRR)

The XRR measurements were performed at the I07 beamline (Diamond Light Source, UK) [39]. The data was collected using the double crystal deflector (DCD) which enables change of the incident angle, θ , without rotating the liquid sample, and the moving Pilatus 100k detector mounted on a diffractometer. This beamline set-up is optimal for data collection at liquid interfaces, including the air-water interface [40]. Briefly, the monochromatic X-ray beam with energy of 12.5 keV and size of 60 μm (vertical) x 200 μm (horizontal) hits the air-

water interface at varying θ , and the reflected beam intensity ($R(Q)$) is detected as a function of the momentum transfer perpendicular to the interface, $Q = \frac{4\pi\sin(\theta)}{\lambda}$. The data is then plotted as reflectivity profile, $RQ^4(Q)$ vs Q . to overcome the intrinsic decay $R(Q)$ vs Q^{-4} and hence highlight any mild fringes arising from the thin film at the interface.

The reflectivity measurements of the samples in adsorption Teflon troughs (~ 30 mL sample volume) were performed at RT enclosed in a chamber with a gentle flow of He to minimise background scattering and beam damage. The XRR data was normalised according to the critical edge and no background subtraction was included in the data processing. The layer thickness (t), roughness (σ) and volume fraction (ϕ) were determined from data fitting using the Motofit package in IGOR Pro [32], using the Abelès matrix formalism [41].

6.3 Results

6.3.1 Surface tension

The γ data of Polymer A was discussed in the previous chapters and the data is included here for comparison. The cac of Polymer A was determined to be ~ 0.001 wt%, compared to the more hydrophilic Polymer B cac ~ 0.002 wt%. The γ data is shown in Figure 6.2 vs the cmc of surfactants or cac of the polymer. The minimum γ_{lim} of Polymer A at 2 cac was ~ 44 mN m⁻¹ which was higher than that of Polymer B ($\gamma_{\text{lim}} \sim 42$ mN m⁻¹). The γ of polymers at 0.2 cac followed the same trend, with $\gamma \sim 55$ mNm⁻¹ in Polymer A compared to lower $\gamma \sim 52$ mNm⁻¹ in Polymer B.

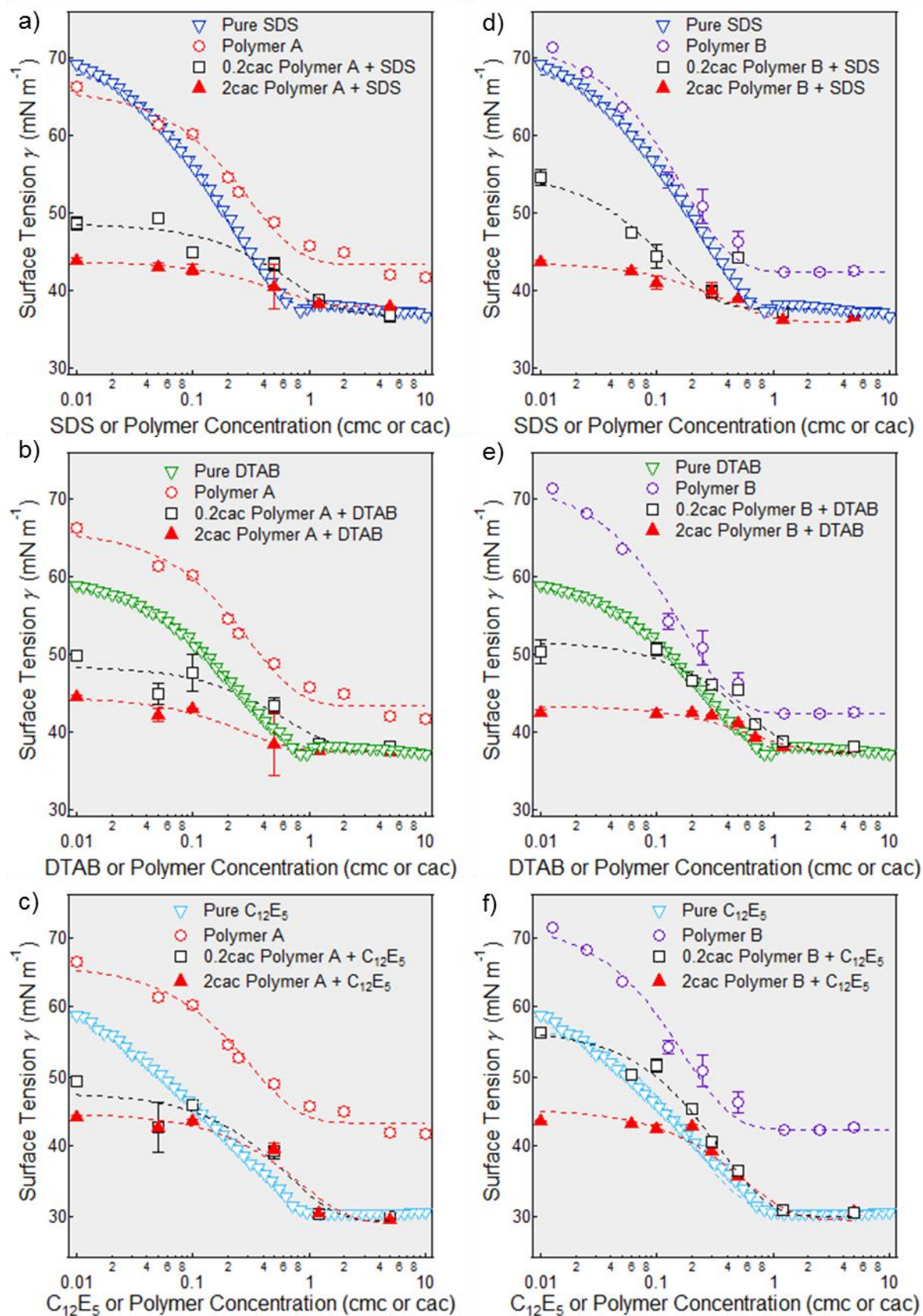


Figure 6.2 Equilibrium γ data of polymer/surfactant mixtures vs surfactant or polymer concentration (in their respective cmc and cac). The polymer/surfactant mixtures are as follows: a) SDS and Polymer A, b) DTAB and Polymer A, c) C_{12}E_5 and Polymer A, d) SDS and Polymer B, e) DTAB and Polymer B, and f) C_{12}E_5 and Polymer B. The error bars were determined experimentally as a standard deviation from 3 separate measurements.

6.3.1.1 SDS/polymer

There was a significant synergistic effect at low SDS concentrations (below its cmc) and 0.2 cac Polymer B (Figure 6.2d). The synergistic $\Delta\gamma \sim 3 \text{ mN m}^{-1}$ in mixture of 0.05 cmc SDS and 0.2 cac Polymer B ($\gamma \sim 62 \text{ mN m}^{-1}$ for 0.05 cmc SDS, $\gamma \sim 52 \text{ mN m}^{-1}$ for 0.2 cac Polymer B and $\gamma \sim 49 \text{ mN m}^{-1}$ for 0.05 cmc SDS and 0.2 cac Polymer B), $\Delta\gamma \sim 8 \text{ mN m}^{-1}$ in mixture of 0.1 cmc SDS and 0.2 cac Polymer B ($\gamma \sim 56 \text{ mN m}^{-1}$ for 0.1 cmc SDS, $\gamma \sim 52 \text{ mN m}^{-1}$ for 0.2 cac Polymer B and $\gamma \sim 44 \text{ mN m}^{-1}$ for 0.1 cmc SDS and 0.2 cac Polymer B). The $\gamma \sim 44 \text{ mN m}^{-1}$ of 0.5 cmc SDS and 0.2 cac Polymer B was above that of pure 0.5 cmc SDS ($\gamma \sim 40 \text{ mN m}^{-1}$) and below that of pure 0.2 cac Polymer B ($\gamma \sim 52 \text{ mN m}^{-1}$).

In the SDS mixtures with 2 cac Polymer B a small synergistic effect was observed at SDS concentrations between $\sim 0.1 \text{ cmc}$ ($\Delta\gamma \sim 1 \text{ mN m}^{-1}$; $\gamma \sim 56 \text{ mN m}^{-1}$ for 0.1 cmc SDS, $\gamma \sim 42 \text{ mN m}^{-1}$ for 2 cac Polymer B and $\gamma \sim 41 \text{ mN m}^{-1}$ for 0.1 cmc SDS and 2 cac Polymer B) and $\sim 0.5 \text{ cmc}$ of SDS ($\Delta\gamma \sim 1 \text{ mN m}^{-1}$; $\gamma \sim 40 \text{ mN m}^{-1}$ for 0.5 cmc SDS, $\gamma \sim 42 \text{ mN m}^{-1}$ for 2 cac Polymer B and $\gamma \sim 39 \text{ mN m}^{-1}$ for 0.5 cmc SDS and 2 cac Polymer B). At SDS concentrations above its cmc, we observed competitive adsorption at the interface with the γ data of the polymer/SDS mixtures following that of the pure surfactant ($\gamma \sim 36\text{-}37 \text{ mN m}^{-1}$ of the pure SDS and polymer/surfactant mixtures), suggesting depletion of the polymer from the interface.

The overall γ data of SDS/Polymer B (Figure 6.2d) is very similar to that of the SDS/Polymer A (Figure 6.2a), with a transition from synergistic to competitive adsorption observed at $\sim 0.5 \text{ cmc}$ SDS with the two polymers.

6.3.1.2 DTAB/polymer

No significant synergistic effect (within the experimental errors associated with the γ data) was observed in the mixtures of DTAB/Polymer B (Figure 6.2e) at neither of the polymer concentrations. The γ data of the mixtures mirror that of the pure Polymer B up to DTAB concentrations of $> 0.2 \text{ cmc}$ DTAB in the case of mixtures with 0.2 cac Polymer B ($\gamma \sim 52 \text{ mN m}^{-1}$) and DTAB concentrations $\sim 0.5 \text{ cmc}$ and above in mixtures with 2 cac Polymer B ($\gamma \sim 42 \text{ mN m}^{-1}$). At higher DTAB concentrations the γ data followed that of pure DTAB, indicating competitive adsorption between the polymer and DTAB with the polymer depleted from the interface.

This γ behaviour of DTAB/Polymer B (Figure 6.2e) differs to that of DTAB/Polymer A mixtures (Figure 6.2b), where a pronounced synergistic effect was observed, especially at DTAB concentrations below its cmc. The synergistic γ lowering (as reported in DTAB/anionic polymers before) arises due to polymer/surfactant complexation at the interface [42]. However, the γ data of DTAB/Polymer B mixtures suggested the depletion of DTAB molecules from the interface, with possible strong polymer/surfactant interactions in the bulk, hence γ data followed that of pure Polymer B at low DTAB concentrations.

6.3.1.3 $C_{12}E_5$ /polymer

No synergistic effect was observed in Polymer B/ $C_{12}E_5$ mixtures (Figure 6.2f). The γ data of the 0.2 cac Polymer B/ $C_{12}E_5$ mixtures mostly followed that of the pure surfactant at $C_{12}E_5$ concentrations below its cmc. In few cases (0.2 cac Polymer B and $C_{12}E_5$ concentrations between ~ 0.1 and 0.5 cmc), the γ was higher than that of pure $C_{12}E_5$ and either close to or slightly lower than that of pure polymer. This was most pronounced in the mixture of 0.1 cmc $C_{12}E_5$ and 0.2 cac Polymer B with $\gamma \sim 52 \text{ mN m}^{-1}$ which corresponded to that of pure 0.2 cac Polymer B, compared to $\gamma \sim 47 \text{ mN m}^{-1}$ of 0.1 cmc $C_{12}E_5$. Such γ behaviour implied some sort of polymer/surfactant complexation and interactions at the interface. The γ data of 2 cac Polymer B/ $C_{12}E_5$ mixtures was approximately that of the pure polymer ($\gamma \sim 42 \text{ mN m}^{-1}$) until the γ data matched that of the pure surfactant at concentrations > 0.2 cmc $C_{12}E_5$.

The γ behaviour of $C_{12}E_5$ /Polymer B (Figure 6.2f) is similar to that of $C_{12}E_5$ /Polymer A (Figure 6.2c), with pronounced competitive adsorption at surfactant concentrations > 0.2 cmc, with likely polymer depletion from the interface. The γ higher than the pure $C_{12}E_5$ in mixtures of 0.2 cac Polymer B and $C_{12}E_5$ at intermediate surfactant concentrations indicative of polymer/surfactant interactions was not observed in the mixtures of higher Polymer B concentrations or any Polymer A concentrations studied with $C_{12}E_5$.

6.3.2 Interfacial layer structure determined from XRR data fitting

The pure polymer data at 0.2 and 2 cac concentrations was fitted using a 1-layer model (Figure 6.3). The data of pure surfactants was fitted using a 1-layer model at low concentrations and a 2-layer model with increasing concentration. The top layer is assigned to the hydrocarbon tail, with the lower layer assigned to the surfactant headgroup with fitted ρ in the case of the charged surfactants allowing for counter-ion dissociation.

Three series of polymer/surfactant mixtures were then fitted using different models, as previously used for NR data fitting. The surfactant concentrations were 0.05, 0.5 and 5 cmc, polymer concentrations used were 0.2 and 2 cac. The polymer/surfactant mixtures containing 0.05 cmc of surfactant were all fitted using a 1-layer model. The mixtures containing 0.5 cmc surfactant were all fitted using a 2-layer model, in case of SDS and C₁₂E₅ the top layer was assigned to the surfactant and the layer underneath fitted as a polymer layer and in case of DTAB the top layer was assigned to the polymer with the layer underneath assigned to the surfactant. The mixtures containing 5 cmc surfactant, were fitted using a 3-layer model, with the top layer assigned to the surfactant hydrocarbon tails, the middle layer fitted as the surfactant headgroup with fitted ρ (to allow for counterion dissociation), with the bottom layer assigned to the polymer.

As it is not possible to determine Γ of adsorbing species, the only indication of the interfacial layer composition is from the fitted ρ of a mixed polymer/surfactant layer and ϕ determined from the ratios of the two adsorbing species.

6.3.2.1 Pure Polymers: XRR data fitting

There was a distinct difference in the XRR curve for the two PEG-*g*-PVAc co-polymers (Figure 6.3 and Table 6.1).

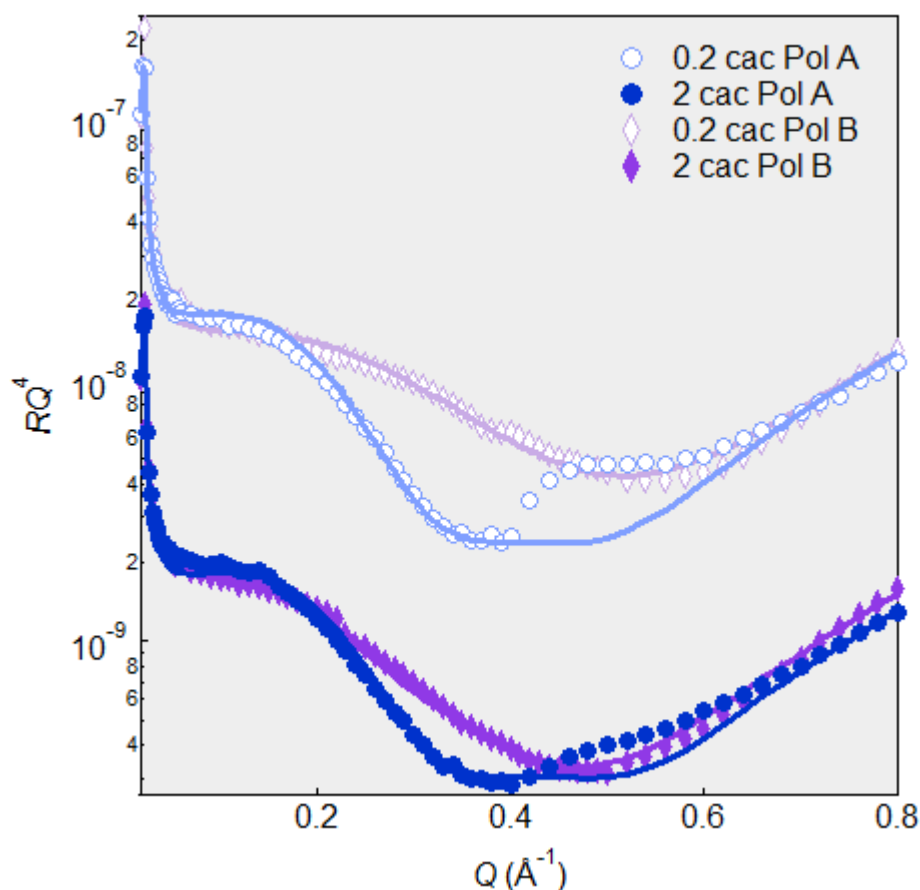


Figure 6.3 Fitted XRR data of pure PEG-g-PVAc polymers (Polymer A data shown in blue circles and Polymer B shown in purple diamonds) at two concentrations: 0.2 and 2 cac (empty and filled markers, respectively).

Table 6.1 XRR fitting parameters: thickness (t), scattering length density (σ), solvent volume fraction (φ_{water}) and roughness of the layer (σ) of the two PEG-g-PVAc polymers (Polymer A and Polymer B) determined from a 1-layer fit of XRR data.

	PEG-g-PVAc conc (cac)	Layer 1				Bkg σ_{bkg} (Å)
		t_1 (Å)	ρ_1 (10^{-6} Å^{-2})	$\varphi_{\text{water-1}}$ (%)	σ_1 (Å)	
Polymer A	0.2	20.1	10.678	6	4.0	2.9
	2	19.5	10.678	0	3.7	2.7
Polymer B	0.2	10.4	10.655	16	2.8	5.2
	2	19.3	10.655	1	3.4	6.0

The thickness of Polymer B increased with increasing polymer concentration, from $t \sim 10.4 \text{ Å}$ at 0.2 cac Polymer B to $t \sim 19.3 \text{ Å}$ at 2 cac Polymer B, with decreasing $\varphi_{\text{water}} \sim 16\%$ to 1% respectively. Such a clear increase in the interfacial layer t was not observed from the XRR fitting of Polymer A, with $t \sim 20.1 \text{ Å}$ at 0.2 cac Polymer A and $t \sim 19.5 \text{ Å}$ at 2 cac Polymer A, with smaller φ_{water} compared to Polymer B, at $\sim 6\%$ decreasing to $\sim 0\%$ respectively with increasing Polymer A concentration.

The XRR data fitting of the Polymer A interfacial layer did not mimic the fitted parameters determined from NR data fitting, especially at the lower polymer concentration ($t \sim 10.4 \text{ \AA}$ at 0.2 cac Polymer A and $t \sim 26.1 \text{ \AA}$ at 2 cac Polymer A, described in previous chapters). The discrepancy between the NR and XRR data fitting arises from the intrinsic difference between the two techniques. In NR, the neutron beam interacts with the nuclei of atoms whereas in XRR the X-ray beam interacts with the electron cloud of the atom. As the electron cloud is more dispersed than the atomic nucleus, the size of the studied material that the beam ‘sees’ will be different [30]. The XRR ρ is additionally more influenced by the presence or absence of any charged species (compared to the neutron ρ), such as surfactant counterions, in the material. Therefore, an additional fitting parameter determined from the XRR fitting of charged surfactant layers is the counterion association/dissociation with the surfactant headgroup, $\phi_{\text{counterion}}$. This will become relevant in the next section, when dealing with charged surfactants and their mixtures with the neutral polymers.

6.3.2.2 SDS and SDS/polymer mixtures

6.3.2.2.1 Pure SDS: XRR data fitting

A 1-layer model fitted the data of pure SDS well up to and including 0.5 cmc SDS, with the fitted data shown in Figure 6.4 and Table 6.2, with increasing t from ~ 12 to 17 \AA . Increasing the concentration of SDS to above its cmc (1.2 and 5 cmc) required use of a 2-layer fitting model, with $t_1 \sim 10 \text{ \AA}$ (hydrocarbon tail) and $t_2 \sim 6$ and 5 \AA (headgroup), respectively, with counterion $\phi_{\text{counterion}} \sim 50$ and 71% associated with the headgroup.

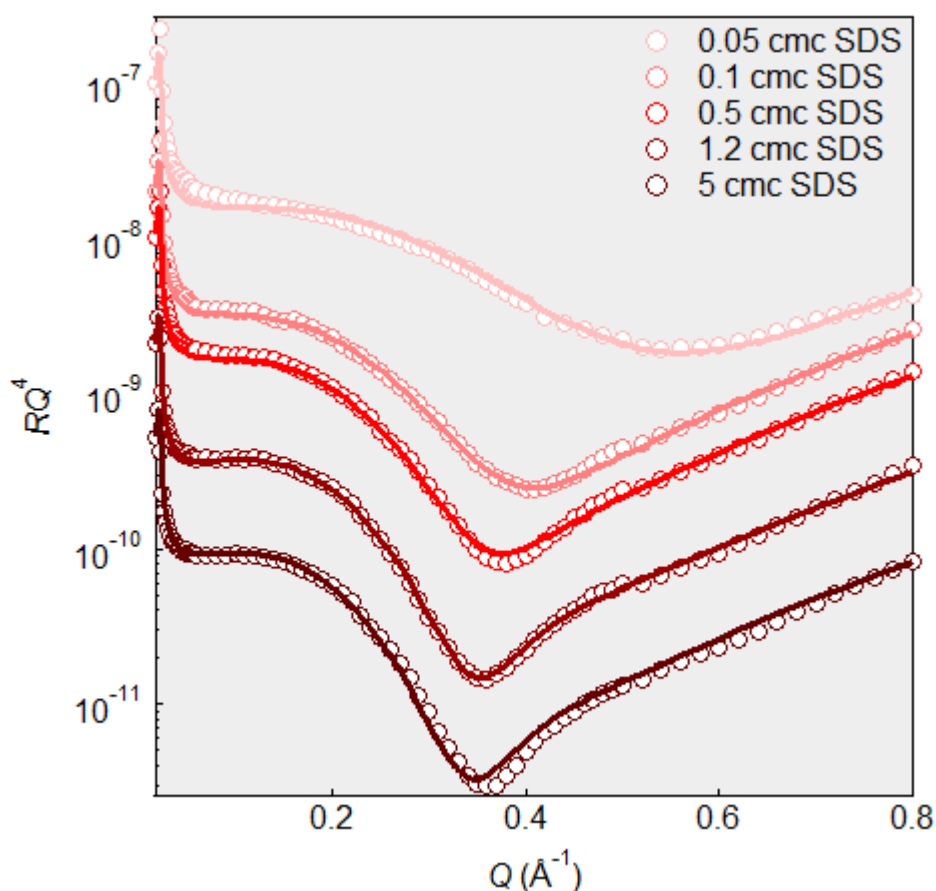


Figure 6.4 Fitted XRR data of pure SDS. Concentrations 0.05 cmc to 0.5 cmc SDS were fitted to a 1-layer model, with the concentrations 1.2 and 5 cmc SDS were fitted to a 2-layer model.

Table 6.2 XRR fitting parameters: thickness (t), scattering length density (σ), solvent volume fraction (φ_{water}) and roughness of the layer (σ) of pure DTAB determined from a 1-layer (at 0.05 cmc DTAB) and a 2-layer model (at concentrations 0.1 to 5 cmc) fit of XRR data. The superscripts for the fitted ρ values in the table correspond to the following headgroup/counterion associations: ¹ 50% counterion, ² 71% counterion associated with the surfactant headgroup. 100% counterion association is assumed when not stated otherwise.

SDS conc (cmc)	Layer 1				Layer 2				Bkg σ_{bkg} (\AA)
	t_1 (\AA)	ρ_1 (10^{-6}\AA^{-2})	$\varphi_{\text{water-1}}$ (%)	σ_1 (\AA)	t_2 (\AA)	ρ_2 (10^{-6}\AA^{-2})	$\varphi_{\text{water-2}}$ (%)	σ_2 (\AA)	
0.05	11.9	10.94	19	3.1	-	-	-	-	4.0
0.1	14.9	10.94	1	4.5	-	-	-	-	3.9
0.5	16.9	10.94	0	4.8	-	-	-	-	3.0
1.2	9.5	7.773	0	4.1	5.7	29.722 ¹	74	4.0	4.6
5	10.3	7.773	0	4.2	5.2	31.01 ²	71	4.9	4.7

6.3.2.2.2 SDS/polymer mixtures: XRR data fitting using a 1-layer model

The SDS/polymer mixtures were initially fitted using a single layer model (Figure 6.5, Table 6.3).

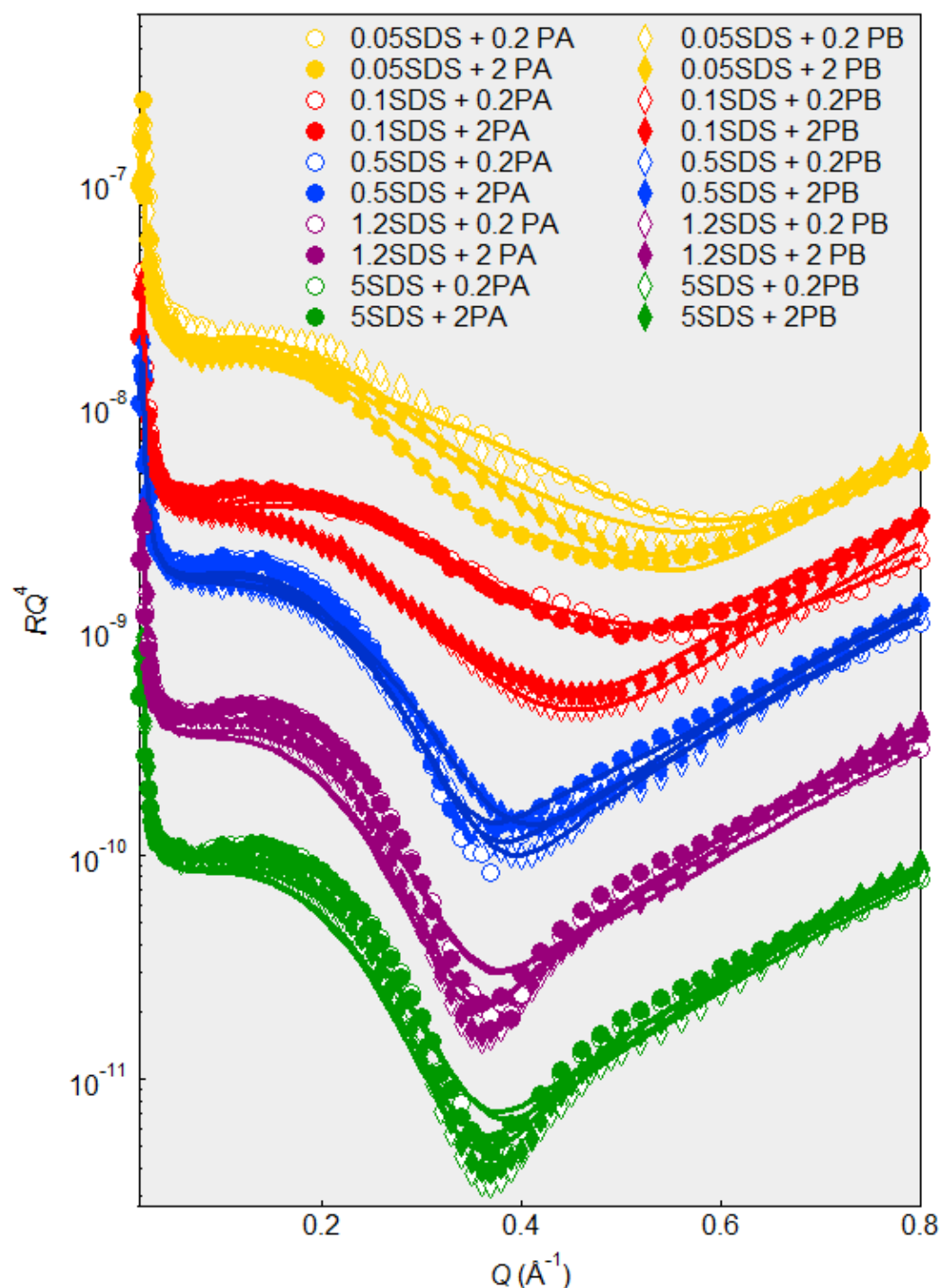


Figure 6.5 Fitted XRR data of SDS/polymer mixtures using a 1-layer model. The data is offset for clarity, with increasing SDS concentration. The mixtures of SDS/Polymer A are shown in circles and mixtures of SDS/Polymer B are shown in diamonds. In both cases, the lower polymer concentration (0.2 cac) is represented by empty markers, and 2 cac polymer concentration represented by filled markers.

Table 6.3 The fitting parameters: thickness (t), scattering length density (σ), solvent volume fraction (φ_{water}) and roughness of the layer (σ) of 1-layer model for mixtures of SDS/Polymers A and SDS/Polymer B. The superscripts for the fitted ρ values in the table correspond to the following polymer/surfactant volume fractions: ¹ 8% Polymer A + 92% SDS, ² 1% Polymer A + 99% SDS, ³ 1% Polymer A + 99% SDS, ⁴ 2% Polymer A + 98% SDS, ⁵ 0.5% Polymer A + 99.5% SDS, ⁶ 82% Polymer A + 18% SDS, ⁷ 0.5% Polymer A + 99.5% SDS, ⁸ 0.5% Polymer A + 99.5% SDS, ⁹ 1% Polymer A + 99% SDS, ¹⁰ 0% Polymer A + 100% SDS, and ¹¹ 9% Polymer B + 91% SDS, ¹² 12% Polymer B + 88% SDS, ¹³ 2% Polymer B + 98% SDS, ¹⁴ 0% Polymer B + 100% SDS, ¹⁵ 0.5% Polymer B + 99.5% SDS, ¹⁶ 13% Polymer B + 87% SDS, ¹⁷ 55% Polymer B + 45% SDS, ¹⁸ 1% Polymer B + 99% SDS, ¹⁹ 3% Polymer B + 97% SDS, ²⁰ 0.5% Polymer B + 99.5% SDS.

	PEG-g-PVAc	SDS	Layer 1				Bkg
			t_1 (Å)	ρ_1 (10^{-6} \AA^{-2})	$\varphi_{\text{water-1}}$ (%)	σ_1 (Å)	
Polymer A	conc (cac)	conc (cmc)					
	0.2	0.05	20.0	10.918 ¹	2	2.7	6.5
	0.2	0.1	14.6	10.937 ²	0	2.5	4.4
	0.2	0.5	17.3	10.936 ³	1	4.4	2.5
	0.2	1.2	17.5	10.94 ⁴	1	4.2	2.5
	0.2	5	16.7	10.939 ⁵	0	4.4	2.5
	2	0.05	18.4	10.726 ⁶	5	3.5	3.4
	2	0.1	12.4	10.939 ⁷	1	2.7	3.2
	2	0.5	18.0	10.939 ⁸	0	4.3	2.5
	2	1.2	17.3	10.936 ⁹	0	4.3	2.5
2	5	17.0	10.94 ¹⁰	0	4.4	2.5	
Polymer B	0.2	0.05	16.6	10.914 ¹¹	1	3.0	4.4
	0.2	0.1	14.0	10.905 ¹²	6	3.8	5.9
	0.2	0.5	15.8	10.934 ¹³	3	4.6	3.0
	0.2	1.2	17.3	10.94 ¹⁴	1	5.0	2.5
	0.2	5	17.1	10.939 ¹⁵	0	4.9	2.5
	2	0.05	16.3	10.902 ¹⁶	0	3.3	6.2
	2	0.1	16.0	10.783 ¹⁷	4	3.7	5.9
	2	0.5	15.1	10.937 ¹⁸	0	4.4	3.6
	2	1.2	16.9	10.93 ¹⁹	0	4.9	2.5
	2	5	17.1	10.939 ²⁰	0	4.8	2.5

Although similar in t , there was a minute overall decrease in the layer t in polymer/SDS mixtures with Polymer A ($t \sim 20$ and 18 \AA in 0.05 cmc SDS and 0.2 cac Polymer A and 2 cac Polymer A respectively, decreased to $t \sim 17 \text{ \AA}$ in 5 cmc SDS and both Polymer A concentrations) and a minute increase in the t of the layer in Polymer B/SDS mixtures ($t \sim 16 \text{ \AA}$ in 0.05 cmc SDS and Polymer B at both concentrations, increased to $t \sim 17 \text{ \AA}$ in 5 cmc SDS and both Polymer B concentrations). Compared to mixtures with other surfactants, there was a marked decrease of φ_{polymer} with increasing SDS concentration in mixtures containing both polymers. The $\varphi_{\text{polymer}} \sim 8\%$ in mixtures of 0.05 cmc SDS with both polymers at 0.2 cac, which decreased to $\varphi_{\text{polymer}} < 1\%$ in mixtures of 5 cmc SDS with the two polymers. There was however

a substantial difference in the φ_{polymer} in SDS/polymer mixtures containing higher concentration of the two polymers (2 cac). At 0.05 cmc SDS and 2 cac Polymer A, $\varphi_{\text{polymer}} \sim 82\%$ but decreased rapidly to $\sim 1\%$ in the mixture containing 0.1 cmc SDS and 2 cac Polymer A. Contrasting, the φ_{polymer} increased from $\sim 13\%$ to $\sim 55\%$ in the mixtures containing 2 cac Polymer B and 0.05 cmc SDS and 0.1 cmc SDS, respectively. Only after this initial increase, the φ_{polymer} decreased rapidly to $\sim 1\%$ in 0.5 cmc SDS and 2 cac Polymer B.

6.3.2.2.3 SDS/polymer mixtures: XRR data fitting using a multi-layer model

Three concentrations of SDS and the two polymers at 0.2 and 2 cac were then fitted using a multilayer model, where applicable, and the results are described below (Figure 6.6, Table 6.4).

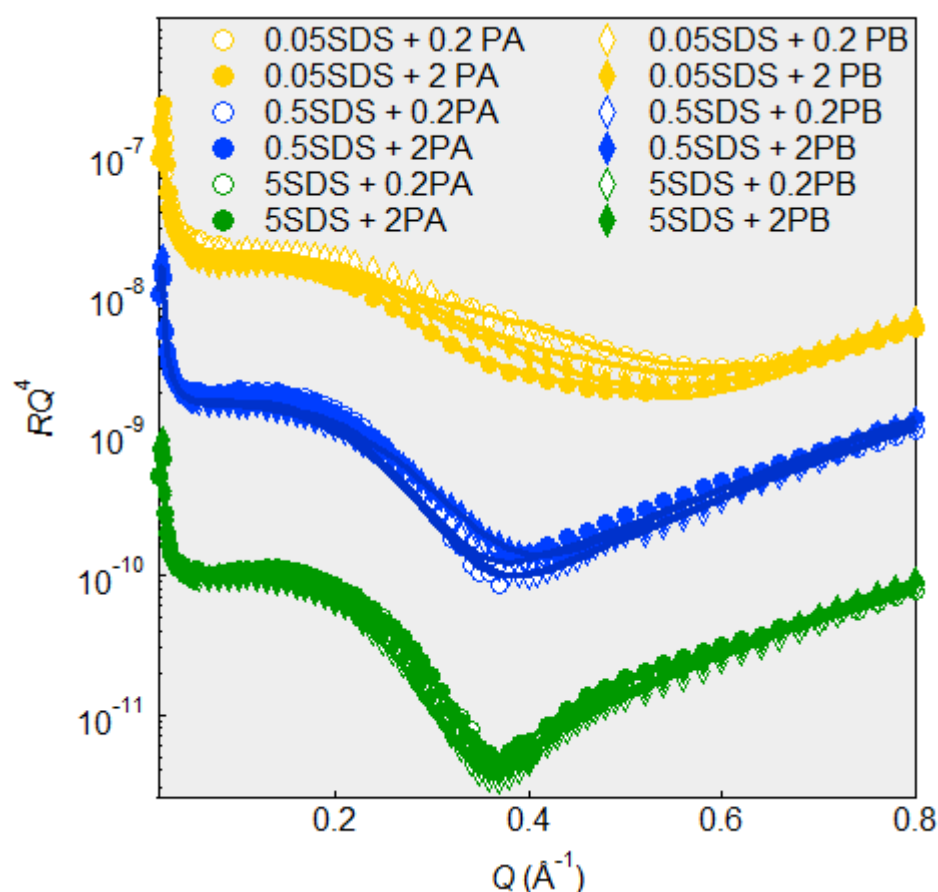


Figure 6.6 Fitted XRR data of SDS/polymer mixtures using a 1-layer model for SDS/polymer mixtures containing: 0.05 cmc SDS (yellow), 2-layer model for 0.5 cmc SDS (blue) and 5 cmc SDS concentration (green). The data is offset for clarity, with increasing SDS concentration. The mixtures of SDS/Polymer A are shown in circles and mixtures of SDS/Polymer B are shown in diamonds. In both cases, the lower polymer concentration (0.2 cac) is represented by empty markers, and 2 cac polymer concentration represented by filled markers.

Table 6.4 The fitting parameters: thickness (t), scattering length density (σ), solvent volume fraction (ϕ_{water}) and roughness of the layer (σ) for the optimised multilayer models for mixtures of PEG-g-PVAc co-polymers (Polymer A and Polymer B) and SDS, as well as the pure systems. The superscripts for the fitted scattering length density (SLD) ρ values in the table correspond to the following polymer/surfactant volume fractions: ¹ 8% Polymer A + 92% SDS, ² 44% counterion associated with SDS headgroup, ³ 82% Polymer A + 18% SDS, ⁴ 90.4% counterion associated with SDS headgroup, and ⁵ 9% Polymer B + 91% SDS, ⁶ 77% counterion associated with SDS headgroup, ⁷ 13% Polymer B + 87% SDS, ⁸ 28% counterion associated with SDS headgroup.

	PEG-g-PVAc SDS		Layer 1				Layer 2				Layer 3				Bkg σ_{bkg} (\AA)
	conc (cac)	conc (cmc)	t_1 (\AA)	ρ_1 (10^{-6}\AA^{-2})	$\phi_{\text{water-1}}$ (%)	σ_1 (\AA)	t_2 (\AA)	ρ_2 (10^{-6}\AA^{-2})	$\phi_{\text{water-2}}$ (%)	σ_2 (\AA)	t_3 (\AA)	ρ_3 (10^{-6}\AA^{-2})	$\phi_{\text{water-3}}$ (%)	σ_3 (\AA)	
Polymer A	0.2	0.05	20.0	10.918 ¹	2	2.7	-	-	-	-	-	-	-	-	6.5
	0.2	0.5	13.2	10.94	0	4.7	5.0	10.678	12	2.7	-	-	-	-	2.7
	0.2	5	9.2	7.773	0	3.3	5.9	29.374 ²	74	3.9	6.7	10.678	32	2.6	2.6
	2	0.05	18.4	10.726 ³	5	3.5	-	-	-	-	-	-	-	-	3.4
	2	0.5	13.9	10.94	0	4.5	4.4	10.678	8	3.0	-	-	-	-	2.7
	2	5	9.7	7.773	0	3.0	4.4	32.216 ⁴	69	4.5	4.9	10.678	32	4.1	3.2
	0.2	-	20.1	10.678	6	4.0	-	-	-	-	-	-	-	-	2.9
	2	-	19.5	10.678	0	3.7	-	-	-	-	-	-	-	-	2.7
Polymer B	0.2	0.05	16.6	10.914 ⁵	1	3.0	-	-	-	-	-	-	-	-	4.4
	0.2	0.5	14.3	10.94	0	4.8	3.7	10.655	48	3.8	-	-	-	-	2.8
	0.2	5	9.7	7.773	0	4.1	3.6	31.36 ⁶	55	4.8	2.3	10.655	84	5.4	5.6
	2	0.05	16.3	10.902 ⁷	0	3.3	-	-	-	-	-	-	-	-	6.2
	2	0.5	14.9	10.94	1	4.3	5.7	10.655	84	3.2	-	-	-	-	3.9
	2	5	7.9	7.773	0	4.0	8.2	28.405 ⁸	80	4.2	2.2	10.655	17	4.7	5.9
	0.2	-	10.4	10.655	16	2.8	-	-	-	-	-	-	-	-	5.2
	2	-	19.3	10.655	1	3.4	-	-	-	-	-	-	-	-	6.0
SDS	-	0.05	11.9	10.94	19	3.1	-	-	-	-	-	-	-	-	4.0
	-	0.5	16.9	10.94	0	4.8	-	-	-	-	-	-	-	-	3.0
	-	5	10.3	7.773	0	4.2	5.2	31.01	71	4.9	-	-	-	-	4.7

In mixtures of 0.05 cmc SDS with Polymer A, $t \sim 20$ and 18\AA in mixtures containing 0.2 and 2 cac, respectively, which is very similar to the thickness of the pure polymer layer ($t \sim 20$ and 19\AA , respectively). The ϕ_{polymer} calculated from the fitted ρ of the layer showed $\phi_{\text{polymer}} \sim 8\%$ in mixtures containing 0.05 cmc SDS and 0.2 cac Polymer A and $\phi_{\text{polymer}} \sim 82\%$ in mixtures containing 0.05 cmc SDS and 2 cac Polymer A. Therefore, the thickness of the mixtures of 0.2 cac Polymer A and 0.05 cmc SDS, compared to $t \sim 12 \text{\AA}$ of pure 0.05 cmc SDS layer, indicates synergistic adsorption of SDS and Polymer A in this mixture. The similar t of 0.05 cmc SDS and 2 cac Polymer A to that of pure polymer ($t \sim 18 \text{\AA}$ and 19\AA , respectively), together with $\phi_{\text{polymer}} \sim 82\%$ suggests smaller synergistic effect with the polymer being the major species adsorbed at the interfacial layer. Compared to the mixtures of 0.05 cmc SDS and Polymer B, the layer $t \sim 17$ and 16\AA with $\phi_{\text{polymer}} \sim 9$ and 13% in systems with 0.2 cac and 2 cac Polymer B indicate a clear synergistic adsorption of the mixtures at this SDS concentration.

In the mixtures of Polymer A and 0.5 cmc SDS, the data was best fitted using a 2-layer model, with the t_1 of SDS ~ 13 and 14 \AA (compared to pure SDS $t \sim 17 \text{ \AA}$ at 0.5 cmc) and t_2 of the polymer layer ~ 5 and 4 \AA and $\phi_{\text{water-2}} \sim 12$ and 8% in the mixtures containing 0.5 cmc SDS and 0.2 cac and 2 cac Polymer A, respectively. In the mixtures of 0.2 and 2cac Polymer B and 0.5 cmc SDS, the top layer assigned to the surfactant was fitted with similar $t_1 \sim 14$ and 15 \AA as in the case of Polymer A, however the t_2 of the polymer layer was fitted as ~ 4 and 6 \AA with much higher $\phi_{\text{water-2}} \sim 48$ and 84% compared to the mixtures containing Polymer A. Therefore, overall there is less polymer associated with the interface in the case of Polymer B compared to Polymer A.

The same behaviour with less polymer associated with the interfacial layer in the mixtures of Polymer B than Polymer A is also evident in mixtures containing 5 cmc SDS, where a polymer layer with $t_3 \sim 2 \text{ \AA}$ ($\phi_{\text{water-3}} \sim 84$ and 17%) in the mixtures of Polymer B compared to $t_3 \sim 7$ and 5 \AA ($\phi_{\text{water-3}} \sim 32\%$) in the mixtures of Polymer A.

SDS interacts with the PEG backbone *via* hydrophobic interactions and electrostatic interactions arising from positive charge formation followed partial protonation of the PEG ether oxygens [43]. It was shown before that increasing the grafting density of PEG side chains on a methacrylate backbone led to significant SDS binding suppression [44]. Admittedly, bottle-brush co-polymers have vastly higher grafting density compared to the comb co-polymers studied here, with PEG forming the backbone rather than side chains of Polymers A and B. Still, the minutely smaller grafting density of Polymer A (better described as smaller number of grafts in the overall structure) would lead to SDS adsorption to the PEG backbone with less steric hindrance, and hence more facile formation of polymer/surfactant complexes. It was also reported that the cac of SDS/PEG decreased with increasing PEG MW in the range of between 1000 and 8000 Da, together with decreasing surfactant aggregation number [45]. This observation partially contradicts the behaviour observed with the comb co-polymers, which can be attributed to the fact the co-polymers are non-linear and contain PVAc side chains. However, the lower surfactant aggregation number of SDS associated with PEG of higher MW (*i.e.* Polymer B) could account for the lower complexation at the interface observed in the system.

6.3.2.3 DTAB and DTAB/polymer mixtures

6.3.2.3.1 Pure DTAB: XRR data fitting

The data of pure DTAB at the air-water interface (Figure 6.7, Table 6.5) was fitted using a 1-layer model ($t \sim 13 \text{ \AA}$) only at the lowest concentration studied: 0.05 cmc DTAB. In concentrations 0.1-5 cmc DTAB, the interfacial layer was best fitted using a 2-layer model, with a separate layer for the hydrocarbon tails ($t_1 \sim 5$ to 8 \AA with increasing DTAB concentration) and the charged headgroup ($t_2 \sim 12 \text{ \AA}$ in 0.1 cmc DTAB and $t_2 \sim 3$ to 6 \AA with increasing DTAB concentrations 0.5 to 5 cmc). The high $t_2 \sim 12 \text{ \AA}$ of the 0.1 cmc DTAB layer is also associated with high $\varphi_{\text{water-2}} \sim 74\%$, compared to $\varphi_{\text{water-2}} \sim 22$ to 40% in 0.5 to 5 cmc DTAB concentrations. The different fitted ρ_2 of the headgroup layer is due to different levels of counterion dissociation from the headgroup ($\varphi_{\text{counterion}} \sim 66, 95, 93$ and 90% in 0.1, 0.5, 1.2 and 5 cmc DTAB, respectively).

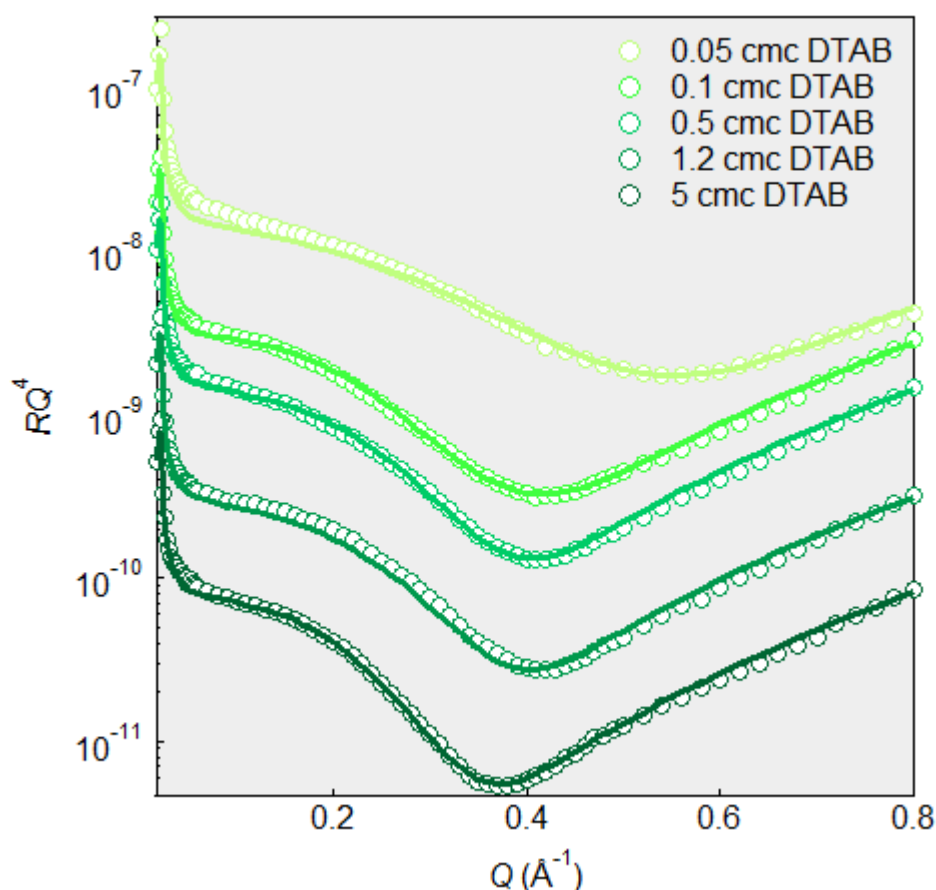


Figure 6.7 Fitted XRR data of pure DTAB. 0.05 cmc DTAB was fitted to a 1-layer model, with the concentrations 0.1 to 5 cmc DTAB fitted to a 2-layer model

Table 6.5 The fitting parameters: thickness (t), scattering length density (ρ), solvent volume fraction (φ_{water}) and roughness of the layer (σ) of pure DTAB determined from a 1-layer (at 0.05 cmc DTAB) and a 2-layer model (at concentrations 0.1 to 5 cmc) fit of XRR data. The superscripts for the fitted ρ values in the table correspond to the following headgroup/counterion associations: ¹ 66% counterion, ² 95% counterion, ³ 93% counterion, ⁴ 90% counterion associated with the surfactant headgroup. 100% counterion association is assumed unless otherwise stated.

DTAB conc (cmc)	Layer 1				Layer 2				Bkg σ_{bkg} (Å)
	t_1 (Å)	ρ_1	$\varphi_{\text{water-1}}$	σ_1 (Å)	t_2 (Å)	ρ_2	$\varphi_{\text{water-2}}$	σ_2 (Å)	
		(10^{-6} Å^{-2})	(%)			(10^{-6} Å^{-2})	(%)		
0.05	13.7	9.517	2	3.1	-	-	-	-	3.2
0.1	5.1	7.773	0	3.7	11.8	12.31 ¹	74	3.1	4.8
0.5	7.1	7.773	0	4.1	3.3	13.886 ²	22	4.4	4.5
1.2	7.8	7.773	0	4.3	4.1	13.79 ³	27	4.9	3.6
5	8.2	7.773	0	4.2	5.5	13.578 ⁴	40	4.8	4.8

6.3.2.3.2 DTAB/polymer mixtures: XRR data fitting using a 1-layer model

There was a clear difference observed in the XRR 1-layer fitting of PEG-*g*-PVAc polymers with DTAB (Figure 6.8, Table 6.6). In the case of Polymer A, the t of the interfacial layer remains between ~ 15 and 20 Å in all polymer/DTAB concentrations. Compared to polymer/DTAB mixtures with Polymer B, where with increasing DTAB concentration the layer t decreased from ~ 20 to 12 Å , with both concentrations of the polymer. Both the φ_{water} ($< 7\%$ in all cases) and φ_{polymer} was comparable between the two polymers and with increasing DTAB concentration. Interestingly, the φ_{polymer} was fitted to be $> 90\%$ in all cases, indicative of strong cooperative adsorption at the interface, possibly with the polymer depleting the interface of DTAB in order to form polymer/surfactant complexes in the bulk [46].

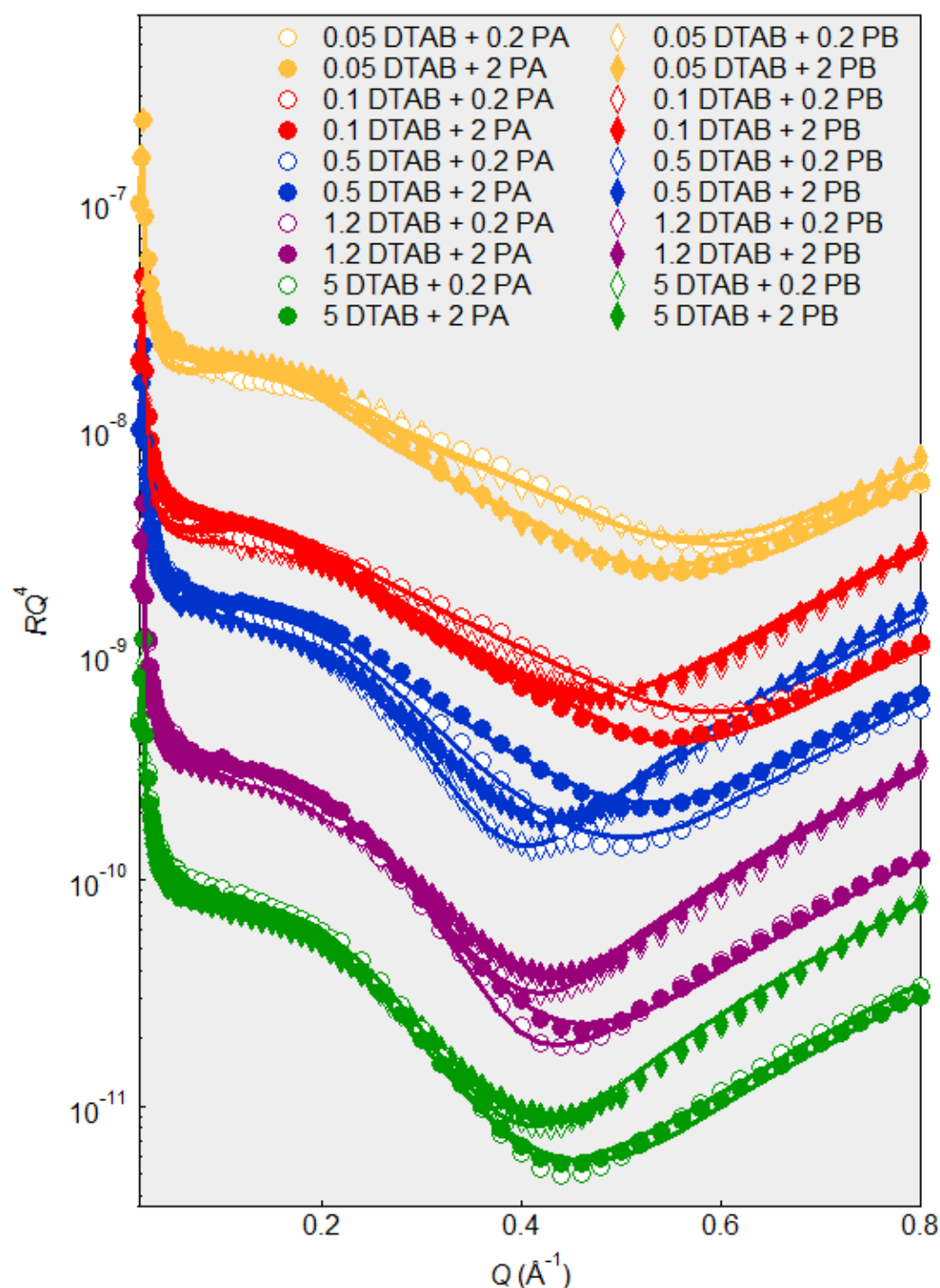


Figure 6.8 Fitted XRR data of DTAB/polymer mixtures using a 1-layer model. The data is offset for clarity, with increasing DTAB concentration. The mixtures of DTAB/Polymer A are shown in circles and mixtures of DTAB/Polymer B are shown in diamonds. In both cases, the lower polymer concentration (0.2 cac) is represented by empty markers, and 2 cac polymer concentration represented by filled markers.

Table 6.6 The fitting parameters: thickness (t), scattering length density (σ), solvent volume fraction (φ_{water}) and roughness of the layer (σ) of 1-layer model for mixtures of DTAB/Polymers A and DTAB/Polymer B. The superscripts for the fitted scattering length density (SLD) ρ values in the table correspond to the following polymer/surfactant volume fractions: ¹ 97% Polymer A + 3% DTAB, ² 91% Polymer A + 9% DTAB, ³ 90% Polymer A + 10% DTAB, ⁴ 94% Polymer A + 6% DTAB, ⁵ 98% Polymer A + 2% DTAB, ⁶ 98% Polymer A + 2% DTAB, ⁷ 99.5% Polymer A + 0.5% DTAB, ⁸ 97% Polymer A + 3% DTAB, ⁹ 99% Polymer A + 1% DTAB, ¹⁰ 95% Polymer A + 5% DTAB, and ¹¹ 96% Polymer B + 4% DTAB, ¹² 93% Polymer B + 7% DTAB, ¹³ 97% Polymer B + 3% DTAB, ¹⁴ 97% Polymer B + 3% DTAB, ¹⁵ 96% Polymer B + 4% DTAB, ¹⁶ 97% Polymer B + 3% DTAB, ¹⁷ 98% Polymer B + 2% DTAB, ¹⁸ 88% Polymer B + 12% DTAB, ¹⁹ 96% Polymer B + 4% DTAB, ²⁰ 95% Polymer B + 5% DTAB.

	PEG-g-PVAc	DTAB	Layer 1				Bkg
	conc (cac)	conc (cmc)	t_1 (Å)	ρ_1 (10^{-6} Å^{-2})	$\varphi_{\text{water-1}}$ (%)	σ_1 (Å)	σ_{bkg} (Å)
Polymer A	0.2	0.05	17.9	10.641 ¹	4	2.7	5.9
	0.2	0.1	17.4	10.577 ²	5	2.8	5.8
	0.2	0.5	15.7	10.569 ³	3	3.7	5.5
	0.2	1.2	15.4	10.6 ⁴	3	4.2	3.0
	0.2	5	15.6	10.659 ⁵	1	4.1	3.4
	2	0.05	17.9	10.659 ⁶	1	3.1	4.8
	2	0.1	19.8	10.675 ⁷	1	3.2	5.1
	2	0.5	17.5	10.643 ⁸	0	3.3	6.0
	2	1.2	15.2	10.667 ⁹	2	4.1	4.7
	2	5	16.9	10.619 ¹⁰	1	4.2	4.8
Polymer B	0.2	0.05	20.0	10.606 ¹¹	2	2.8	6.0
	0.2	0.1	12.5	10.57 ¹²	7	3.3	5.8
	0.2	0.5	13.5	10.621 ¹³	1	4.6	2.7
	0.2	1.2	12.6	10.615 ¹⁴	1	4.5	3.2
	0.2	5	13.1	10.593 ¹⁵	2	4.4	3.2
	2	0.05	19.9	10.621 ¹⁶	1	3.2	5.9
	2	0.1	19.2	10.63 ¹⁷	5	3.3	6.0
	2	0.5	12.6	10.513 ¹⁸	1	4.2	4.8
	2	1.2	12.1	10.613 ¹⁹	5	4.3	3.2
	2	5	12.1	10.604 ²⁰	1	4.4	3.2

6.3.2.3.3 DTAB/polymer mixtures: XRR data fitting using a multi-layer model

For a better understanding of the DTAB/polymers complexation, a multilayer model (where applicable) was used to fit the XRR data at three surfactant concentrations (Figure 6.9, Table 6.7). The fitted layers are described in detail below.

The t of the 1-layer model at 0.05 cmc DTAB with Polymer A is $\sim 18 \text{ Å}$ and $\sim 20 \text{ Å}$ with Polymer B, in both cases independent of the polymer concentration.

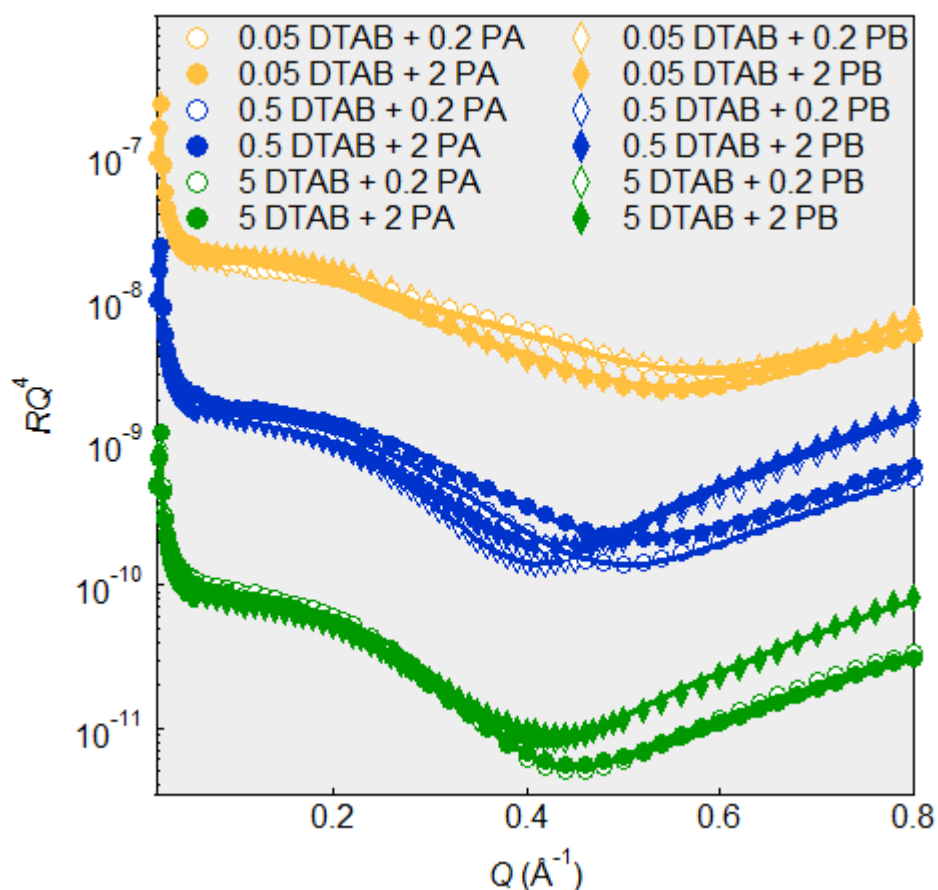


Figure 6.9 Fitted XRR data of DTAB/polymer mixtures using a 1-layer model for DTAB/polymer mixtures containing: 0.05 cmc DTAB (yellow), 2-layer model for 0.5 cmc DTAB (blue) and 5 cmc DTAB concentration (green). The data is offset for clarity, with increasing DTAB concentration. The mixtures of DTAB/Polymer A are shown in circles and mixtures of DTAB/Polymer B are shown in diamonds. In both cases, the lower polymer concentration (0.2 cac) is represented by empty markers, and 2 cac polymer concentration represented by filled markers.

In the mixtures of 0.5 cmc DTAB with both polymers, the layer at the top of the interface is assigned to the polymer with the surfactant layer underneath. The main difference between mixtures of DTAB at this concentration and the two polymers is in the surfactant layer t_2 . In the case of Polymer A and 0.5 cmc DTAB, the $t_2 \sim 11$ and 12 \AA with increasing Polymer A concentration, whereas the $t_2 \sim 14$ and 16 \AA with increasing Polymer B concentration. This thicker surfactant layer associated with the polymer layer at the interface indicates stronger cooperative adsorption of Polymer B with DTAB at these concentration mixtures. Polymer B contains approximately the same amount of PVAc as Polymer A, however the PVAc is distributed in a larger number of shorter grafts and therefore we can envisage decreased steric hindrance between adsorbing DTAB molecules, compared to adsorption onto lower number of grafts. This behaviour differs to a simple variation of grafting density, which is commonly reported as one of the main influences of polymer/surfactant interactions.

In mixtures containing 5 cmc DTAB, there was no obvious trend or difference in adsorption behaviour and interactions observed in the t , φ_{polymer} or φ_{water} in the polymer/surfactant mixtures, with all systems consistent with competitive adsorption at the air-water interface and depletion of the polymer to form a “hanging” layer underneath the surfactant. There was some difference observed between the fitted ρ_2 of the DTAB headgroup, which is attributed to different level of counterion dissociation from the headgroup, but could potentially also be attributed to interactions of the DTAB headgroup with the polymer, especially in the case of 5 cmc DTAB and 2 cac Polymer B, where the fitted $\rho_2 \sim 12.4 \times 10^{-6} \text{ \AA}^{-2}$ was relatively small compared to the theoretical DTAB $\rho_2 \sim 14.1 \times 10^{-6} \text{ \AA}^{-2}$, which when assigned to the dissociation accounted for only $\sim 33\%$ counterion associated with the headgroup.

Table 6.7 The fitted parameters: thickness (t), scattering length density (σ), solvent volume fraction (φ_{water}) and roughness of the layer (σ) for the optimised multilayer models for mixtures of PEG-g-PVAc co-polymers (Polymer A and Polymer B) and DTAB, as well as the pure systems. The superscripts for the fitted scattering length density (SLD) ρ values in the table correspond to the following polymer/surfactant volume fractions: ¹ 97% Polymer A + 3% DTAB, ² 82% counterion associated with DTAB headgroup, ³ 98% Polymer A + 2% DTAB, ⁴ 87% counterion associated with DTAB headgroup, and ⁵ 96% Polymer B + 4% DTAB, ⁶ 100% counterion associated with DTAB headgroup, ⁷ 97% Polymer B + 3% DTAB, ⁸ 33% counterion associated with DTAB headgroup.

	PEG-g-PVAc DTAB		Layer 1				Layer 2				Layer 3				Bkg
	conc (cac)	conc (cmc)	t_1 (\AA)	ρ_1 (10^{-6} \AA^{-2})	$\varphi_{\text{water-1}}$ (%)	σ_1 (\AA)	t_2 (\AA)	ρ_2 (10^{-6} \AA^{-2})	$\varphi_{\text{water-2}}$ (%)	σ_2 (\AA)	t_3 (\AA)	ρ_3 (10^{-6} \AA^{-2})	$\varphi_{\text{water-3}}$ (%)	σ_3 (\AA)	
Polymer A	0.2	0.05	17.9	10.641 ¹	4	2.7	-	-	-	-	-	-	-	-	5.9
	0.2	0.5	12.4	10.678	11	3.7	10.6	9.517	7	4.3	-	-	-	-	3.5
	0.2	5	6.6	7.773	0	3.0	5.6	13.15 ²	55	2.9	3.5	10.678	40	3.9	3.8
	2	0.05	17.9	10.659 ³	1	3.1	-	-	-	-	-	-	-	-	4.8
	2	0.5	13.5	10.678	1	3.3	12.0	9.517	21	4.4	-	-	-	-	3.3
	2	5	6.7	7.773	0	3.5	3.5	13.447 ⁴	27	4.9	4.7	10.678	8	4.5	4.2
	0.2	-	20.1	10.678	6	4.0	-	-	-	-	-	-	-	-	2.9
	2	-	19.5	10.678	0	3.7	-	-	-	-	-	-	-	-	2.7
Polymer B	0.2	0.05	20.0	10.606 ⁵	2	2.8	-	-	-	-	-	-	-	-	6.0
	0.2	0.5	16.5	10.655	2	4.6	13.9	9.517	25	3.2	-	-	-	-	3.6
	0.2	5	6.7	7.773	0	3.8	4.3	14.133 ⁶	41	3.6	4.2	10.655	47	3.6	4.0
	2	0.05	19.9	10.621 ⁷	1	3.2	-	-	-	-	-	-	-	-	5.9
	2	0.5	12.3	10.655	9	4.3	16.0	9.517	3	3.0	-	-	-	-	4.1
	2	5	5.9	7.773	0	3.8	3.4	12.398 ⁸	34	3.0	3.9	10.655	8	3.7	3.8
	0.2	-	10.4	10.655	16	2.8	-	-	-	-	-	-	-	-	5.2
	2	-	19.3	10.655	1	3.4	-	-	-	-	-	-	-	-	6.0
DTAB	-	0.05	13.7	9.517	2	3.1	-	-	-	-	-	-	-	-	3.2
	-	0.5	7.1	7.773	0	4.1	3.3	13.886	22	4.4	-	-	-	-	4.5
	-	5	8.2	7.773	0	4.2	5.5	13.578	40	4.8	-	-	-	-	4.8

6.3.2.4 $C_{12}E_5$ and $C_{12}E_5$ /polymer mixtures

6.3.2.4.1 Pure $C_{12}E_5$: XRR data fitting

All concentrations of $C_{12}E_5$ were fitted using a 2-layer model (Figure 6.10, Table 6.8), accounting for the much larger headgroup compared to those of SDS or DTAB. Overall, increase in both the hydrocarbon tail t_1 from ~ 4 to 8 \AA , and the headgroup t_2 from ~ 12 to 14 \AA was observed. The $\phi_{\text{water-2}} \sim 66\%$ at the lowest $C_{12}E_5$ concentration studied, accounting partially for the relatively high t of such a low surfactant concentration. In the higher concentrations of $C_{12}E_5$, the $\phi_{\text{water-2}} \sim 0 - 40\%$. As the $C_{12}E_5$ headgroup is non-ionic, the ρ_2 was kept constant as there is no counterion present that could dissociate. The data at 1.2 cmc $C_{12}E_5$ cannot be fitted well using either of the fitting models.

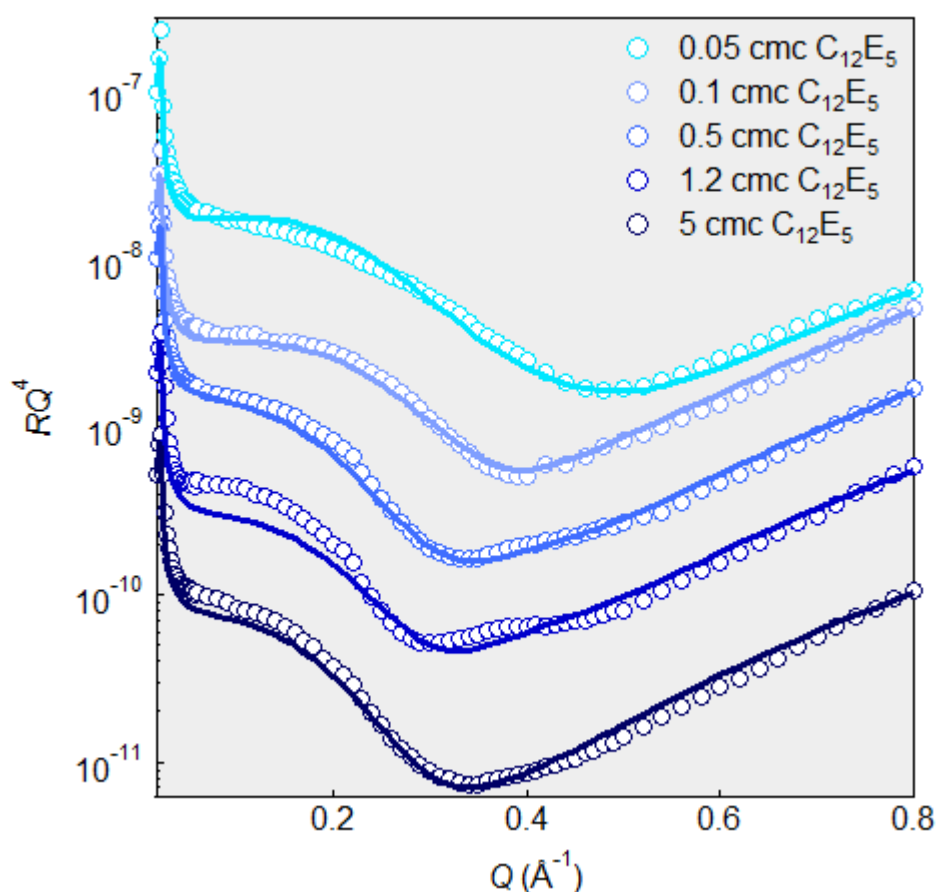


Figure 6.10 Fitted XRR data of pure $C_{12}E_5$. All concentrations (0.05 to 5 cmc) were fitted to a 2-layer model.

Table 6.8 The fitted parameters: thickness (t), scattering length density (ρ), solvent volume fraction (ϕ_{water}) and roughness of the layer (σ) of pure C_{12}E_5 determined from a 2-layer model (at concentrations 0.05 to 5 cmc) fit of XRR data.

C_{12}E_5 conc (cmc)	Layer 1				Layer 2				Bkg σ_{bkg} (Å)
	t_1 (Å)	ρ_1 (10^{-6}Å^{-2})	$\phi_{\text{water-1}}$ (%)	σ_1 (Å)	t_2 (Å)	ρ_2 (10^{-6}Å^{-2})	$\phi_{\text{water-2}}$ (%)	σ_2 (Å)	
0.05	4.1	7.773	0	3.2	11.8	10.434	66	3.8	5.4
0.1	5.1	7.773	0	3.0	12.4	10.434	0	2.6	2.5
0.5	8.3	7.773	0	3.7	11.9	10.434	31	4.5	3.5
1.2	8.3	7.773	0	3.2	13.0	10.434	36	3.6	2.9
5	8.3	7.773	0	3.7	13.9	10.434	40	3.0	3.9

6.3.2.4.2 C_{12}E_5 /polymer mixtures: XRR data fitting using a 1-layer model

A 1-layer model was first used to fit the XRR data of C_{12}E_5 /polymer mixtures (Figure 6.11, Table 6.9). In both cases, the layer t increased with increasing C_{12}E_5 concentration ($t \sim 15 \text{Å}$ to 21Å in Polymer A mixtures and $t \sim 19 \text{Å}$ to 21Å in Polymer B mixtures, with increasing C_{12}E_5 concentration). The main difference between the two polymers with C_{12}E_5 was in the ϕ_{water} , with higher ϕ_{water} on average in the mixtures containing Polymer B. The higher ϕ_{water} in an interfacial layer contributes to the layer swelling and therefore slight increase in the layer t , as demonstrated by $\Delta t \sim 1 \text{Å}$ between the mixtures of C_{12}E_5 /Polymer A and C_{12}E_5 /Polymer B. The ϕ_{polymer} in all the mixtures was $> 74\%$, suggesting the polymer was the dominant adsorbing species in the mixtures. This high ϕ_{polymer} determined from XRR data fitting contradicted the 1-layer model fitting obtained from NR data in the case of Polymer A.

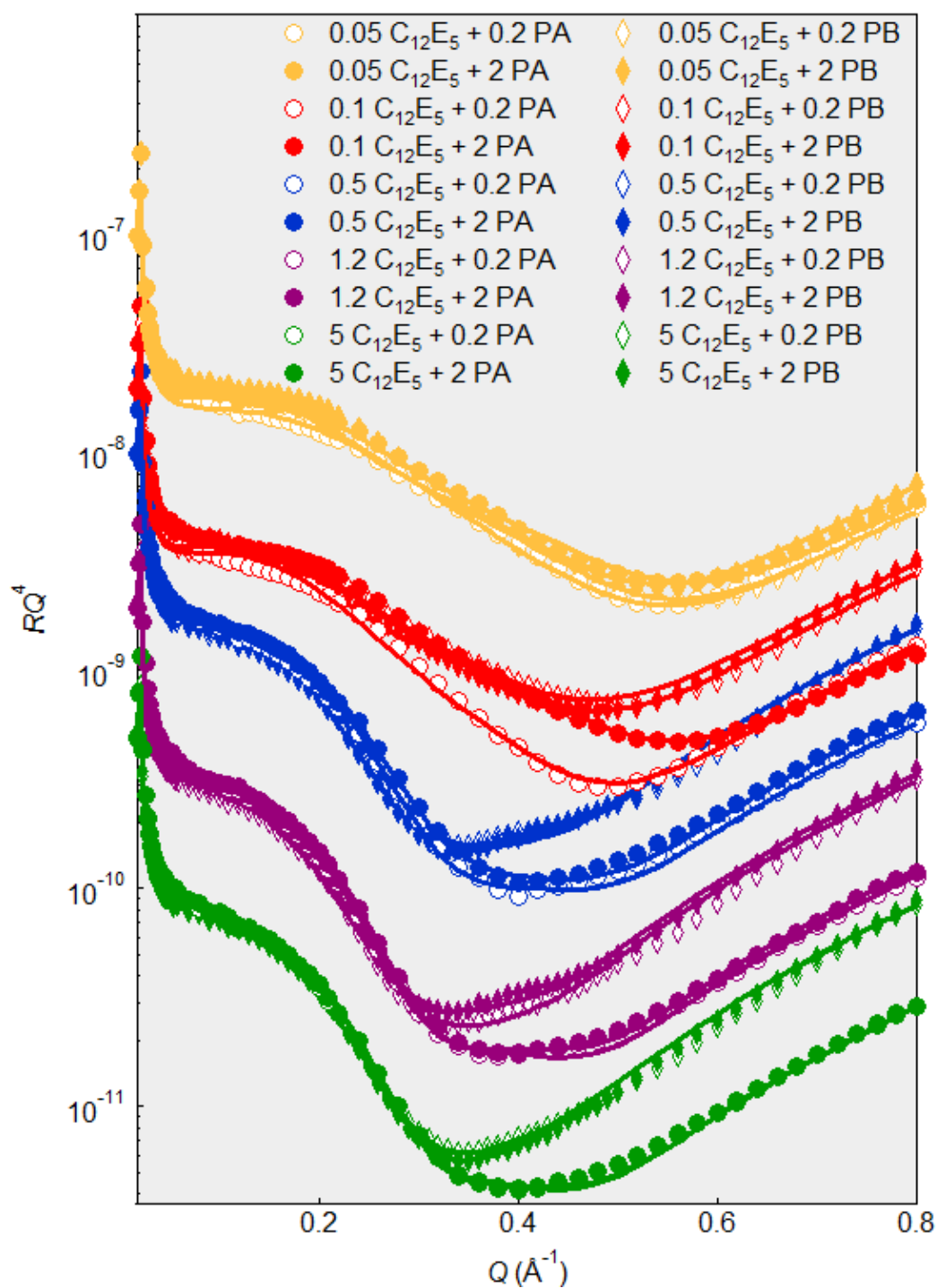


Figure 6.11 Fitted XRR data of $C_{12}E_5$ /polymer mixtures using a 1-layer model. The data is offset for clarity, with increasing $C_{12}E_5$ concentration. The mixtures of $C_{12}E_5$ /Polymer A are shown in circles and mixtures of $C_{12}E_5$ /Polymer B are shown in diamonds. In both cases, the lower polymer concentration (0.2 cac) is represented by empty markers, and 2 cac polymer concentration represented by filled markers.

Table 6.9 The fitting parameters: thickness (t), scattering length density (σ), solvent volume fraction (ϕ_{water}) and roughness of the layer (σ) of 1-layer model for mixtures of $C_{12}E_5$ /Polymers A and $C_{12}E_5$ /Polymer B. The superscripts for the fitted scattering length density (SLD) ρ values in the table correspond to the following polymer/surfactant volume fractions: ¹ 86% Polymer A + 14% $C_{12}E_5$, ² 97% Polymer A + 3% $C_{12}E_5$, ³ 93% Polymer A + 7% $C_{12}E_5$, ⁴ 85% Polymer A + 15% $C_{12}E_5$, ⁵ 91% Polymer A + 9% $C_{12}E_5$, ⁶ 99% Polymer A + 1% $C_{12}E_5$, ⁷ 98% Polymer A + 2% $C_{12}E_5$, ⁸ 99% Polymer A + 1% $C_{12}E_5$, ⁹ 88% Polymer A + 12% $C_{12}E_5$, ¹⁰ 78% Polymer A + 22% $C_{12}E_5$, and ¹¹ 99% Polymer B + 1% $C_{12}E_5$, ¹² 95% Polymer B + 5% $C_{12}E_5$, ¹³ 90% Polymer B + 10% $C_{12}E_5$, ¹⁴ 74% Polymer B + 26% $C_{12}E_5$, ¹⁵ 84% Polymer B + 16% $C_{12}E_5$, ¹⁶ 98% Polymer B + 2% $C_{12}E_5$, ¹⁷ 98% Polymer B + 2% $C_{12}E_5$, ¹⁸ 86% Polymer B + 14% $C_{12}E_5$, ¹⁹ 75% Polymer B + 25% $C_{12}E_5$, ²⁰ 92% Polymer B + 8% $C_{12}E_5$.

	PEG-g-PVAc conc (cac)	$C_{12}E_5$ conc (cmc)	Layer 1				Bkg σ_{bkg} (Å)
			t_1 (Å)	ρ_1 (10^{-6}Å^{-2})	$\phi_{\text{water-1}}$ (%)	σ_1 (Å)	
Polymer A	0.2	0.05	14.7	10.465 ¹	17	3.2	5.7
	0.2	0.1	18.4	10.632 ²	3	3.8	6.0
	0.2	0.5	20.0	10.571 ³	14	4.6	2.8
	0.2	1.2	21.5	10.445 ⁴	13	5.0	2.6
	0.2	5	21.2	10.545 ⁵	21	4.9	2.9
	2	0.05	17.5	10.65 ⁶	0	3.0	5.3
	2	0.1	19.8	10.647 ⁷	1	3.1	5.6
	2	0.5	19.8	10.665 ⁸	12	4.5	3.3
	2	1.2	21.0	10.488 ⁹	11	4.9	2.5
	2	5	20.9	10.324 ¹⁰	2	4.9	2.6
Polymer B	0.2	0.05	18.8	10.632 ¹¹	2	3.1	5.9
	0.2	0.1	16.7	10.58 ¹²	4	3.2	6.0
	0.2	0.5	21.0	10.493 ¹³	26	4.6	2.5
	0.2	1.2	22.5	10.25 ¹⁴	34	5.2	2.5
	0.2	5	21.3	10.402 ¹⁵	26	5.1	3.3
	2	0.05	19.9	10.627 ¹⁶	1	3.1	6.0
	2	0.1	21.7	10.628 ¹⁷	0	3.3	6.0
	2	0.5	21.8	10.44 ¹⁸	22	4.8	2.5
	2	1.2	22.7	10.273 ¹⁹	13	5.1	2.5
	2	5	20.7	10.538 ²⁰	26	5.2	3.8

6.3.2.4.3 $C_{12}E_5$ /polymer mixtures: XRR data fitting using a multi-layer model

The XRR data fitted using a multi-layer model for $C_{12}E_5$ /polymer mixtures is shown in Figure 6.12, Table 6.10.

In the mixtures of 0.05 cmc $C_{12}E_5$, the t of the mixed polymer/surfactant layer was higher in mixtures containing Polymer B ($t \sim 19$ and 20Å compared to $t \sim 15$ and 18Å in mixtures containing Polymer A).

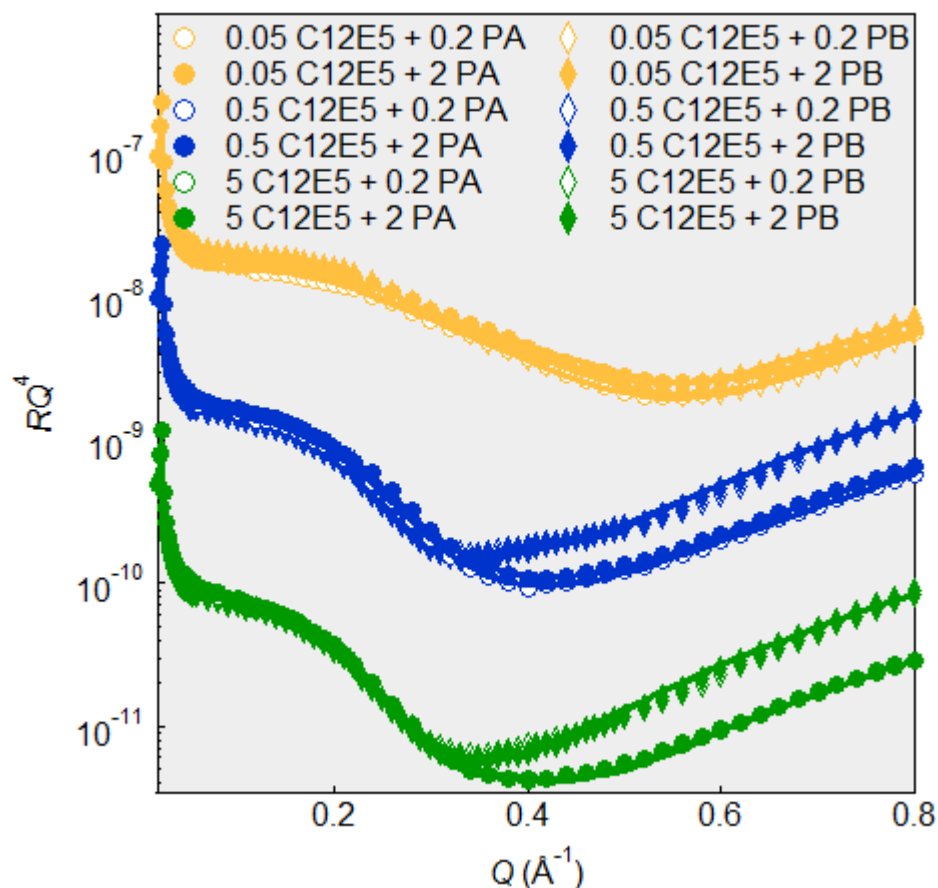


Figure 6.12 Fitted XRR data of $C_{12}E_5$ /polymer mixtures using a 1-layer model for $C_{12}E_5$ /polymer mixtures containing: 0.05 cmc $C_{12}E_5$ (yellow), 2-layer model for 0.5 cmc $C_{12}E_5$ (blue) and 5 cmc $C_{12}E_5$ concentration (green). The data is offset for clarity, with increasing $C_{12}E_5$ concentration. The mixtures of $C_{12}E_5$ /Polymer A are shown in circles and mixtures of $C_{12}E_5$ /Polymer B are shown in diamonds. In both cases, the lower polymer concentration (0.2 cac) is represented by empty markers, and 2 cac polymer concentration represented by filled markers.

The same trend of higher overall t in mixtures with Polymer B compared to Polymer A mixtures was observed in 0.5 cmc $C_{12}E_5$ /polymer mixtures. The increase of the overall t was caused by thicker polymer layer, with fitted $t_2 \sim 11 \text{ \AA}$ in mixtures containing Polymer A and $t_2 \sim 14 \text{ \AA}$ in mixtures containing Polymer B. It is important to note that the $\phi_{\text{water-2}}$ of the polymer layer was also increased in the mixtures of Polymer B ($\phi_{\text{water-2}} \sim 36$ and 32% compared to $\phi_{\text{water-2}} \sim 1$ and 6% in mixtures of Polymer A), which partially accounted for the layer t increase. The difference in the adsorption behaviour could also be rationalised by the presence of longer PEG backbone in Polymer B available to complex with $C_{12}E_5$ molecules below its cmc. Interestingly, the t_1 of the surfactant layer followed the opposite trend, with thicker $C_{12}E_5$ layer in mixtures containing Polymer A ($t_1 \sim 9 \text{ \AA}$ compared to $t_1 \sim 7\text{-}8 \text{ \AA}$ in mixtures with Polymer B). In any case, the t_1 assigned to the $C_{12}E_5$ layer at the top of the interface was much smaller than the overall $t \sim 20 \text{ \AA}$ of a pure 0.5 cmc $C_{12}E_5$ (hydrocarbon tail $t_1 \sim 8 \text{ \AA}$ and headgroup $t_2 \sim 12 \text{ \AA}$). This would suggest the $C_{12}E_5$ molecules were tilted at the interface, both the tails and the headgroups.

The same overall C₁₂E₅ layer t decrease compared to the pure surfactant was observed in mixtures above the surfactant cmc. The most prominent difference of the mixtures compared to the pure 5 cmc C₁₂E₅ layer was in the much lower surfactant headgroup $t_2 \sim 6\text{-}8 \text{ \AA}$ in the C₁₂E₅/polymer mixtures in the case of both polymers, compared to $t_2 \sim 14 \text{ \AA}$ in the pure C₁₂E₅. This again suggested a strongly tilted headgroup layer, with less tilted hydrocarbon tails relative to the pure surfactant ($t_1 \sim 5\text{-}7 \text{ \AA}$ in C₁₂E₅/polymer mixtures, compared to $t_1 \sim 8 \text{ \AA}$ in pure C₁₂E₅). Lastly, there was a difference in the adsorption between the two polymers and 5 cmc C₁₂E₅, with lower polymer $t_3 \sim 10$ and 7 \AA in the mixtures of Polymer B compared to $t_3 \sim 13$ and 8 \AA in the mixtures of Polymer A at the given C₁₂E₅ concentration. The $\phi_{\text{water-3}}$ of the mixtures containing Polymer B was higher ($\phi_{\text{water-3}} \sim 28$ and 36%) than those containing Polymer A ($\phi_{\text{water-3}} \sim 21$ and 26%), and so the difference in the layer t_3 cannot be attributed to a simple layer solvation and subsequent swelling. Overall, the more hydrophobic Polymer A also possessed longer PVAc grafts, compared to Polymer B, which when stretched would account for higher t of the “hanging” polymer layer as observed by NR.

Table 6.10 The fitting parameters: thickness (t), scattering length density (σ), solvent volume fraction (ϕ_{water}) and roughness of the layer (σ) for the optimised multilayer models for mixtures of PEG-g-PVAc co-polymers (Polymer A and Polymer B) and C₁₂E₅, as well as the pure systems. The superscripts for the fitted scattering length density (SLD) ρ values in the table correspond to the following polymer/surfactant volume fractions: ¹ 97% Polymer A + 3% C₁₂E₅, ² 99% Polymer A + 1% C₁₂E₅, and ³ 99% Polymer B + 1% C₁₂E₅, ⁴ 98% Polymer B + 2% C₁₂E₅.

	PEG-g-PVAc C ₁₂ E ₅		Layer 1				Layer 2				Layer 3				Bkg
	conc (cac)	conc (cmc)	t_1 (\AA)	ρ_1 (10^{-6} \AA^{-2})	$\phi_{\text{water-1}}$ (%)	σ_1 (\AA)	t_2 (\AA)	ρ_2 (10^{-6} \AA^{-2})	$\phi_{\text{water-2}}$ (%)	σ_2 (\AA)	t_3 (\AA)	ρ_3 (10^{-6} \AA^{-2})	$\phi_{\text{water-3}}$ (%)	σ_3 (\AA)	
Polymer A	0.2	0.05	14.7	10.465 ¹	17	3.2	-	-	-	-	-	-	-	-	5.7
	0.2	0.5	8.8	9.098	24	3.9	10.7	10.678	1	2.5	-	-	-	-	5.6
	0.2	5	5.3	7.773	0	4.6	5.8	10.434	10	2.8	12.5	10.678	21	3.6	2.7
	2	0.05	17.5	10.65 ²	0	3.0	-	-	-	-	-	-	-	-	5.3
	2	0.5	8.5	9.098	33	3.9	11.0	10.678	6	3.1	-	-	-	-	5.1
	2	5	6.6	7.773	0	4.1	6.8	10.434	4	4.6	8.1	10.678	26	5.6	3.7
	0.2	-	20.1	10.678	6	4.0	-	-	-	-	-	-	-	-	2.9
	2	-	19.5	10.678	0	3.7	-	-	-	-	-	-	-	-	2.7
Polymer B	0.2	0.05	18.8	10.632 ³	2	3.1	-	-	-	-	-	-	-	-	5.9
	0.2	0.5	7.1	9.098	65	4.3	13.9	10.655	36	4.0	-	-	-	-	2.5
	0.2	5	5.7	7.773	0	4.6	5.8	10.434	2	4.7	9.9	10.655	28	5.4	4.6
	2	0.05	19.9	10.627 ⁴	1	3.1	-	-	-	-	-	-	-	-	6.0
	2	0.5	7.7	9.098	65	4.5	13.7	10.655	32	5.2	-	-	-	-	2.5
	2	5	7.4	7.773	0	4.1	7.6	10.434	4	3.7	7.2	10.655	36	4.7	3.5
	0.2	-	10.4	10.655	16	2.8	-	-	-	-	-	-	-	-	5.2
	2	-	19.3	10.655	1	3.4	-	-	-	-	-	-	-	-	6.0
C ₁₂ E ₅	-	0.05	4.1	7.773	0	3.2	11.8	10.434	66	3.8	-	-	-	-	5.4
	-	0.5	8.3	7.773	0	3.7	11.9	10.434	31	4.5	-	-	-	-	3.5
	-	5	8.3	7.773	0	3.7	13.9	10.434	40	3.0	-	-	-	-	3.9

6.4 Conclusions

Interactions of three surfactants carrying different charges (anionic SDS, cationic DTAB and non-ionic C₁₂E₅) and two PEG-g-PVAc co-polymers (varying in hydrophobicity and PVAc graft length and number) were investigated at the air-water interface using equilibrium surface tension measurements and X-ray reflectivity (XRR). The effect of the polymer architecture on the polymer/surfactant interactions and interfacial layer structure is discussed.

6.4.1 Surface tension

The overall γ data of SDS/Polymer B was very similar to that of the SDS/Polymer A, with a transition from synergistic to competitive adsorption observed at ~ 0.5 cmc SDS with the two polymers. Similarly, the competitive adsorption at concentrations of C₁₂E₅ > 0.2 cmc in the mixtures of the two PEG-g-PVAc co-polymers was prominent, with polymer depletion from the interface. However, γ higher than the pure C₁₂E₅ surfactant in mixtures of 0.2 cac Polymer B and C₁₂E₅ at intermediate surfactant concentrations indicative of polymer/surfactant interactions was observed. The most striking difference in γ behaviour of the studied surfactant/polymer mixtures was observed in the case of DTAB. There was no pronounced synergistic effect observed in DTAB/Polymer B mixtures but significant synergistic γ lowering was observed in the DTAB/Polymer A mixtures, especially at DTAB concentrations below its cmc.

6.4.2 Interfacial layer structure determined by XRR

Using a 1-layer model to fit the XRR data of surfactant/polymer mixtures we observed an overall layer t decrease in the case of SDS and DTAB with both polymers studied with increasing surfactant concentration, and a layer t increase with increasing concentration of C₁₂E₅. The φ_{polymer} determined from the fitted ρ of the 1-layer model suggested the main adsorbing species was the polymer in the mixtures containing DTAB ($\varphi_{\text{polymer}} > 90\%$ in all DTAB/polymer mixtures studied) and C₁₂E₅ ($\varphi_{\text{polymer}} > 74\%$ in all C₁₂E₅/polymer mixtures studied). The φ_{polymer} decreased with increasing SDS concentration in mixtures of SDS with both polymers, until $\varphi_{\text{polymer}} < 3\%$ in all mixtures containing SDS above its cmc. From the 1-layer fitting of XRR data we would therefore expect the strongest cooperative adsorption/interactions at the air-water interface between DTAB and the polymers, still

relatively strong interactions between C₁₂E₅ and the polymers, and a depletion of the polymers with increasing SDS concentration (*i.e.* competitive adsorption). The 1-layer XRR fitting of SDS/Polymer A mixtures largely agreed with the 1-layer fitting of NR data of the same system. The 1-layer XRR data fitting of mixtures of DTAB and C₁₂E₅ with Polymer A however disagreed with the NR data fitting, where XRR data fitting suggested a much higher $\varphi_{\text{Polymer A}}$ in the mixtures than when determined from NR fitting (and I). The physical models used for multilayer fittings of the chosen surfactant concentrations (0.05, 0.5 and 5 cmc) with Polymer A were however consistent with those used to fit the NR data. As discussed previously, the lack of ρ contrast and possible variations *via* isotopic substitution in the case of XRR studies is one of the limiting factors of the technique and could be one of the reasons for suboptimal data fitting results.

The multilayer models in overall provided better contrast between the adsorbing species at the interface (*e.g.* $\rho_{\text{water}} \sim 9.41 \times 10^{-6} \text{ \AA}^{-2}$, $\rho_{\text{Polymer A}} \sim 10.68 \times 10^{-6} \text{ \AA}^{-2}$ and $\rho_{\text{SDS}} \sim 10.66 \times 10^{-6} \text{ \AA}^{-2}$, compared to $\rho_{\text{SDS-headgroup}} \sim 26.7\text{-}32.8 \times 10^{-6} \text{ \AA}^{-2}$ and $\rho_{\text{SDS-tail}} \sim 7.77 \times 10^{-6} \text{ \AA}^{-2}$). From the multilayer XRR data fitting, we have learnt that:

- a) at 0.5 cmc SDS, the average t_1 of the surfactant layer was comparable between the two polymers ($t_1 \sim 1 \text{ \AA}$ higher in case of SDS/Polymer B mixtures compared to SDS/Polymer A). The average t_2 of the polymer layer was also fitted with alike values however the $\varphi_{\text{water-2}}$ was much higher in the case of SDS/Polymer B mixtures. The higher solvation of the Polymer B layer is also evident at the SDS concentration above its cmc, coupled with much lower t_3 of the polymer layer in 5 cmc SDS/Polymer B mixture ($t_3 \sim 2 \text{ \AA}$) compared to 5 cmc SDS/Polymer A ($t_3 \sim 5\text{-}7 \text{ \AA}$). From the γ data we have observed strong competitive adsorption at the interface, so we could expect less surfactant/polymer interactions at the interface and so the polymer with higher hydrophobicity and longer grafts (Polymer A) forming a thicker “hanging” polymer layer.
- b) at 0.5 cmc DTAB, the polymer layer was thicker in the mixtures with Polymer B ($t_2 \sim 14\text{-}16 \text{ \AA}$) compared to DTAB/Polymer A mixtures ($t_2 \sim 11\text{-}12 \text{ \AA}$). The higher t_2 can be attributed to more favourable interactions between the DTAB layer on top of the interface, with attractive forces between the DTAB headgroups and PVAc grafts of the polymer. Even though the Mn of the PVAc is very similar in the two polymers ($\sim 9 \text{ kDa}$ compared to $\sim 8.5 \text{ kDa}$), there is more PVAc grafts per PEG backbone in the Polymer B structure available, resulting in less steric hindrance between the interacting DTAB/PVAc when

the PVAc monomers adsorbed to higher number of grafts rather than fewer longer grafts. At DTAB concentrations above its cmc no significant difference was observed between the interfacial structures of the two polymers and DTAB, indicating competitive adsorption at this DTAB concentration with both polymers depleted from the interface equally.

- c) at 0.5 cmc C₁₂E₅, the surfactant layer t_1 was marginally higher in the mixtures of C₁₂E₅/Polymer A ($t_1 \sim 9 \text{ \AA}$) than in C₁₂E₅/Polymer B ($t_1 \sim 7\text{-}8 \text{ \AA}$). The polymer layer t_2 , however, was higher for Polymer B mixtures ($t_2 \sim 14 \text{ \AA}$) compared to C₁₂E₅/Polymer A ($t_2 \sim 11 \text{ \AA}$). Such behaviour suggests stronger interactions between the surfactant and Polymer B, which can be justified by the overall higher PEG backbone content in Polymer B interacting with the C₁₂E₅ headgroup *via* hydrophobic interactions. Surprisingly, at C₁₂E₅ concentrations above its cmc the polymer layer t_3 was higher in the mixtures containing Polymer A. The higher t_3 in the case of Polymer A in a surfactant/polymer system in the regime of competitive adsorption at the interface (*c.f.* SDS/PEG-*g*-PVAc at high SDS concentrations) could again be attributed to the higher overall hydrophobicity and longer PVAc grafts of the Polymer A depleted from the interface to form a “hanging” layer proximal to the surfactant layer at the top of the interface.

6.5 References

1. Péron, N., et al., *Competitive adsorption of sodium dodecyl sulfate and polyethylene oxide at the air/water interface*. Journal of Colloid and Interface Science, 2007. **313**(2): p. 389-397.
2. Lytle, D.J., et al., *Structure of a Dodecyltrimethylammonium Bromide Layer at the Air/Water Interface Determined by Neutron Reflection: Comparison of the Monolayer Structure of Cationic Surfactants with Different Chain Lengths*. Langmuir, 1995. **11**(3): p. 1001-1008.
3. López-Esparza, R., et al., *Interaction between poly(ethylene glycol) and two surfactants investigated by diffusion coefficient measurements*. Journal of Colloid and Interface Science, 2006. **300**(1): p. 105-110.
4. Karamyan, D.R., et al., *Kinetics of the Non-Catalysed Hydrolysis of Vinyl Acetate in an Aqueous Medium*. International Polymer Science and Technology, 2004. **31**(1): p. 49-51.
5. Briddick, A., et al., *Surfactant and Plasticizer Segregation in Thin Poly(vinyl alcohol) Films*. Langmuir, 2016. **32**(3): p. 864-872.

6. Feitosa, E., Brown, W., and Hansson, P., *Interactions between the Non-ionic Surfactant C12E5 and Poly(ethylene oxide) Studied Using Dynamic Light Scattering and Fluorescence Quenching*. Vol. 29. 1996. 2169-2178.
7. Jones, M.N., *The interaction of sodium dodecyl sulfate with polyethylene oxide*. Journal of Colloid and Interface Science, 1967. **23**(1): p. 36-42.
8. Bárány, S., *Interaction between water soluble polymers and surfactants*. 2001. **166**(1): p. 71-92.
9. Heydari, N., et al., *Novel application of PEG/SDS interaction as a wettability modifier of hydrophobic carbonate surfaces*. Petroleum Science, 2019. **16**(2): p. 318-327.
10. Singh, R., Chauhan, S., and Sharma, K., *Surface Tension, Viscosity, and Refractive Index of Sodium Dodecyl Sulfate (SDS) in Aqueous Solution Containing Poly(ethylene glycol) (PEG), Poly(vinyl pyrrolidone) (PVP), and Their Blends*. Journal of Chemical & Engineering Data, 2017. **62**(7): p. 1955-1964.
11. Banerjee, S., et al., *Surfactant–polymer interactions: molecular architecture does matter*. Soft Matter, 2015. **11**(12): p. 2504-2511.
12. Zhao, L. and Lin, Z., *Self-assembly of non-linear polymers at the air/water interface: the effect of molecular architecture*. Soft Matter, 2011. **7**(22): p. 10520-10535.
13. Wesley, R.D., Cosgrove, T., and Thompson, L., *Interactions of Star Polymers with Surfactants*. Langmuir, 1999. **15**(24): p. 8376-8382.
14. Guo, Y., et al., *Effects of nonionic surfactant and salts on the interactions between oppositely charged star-shaped copolymer and ionic surfactant in aqueous solutions*. Journal of Molecular Liquids, 2018. **266**: p. 789-796.
15. Middleton, H., et al., *Interaction of Sodium Dodecyl Sulfate with Methacrylate–PEG Comb Copolymers*. Langmuir, 2005. **21**(11): p. 5174-5178.
16. Yang, B.-S., et al., *Interaction of Surfactant Lamellar Phase and a Strictly Alternating Comb-Graft Amphiphilic Polymer Based on PEG*. Langmuir, 2001. **17**(21): p. 6692-6698.
17. Hofman, A.H., et al., *Interaction Strength in Poly(4-vinylpyridine)–*n*-Alkylphenol Supramolecular Comb-Shaped Copolymers*. Macromolecules, 2015. **48**(5): p. 1554-1562.
18. Băran, A., et al., *Peculiarities of linear and hyperbranched polyglycidols in water and aqueous surfactant solutions*. European Polymer Journal, 2017. **94**: p. 162-172.
19. Lai, N., et al., *Effect of sodium dodecyl benzene sulfonate to the displacement performance of hyperbranched polymer*. 2016. **89**(1): p. 70-79.
20. Cheng, Y., Zhao, L., and Li, T., *Dendrimer–surfactant interactions*. Soft Matter, 2014. **10**(16): p. 2714-2727.

21. Marinova, K.G., et al., *Physico-chemical factors controlling the foamability and foam stability of milk proteins: Sodium caseinate and whey protein concentrates*. Food Hydrocolloids, 2009. **23**(7): p. 1864-1876.
22. Griffin, W.C.J.J.S.C.C., *Classification of surface-active agents by "HLB"*. 1949. **1**: p. 311-326.
23. Pasquali, R.C., Sacco, N., and Bregni, C.J.L.A.J.P., *The studies on hydrophilic-lipophilic balance (HLB): sixty years after William C. Griffin's pioneer work (1949-2009)*. 2009. **28**(2): p. 313-317.
24. Kunieda, H. and Shinoda, K., *Evaluation of the hydrophile-lipophile balance (HLB) of nonionic surfactants. I. Multisurfactant systems*. Journal of Colloid and Interface Science, 1985. **107**(1): p. 107-121.
25. Griffin, W.C.J.J.S.C.C., *Calculation of HLB values of non-ionic surfactants*. 1954. **5**: p. 249-256.
26. Larin, D.E. and Govorun, E.N., *Surfactant-Induced Patterns in Polymer Brushes*. Langmuir, 2017. **33**(34): p. 8545-8552.
27. Melzak, K.A., et al., *Chain Length and Grafting Density Dependent Enhancement in the Hydrolysis of Ester-Linked Polymer Brushes*. Langmuir, 2015. **31**(23): p. 6463-6470.
28. Norde, W. and Gage, D., *Interaction of Bovine Serum Albumin and Human Blood Plasma with PEO-Tethered Surfaces: Influence of PEO Chain Length, Grafting Density, and Temperature*. Langmuir, 2004. **20**(10): p. 4162-4167.
29. Sinha, S.K., *Reflectivity using neutrons or X-rays? A critical comparison*. Physica B: Condensed Matter, 1991. **173**(1): p. 25-34.
30. Skoda, M.W.A., *Recent developments in the application of X-ray and neutron reflectivity to soft-matter systems*. Current Opinion in Colloid & Interface Science, 2019. **42**: p. 41-54.
31. Braun, L., et al., *Polymers and surfactants at fluid interfaces studied with specular neutron reflectometry*. Advances in Colloid and Interface Science, 2017. **247**: p. 130-148.
32. Nelson, A., *Co-refinement of multiple-contrast neutron/X-ray reflectivity data using MOTOFIT*. 2006. **39**(2): p. 273-276.
33. Muir, B.W., et al., *A Comparative X-Ray and Neutron Reflectometry Study of Plasma Polymer Films Containing Reactive Amines*. 2007. **4**(4): p. 433-444.
34. Micciulla, S., Gerelli, Y., and Schneck, E., *Structure and Conformation of Wild-Type Bacterial Lipopolysaccharide Layers at Air-Water Interfaces*. Biophysical Journal, 2019. **116**(7): p. 1259-1269.

35. Mazza, A.R., et al., *Revealing interfacial disorder at the growth-front of thick many-layer epitaxial graphene on SiC: a complementary neutron and X-ray scattering investigation*. *Nanoscale*, 2019. **11**(30): p. 14434-14445.
36. Hossain, K.R., et al., *X-ray and Neutron Reflectivity Study Shows That CLIC1 Undergoes Cholesterol-Dependent Structural Reorganization in Lipid Monolayers*. *Langmuir*, 2017. **33**(43): p. 12497-12509.
37. Campbell, R.A., *Recent advances in resolving kinetic and dynamic processes at the air/water interface using specular neutron reflectometry*. *Current Opinion in Colloid & Interface Science*, 2018. **37**: p. 49-60.
38. Kuk Kim, D., *Polymer-Surfactant Mixtures at the Air-Water Interface: A Surface Tension and Foaming Study*, in *School of Chemistry*. 2017, University of Bristol.
39. Nicklin, C., et al., *Diamond beamline I07: a beamline for surface and interface diffraction*. *J Synchrotron Radiat*, 2016. **23**(Pt 5): p. 1245-1253.
40. Arnold, T., et al., *Implementation of a beam deflection system for studies of liquid interfaces on beamline I07 at Diamond*. *J Synchrotron Radiat*, 2012. **19**(3): p. 408-416.
41. Heavens, O.S., *Optical properties of thin films*. *Reports on Progress in Physics*, 1960. **23**(1): p. 1-65.
42. Stubenrauch, C., et al., *Polymer/Surfactant Complexes at the Water/Air Interface: A Surface Tension and X-ray Reflectivity Study*. *Langmuir*, 2000. **16**(7): p. 3206-3213.
43. Schwuger, M.J., *Mechanism of interaction between ionic surfactants and polyglycol ethers in water*. *Journal of Colloid and Interface Science*, 1973. **43**(2): p. 491-498.
44. Varga, I., et al., *Effect of Graft Density on the Nonionic Bottle Brush Polymer/Surfactant Interaction*. *Langmuir*, 2009. **25**(19): p. 11383-11389.
45. Mészáros, R., Varga, I., and Gilányi, T., *Effect of Polymer Molecular Weight on the Polymer/Surfactant Interaction*. *The Journal of Physical Chemistry B*, 2005. **109**(28): p. 13538-13544.
46. Langevin, D., *Polyelectrolyte and surfactant mixed solutions. Behavior at surfaces and in thin films*. *Advances in Colloid and Interface Science*, 2001. **89-90**: p. 467-484.

7 Interactions of Anionic SDS with Cationic DEEDMAC Vesicles at Interfaces and Under Confinement

Interactions mediated by anionic SDS and cationic DEEDMAC vesicles were investigated in solution and at interfaces. DLS and ζ -potential studies indicated strong SDS/DEEDMAC complexation in solution, with charge reversal observed upon SDS addition to positively charged DEEDMAC vesicles. Surface tension measurements and X-ray reflectivity (XRR) were performed at air-water interface. DEEDMAC bilayers were formed via vesicle rupture on mica surface, and the structure and interactions with SDS were investigated by XRR and by the surface force apparatus (SFA) at solid-liquid interface. Finally, the bulk and interfacial structures were imaged using transmission electron microscopy (TEM), cryoTEM and confocal microscopy.

7.1 Introduction

Cationic vesicles, such as those of quaternary ammonium surfactant DEEDMAC, are mimics to liposomes and promising drug and gene delivery vectors [1, 2]. It is of fundamental, as well as practical, importance to study the interactions between such vesicles and oppositely charged (anionic) surfactants. These interactions can account for the performance in their applications, and also contribute to possible vesicular rupture, aggregation and destabilisation of such dispersions. An example is the formation of catanionic vesicles comprising of cationic DDAB (didodecyldimethylammonium bromide) and anionic SDS. The phase behaviour of both cationic-rich [3] and anionic-rich [4] catanionic DDAB/SDS vesicles was studied, as well as DNA adsorption and release from such vesicles was observed [5].

The most widely used and well-studied cationic lipid is DOTAP, which is efficient carrier in nucleic acid (DNA transfection) and protein delivery [6]; however, there are some limitations to its use [7]. It is of interest to study other cationic lipids and surfactants, as well as their mixtures with co-lipids and co-surfactants, which could be used for drug and vaccine delivery [8], gene therapy [9], and other applications, such as lubrication enhancement [10] and fabric softening [11, 12].

Cationic block co-polypeptides consisting of poly(*L*-lysine)-*b*-poly(*L*-leucine) were shown to form complexes with anionic (POPS⁻, palmitoyloleoyl phosphatidylserine) and zwitterionic (DOPC, dioleoylphosphatidylcholine) liposomes *via* electrostatic interactions without any vesicle rupture. Such complexes have a large loading potential and are a promising system for drug delivery applications [13]. It is the complexation of anionic SDS molecules and micelles (where micelles can be taken as smaller non-hollow analogues of liposomes) with cationic DEEDMAC vesicles that are the focus of this chapter.

Double tailed surfactants are commonly used as lipid analogues. Vesicles containing DDAB (didecyldimethylammonium bromide) were shown to have improved cell uptake compared to DDAB-free vesicles, which can be loaded with curcumin for potential cancer therapy drug delivery [14]. DODAB (dioctadecyldimethylammonium bromide) vesicles were shown to have bactericidal properties, *via* vesicle adhesion to the bacterial membranes [15]. One of the cationic double tailed surfactants is DEEDMAC, used as a biodegradable fabric softener [16, 17]. It is a quaternary ammonium ester (not fully quaternised, at least 5% is present as an amine) with a mixed hydrocarbon chain distribution of C₁₆ and C₁₈. The ester linkage in the DEEDMAC structure improves its biodegradability, especially the kinetics, over the previously used DTDMAC (ditallowdimethyl ammonium chloride) while the same physicochemical properties have been largely retained [16].

The ester linkage and fast biodegradability kinetics however also contribute to limited shelf-life of DEEDMAC vesicles; therefore often DEEDMAC pastes contain a co-solvent and are stored at lower pH (~ 2.5) to prevent hydrolysis. Should hydrolysis occur, the presence of free fatty acids in the solution causes formation of a 3D network and viscosity increase [18]. Gelation upon SDS addition to DEEDMAC vesicles was observed in one case (Figure F.1 in Appendix).

7.1.1 Vesicle formation

Vesicles are formed by surfactant bilayers after a dry film is hydrated, and during agitation, for example by sonication, the surfactant bilayers self-close to form multilamellar vesicles (MLV) and limit the unfavourable interactions of hydrophobic tails with water. These initial vesicles are relatively large and require an energy input in order to reduce in size and the number of constituent bilayers. The energy is often provided by a prolonged sonication, or extrusion through a polycarbonate membrane of specific pore size.

Vesicle formation through sonication usually yields small unilamellar vesicles (SUV), while the diameter of vesicles formed *via* extrusion method depends on the pore size of the polycarbonate membrane, with a 100 nm membrane often resulting in uniform large unilamellar vesicles (LUV) with diameter ~120 nm. However, this is not true in all cases, as the vesicle formation is highly dependent on the conditions. Therefore, it is possible to vary the conditions (such as temperature, sonication time and concentration) to influence the size of the final vesicles formed. DEEDMAC vesicles were shown to exist in a range of sizes and lamellarity, ranging from SUVs to large multilamellar vesicles (LMV), using different techniques: stirring and sonication with varying time, flow extrusion. In this study, vesicles were formed by: a) stirring followed by sonication over prolonged time (24 hour) at 60°C and b) stirring and sonication (2 hours) followed by extrusion at 60°C. There are many other liposome/vesicle formation methods available, as outlined in literature [19]. The results presented in this chapter were obtained using DEEDMAC vesicles prepared by the extrusion method.

SFA studies of DEEDMAC bilayers prepared using the Langmuir-Blodgett (LB) deposition method have been reported previously [20, 21], investigating DEEDMAC interactions with cationic and neutral polymers, showing a modified DLVO interaction with polymer bridging the two surfaces. However, there remains a lack of understanding of the interfacial behaviour of DEEDMAC/SDS complexes, especially at the solid-liquid interface. Additionally, from a practical point of view, studying interfacial layers formed by vesicle rupture (also called vesicle fusion) is more relevant to the DEEDMAC application as fabric softener, compared to bilayers formed by a closely controlled LB deposition method. Vesicle rupture is a long-established technique to form bilayers on solid surfaces [22]. By controlling the conditions, it is possible to form mixed lipid bilayers that mimic cell membranes [23]. Furthermore, a bilayer composed of a mixture of anionic and cationic lipids was formed by vesicle fusion [24]. This range of lipid and lipid-interacting structures formed following vesicle fusion highlights the effectiveness of this simple deposition technique, yet no studies have been reported on DEEDMAC bilayers formed by this method. When the bilayers are prepared by the LB method, the surface is pulled through a DEEDMAC monolayer assembled at the air-water interface at specific surface pressure. It is possible to create a monolayer by pulling a surface through this once, or a bilayer by pulling the surface through the interface twice. In the present work, we show a simple alternative, as the rupture of the vesicles from the dispersion forms bilayers on a clean mica surface.

In this study, we have employed synchrotron X-ray reflectivity (XRR) and surface force apparatus (SFA) to study the structure and interactions of DEEDMAC bilayers and SDS at the solid-liquid interface (Figure 7.1), to correlate with their solution behaviour revealed using dynamic light scattering (DLS). We have briefly investigated the air-water interface using surface tension measurements and XRR at the interface. Finally, TEM, cryoTEM and confocal microscopy images were obtained.

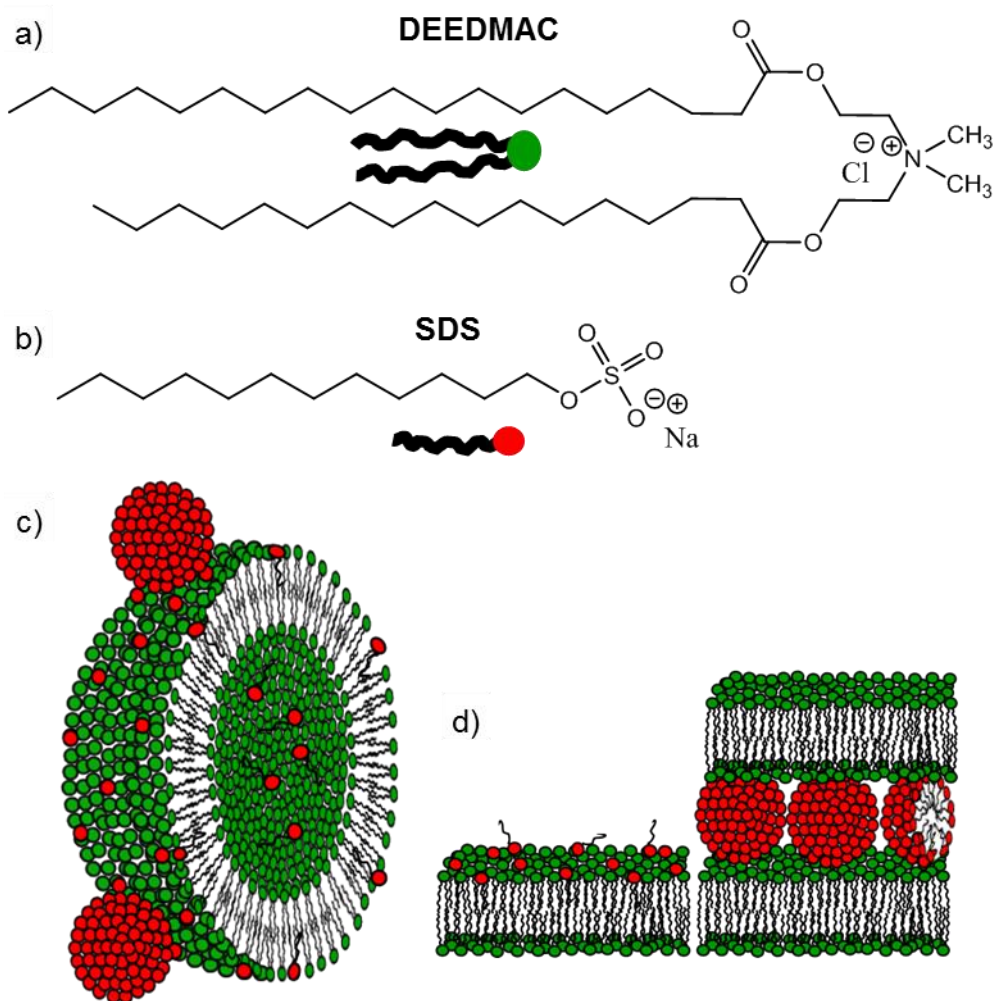


Figure 7.1 Chemical structures of a) double tailed cationic surfactant DEEDMAC and b) SDS. Schematic representations of possible interactions and complex structures formation c) in the bulk and d) at interfaces.

7.2 Methods

7.2.1 Materials

The double-tailed cationic surfactant DEEDMAC (diethoxyester dimethylammonium chloride, $C_{42}H_{84}NClO_4$) was delivered as a paste with isopropanol as solvent. The paste was

dissolved in chloroform (99.1%, stabilised with EtOH, VWR Chemicals) and dried to ensure evaporation of the isopropanol together with chloroform. SDS (sodium dodecylsulfate, Sigma Aldrich) was recrystallised from EtOH (absolute >99.8%, Sigma Aldrich) before use. DEEDMAC vesicles were doped with Nile Blue (Nile Blue A, $(C_{20}H_{20}ClN_3O)_2SO_4$, >75%, Sigma-Aldrich) and SDS was doped with fluorescein (fluorescein free acid, $C_{20}H_{12}O_5$, 95%, Sigma-Aldrich) hydrophobic dyes during sample preparation for confocal imaging, described later. MilliQ water (Millipore, resistivity 18.2 M Ω cm, <5 ppb organic matter) was used for solution preparations. Muscovite mica ($KAl_2(Si_3Al)O_{10}(OH)_2$) of A1 special grade was purchased from S & J Trading Inc.

7.2.2 Vesicle preparation

The DEEDMAC paste was dispersed in chloroform and dried to form a thin film using a flow of Argon and rotary evaporation. The dried film was then re-dispersed at a concentration of 25 mg mL⁻¹ in MilliQ by stirring (~1 hour) and sonication (1-4 hours) at 60°C. The re-dispersed DEEDMAC was then extruded at ~ 7 bar pressure and temperature controlled by a water bath at 60°C (10 mL LIPEX extruder, Thermobarrel, Northern Lipids Inc., connected to a Grant Scientific water bath, Optima T100+TC120). The solution was passed six times through a 200 nm polycarbonate membrane and then six times through a 100 nm polycarbonate membrane (both Whatman Nuclepore Track-Etch, diameter 25 mm), yielding dispersion of unilamellar vesicles with average size of 20-10 nm as determined by DLS, depending on the sonication time.

7.2.3 DLS and ζ -potential measurements

DLS and ζ -potential measurements were performed on a Nano Zetasizer ZS (Malvern Instruments Ltd.). Approximately 0.8 mL of a sample solution was injected into a plastic folded capillary cell (Malvern Instruments, DTS1070) and both the hydrodynamic radius, d_h and ζ -potential were determined following 10 s equilibration time. The d_h was measured at 173° backscatter angle. The ζ -potential (measure of a surface charge on the outer slipping plane of a particle or vesicle) was determined by a conversion of electrophoretic mobility, μ_e , by the Zetasizer Software 7.12, using the Smoluchowski method.

7.2.4 Surface Tension

The equilibrium γ data was obtained using the Wilhelmy plate method on a force tensiometer (K100, Krüss GmbH), as described in more detail in previous chapters. The Wilhelmy plate was flamed before each measurement to ensure cleanliness and surface activation. The data of DEEDMAC/SDS mixtures was recorded with 24 h between the measurements, accounting for the possible adsorption of SDS inside of the DEEDMAC vesicles and hence increasing the γ . The error bars depicted are therefore not only deviations arising from the technique uncertainties, but also account for the change in γ data within a 24-h period.

7.2.5 XRR at solid-liquid and air-water interfaces

XRR data at both solid-liquid and air-water interfaces was performed at I07 beamline (Diamond, UK). The set-up for an air-water XRR experiment was described earlier, using adsorption troughs and DCD to allow for varying incident angle (θ), at 12.5 keV, and therefore accessing the Q range (0.02 – 0.8 Å⁻¹). The same energy (12.5 keV) was used to obtain XRR data at the solid-liquid interface (Q range 0.02 – 0.7 Å⁻¹), using the “bending mica” technique [25]. The sample was mounted on a hexapod which allowed movement in 3 directions, as well as rotation along each of the movement axis. The θ was therefore varied by the sample rotation along its axis and not by DCD. The sample alignment was also less trivial, as described in more detail in literature [26, 27]. The data was corrected for the beam footprint and normalised according to the critical edge and no background subtraction was applied. Thickness, t , of the interfacial layer at both interfaces was determined from Kiessig fringes spacing, ΔQ , where

$$t = \frac{2\pi}{\Delta Q}.$$

7.2.6 Surface force apparatus (SFA)

The surface force apparatus (SFA) was first described by Tabor and Winterton in the late 1960s [28, 29], when the van der Waals forces were measured between two mica surfaces in air. The SFA was later modified, most notably by Israelachvili in the 1970s, to include studies of adsorbed thin films on the mica surfaces [30, 31] and surface forces measurements in liquids [32-34]. The next significant step in the advancement of the technique was reported by Klein in the early 1990s, where the addition of a sectored piezoelectric tube and the control of its lateral movement enabled studies of shearing forces between the adsorbed thin films [35]. This development opened up the possibilities of studying lubrication properties of thin films both in

air and in liquid [36-38]. Since then, ongoing effort has been put into the SFA modification, such as the development of the SFA2000 which was designed to consist of fewer parts therefore requiring less stringent machining and easier assembly [39]. Furthermore, a prototype device for 3D detection of the forces and displacement was described [40], resonance shear measurements were implemented alongside SFA [41], and in general improvements in the optics and data fitting approach have been developed [42]. Variation of the substrate from mica to cationic sapphire enabled the study of adsorbing anionic species such as SDS [43]. A numerous number of systems have been investigated using the SFA, *e.g.* polymers in aqueous [44] and non-aqueous solvents [45], polymer brushes [46], polymersomes [47], lipid vesicle dispersions [48], ionic liquids [49], and graphene surface energy [50].

Due to the relatively large contact area between the two surfaces, the precise measurements are extremely sensitive to sample inhomogeneity and contamination, therefore the cleaning procedure and sample preparation must be performed with utmost care.

7.2.6.1 Cleaning procedure

Glassware used for SFA experiment was cleaned in a Piranha bath (3:1 H₂SO₄:H₂O₂), followed by rinsing and soaking in MilliQ water, rinsing with absolute ethanol (EtOH) and drying with N₂ flow. All metal parts of the SFA and acid-resistant tools were sonicated in acetone:EtOH mixture (50:50), rinsed with MilliQ and soaked in 10% nitric acid bath, followed by the same rinsing procedure. All non-acid-resistant parts (such as the plastic connectors of the tubing, and the PTFE tubing itself) were sonicated in EtOH bath for 30 min, and thoroughly rinsed with MilliQ and EtOH, prior to drying with N₂ flow. The syringes used for sample injection were rinsed with MilliQ, and EtOH, dried, UV ozone cleaned for 10 min, rinsed with EtOH and finally dried with N₂ flow.

7.2.6.2 Sample preparation

Muscovite mica was cleaved under laminar flow hood to a thickness ~ 2-5 μm (as determined by the colour of the cleaved sheet under light, Figure 7.2a) and was cut using a hot Pt wire (99.999%, Sigma Aldrich) with the wire always downstream from the piece to be cut, and the cut sheet was laid down on and adhered to a much thicker freshly cleaved mica “backing” sheet to avoid contamination. The thinly cleaved mica adhered to the backing sheet was then coated by ~ 40 nm thin layer of silver (Ag beads, 99.9999%, Sigma Aldrich) using the thermal evaporation method (Edwards Coating System E306A). The silvered mica sheet was placed ~

30 cm above the Ag beads contained in a molybdenum boat which was heated by passing a current of ~ 35 A under high vacuum ($\sim 10^{-6}$ Torr). The silvered mica backing sheet was then stored in a desiccator unit under vacuum. For each experiment, a piece of thinly cleaved back-silvered mica was cut into two ~ 1 cm² pieces to assure consistent thickness of the two mica surfaces. The mica pieces were then glued onto quartz cylindrical disks using a thermal responsive glue (Epon 1004, Shell) melted at $\sim 180^\circ\text{C}$. The molten glue was carefully agitated by slow circular motions to eliminate any air bubbles present. Mica was then placed over the uniform layer of melted glue, silvered side down and exposing the clean surface on top (thus referred to as back-silvered mica). The quartz cylinder was promptly taken off the hot plate for the glue to harden and to minimise any possibility of burning the mica piece. The prepared surfaces on the glass cylinders were stored in a glass petri dish (Figure 7.2b) in a laminar flow hood before being mounted onto the top and bottom stage holders of the SFA in a cross-cylindrical geometry into the relevant holders.

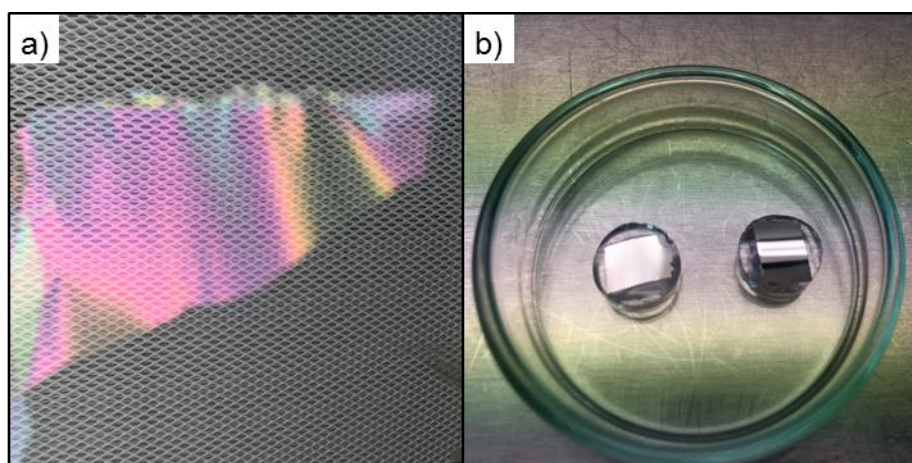


Figure 7.2 a) example of thinly cleaved mica of thickness suitable for an SFA measurement, as observed by the purple colour. b) back-silvered mica glued onto two quartz cylindrical disks, used as top and bottom surfaces.

7.2.6.3 Bristol set-up and measurement procedure

The main mechanical components of the Bristol SFA were based on the design by Klein (referred to as surface force balance, SFB) [35], with a few modifications, mainly in the control of the motor and spectrometer-camera pairing, outlined in [51]. A linear actuator motor was used to drive the bottom surface into contact with a range of movement of 20 mm, with precise control over the step size and speed ($100 \mu\text{m s}^{-1}$ down to 1 nm s^{-1}). An sCMOS camera (100 frames per second) is used to record the fringes from the spectrometer.

The normal force, F_N , applied is determined from the deflection of the horizontal leaf springs with known spring constant, k , according to the Hooke's law (Equation 7.1)

$$F_N = k\Delta x, \quad \text{Equation 7.1}$$

where Δx is the deflection of the spring.

The bottom surface was mounted in a so-called boat attached to a pair of horizontal leaf springs (spring constant $k_N = 100 \text{ N m}^{-1}$, Figure 7.3a). The downward and upward motion of the bottom surface is controlled by a linear stepping motor (Physik Instrumente GmbH & Co. KG), with a precisely controlled step-size $< 1 \text{ nm}$. The top surface was mounted on top of a four-sectored piezoelectric tube which was attached to a set of vertical springs ($k_s = 120 \text{ N m}^{-1}$, Figure 7.3b).

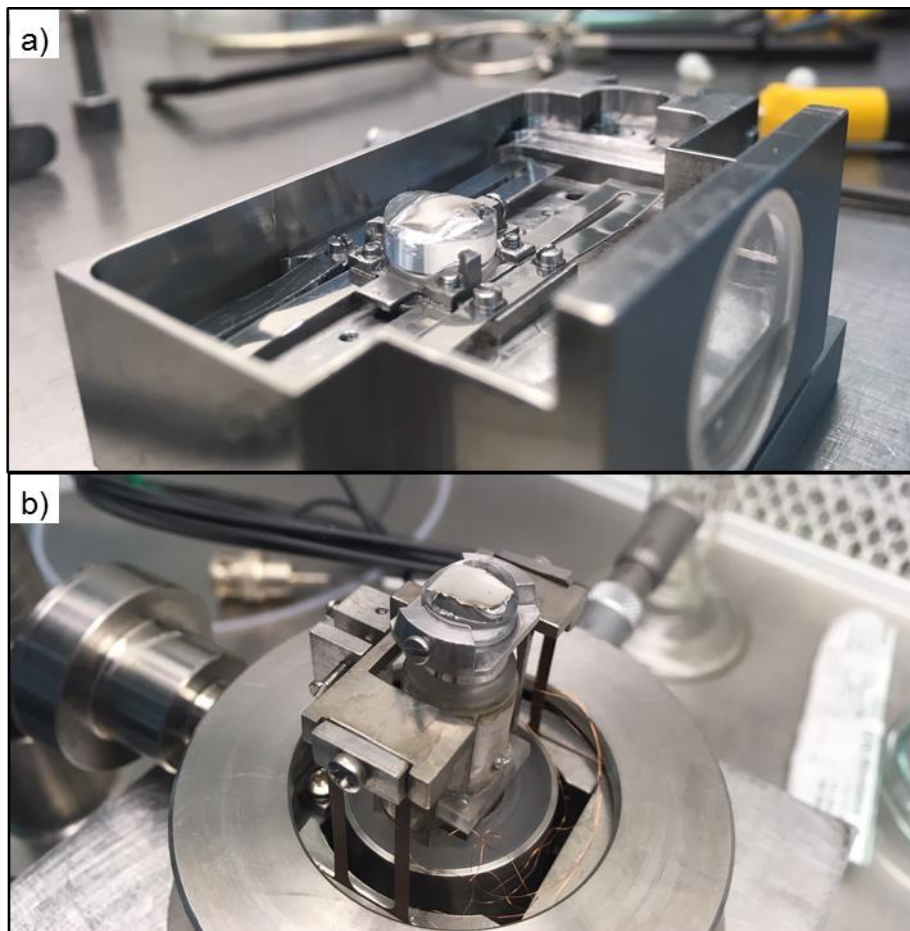


Figure 7.3 Back-silvered mica glued on quartz disks mounted on a) set of horizontal leaf springs in the boat and b) attached to the sectored piezoelectric tube and a set of vertical springs.

The two back-silvered mica surfaces create an optical cavity when brought together, where the light reflected between the two surfaces produces constructive interference giving rise to wavelength spectrum of narrow bright bands, known as fringes of equal chromatic order (FECO). The position of FECO then enables calculation of separation distance, D by the transfer matrix method [52], described later in 7.2.6.4.1. Multiple beam interferometry is used

to determine the separation distance, D , between two mica surfaces under applied normal force, F_N , and shearing force, F_s .

The top surface can be moved laterally by applying voltage to the piezoelectric tube, with the lateral displacement detected by a capacitance probe (Accumeasure 9000 MT Instruments). The normal and shear motions, as well as spectrometer and camera, were controlled via a home-build interface in LabView (written by Tim Snow [53]).

Liquid sample addition was enabled through a set of syringes and tubing, allowing for a solution exchange *via* withdrawal of the old solution into a refusal syringe, and subsequent injection of the new solution from a separate syringe. Repeating this process multiple times enabled a complete solution exchange while the surfaces were kept hydrated. All SFA measurements were performed at room temperature (RT), in absence of Ca^{2+} or low pH (unlike previously reported SFA studies of DEEDMAC bilayers [20, 21]). Altogether, three separate SFA experiments were performed to ensure repeatability of the measurements. In each experiment, and at each change of medium in which the mica substrates were immersed (*i.e.* following sample injections), multiple measurements were taken, repeating approach and retraction of the surfaces at the same contact spot at least 3 times, with a minimum of 3 different contact spots measured for each sample. For clarity, only one approach and retraction runs are shown in this chapter, as the focus of the study was the influence of SDS addition to DEEDMAC bilayers and no strong hysteresis or effect of incubation/adsorption time was observed. The repeatability/variation in the determined separation distance is represented by the uncertainty in t calculated from each contact spot.

For each contact spot, the surfaces were brought into contact leading to a jump-in and flattening of FEEO. The motor position was noted, and the surfaces were pulled apart while observing any jump-out distance. An automated sequence of steps of defined step size, speed and waiting time was set-up using the LabView interface for the following approach and retraction runs. For approach, each run was started $\sim 10 \mu\text{m}$ from expected contact, with a common sequence of steps as follows:

- 1) slow approach over short step size while the surfaces are far apart, allowing for observation of any weak interaction forces: 200 steps of $0.02 \mu\text{m}$ and approach speed of $0.02 \mu\text{m s}^{-1}$

- 2) medium step size and speed when surfaces approach contact: 100 steps of 0.05 μm , approach speed of 0.05 $\mu\text{m s}^{-1}$
- 3) relatively large step size and speed where the surfaces are pushed together and relatively large normal force is applied: 200 steps of 0.1 μm , approach speed of 0.1 $\mu\text{m s}^{-1}$

In the case of retraction run, the number of steps and their length and speed were determined from the expected jump-out distance. A common sequence of steps during retraction of surfaces would be:

- 1) large step size and speed as most surfaces studied experienced relatively strong adhesion forces and hence large jump-out distance: 20 steps of 0.5 μm , retraction speed of 0.5 $\mu\text{m s}^{-1}$
- 2) medium step size and speed when motor position approaches that of expected jump-out distance: 30 steps of 0.1 μm at retraction speed of 0.1 $\mu\text{m s}^{-1}$
- 3) small step size and speed allowing for precise detection of the jump-out distance: 300 steps of 0.02 μm , retraction speed of 0.02 $\mu\text{m s}^{-1}$

The number of steps, their size and speed were adjusted to each sample and contact spot. The waiting time before each step was taken was kept consistent at 5 s for all the measurements performed.

7.2.6.4 Data analysis

Firstly, the bare mica surfaces were brought into contact and t of the mica itself was calculated from the FECO. The fringe pixel position is compared to a Hg lamp calibration image with precisely known wavelengths (546.07, 576.95 and 579.07 nm) detected by the spectrometer. A straight-line calibration plot of the known wavelengths vs pixel position detected was obtained, which then enabled the conversion of pixel position detected from the FECO of experimental data into their corresponding wavelengths. From this information, the separation distance (D) can be calculated, using either the Israelachvili equation (Equation 7.2) [31] or the transfer matrix method [52]. The Israelachvili equation takes the form of:

$$\tan(k \mu_3 D) = \frac{2\bar{\mu} \sin\left(n\pi \frac{\Delta\lambda_n}{\lambda}\right)}{(1 + \bar{\mu}^2) \cos\left(n\pi \frac{\Delta\lambda_n}{\lambda}\right) \pm (\bar{\mu}^2 - 1)}, \quad \text{Equation 7.2}$$

where μ_3 is the refractive index of the sample, $\bar{\mu}$ is the mica refractive index, n is the fringe order, λ is the wavelength/position of the tracked fringe and $\Delta\lambda$ is the shift of the tracked fringe wavelength/position relative to the mica-mica contact fringe position. The use of this equation is relatively straightforward when the refractive indices of the sample are known, however there is a limitation of its use at separation distances larger than ~ 200 nm [54] due to poor trackability of the contact fringe.

In this study, the transfer matrix method was therefore used to determine the separation of the mica surfaces, as implemented into a Python script (written by Tim Snow [53]) for FEKO analysis.

7.2.6.4.1 *The transfer matrix method*

The transfer matrix method was described by Kienle and Kuhl relatively recently [52], as an analysis method of interferometry data, such as those obtained during SFA experiments, and the calculation of optical thin film thickness based on the variation of refractive indices without the need of contact measurement.

The transfer matrix method is based on the description of light passing through a medium as a sum of two-dimensional matrices [55] which describe the position (x), refractive index (n_x) and thickness (z) of each layer. In a typical SFA experiment, the light will pass through the following 7 layers: air, silver, mica, sample cavity, mica, silver, and air. Each of these layers can then be described by the following matrix, M_x :

$$M_x = \begin{bmatrix} \cos\left(\frac{2\pi n_x z_x}{\lambda}\right) & \frac{-i}{p_x} \sin\left(\frac{2\pi n_x z_x}{\lambda}\right) \\ -ip_x \sin\left(\frac{2\pi n_x z_x}{\lambda}\right) & \cos\left(\frac{2\pi n_x z_x}{\lambda}\right) \end{bmatrix}, \quad \text{Equation 7.3}$$

where λ is the wavelength of the incident beam and p_x is the dielectric value of the layer, defined as:

$$p_x = n_x \cos(\theta), \quad \text{Equation 7.4}$$

where θ is the incidence angle at which the light travels with respect to the z-axis of the layers.

A matrix M_x is created for each λ and layer, and the product of each of these M_x gives rise to the system matrix, M [56]. The transmittance, T , of light that travels through the layers of the system can then be written as:

$$T = \left| \frac{2p_n}{(M_{11}+M_{12}p_1)p_n+(M_{11}+M_{12})p_1} \right|^2. \quad \text{Equation 7.5}$$

The calculation can be performed on a range of wavelengths and thicknesses to produce a 2D representation of fringe positions, which can then be matched to the experimental data obtained. Such calculations require more computational power compared to the more straightforward use of the Israelachvili equation, however in return produce more accurate results as no approximations are used and the wave behaviour is determined exactly.

The position of FECO is determined from the experimental data by fitting Gaussian functions to the regions of interest along several lines to locate the pixels of the fringe peaks using intensity thresholds:

$$f(x) = ae^{\left(\frac{-(x-b)^2}{2c^2}\right)}. \quad \text{Equation 7.6}$$

The fringe positions (and their corresponding wavelengths obtained by comparison to Hg lamp calibration) can then be converted into a one-dimensional fringe location array, a , which is compared to the theoretically calculated fringe location array, b . The closest match, according to Equation 7.7, to the experimental data is then taken as the separation distance for the FECO image recorded at the time.

$$c_{ab}[k] = \sum_n a * [m] \times b[m + k]. \quad \text{Equation 7.7}$$

The fringe position calculation is performed for each data point recorded and evaluated using the transfer matrix method to determine D during the approach and retraction of the surfaces, and plotted as F_N vs D .

Finally, due to mica birefringence the FECO are often separated into a β and γ doublet, depending on the orientation of the two mica pieces relative to each other. The largest doublet

separation is observed when mica surfaces are at 90° relative to each other, and no separation between β and γ , *i.e.* a singlet, is observed at 0° rotation of the surfaces. The FECO splitting into the doublet influences the accuracy of the calculation, and so either the average fringe position or the β fringe position, should be used. In the data presented in this chapter, the position of the β fringe was used for the calculations.

7.2.6.4.2 Debye length determination

The Debye length, κ^{-1} , determined from Equation 7.8 is a measure of the screening length of charges in solution, or in simple terms it is the distance over which electrostatic effects are experienced [49, 57].

$$\kappa^{-1} = \left(\frac{e^2 \sum_i \rho_i z_i^2}{\epsilon_0 \epsilon_r k_B T} \right)^{-\frac{1}{2}}, \quad \text{Equation 7.8}$$

where e is the charge of an electron, ρ_i is the bulk number density of the i -th ion, z_i is the valency of the i -th ion, ϵ_0 is the permittivity of free space, ϵ_r is the dielectric constant, k_B is the Boltzmann constant and T is the temperature.

In this study, κ^{-1} was determined by fitting an exponential decay to the log-normal plot of normal force/radius *vs* separation distance (Figure 7.13). Such fitting follows the DLVO (Derjaguin, Landau, Verwey and Overbeek) theory, where the total force, $F(D)_{DLVO}$, is a sum of attractive van der Waals interactions, $F(D)_{vdWaals}$, and repulsive electrostatic double layer, $F(D)_{edl}$, [58]:

$$F(D)_{DLVO} = F(D)_{vdWaals} + F(D)_{edl}, \quad \text{Equation 7.9}$$

$$F(D)_{vdWaals} = \frac{AR}{6D^2}, \quad \text{Equation 7.10}$$

$$F(D)_{edl} = \frac{128\pi k_B T \rho R}{\kappa} \left(\tanh \left(\frac{ze\psi_0}{4k_B T} \right) \right)^2 e^{-\kappa D}, \quad \text{Equation 7.11}$$

Where A is the Hamaker constant, R is the radius of surface, D is the separation distance, k_B is the Boltzmann constant, T is the temperature, ρ is the bulk concentration of ions in solution, z

is valency of the ions in solution, e is the electron charge, ψ_0 is the surface potential and κ^{-1} is the Debye length.

For the purposes of κ^{-1} determination (Equation 7.13), the expression for $F(D)_{\text{vdWaaals}}$ is a constant, and $\frac{128\pi\kappa_B T \rho R}{\kappa} \left(\tanh\left(\frac{ze\psi_0}{4\kappa_B T}\right)\right)^2$ portion of $F(D)_{\text{edl}}$ is also a constant.

The DLVO theory is often not sufficient to describe colloidal system, such as in a system of liquid droplets [47], and the overall force can be expressed as:

$$F(D) = aD^{-\frac{5}{4}} + be^{\kappa D}, \quad \text{Equation 7.12}$$

where a and b are constants, D is the separation distance and κ is the reciprocal value of Debye length. The term $aD^{-\frac{5}{4}}$ originates from the osmotic repulsion and the term $be^{\kappa D}$ originates from the electrostatic double layer repulsion. Such modification still follows the general expression:

$$y = y_0 + Ae^{\kappa x}, \quad \text{Equation 7.13}$$

Where y and x are experimentally obtained normalised force and separation distance, and y_0 , A and κ are the fitting parameters to the exponential decay of a log-normal plot. The value of κ^{-1} is then simply obtained from the reciprocal value of such fit.

7.2.7 Transmission electron microscopy (TEM)

Transmission electron microscopy (TEM) was used to image samples of DEEDMAC vesicles and SDS. Two TEM techniques were used: negative stain TEM and cryoTEM. The TEM images were collected with technical assistance from Judith Mantell at the Wolfson Bioimaging Centre.

7.2.7.1 Negative stain TEM

The negative stain TEM is a commonly used technique, with sample preparation methods constantly improving [59]. Negative stain (3% aqueous solution of uranyl acetate, UA) was applied to samples of DEEDMAC vesicles and SDS. Firstly, 5 μL was dropped on a lacey

carbon grid and allowed to rest for 1 minute after which it was dabbed with filter paper and 5 μL of the UA solution was applied. The carbon grid was gently waved to allow for mixing of the negative stain, which was then dabbed off. The negative stain TEM was collected on FEI Tecnai 12 120kV BioTwin Spirit TEM.

7.2.7.2 cryoTEM

Sample preparation for cryoTEM is nontrivial as the sample has to be vitrified rapidly to eliminate formation of crystallised ice which would obscure the view and influence any structures formed near it [60]. No staining agent was used during the sample preparation for cryoTEM. A lacey carbon grid was first glow discharged for 20 s (Leica EM ACE 600). The lacey carbon was then moved to a humidity-controlled chamber (Leica EM GP) and 5 μL of sample was injected on the lacey carbon grid using a pipette, blotted for 1.2 and 1.5 s (two sets of samples to find the optimum blotting time and therefore film thickness) with a filter paper and then rapidly plunged in liquid ethane to vitrify (Figure 7.4). The sample was then stored in liquid nitrogen until imaged. The samples were imaged on a FEI Tecnai 20 200kV Twin Lens TEM equipped with cryo-equipment (Gatan cryo-transfer holder and FEI cold box).

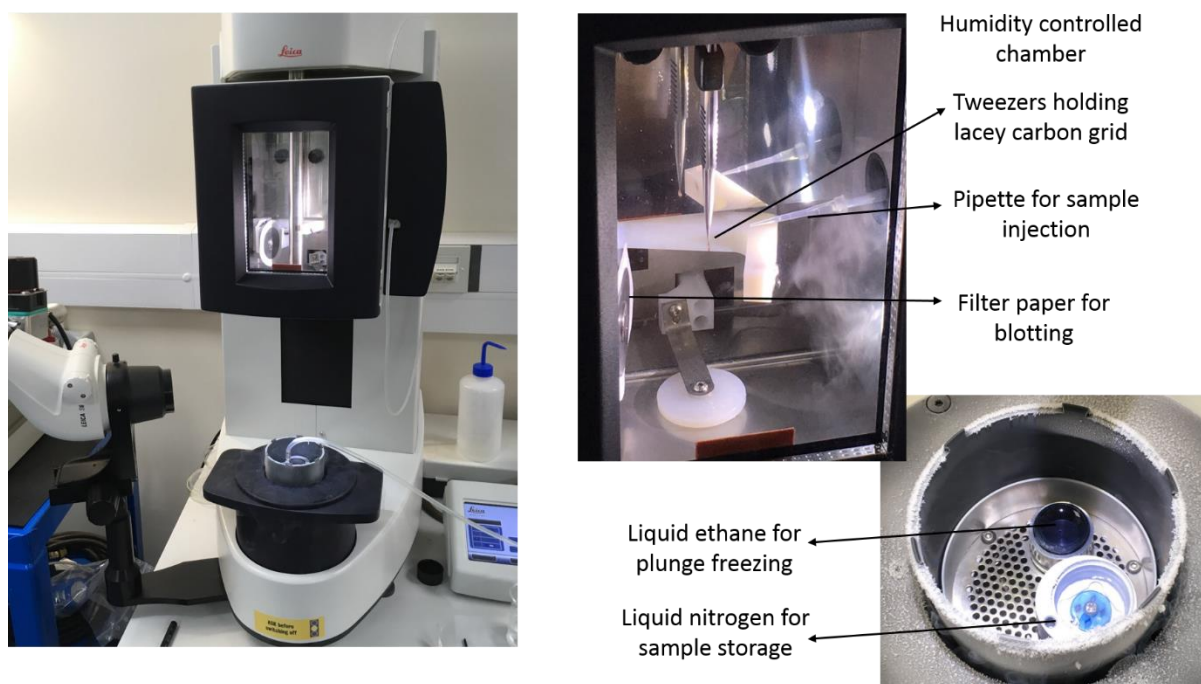


Figure 7.4 An outline of sample vitrification and storage, as prepared for cryoTEM.

7.2.8 Confocal Microscopy

The confocal microscopy images were collected on a Leica SP8 AOBS confocal laser scanning microscope (STED 1 at Wolfson Bioimaging Centre), attached to a Leica DM8i8 inverted epifluorescence microscope, with a 100x HC PL APO CS2 oil lens (100x magnification, 0.09 mm, working distance, 1.4 numerical aperture). The images were collected with the technical assistance of Alan Leard. Two STED lasers were used, one excited at 488 nm and detected by the hyperdetector HyD1SMD 1 set to detect wavelengths between 498 and 535 nm aimed to detect SDS-fluorescein. The second laser was excited at 633 nm and detected by HyD3SMD2 (wavelengths between 643 and 737 nm), sensitive to the DEEDMAC-Nile Blue complexes. The two separate colour channels were then both included in a single picture.

7.2.8.1 Sample preparation

DEEDMAC was doped with Nile Blue (~ 500:1 DEEDMAC:Nile Blue molecules) during the first step of vesicle preparation, *i.e.* Nile Blue and DEEDMAC paste were both dissolved in chloroform, which was then dried into a thin film, re-dissolved in water and extruded. The Nile Blue is a hydrophobic dye and so it was assumed the dye molecules were incorporated into the hydrophobic parts of the DEEDMAC vesicles, *i.e.* the hydrocarbon tail region.

Similarly, SDS was doped with hydrophobic fluorescein which would associate with the hydrocarbon tail of the SDS and therefore be present in higher concentrations in samples containing SDS micelles compared to free SDS molecules. The fluorescein was dissolved in chloroform (1 mg mL^{-1}) and ~ 40 μL added to 2 mL aqueous solution of 10 cmc SDS (~ 1300:1 SDS:fluorescein molecules, *i.e.* 1 fluorescein molecule every ~ 20 SDS micelles [61]).

DLS and ζ -potential measurements of dye-doped DEEDMAC and SDS were consistent with pure samples of DEEDMAC vesicles and SDS, and so the dye molecules are not thought to disturb the inherent structures. The two hydrophobic dyes used were excited at different wavelength and so enabling the use of two separate lasers and a dedicated channel to each emission wavelength, hence a complete separation of the DEEDMAC (represented in green) and SDS (represented in red) molecules in confocal images.

7.3 Results

7.3.1 DLS and ζ -potential

The hydrodynamic diameter d_h determined by DLS and the ζ -potential data are summarised in (Figure 7.5a). Firstly, d_h of pure DEEDMAC vesicle dispersion was measured as $\sim 27 \pm 8$ nm, with the average ζ -potential ~ 66 mV. The ζ -potential distribution however was very wide, with values ± 100 mV on average (with peaks in the measurement recorded only at positive values).

With SDS addition at 0.05 cmc, the size of the vesicles increased very slightly to $d_h \sim 34 \pm 8$ nm, and so did the positive charge. Surprisingly, the charge distribution became much smaller, with a value of $\sim 79 \pm 10$ mV, suggesting formation of more uniformly charged particles in the dispersion. Increasing the SDS concentration to 0.1 cmc did not cause an increase in the average $d_h \sim 34$ nm; however, the size distribution increased to ± 24 nm, suggesting an array of structures present in the bulk, where SDS molecules could be adsorbing onto the DEEDMAC vesicle outer bilayer and causing a slight d_h increase, as well as penetrating the bilayer and causing vesicle rupture leading to smaller d_h . Any adsorption of SDS to the outer DEEDMAC bilayer was however not enough to cause charge reversal (ζ -potential $\sim 81 \pm 14$ mV). Increasing the SDS concentration to 0.5 cmc caused decrease in the ζ -potential to $\sim 62 \pm 6$ mV, indicative of larger number of SDS molecules adsorbing to the vesicle bilayer surface, also manifested by significant d_h increase to $\sim 55 \text{ nm} \pm 33$ nm.

At concentration of 1 cmc SDS, there was a charge reversal observed to ζ -potential $\sim -57 \pm 6$ mV, and d_h increase to $\sim 67 \pm 60$ nm. This data suggested SDS/DEEDMAC complexation has taken place [62], with SDS adsorbed onto the DEEDMAC vesicles in high enough concentration to overturn the initial positive charge. It is highly unlikely the negative charge measured is purely from SDS micelles in the solution, yet the pure SDS micelles in solution could contribute to the average ζ -potential value. Before the complete charge reversal, there was expected to be a charge neutralisation and flocculation of the particles. The flocculation was not observed, and the charge reversal point was found to be between 0.5 and 1 cmc SDS.

At 2 cmc SDS, the size decreased slightly ($d_h \sim 55 \pm 49$ nm), possibly indicative of SDS molecules interdigitating into the vesicle bilayer and penetrating inside the vesicle [62]. The charge however did not increase, so this hypothesis could not be confirmed.

At 5 cmc SDS, the size increased markedly, up to $d_h \sim 92 \pm 88$ nm, with ζ -potential $\sim -83 \pm 12$ mV. This is not possible to explain purely by SDS molecules and/or micelle adsorption onto the vesicles, as the size increase was much higher than few SDS micelles (SDS micelle $d \sim 4$ to 5 nm [63-65]). It is therefore postulated the SDS micelles acted as bridging points between two or more vesicles. The ζ -potential remained negative, and so a full coverage of the vesicle by SDS was still assumed. The size distribution was high at this point, as the bridging and aggregation behaviour contributed to a number of possible cluster sizes produced. A schematic representation of the possible DEEDMAC/SDS complexes in the bulk is shown below (Figure 7.5b), bar the bridging between two or more vesicles.

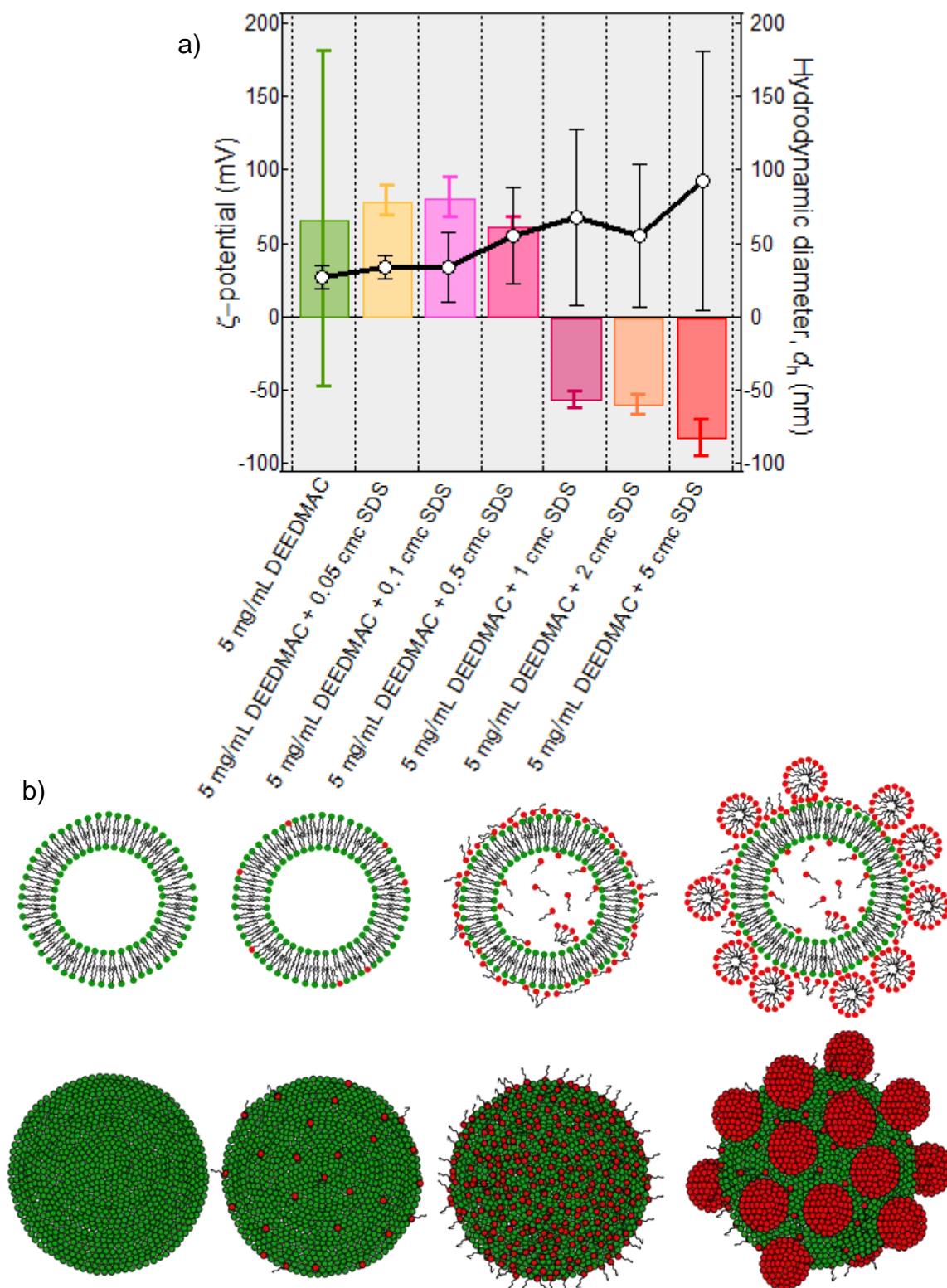


Figure 7.5 a) DLS and ζ -potential measurement correlated to a 2D sliced and a “3D” schematic representation of the bulk (b). With increasing SDS concentration, the size of the DEEDMAC vesicles increases steadily indicating SDS adsorption onto the vesicle surface. This is also confirmed by the surface charge reversal, implying the vesicle surface fully coated by the anionic SDS. At SDS concentrations above its cmc, we could speculate whole SDS micelles could adsorb onto the cationic vesicle surface, and also provide bridging between two or more vesicles.

7.3.2 Surface Tension

Dynamic surface tension measurements of 0.8 mM (equivalent to $\sim 0.6 \text{ mg mL}^{-1}$) DEEDMAC and SDS mixtures were previously described by Cocquyt *et al.* [62]. It was reported that the γ of pure DEEDMAC was approximately equal to that of water at $\sim 72 \text{ mN m}^{-1}$, and decreased after addition of SDS, but later (after approximately 2 hours) increased again suggesting the SDS adsorbed inside into inner bilayers of the vesicle and was therefore not at the interface anymore and so did not contribute to γ lowering.

In the current work (Figure 7.6), the surface tension was lowered upon addition of DEEDMAC itself quite significantly, reaching a plateau at $\sim 47 \text{ mN m}^{-1}$ at DEEDMAC concentrations of 0.5 mg mL^{-1} and above. Two DEEDMAC concentrations were then chosen, above and below that of previously studied: 0.05 and 5 mg mL^{-1} (labelled as Point 1 and 2), and γ of their mixtures with SDS was measured.

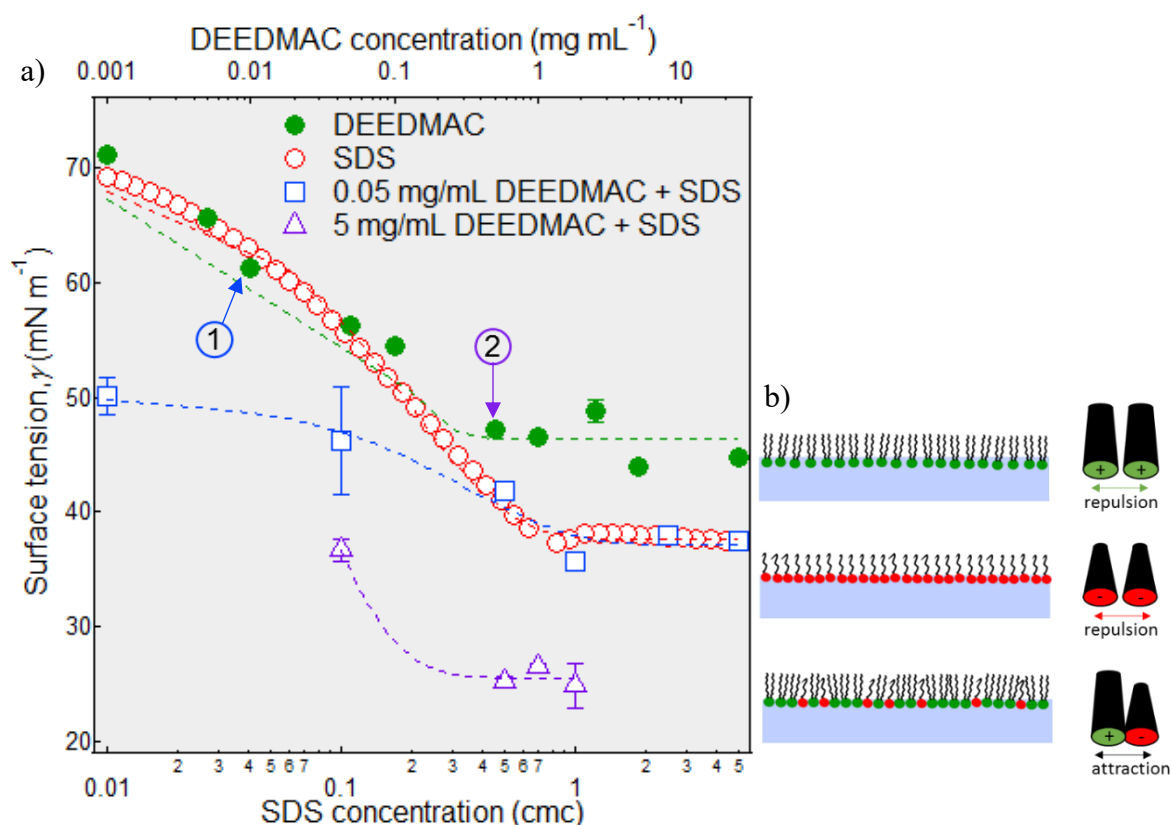


Figure 7.6 The surface tension data of DEEDMAC vesicles (green), SDS (red) and their mixtures containing 0.05 and 5 mg mL^{-1} DEEDMAC vesicle dispersion with increasing SDS concentration (blue and purple, respectively). The data point marked as 1 highlights the value of pure 0.05 mg mL^{-1} DEEDMAC, and data point marked as 2 shows the value of pure 5 mg mL^{-1} DEEDMAC vesicle dispersion. The schematic representation in b) is a possible interfacial layer, with the charged headgroups and the interactions involved.

A strong synergistic effect ($\Delta\gamma > 10 \text{ mN m}^{-1}$) was observed after addition of SDS to the DEEDMAC system at both DEEDMAC concentrations. With increasing SDS concentration to above 0.5 cmc, γ data overlapped with that of pure SDS in 0.05 mg mL^{-1} DEEDMAC/SDS but synergistic γ lowering in mixtures of 5 mg mL^{-1} DEEDMAC/SDS ($\Delta\gamma \sim 13 \text{ mN m}^{-1}$). The synergistic γ lowering could be attributed to better packing of the molecules at the interface, with attractive forces between the oppositely charged head groups of anionic SDS and cationic DEEDMAC, compared to the pure surfactant systems with repulsive forces between the likely charged headgroups (Figure 7.6b).

In the majority of the systems studied (bar 0.05 mg mL^{-1} DEEDMAC and 0.1 cmc SDS), there was no significant increase of γ with time observed within a 24-hour period (as demonstrated with the error bars of the data points in Figure 7.6), therefore we could not conclude that SDS molecules migrated from the surface into the vesicles at the concentrations tested.

7.3.3 XRR at air-water interface

The organisation of DEEDMAC and SDS at the air-water interface was investigated using XRR. The thickness, t , of the interfacial layer was determined from the fringe spacing, as depicted in Figure 7.7. A layer of pure DEEDMAC adsorbed at the interface from a solution containing 5 mg mL^{-1} of $\sim 20 \text{ nm}$ large unilamellar vesicles was evaluated to be $\sim 2 \text{ nm}$ thick, which corresponded to a DEEDMAC monolayer at the air-water interface (previously reported DEEDMAC bilayer t ranged from compressed $\sim 3 \text{ nm}$ to 5.4 nm at mica surfaces [20, 21] and $\sim 3.5 \text{ nm}$ in vesicle solution [66]).

This t decreased to $\sim 1.7 \text{ nm}$ upon addition of low concentration of SDS (0.1 cmc SDS), which could be attributed to a compressed interfacial monolayer containing strongly interacting DEEDMAC and SDS, with SDS molecules intercalated in the layer. With addition of higher SDS concentration, the layer thickness increased, suggesting some form of interfacial restructuring between the DEEDMAC and SDS, forming complexes between the oppositely charged surfactants.

This complexation was even more pronounced in the case of SDS concentrations above its cmc. In these cases, there was a layer of thickness $\sim 2 - 2.9 \text{ nm}$ that can be attributed to a monolayer of DEEDMAC at the interface, with regions of higher thickness accounting for DEEDMAC/SDS complexes. A layer thickness of $\sim 21 \text{ nm}$ in the case of 5 cmc SDS with

DEEDMAC could be accounted for by either a multilayer structure alternating DEEDMAC and SDS bilayers, a multilayer structure alternating DEEDMAC bilayers and SDS micelles, or a layer of small DEEDMAC vesicles at the interface, possibly interacting with some SDS molecules. The option of DEEDMAC vesicles and no complexation with SDS is highly unlikely, as it was the presence of high concentration of SDS that lead to the increase in the layer thickness. Additionally, the change in the interfacial layer structure compared to pure DEEDMAC or SDS layers with strong interactions also agreed with the synergistic γ lowering of the DEEDMAC/SDS complexes compared to the pure surfactant systems (*cf.* Figure 7.6).

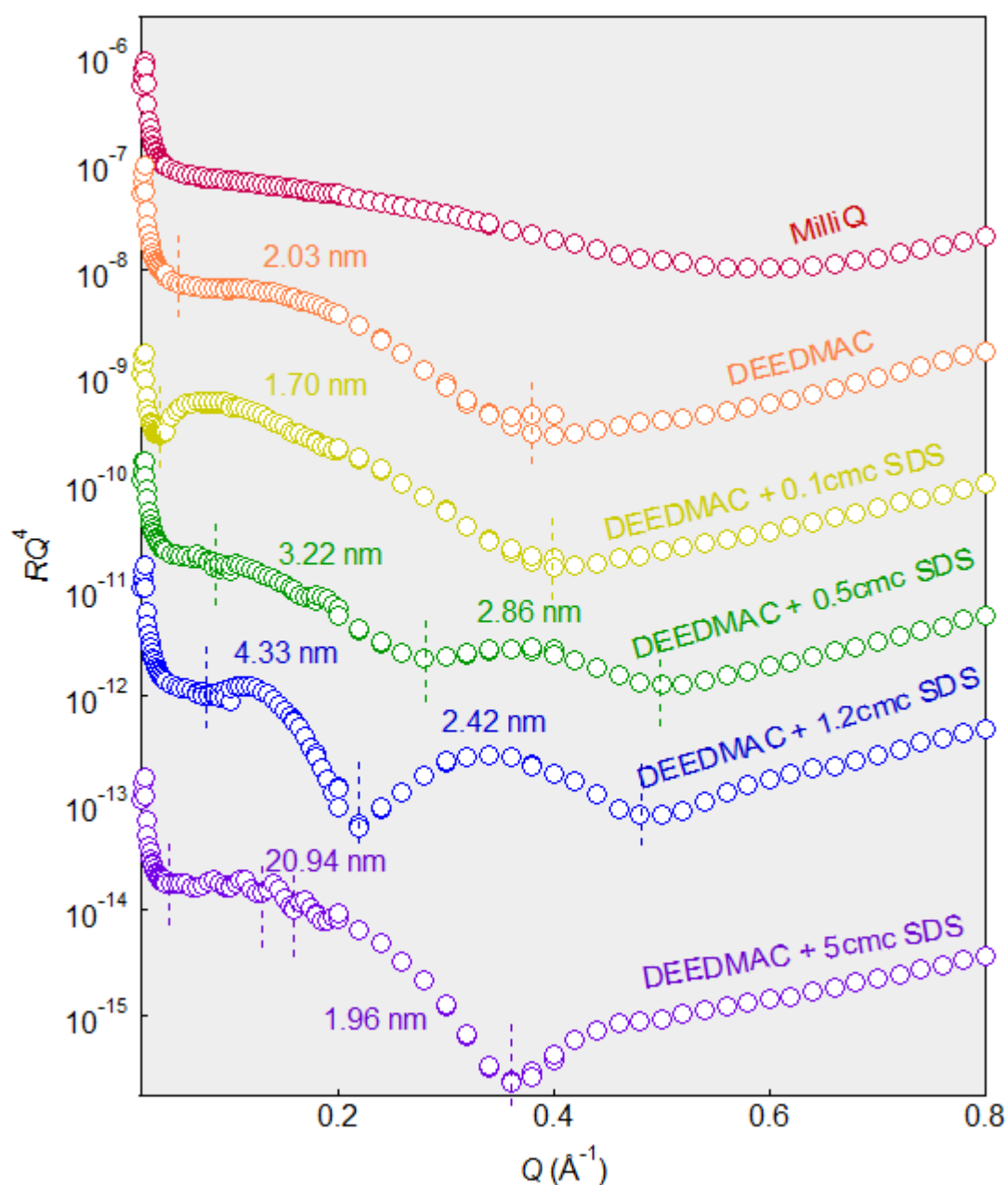


Figure 7.7 XRR data of DEEDMAC/SDS mixtures at the air-water interface, with layer t determined from the fringe spacing marked by dashed lines.

7.3.4 DEEDMAC/SDS adsorption at solid-liquid interface: XRR study

XRR at the solid-liquid interface following injection of 5 mg mL⁻¹ DEEDMAC vesicle dispersion onto a mica surface showed strong adsorption of DEEDMAC (Figure 7.8) due to the electrostatic attraction between the negatively charged mica surface and the cationic DEEDMAC head groups. The thickness determined from the fringe spacing was initially ~ 3.9 nm, which corresponded to a formation of a bilayer [66], but after few minutes allowed for equilibration, t decreased to ~ 2.9 nm. This layer t decrease could be a result of tighter packing of the bilayer, with higher coverage of the surface but overall lower thickness.

Contrary to our expectations based on the DLS data, there was no increase in the thickness observed upon addition of SDS. At concentrations >0.5 cmc SDS, no Kiessig fringes were observed and therefore the thickness of the interfacial layer could not be determined purely by this method. A possible explanation for such a behaviour is the fact that the XRR is relatively sensitive to the surface roughness and so it could be argued that the XRR is not the ideal method to study systems with relatively high surface roughness. The relationship between the surface roughness and thickness in thin films on solid surfaces has been the subject of many studies and has been discussed in a great deal [67-72]. The main influence of the roughness on the layer thickness determined by XRR is due to the electron density distribution difference between that of smooth and rough layers, and so the smoothing of ρ profile distribution at the interface.

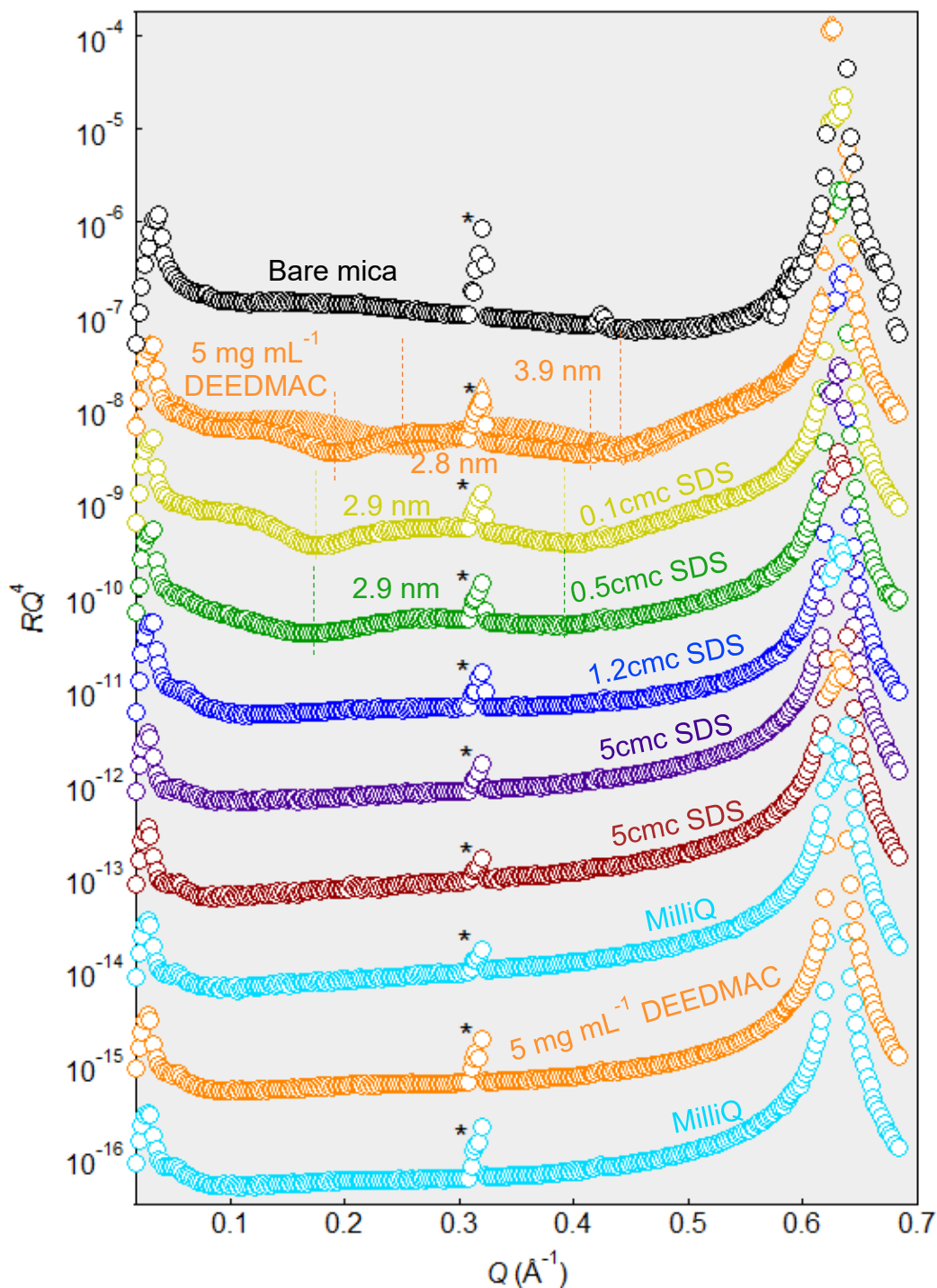


Figure 7.8 XRR curves for DEEDMAC with increasing SDS concentration, with t determined from fringe spacing. The * marks the mica half-Bragg peak.

In summary, DEEDMAC bilayer was successfully formed at the mica-water interface following a simple vesicle rupture method at RT, at neutral pH and without any presence of CaCl_2 or external forces. Furthermore, indication of SDS/DEEDMAC interactions at the solid-liquid interface was observed however XRR may not be the ideal technique to investigate these rough interfacial layers formed following SDS/DEEDMAC complexation.

7.3.5 DEEDMAC/SDS adsorption at solid-liquid interface: SFA study

Firstly, the thickness of bare mica in air was determined ($\sim 3.7 \mu\text{m}$), all surface separation values (and therefore layer t) determined from FECO were then related to this mica t , representing 0 nm surface separation. A jump-in of two mica surfaces was observed, due to the short-range attractive van der Waals forces [28, 73], and a jump-out distance ($\sim 80 \mu\text{m}$) when the adhesion forces between the two mica surfaces was overcome by the force applied pulling the surfaces apart. A long jump-out distance (order of μm) is indicative of large adhesion forces between the clean mica surfaces with no contamination. The jump-out during retraction of the mica surfaces observed when the mica surfaces were submerged in DEEDMAC/SDS samples are indicative of adhesion forces between the two coated surfaces, with varying degrees of the jump-out distance accounting for different adhesion forces between the surfaces. The SFA data is evaluated quantitatively where a plot of normalised force over the contact radius vs separation distance determined by monochromatic beam interferometry from FECO is presented. The interactions between the mica surfaces immersed in solution of adsorbing species (DEEDMAC and SDS) can be evaluated qualitatively: from the jump-in distance during surfaces approach (the larger the jump-in distance the larger the attractive interactions) and jump-out distance (the larger the distance the larger the adhesive interactions between the two surfaces).

7.3.5.1 Representative DEEDMAC/SDS mixtures at mica-air interface: SFA study

Following an injection of DEEDMAC vesicle dispersion, on first approach the Debye length $\kappa^{-1} \sim 12 \text{ nm}$ (not shown), indicating longer range screening layer, likely due to dispersed counterions near the surface. On the second approach, κ^{-1} decreased to $\sim 4 \text{ nm}$, suggesting much shorter-ranged interactions between the DEEDMAC bilayers adsorbed on the mica surfaces and no vesicles in the solution (Figure 7.9). The onset of interactions between the two surfaces was observed at $\sim 20 \text{ nm}$ (corresponding to average vesicle size), represented by the increase in the force needed to bring the surfaces closer. Applying higher force possibly led to the DEEDMAC vesicle deformation at first, followed by vesicle rupture and fusion, until a hard wall separation was reached at $\sim 7.5 \text{ nm}$, equivalent to a bilayer $t \sim 3.8 \text{ nm}$, which is in agreement with bilayer t determined from XRR data at the solid-liquid interface ($\sim 3.4 \pm 0.5 \text{ nm}$, Figure 7.8), and correlated well to DEEDMAC monolayer t formed at the air-water interface ($t \sim 2 \text{ nm}$ determined by XRR, Figure 7.7), as well as bilayer $t \sim 3\text{-}5 \text{ nm}$ determined in presence of CaCl_2 solution and lower pH using the SFA [20, 21]. The κ^{-1} values of

DEEDMAC bilayer formed by LB deposition were reported before, as $\kappa^{-1} \sim 2.8$ nm in 4.5 mM CaCl_2 solution and decreased to $\kappa^{-1} \sim 1.0$ nm in 27 mM CaCl_2 , when surfaces brought together quasi-statically (at least 30 s equilibration time allowed at each distance separation step) [21]. When the surfaces coated by DEEDMAC bilayers (LB method) were brought into contact dynamically (approach rate of 2.6 nm s^{-1}), the $\kappa^{-1} \sim 3.5$ nm in 4.5 mM CaCl_2 solution [20]. A jump out distance (~ 100 nm) was observed upon retraction of the surfaces, indicative of adhesion between the two DEEDMAC bilayers adsorbed to the mica surfaces.

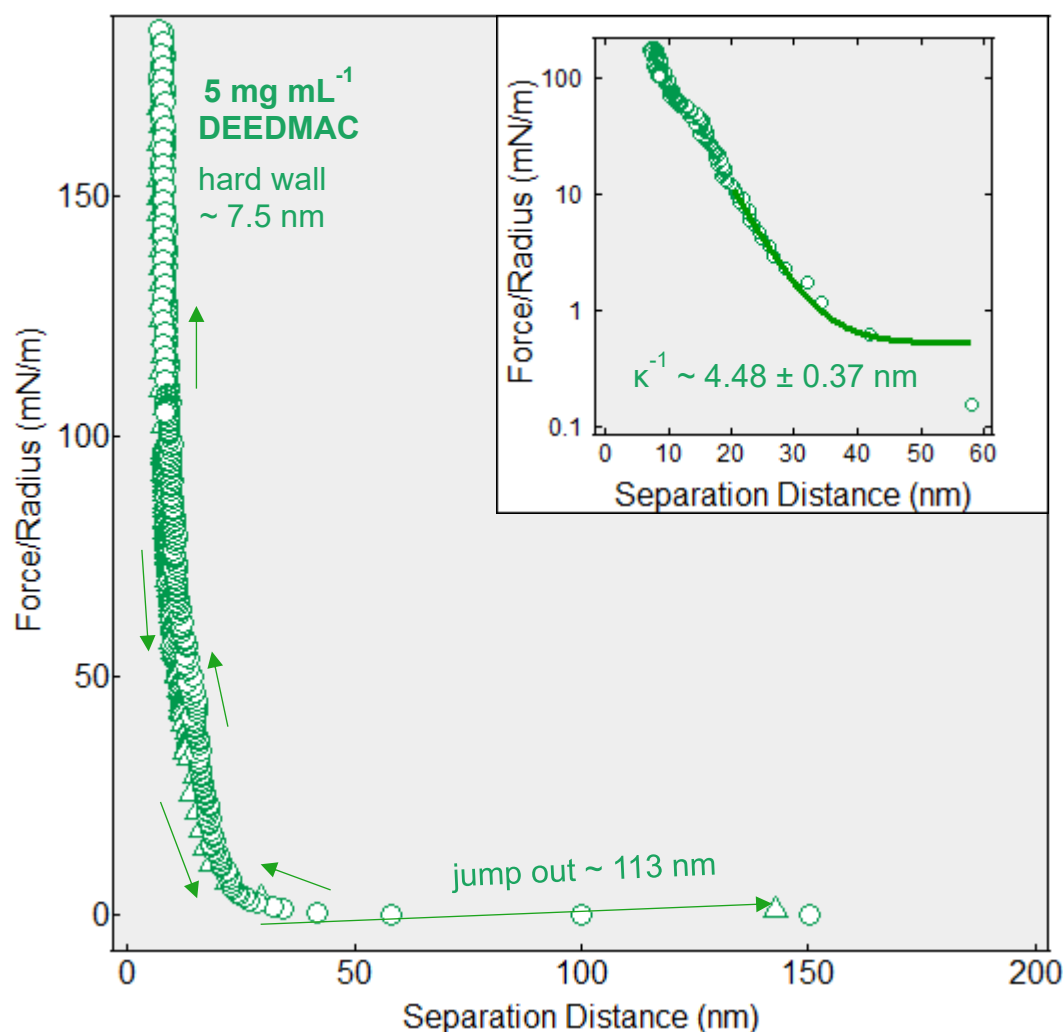


Figure 7.9 Normalised force vs separation distance of two mica surfaces immersed in a solution containing 5 mg mL^{-1} vesicle dispersion. The approach of the mica surfaces is represented by the circular data points, whereas the data measured during retraction of the surfaces is represented by triangles. The inset shows the log-normal plot of the normalised force vs separation, with fitted exponential decay to determine Debye length, κ^{-1} .

The onset of interactions between the surfaces upon addition of SDS below its cmc (0.5 cmc) was observed at larger separation distance ~ 50 nm (Figure 7.10). The layer t decreased to ~ 2.8 nm, possibly indicative of SDS adsorbing into the DEEDMAC bilayer, due to the strong attractive electrostatic forces between the oppositely charged surfactants. These strong attractive forces were also confirmed by a large jump-out distance (~ 400 nm) during retraction of the two surfaces. Additionally, a slight discontinuity in the force vs separation distance was observed at surface separation ~ 10 nm, where ~ 3 nm thick layer was squeezed out during the approach. This squeezed out $t \sim 1.5$ nm from each bilayer could correspond to a patchy DEEDMAC monolayer peeling off, with SDS subsequently adsorbing in its place. The increased $\kappa^{-1} \sim 13.5$ nm was also indicative of a layer of more diffuse ions near the mica surface and DEEDMAC bilayer.

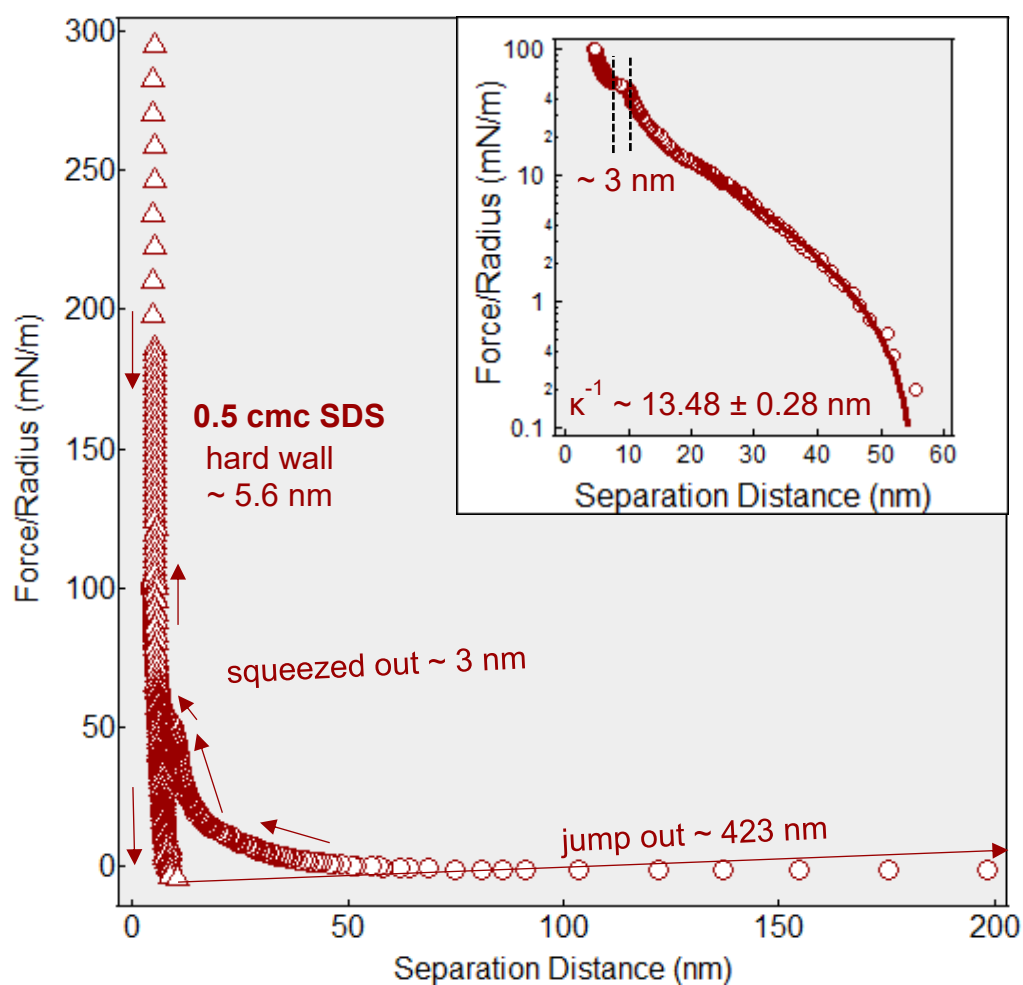


Figure 7.10 Normalised force vs separation distance of two mica surfaces with adsorbed DEEDMAC bilayer immersed in a solution containing 0.5 cmc SDS. The approach of the mica surfaces is represented by the circular data points, whereas the data measured during retraction of the surfaces is represented by triangles. The inset shows the log-normal plot of the normalised force vs separation, with fitted exponential decay to determine Debye length, κ^{-1} .

Upon addition of SDS above its cmc (Figure 7.11), the presence of a ~ 19 nm thick surface layer was observed, indicating adsorption of SDS aggregates on to the cationic bilayer, with likely formation of multilayer structure with any free DEEDMAC bilayer segments adsorbing in an alternating DEEDMAC/SDS fashion. Yet again, there was a discontinuity observed in the force vs separation distance curve, with a small jump-in of ~ 3 nm size at ~ 50 nm separation distance, soon after any interaction between the surfaces was observed. It is not possible to determine the exact composition of such multilayer; however, we would expect ~ 3 -5 DEEDMAC/SDS layers on top of each other. The jump-out distance upon retraction of the surfaces decreased to only ~ 18 nm, indicative of much weaker adhesion forces between the two surfaces compared to the lower SDS concentration, as well as κ^{-1} decreased to ~ 5 nm. The smaller adhesion forces between the DEEDMAC/SDS multilayers were later confirmed by injection of water and subsequent layer t decrease, meaning part of the multilayer has been washed off.

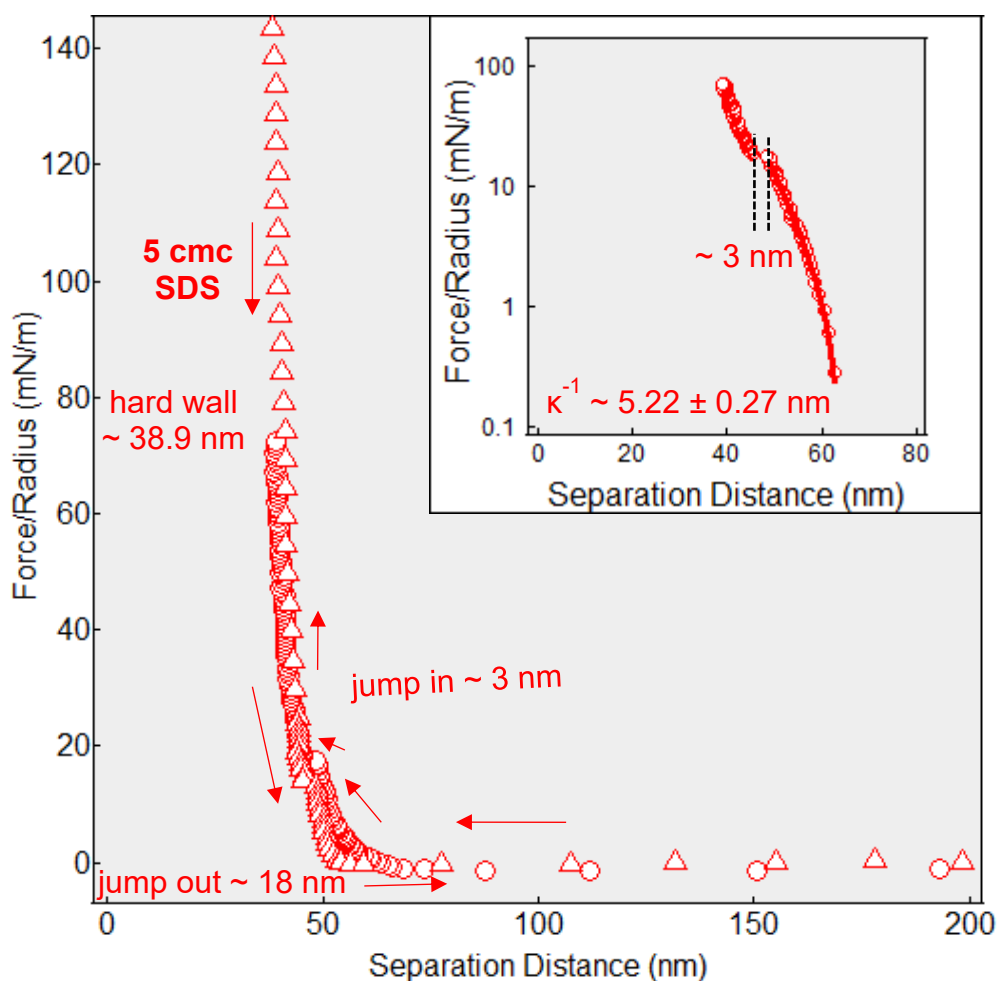


Figure 7.11 Normalised force vs separation distance of two mica surfaces with adsorbed DEEDMAC bilayer immersed in a solution containing 5 cmc SDS. The approach of the mica surfaces is represented by the circular data points, whereas the data measured during retraction of the surfaces is represented by triangles. The inset shows the log-normal plot of the normalised force vs separation, with fitted exponential decay to determine Debye length, κ^{-1} .

7.3.5.2 Comprehensive summary of DEEDMAC/SDS interfacial structures: SFA study

A comprehensive study of the interfacial structures comprising of DEEDMAC bilayers formed by vesicle fusion and their interaction with increasing SDS concentrations was performed using the SFA, with the collected data shown in Figure 7.12 and Figure 7.13, with a summary of the determined layer t and κ^{-1} shown in Figure 7.14.

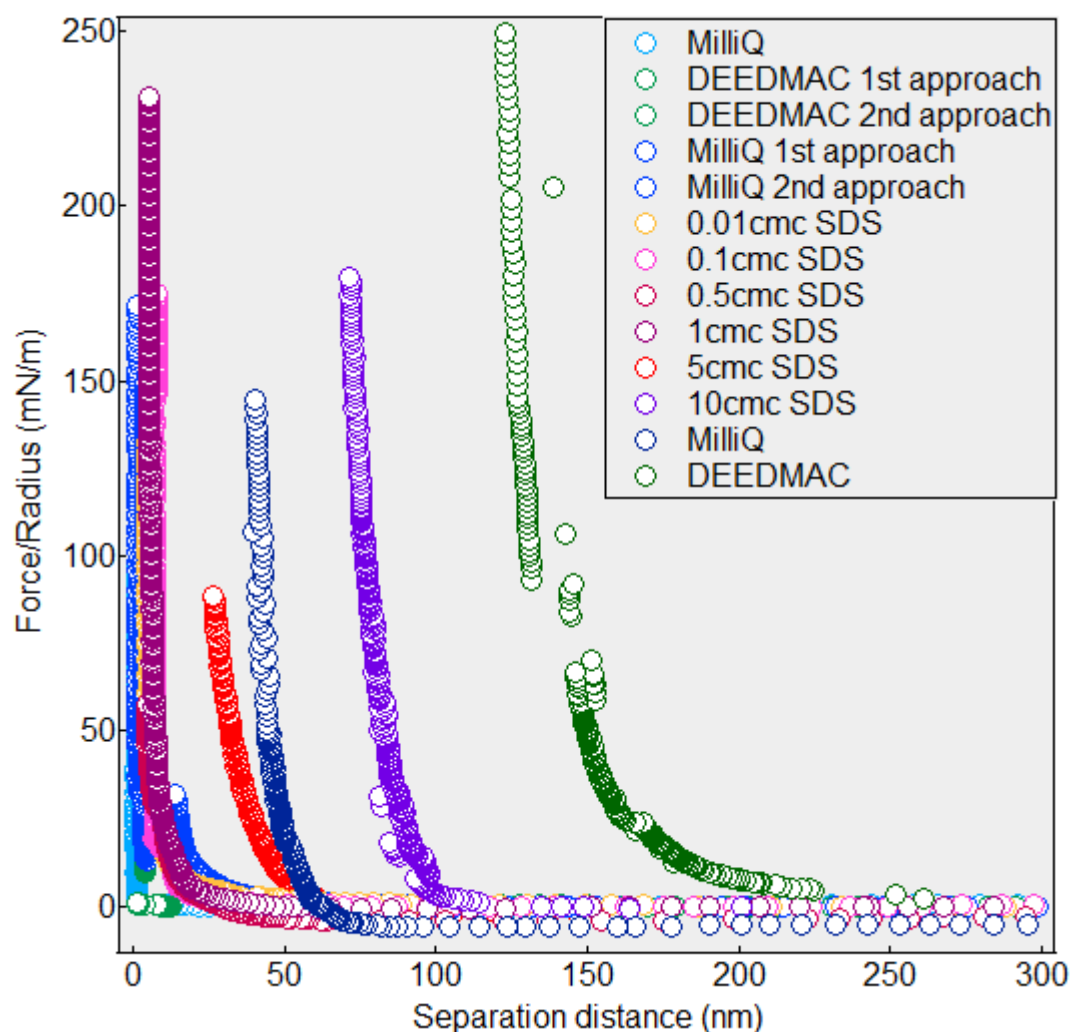


Figure 7.12 A summary of normalised force vs separation distance of two mica surfaces with adsorbed DEEDMAC bilayer immersed in a solution of increasing SDS concentration. Only the data collected during approach of the mica surfaces is shown.

The DEEDMAC bilayer formation (Figure 7.9) and its interaction with increasing SDS concentrations (Figure 7.10 and Figure 7.11) was discussed above in more detail. The layer thickness, t , shown in Figure 7.14, was determined as half of the hard wall separation, therefore assuming symmetrical adsorption to the two mica surfaces. Formation of DEEDMAC bilayer following vesicle rupture at the mica surface was confirmed by layer $t \sim 4 \pm 2$ nm, with the

uncertainty in t arising from layer roughness and patchiness. This bilayer t decreased slightly following rinsing with MilliQ ($t \sim 2$ nm) but remained stable and was not washed off following ~ 24 -hour long incubation period. Subsequent injection of SDS solution up to its cmc led to steady but small layer t increase, to ~ 4 nm after injection of 1 cmc SDS solution. Marked layer t increase was observed following injection of 5 and 10 cmc SDS, with $t \sim 13$ and 39 nm respectively, indicative of strong complexation between SDS and DEEDMAC, likely forming multilayers of alternating DEEDMAC/SDS bilayers, with possibility of SDS micelles included in the multilayer structure especially at the higher SDS concentration. Rinsing with MilliQ demonstrated the stability of these adsorbed SDS/DEEDMAC multilayers at the surface with only partial removal of the adsorbed species and layer t decrease to ~ 20 nm. The DEEDMAC layer stability is especially relevant to the use of DEEDMAC dispersions as fabric softeners added to wash cycles, where the DEEDMAC deposition onto the fabric surface provides the softening effect [74]. Finally, injection of additional DEEDMAC vesicles led to a substantial t increase to ~ 73 nm, *i.e.* $\Delta t \sim 50$ nm at each surface, which could be accounted for by a formation of network consisting of DEEDMAC vesicles adsorbed on top of the SDS/DEEDMAC multilayers. A final rinsing with MilliQ water caused a decrease of the separation thickness, which would be expected as the vesicles would be easier to remove from the surface of the multilayer. However, the separation distance between the two mica surfaces remained at ~ 100 nm following the final rinsing, showcasing the stability of the adsorbed DEEDMAC/SDS multilayers on negatively charged mica surface after multiple rinsing with MilliQ and application of normal force.

Debye length, κ^{-1} was determined according to Equation 7.9 and 7.13 from fitting of the log-normal plot of normalised force over radius *vs* separation distance data (Figure 7.12) with an exponential decay. The layer t and κ^{-1} are summarised in Figure 7.14. In general, κ^{-1} was relatively high at low SDS concentrations ($\kappa^{-1} \sim 12$ nm) with a marked decrease of κ^{-1} to ~ 3 nm at 5 cmc SDS, with the onset of the κ^{-1} lowering at SDS concentrations between 0.5 and 1 cmc. This κ^{-1} decrease is indicative of SDS adsorption onto the DEEDMAC bilayer, where we would expect surface charge to approach neutralisation and subsequent charge reversal (*cf.* Figure 7.5, at DEEDMAC/0.5 cmc SDS ζ -potential ~ 62 mV compared to ~ -57 mV at DEEDMAC/1 cmc SDS). Addition of more SDS (10 cmc SDS) caused an increase in κ^{-1} to ~ 7 nm, with a final significant increase of κ^{-1} to ~ 17 nm following addition of DEEDMAC to the already adsorbed DEEDMAC/SDS layers. Furthermore, the curvature of the exponential decay at larger separation distances is typical for long range repulsion between the two mica surfaces during approach.

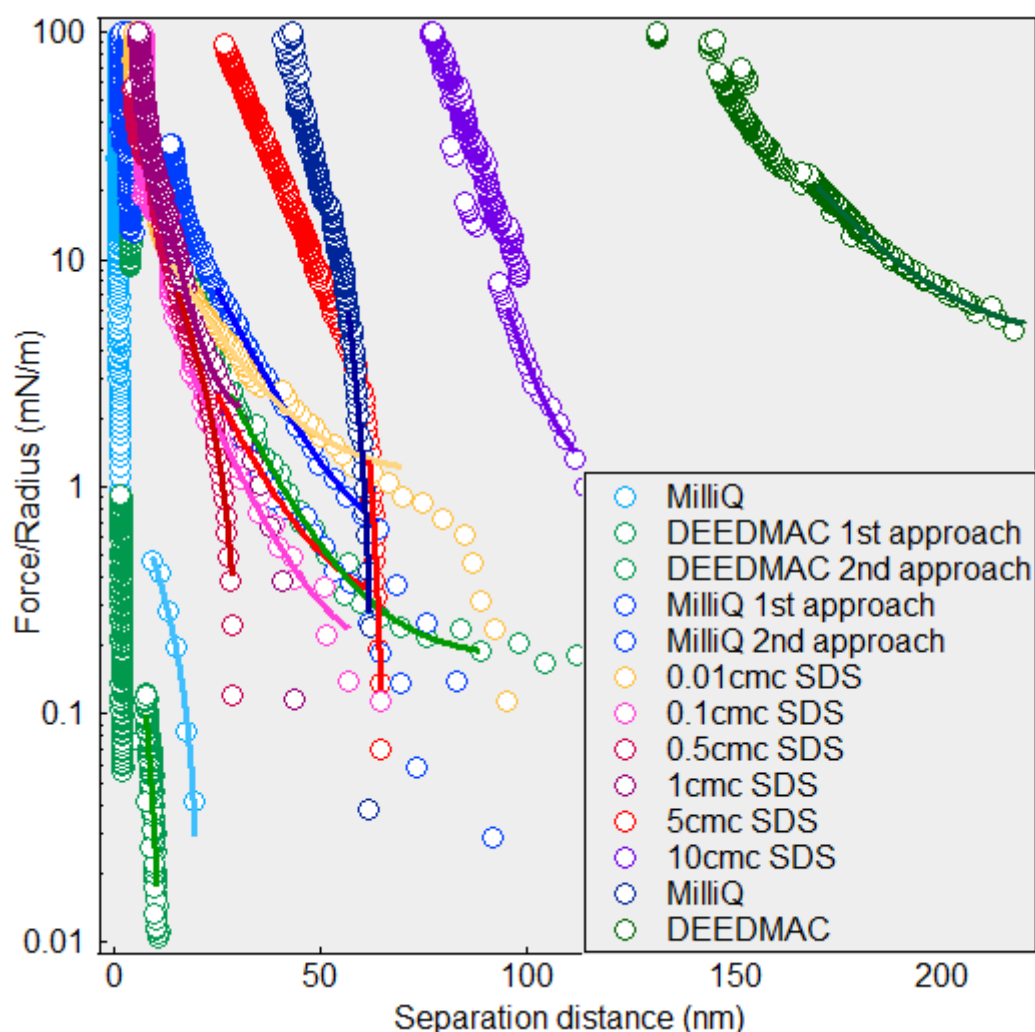


Figure 7.13 A summary of the log-normal plot of normalised force *vs* separation distance, with the data of DEEDMAC and SDS mixtures adsorbed to the mica surface fitted by an exponential decay to determine the Debye length, κ^{-1} .

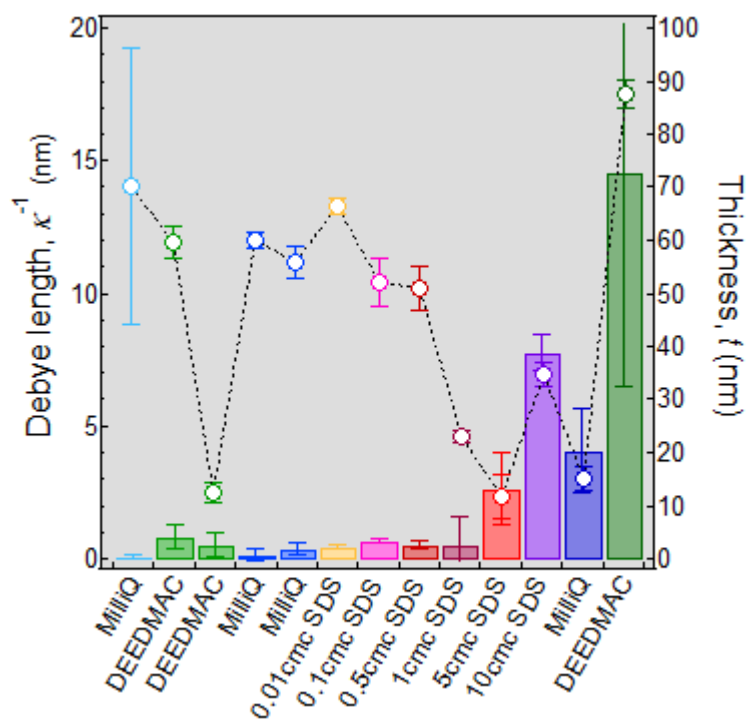


Figure 7.14 Representation of Debye length, κ^{-1} (left axis) determined from exponential decay (line and circle data points) and the thickness, t , (right axis) determined as half of the hard wall separation represented as bar charts.

The FECO of each of the mixed DEEDMAC/SDS systems are shown in Figure 7.15, together with possible structures formed at the solid-liquid interface. As previously mentioned, relatively large surface coverage (or roughness) and thickness inhomogeneity was observed by the deformation of FECO as well as different thicknesses calculated at different contact spots of the same surface, and an almost gel-like network was observed *via* optical microscopy following the final DEEDMAC vesicle injection (Figure F.2 in Appendix). In order to investigate these rough and relatively large-scale complexes more closely, and qualitatively, negative stain TEM and cryoTEM images were obtained.

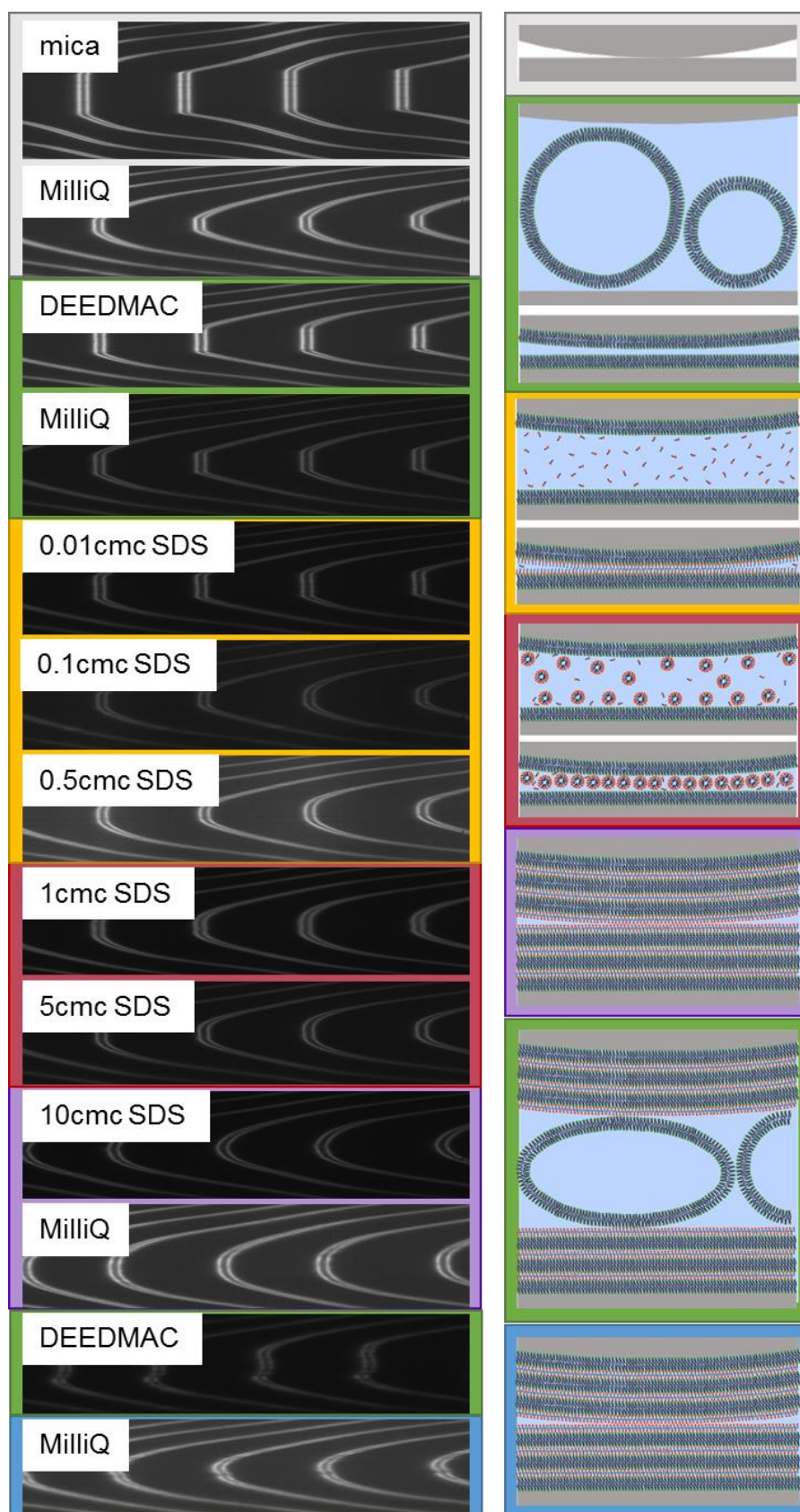


Figure 7.15 Images of FECO corresponding to each system, with a possible schematic representations: bare mica in contact (grey), DEEDMAC bilayer formation (green), SDS adsorption below its cmc as a single layer (yellow), SDS adsorption above its cmc as micelles (red), SDS/DEEDMAC multilayer formation at 10 cmc SDS (purple), DEEDMAC vesicles trapped between the multilayers (green), and stable DEEDMAC/SDS multilayer preserved following rinsing with MilliQ (blue).

7.3.6 Transmission Electron Microscopy (TEM) and confocal microscopy

The microscopy data is presented below for each SDS/DEEDMAC mixed system, and the pure SDS and DEEDMAC, as a combination of negative stain TEM, cryoTEM and confocal microscopy for each system.

The confocal microscopy data was collected as a 3D stack of images. However, the species in the bulk were free to move, and so vesicle diffusion was observed through the stack of the images. Therefore, what may appear like a line in an image created by summing over the 3D stacks was actually a free spherical vesicle moving across the sample. In general, a larger amount of DEEDMAC vesicles was observed on the surfaces of the glass slide and the cover slip, as expected due to the attractive electrostatic interactions between the negatively charged glass surface and cationic DEEDMAC. In general, higher intensity of fluorescein was detected with increasing SDS concentration, as fluorescein is a hydrophobic dye and is incorporated within the hydrocarbon tail of the surfactant [75].

7.3.6.1 *Pure SDS: Confocal microscopy*

No TEM images were recorded for the pure SDS system, as the size of the SDS micelle is approximately the same as the resolution limit of the technique. Wormlike micelles of SDS in high polyelectrolyte concentrations [76], as well as SDS interacting with polymers and cationic surfactants [77, 78] have been imaged by cryoTEM; however, these structures were much larger than simple SDS micelles or free molecules. Confocal microscopy images of pure SDS systems at 0.1, 0.5 and 5 cmc concentration were recorded in the bulk of the sample (Figure 7.16). Higher intensity of the detected fluorescein was seen with increasing SDS concentrations, with the colour balance reflecting that used for relevant DEEDMAC/SDS complexes at the given SDS concentrations.

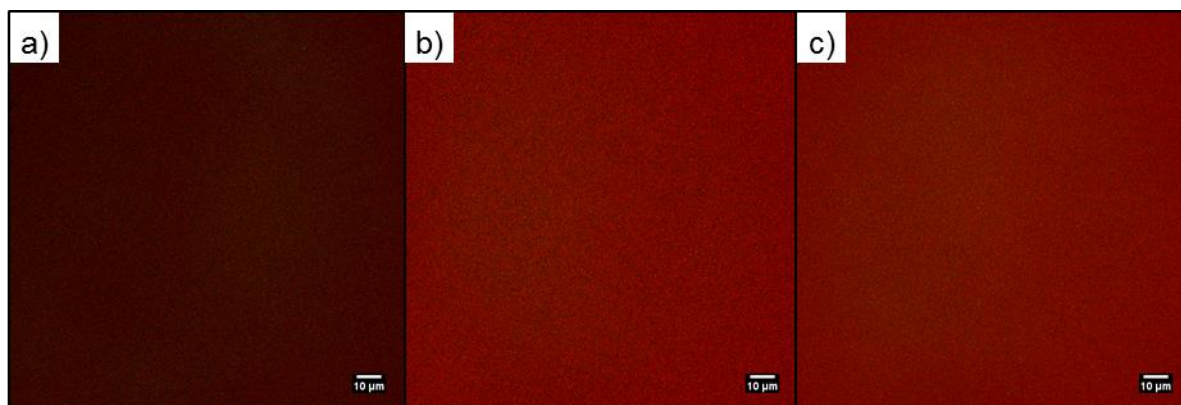


Figure 7.16 Confocal images of a) 0.1 cmc SDS, b) 0.5 cmc SDS and c) 5 cmc SDS doped with fluorescein.

7.3.6.2 Pure DEEDMAC: TEM, cryoTEM and confocal microscopy

The negative stain, cryoTEM and confocal images of 5mg/mL DEEDMAC vesicle dispersion are shown in Figure 7.17. DEEDMAC vesicles of various sizes were present in the sample, ranging in size from ~ 20 nm to a very large ~ 500 nm aggregates, with the majority of the vesicle size in the ~ 20 to 100 nm range (Figure 7.17 a-d). Despite the relatively large vesicle size distribution observed, no multilamellar vesicles were observed. Formation of unilamellar DEEDMAC vesicles (at much higher concentration of 50 mg mL⁻¹) in deionised water was observed by cryoTEM and reported before, with the formation of multilamellar vesicles in isotonic suspension of 1200 ppm CaCl₂ [79]. The bilayer thickness of the vesicles was determined to be ~ 4 nm, with some broken segments of bilayer present (~ 4 nm width and ~ 30 nm length). In the confocal microscopy images (Figure 7.17 e-f) large amount of Nile Blue doped DEEDMAC was seen at the glass surface, with free vesicles/aggregates observed in the bulk of the solution. It is not possible to determine if the structures observed were vesicles or aggregates as the maximum resolution of the technique was on the order of tens of nm to μm scale.

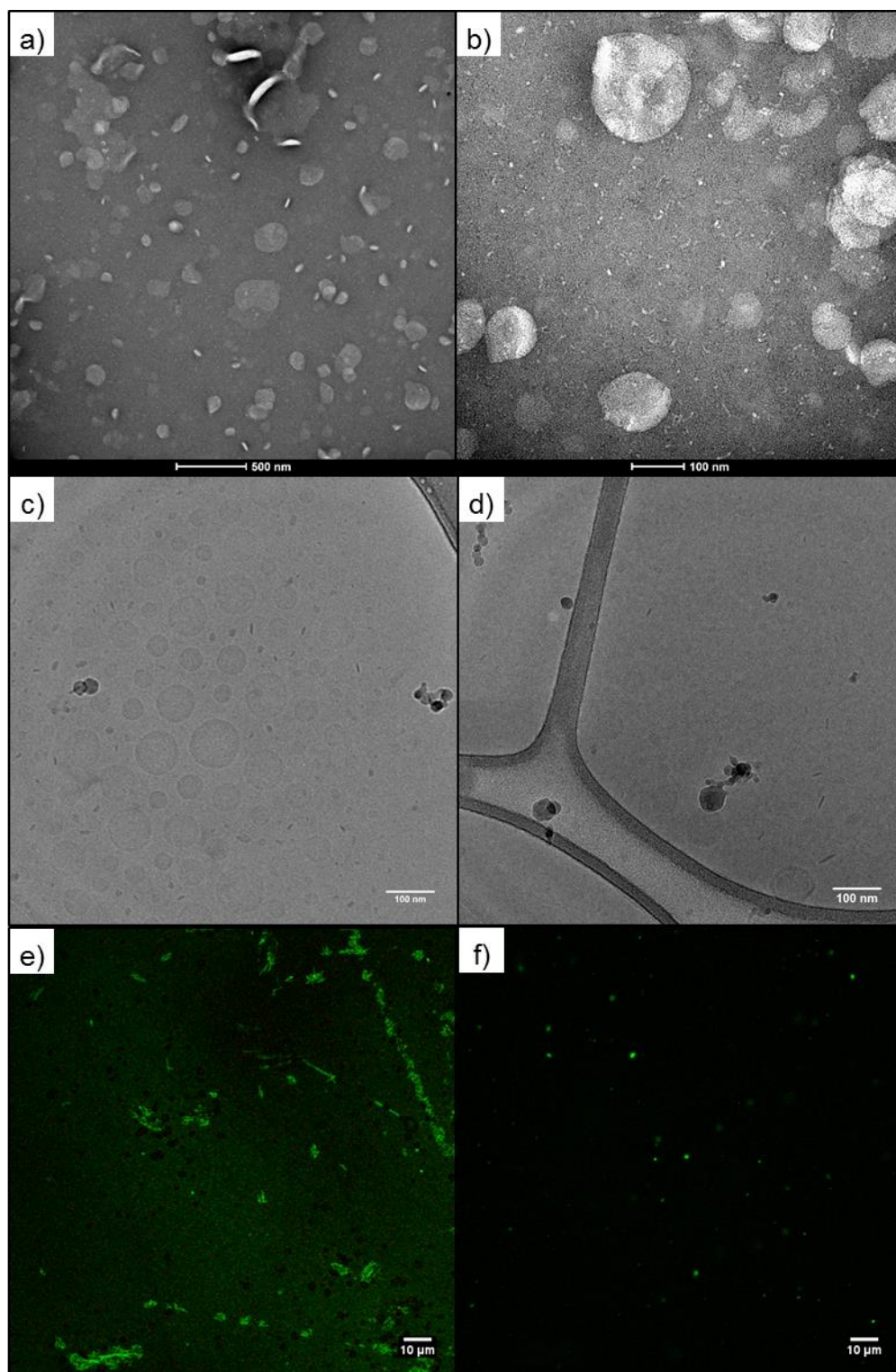


Figure 7.17 Negative stain TEM (a, b), cryoTEM (c, d) and confocal microscopy (e, f) of pure DEEDMAC vesicle dispersion. The Nile Blue doped DEEDMAC is represented by green colour.

7.3.6.3 DEEDMAC and 0.1 cmc SDS: TEM, cryoTEM and confocal microscopy

In the samples containing 0.1 cmc SDS and DEEDMAC vesicles, in some cases spherical vesicles/aggregates of DEEDMAC were partially covered by SDS (Figure 7.18b), indicative of attractive interactions between the two species. The vesicle size distribution was smaller compared to the pure DEEDMAC; however, a large number of straight bilayer segments were present (Figure 7.18c-d). The partial coating of the vesicles by SDS was also confirmed by confocal microscopy, especially in Figure 7.18e.

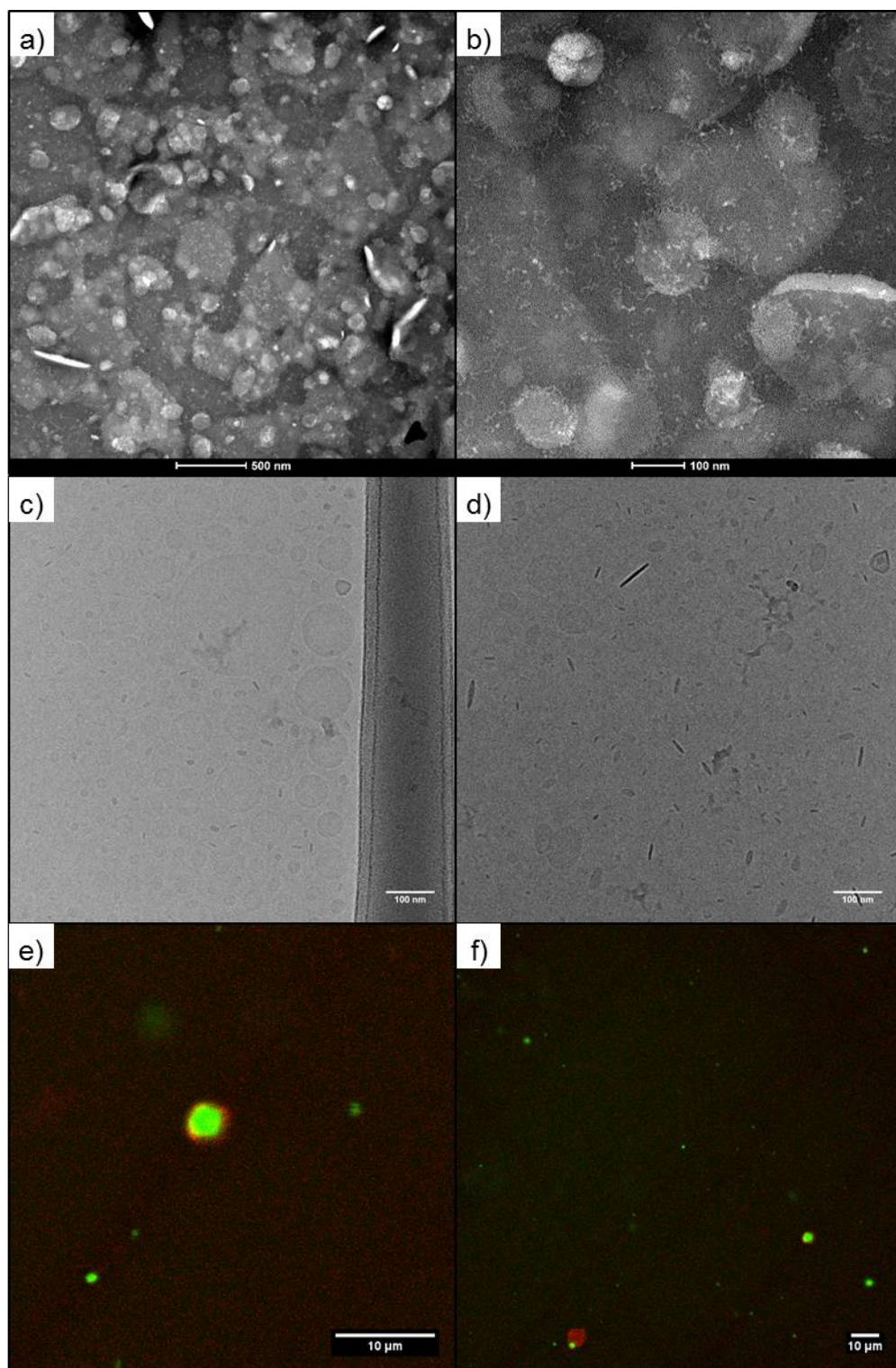


Figure 7.18 Negative stain TEM (a, b), cryoTEM (c, d) and confocal microscopy (e, f) of DEEDMAC vesicle dispersion and 0.1 cmc SDS. The Nile Blue doped DEEDMAC is represented by green colour, and fluorescein doped SDS by red.

7.3.6.4 DEEDMAC and 0.5 cmc SDS: TEM, cryoTEM and confocal microscopy

In the sample containing 0.5 cmc SDS with DEEDMAC (Figure 7.19), aggregation and some broken vesicles forming very large and non-spherical shapes on a μm scale were present. Additionally, formation of multilamellar vesicles was observed, not dissimilar to those formed by a cationic surfactant mixture (SDS and cationic azobenzene derivative) [77]. Several DEEDMAC vesicle bilayer t increased to $\sim 15\text{-}20$ nm and these vesicles appeared to contain species in the vesicle interior (Figure 7.19c); however, it was not possible to distinguish if these species were SDS aggregates, other vesicles, or mixed DEEDMAC/SDS aggregates.

From the TEM images alone we could not directly observe any SDS structures to attribute this change of aggregation behaviour directly to the presence of SDS. However, by combination of TEM and confocal images we can ascribe the SDS/DEEDMAC complexation behaviour with confidence to the presence of increasing SDS concentration, likely near the charge neutralisation point. A network of SDS was seen in the bulk of the sample with DEEDMAC vesicles/aggregates trapped within the SDS network in the confocal images. In the pure sample of 0.5 cmc SDS (Figure 7.16b), there was no network observed in the sample, therefore the network of SDS and DEEDMAC is an effect of DEEDMAC addition. Majority of the DEEDMAC however adsorbed on the glass surfaces, with only few DEEDMAC structures seen embedded in the network.

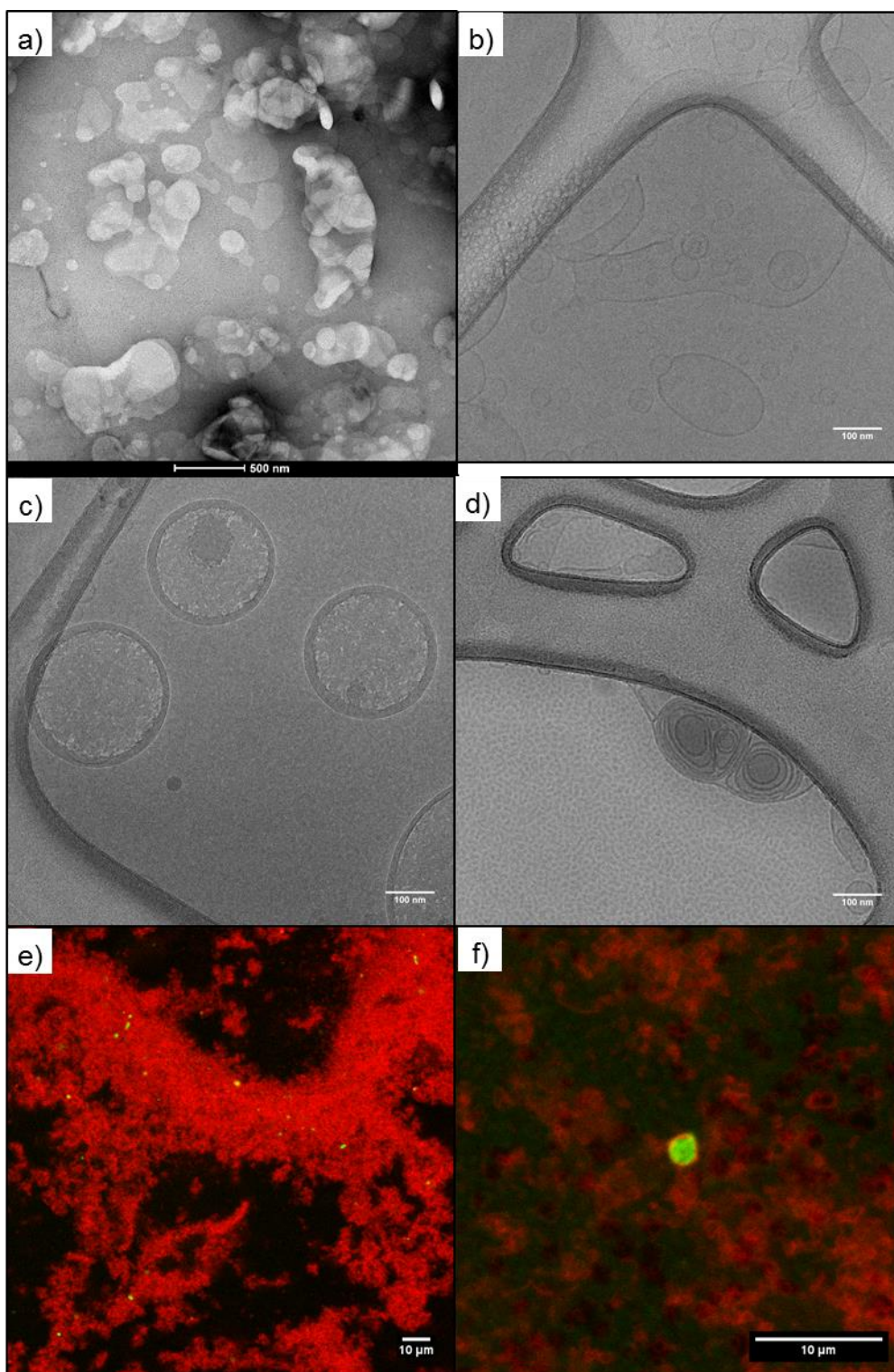


Figure 7.19 Negative stain TEM (a), cryoTEM (b, c, d) and confocal microscopy (e, f) of DEEDMAC vesicle dispersion and 0.5 cmc SDS. The Nile Blue doped DEEDMAC is represented by green colour, and fluorescein doped SDS by red.

7.3.6.5 *DEEDMAC and 5 cmc SDS: TEM, cryoTEM and confocal microscopy*

In the sample containing 5 cmc SDS with DEEDMAC (Figure 7.20), a range of sizes and shapes were seen in the sample, with many of them overlapping and so pointing towards stronger interactions between the species and higher overall aggregation. This was an expected observation, with large t of interfacial layers in these mixtures determined by XRR and SFA. In addition, some ruptured yet spherical micelles in the ~100 nm size range (Figure 7.20c), as well as bilayer segments were observed. The most striking difference (apart from the higher aggregation) compared to the previous concentrations was a clear increase in the thickness and contrast between the bilayer of some vesicles, likely representing a DEEDMAC bilayer coated with SDS (either molecules or micelles, it is not possible to clearly distinguish).

In the confocal microscopy images (Figure 7.20e-f), the majority of the sample was filled with the fluorescein doped SDS. The Nile Blue doped DEEDMAC vesicles were seen in the sample indiscriminately through the bulk of the sample, with more DEEDMAC adsorbed at the glass surfaces, as previously. Compared to pure SDS sample, there was not much difference in the structuring of the bulk liquid, unlike in the previous case. We could not see any multilayer formation or direct association of the surfactants using this technique.

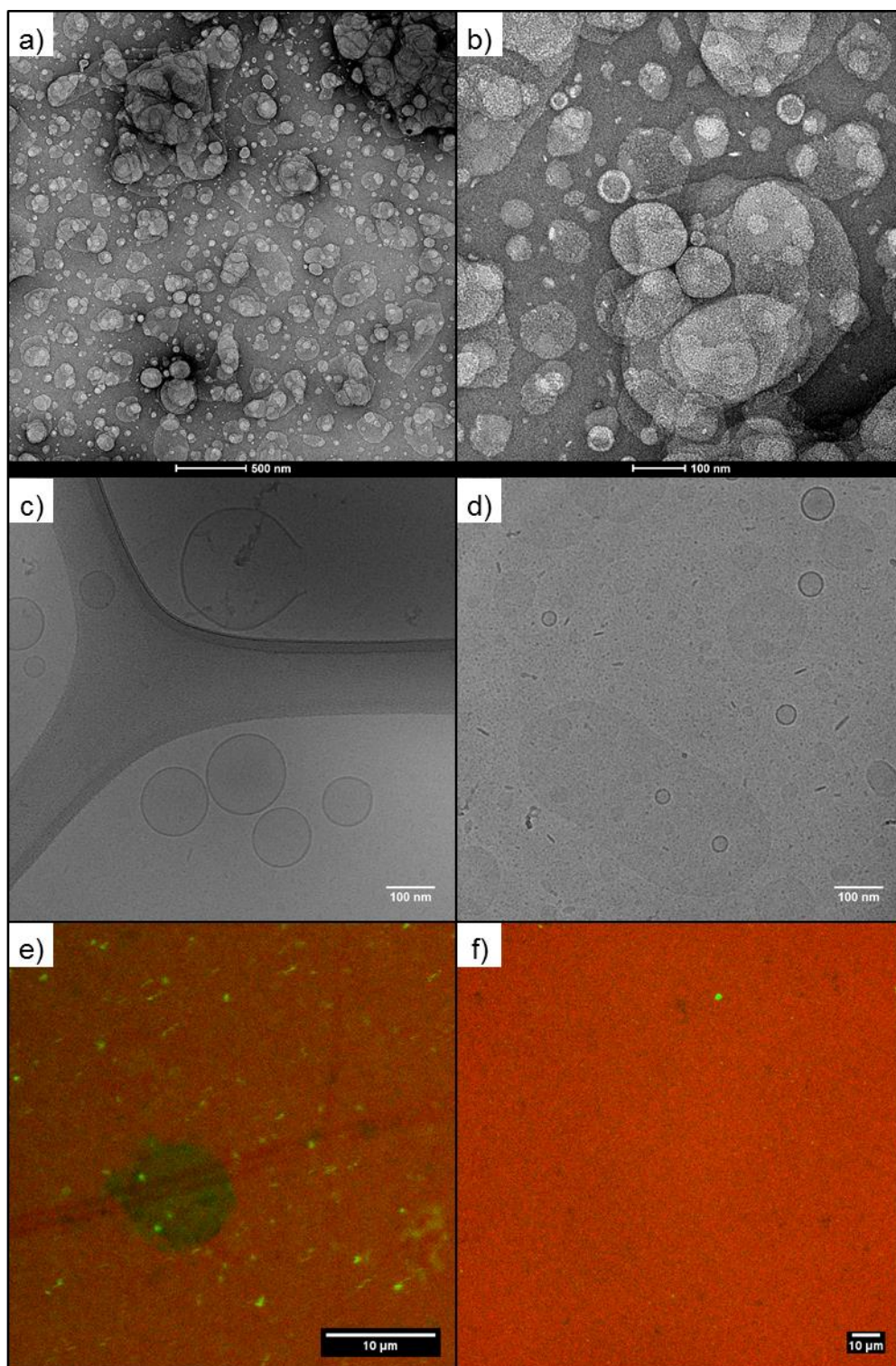


Figure 7.20 Negative stain TEM (a, b), cryoTEM (c, d) and confocal microscopy (e, f) of DEEDMAC vesicle dispersion and 5 cmc SDS. The Nile Blue doped DEEDMAC is represented by green colour, and fluorescein doped SDS by red.

7.4 Conclusions

Complexation between SDS and DEEDMAC vesicle was investigated: a) in bulk by DLS, ζ -potential and microscopy, b) at air-water interface observed by surface tension measurements and XRR, and c) at solid-liquid interface observed by XRR, SFA and microscopy.

7.4.1 DEEDMAC/SDS complexation in bulk

Firstly, the increase in d_h observed by DLS, together with charge reversal from positive to negative values was indicative of SDS adsorption onto the DEEDMAC vesicles in the bulk. This complexation was also visualised by confocal microscopy at low and intermediate SDS concentrations and cryoTEM even at SDS concentrations above its cmc. There was evidence of relatively strong interactions between the DEEDMAC vesicles and SDS in bulk. At SDS concentrations below its cmc, a portion of the DEEDMAC vesicles was coated by patches of SDS molecules. With increasing SDS concentration, less clear evidence of DEEDMAC/SDS complex formation was observed, *e.g.* presence of DEEDMAC bilayer segments and deformed vesicles, DEEDMAC vesicles with higher layer t suggesting adsorption of SDS within the DEEDMAC bilayer, and aggregation of vesicles suggesting bridging interactions by SDS between two or more vesicles.

7.4.2 DEEDMAC/SDS complexation at air-water interface

Synergistic surface tension γ lowering of DEEDMAC/SDS mixtures also pointed towards interactions between DEEDMAC and SDS at the air-water interface. The thicknesses t of these DEEDMAC/SDS complexes were determined by XRR. t of pure DEEDMAC monolayer at the air-water interface was ~ 2 nm (as determined from Kiesig fringe spacing) and increased to ~ 20 nm upon addition of SDS above its cmc.

7.4.3 DEEDMAC/SDS complexation at solid-liquid interface

XRR was also used to study the structures of DEEDMAC vesicles adsorbed onto mica surface followed vesicle rupture. $t \sim 3$ -4 nm suggested formation of a bilayer on the mica surface. SDS was then injected at increasing concentrations on the DEEDMAC bilayer, with initial t decrease to ~ 3 nm at 0.1 and 0.5 cmc SDS, possibly indicative of SDS intercalation into the DEEDMAC bilayer. Increasing SDS concentration however led to disappearance of the pronounced Kiessig fringes likely due to increased roughness and therefore the t could not be determined by XRR

without ρ profile data fitting. As DEEDMAC contains a mixture of tail lengths and ions and together with the expected high roughness the data fitting would carry a lot of uncertainty.

The interfacial structures of DEEDMAC/SDS complexes were then studied using the SFA at the solid-liquid interface and under confinement. A formation of DEEDMAC bilayer was first established, with $t \sim 3\text{-}5$ nm. The bilayer was formed by vesicle rupture, where the normal force applied between the two surfaces would aid in the vesicle deformation until the bending energy of the bilayer reaches a critical level at which the vesicle ruptures. However, the bilayer formation observed by XRR was un-aided by any external force applied and we therefore assume the application of the normal force is not needed to form a DEEDMAC bilayer on mica surface. Addition of SDS below its cmc led to first a decrease in the layer t , possibly caused by the insertion of SDS and slight disruption of the bilayer. Subsequent SDS addition lead to t increase, with especially prominent t increase with SDS above its cmc, forming a DEEDMAC/SDS alternating multilayer with $t > 30$ nm. Further injection of DEEDMAC vesicles again led to significant increase in t , possibly accounted for adsorption of small vesicles onto the already formed alternating layers of DEEDMAC and SDS. These DEEDMAC/SDS complexes at the solid-liquid interface were stable under normal and shearing forces (not discussed) and following MilliQ rinsing.

In summary, a comprehensive study into the interactions of DEEDMAC vesicles and SDS was performed in bulk and at interfaces. Many of these results can be directly related to the application of DEEDMAC in formulations such as fabric softeners, where the surfactant adsorbs to the surface of the fabric and then remains adsorbed during the remainder of the wash cycle, as well as during wear time, providing additional softness.

7.5 References

1. Rajput, S.M., et al., *Drug - Induced Micelle - to - Vesicle Transition of a Cationic Gemini Surfactant: Potential Applications in Drug Delivery*. Chemphyschem, 2018. **19**(7): p. 865-872.
2. Ding, J., et al., *Facile preparation of a cationic poly(amino acid) vesicle for potential drug and gene co-delivery*. Nanotechnology, 2011. **22**(49): p. 494012.
3. Marques, E.F., et al., *Vesicle Formation and General Phase Behavior in the Catanionic Mixture SDS-DDAB-Water. The Cationic-Rich Side*. The Journal of Physical Chemistry B, 1999. **103**(39): p. 8353-8363.

4. Marques, E.F., et al., *Vesicle Formation and General Phase Behavior in the Catanionic Mixture SDS–DDAB–Water. The Anionic-Rich Side*. The Journal of Physical Chemistry B, 1998. **102**(35): p. 6746-6758.
5. Bonincontro, A., et al., *Dynamics of DNA Adsorption on and Release from SDS–DDAB Cat–Anionic Vesicles: a Multitechnique Study*. Langmuir, 2008. **24**(5): p. 1973-1978.
6. Simberg, D., et al., *DOTAP (and other cationic lipids): chemistry, biophysics, and transfection*. Crit Rev Ther Drug Carrier Syst, 2004. **21**(4): p. 257-317.
7. Hojatizade, M., et al., *Evaluation of Immune Response against Leishmaniasis in BALB/c Mice Immunized with Cationic DOTAP/DOPE/CHOL Liposomes Containing Soluble Leishmania major Antigens*. Iranian journal of parasitology, 2019. **14**(1): p. 68-77.
8. Christensen, D., et al., *Cationic liposomes as vaccine adjuvants*. Expert Review of Vaccines, 2011. **10**(4): p. 513-521.
9. Felgner, P.L., et al., *Improved Cationic Lipid Formulations for In Vivo Gene Therapy*. 1995. **772**(1): p. 126-139.
10. Milcovich, G., et al., *Modulating carbohydrate-based hydrogels as viscoelastic lubricant substitute for articular cartilages*. International Journal of Biological Macromolecules, 2017. **102**: p. 796-804.
11. Oikonomou, E.K., et al., *Design of eco-friendly fabric softeners: Structure, rheology and interaction with cellulose nanocrystals*. Journal of Colloid and Interface Science, 2018. **525**: p. 206-215.
12. Oikonomou, E.K., et al., *Fabric Softener–Cellulose Nanocrystal Interaction: A Model for Assessing Surfactant Deposition on Cotton*. The Journal of Physical Chemistry B, 2017. **121**(10): p. 2299-2307.
13. Yaroslavov, A.A., et al., *Biodegradable containers composed of anionic liposomes and cationic polypeptide vesicles*. RSC Advances, 2015. **5**(119): p. 98687-98691.
14. Saengkrit, N., et al., *Influence of curcumin-loaded cationic liposome on anticancer activity for cervical cancer therapy*. Colloids and Surfaces B: Biointerfaces, 2014. **114**: p. 349-356.
15. Martins, L.M.S., Mamizuka, E.M., and Carmona-Ribeiro, A.M., *Cationic Vesicles as Bactericides*. Langmuir, 1997. **13**(21): p. 5583-5587.
16. Giolando, S.T., et al., *Environmental fate and effects of DEEDMAC: A new rapidly biodegradable cationic surfactant for use in fabric softeners*. Chemosphere, 1995. **30**(6): p. 1067-1083.
17. Matthijs, E., et al., *The fate of detergent surfactants in sewer systems*. Water Science and Technology, 1995. **31**(7): p. 321-328.

18. Zhao, X., et al., *Impact of Additives on the Microstructural Properties of DIDMAMS Bilayers: Studied by Molecular Dynamics Simulations*. Langmuir, 2019. **35**(18): p. 6112-6119.
19. Patil, Y.P. and Jadhav, S., *Novel methods for liposome preparation*. Chemistry and Physics of Lipids, 2014. **177**: p. 8-18.
20. Das, S., et al., *Interaction of adsorbed polymers with supported cationic bilayers*. RSC Advances, 2013. **3**(43): p. 20405-20411.
21. Anderson, T.H., et al., *Direct Measurement of Double-Layer, van der Waals, and Polymer Depletion Attraction Forces between Supported Cationic Bilayers*. Langmuir, 2010. **26**(18): p. 14458-14465.
22. Reimhult, E., Höök, F., and Kasemo, B., *Intact Vesicle Adsorption and Supported Biomembrane Formation from Vesicles in Solution: Influence of Surface Chemistry, Vesicle Size, Temperature, and Osmotic Pressure*. Langmuir, 2003. **19**(5): p. 1681-1691.
23. Hardy, G.J., Nayak, R., and Zauscher, S., *Model cell membranes: Techniques to form complex biomimetic supported lipid bilayers via vesicle fusion*. Current Opinion in Colloid & Interface Science, 2013. **18**(5): p. 448-458.
24. Oshima, A. and Sumitomo, K., *Vesicle fusion with bilayer lipid membrane controlled by electrostatic interaction*. Biochemistry and Biophysics Reports, 2017. **11**: p. 58-63.
25. Briscoe, W.H., et al., *Synchrotron XRR study of soft nanofilms at the mica-water interface*. Soft Matter, 2012. **8**(18): p. 5055-5068.
26. Briscoe, W.H., et al., *Applying grazing incidence X-ray reflectometry (XRR) to characterising nanofilms on mica*. Journal of Colloid and Interface Science, 2007. **306**(2): p. 459-463.
27. Speranza, F., et al., *Quiescent bilayers at the mica-water interface*. Soft Matter, 2013. **9**(29): p. 7028-7041.
28. Tabor, D. and Winterton, R.H.S., *The direct measurement of normal and retarded van der Waals forces*. Proceedings of the Royal Society of London. A. Mathematical and Physical Sciences, 1969. **312**(1511): p. 435-450.
29. Tabor, D. and Winterton, R.H.S., *Surface Forces: Direct Measurement of Normal and Retarded van der Waals Forces*. Nature, 1968. **219**(5159): p. 1120-1121.
30. Israelachvili, J., *Interferometric method for determining refractive index and thickness of thin films*. Nature Physical Science, 1971. **229**(3): p. 85.
31. Israelachvili, J.N., *Thin film studies using multiple-beam interferometry*. Journal of Colloid and Interface Science, 1973. **44**(2): p. 259-272.
32. Israelachvili, J.N. and Adams, G.E., *Direct measurement of long range forces between two mica surfaces in aqueous KNO₃ solutions*. Nature, 1976. **262**(5571): p. 774-776.

33. Israelachvili, J.N. and Adams, G.E., *Measurement of forces between two mica surfaces in aqueous electrolyte solutions in the range 0–100 nm*. Journal of the Chemical Society, Faraday Transactions 1: Physical Chemistry in Condensed Phases, 1978. **74**(0): p. 975-1001.
34. Israelachvili, J.J.P.o.t.N.A.o.S.o.t.U.S.o.A., *Direct measurements of forces between surfaces in liquids at the molecular level*. 1987. **84**(14): p. 4722.
35. Klein, J., Perahia, D., and Warburg, S., *Forces between polymer-bearing surfaces undergoing shear*. Nature, 1991. **352**(6331): p. 143-145.
36. Klein, J., et al., *Lubrication forces between surfaces bearing polymer brushes*. Macromolecules, 1993. **26**(21): p. 5552-5560.
37. Chen, M., et al., *Lubrication at physiological pressures by polyzwitterionic brushes*. 2009. **323**(5922): p. 1698-1701.
38. Briscoe, W.H., et al., *Boundary lubrication under water*. Nature, 2006. **444**(7116): p. 191-194.
39. Israelachvili, J., et al., *Recent advances in the surface forces apparatus (SFA) technique*. 2010. **73**(3): p. 036601.
40. Kristiansen, K., et al., *3D Force and Displacement Sensor for SFA and AFM Measurements*. Langmuir, 2008. **24**(4): p. 1541-1549.
41. Watanabe, J., Mizukami, M., and Kurihara, K., *Resonance Shear Measurement of Confined Alkylphenyl Ether Lubricants*. Tribology Letters, 2014. **56**(3): p. 501-508.
42. Schwenzfeier, K.A., et al., *Optimizing multiple beam interferometry in the surface forces apparatus: Novel optics, reflection mode modeling, metal layer thicknesses, birefringence, and rotation of anisotropic layers*. 2019. **90**(4): p. 043908.
43. Xu, Z., Ducker, W., and Israelachvili, J., *Forces between Crystalline Alumina (Sapphire) Surfaces in Aqueous Sodium Dodecyl Sulfate Surfactant Solutions*. Langmuir, 1996. **12**(9): p. 2263-2270.
44. Klein, J. and Luckham, P.J.N., *Forces between two adsorbed polyethylene oxide layers immersed in a good aqueous solvent*. 1982. **300**(5891): p. 429.
45. Klein, J., *Forces between mica surfaces bearing layers of adsorbed polystyrene in cyclohexane*. Nature, 1980. **288**(5788): p. 248.
46. Klein, J., et al., *Reduction of frictional forces between solid surfaces bearing polymer brushes*. Nature, 1994. **370**(6491): p. 634-636.
47. Bartenstein, J.E., *Surface forces mediated by hierarchical polymer assemblies*, in *School of Chemistry*. 2016, University of Bristol.
48. Sorkin, R., et al., *Hydration lubrication and shear-induced self-healing of lipid bilayer boundary lubricants in phosphatidylcholine dispersions*. 2016. **12**(10): p. 2773-2784.

-
49. Smith, A.M., Lee, A.A., and Perkin, S., *The Electrostatic Screening Length in Concentrated Electrolytes Increases with Concentration*. The Journal of Physical Chemistry Letters, 2016. **7**(12): p. 2157-2163.
 50. van Engers, C.D., et al., *Direct Measurement of the Surface Energy of Graphene*. Nano Letters, 2017. **17**(6): p. 3815-3821.
 51. Pilkington, G.A., *Interaction in Dendrimer Nanofluids*, in *School of Chemistry*. 2014, University of Bristol.
 52. Kienle, D.F. and Kuhl, T.L., *Analyzing Refractive Index Profiles of Confined Fluids by Interferometry*. Analytical Chemistry, 2014. **86**(23): p. 11860-11867.
 53. Snow, T., *Polymer Brushes on Charged Surfaces: Synthesis, Characterisation and Interactions*, in *School of Chemistry*. 2016, University of Bristol.
 54. Tadmor, R., Chen, N., and Israelachvili, J.N., *Thickness and refractive index measurements using multiple beam interference fringes (FECO)*. Journal of Colloid and Interface Science, 2003. **264**(2): p. 548-553.
 55. Born, M. and Wolf, E., *Principles of optics: electromagnetic theory of propagation, interference and diffraction of light*. 2013: Elsevier.
 56. Clarkson, M.T., *Multiple-beam interferometry with thin metal films and unsymmetrical systems*. Journal of Physics D: Applied Physics, 1989. **22**(4): p. 475-482.
 57. Tadmor, R., et al., *Debye Length and Double-Layer Forces in Polyelectrolyte Solutions*. Macromolecules, 2002. **35**(6): p. 2380-2388.
 58. Briscoe, W.H., *Colloid Science Principle, Methods and Applications*. Second ed. 2010: Wiley. 329-361.
 59. Scarff, C.A., et al., *Variations on Negative Stain Electron Microscopy Methods: Tools for Tackling Challenging Systems*. Journal of visualized experiments : JoVE, 2018(132): p. 57199.
 60. Thompson, R.F., et al., *An introduction to sample preparation and imaging by cryo-electron microscopy for structural biology*. Methods, 2016. **100**: p. 3-15.
 61. Pisárčik, M., Devínsky, F., and Pupák, M., *Determination of micelle aggregation numbers of alkyltrimethylammonium bromide and sodium dodecyl sulfate surfactants using time-resolved fluorescence quenching*. Open Chemistry, 2015. **13**(1).
 62. Cocquyt, J., et al., *Interaction kinetics of anionic surfactants with cationic vesicles*. Colloids and Surfaces A: Physicochemical and Engineering Aspects, 2007. **298**(1): p. 22-26.
 63. Bergstrom, M. and Skov Pedersen, J., *Structure of pure SDS and DTAB micelles in brine determined by small-angle neutron scattering (SANS)*. Physical Chemistry Chemical Physics, 1999. **1**(18): p. 4437-4446.

64. Chen, S.-H.J.A.R.o.P.C., *Small angle neutron scattering studies of the structure and interaction in micellar and microemulsion systems*. 1986. **37**(1): p. 351-399.
65. Pires, J.M., Moura, A.F.d., and Freitas, L.C.G., *Investigating the spontaneous formation of SDS micelle in aqueous solution using a coarse-grained force field %J Química Nova*. 2012. **35**: p. 978-981.
66. Basavaraj, M.G., et al., *Nanovesicle formation and microstructure in aqueous ditallowethylesterdimethylammonium chloride (DEEDMAC) solutions*. *Journal of Colloid and Interface Science*, 2014. **429**: p. 17-24.
67. Filies, O., et al., *Surface roughness of thin layers—a comparison of XRR and SFM measurements*. *Applied Surface Science*, 1999. **141**(3): p. 357-365.
68. Holy, V., Baumbach, T., and Bessiere, M., *Interface roughness in surface-sensitive X-ray methods*. *Journal of Physics D: Applied Physics*, 1995. **28**(4A): p. A220-A226.
69. Fujii, Y., *Analysis of surface roughness correlation function by X-ray reflectivity*. 2016. **48**(11): p. 1136-1138.
70. Fujii, Y., *Recent Analysis on Surface and Interface Roughness Using X-Ray Reflectivity*. *Journal of Materials Science & Nanotechnology*, 2018. **6**(2).
71. Baumbach, T. and Mikulik, P., *X-ray Reflectivity by Rough Multilayers*, in *X-ray and Neutron Reflectivity: Principles and Applications*. 1999, Springer Berlin Heidelberg: Berlin, Heidelberg. p. 232-280.
72. Gibaud, A., *Specular Reflectivity from Smooth and Rough Surfaces*, in *X-ray and Neutron Reflectivity: Principles and Applications*. 1999, Springer Berlin Heidelberg: Berlin, Heidelberg. p. 87-120.
73. Israelachvili, J.N. and Tabor, D., *The measurement of van der Waals dispersion forces in the range 1.5 to 130 nm*. *Proceedings of the Royal Society of London. A. Mathematical and Physical Sciences*, 1972. **331**(1584): p. 19-38.
74. Kumar, A., et al., *Intact deposition of cationic vesicles on anionic cellulose fibers: Role of vesicle size, polydispersity, and substrate roughness studied via streaming potential measurements*. *Journal of Colloid and Interface Science*, 2016. **473**: p. 152-161.
75. Mathur, A.K., et al., *Surfactant-induced fluorescence changes in fluorescein dye*. 1988. **10**(5): p. 213-218.
76. Almgren, M., et al., *SDS Micelles at High Ionic Strength. A Light Scattering, Neutron Scattering, Fluorescence Quenching, and CryoTEM Investigation*. *Journal of Colloid and Interface Science*, 1998. **202**(2): p. 222-231.
77. Geng, S., et al., *A Light-Responsive Self-Assembly Formed by a Cationic Azobenzene Derivative and SDS as a Drug Delivery System*. *Scientific Reports*, 2017. **7**: p. 39202.
78. Renoncourt, A., et al., *Specific Alkali Cation Effects in the Transition from Micelles to Vesicles through Salt Addition*. *Langmuir : the ACS journal of surfaces and colloids*, 2007. **23**: p. 2376-2381.

79. Saha, A., et al., *Impact of Nearly Water-Insoluble Additives on the Properties of Vesicular Suspensions*. *Industrial & Engineering Chemistry Research*, 2017. **56**(4): p. 899-906.

8 Conclusions and future work

8.1 Conclusions

Interfacial and bulk complexation of polymer/surfactant and surfactant/surfactant systems was investigated. All systems studied here are relevant to practical applications, and the findings are set in such context. The polymer studied is used in laundry and washing-up detergents and was therefore investigated at the air-water interface, with correlation to its foaming behaviour. The double-tailed surfactant is commonly used as a fabric softener and the study was therefore focused on the solid-liquid interface.

8.1.1 PEG-*g*-PVAc polymer/surfactant mixtures

The interfacial structures and behaviour of a neutral amphiphilic co-polymer (consisting of a hydrophilic polyethylene glycol backbone with hydrophobic polyvinyl acetate grafts, PEG-*g*-PVAc) were investigated by a combination of complementary techniques, namely surface tension measurements (both equilibrium, γ , and dynamic, γ_d), X-ray and neutron reflectivity (XRR and NR) and preliminary foaming behaviour measurements. The effect of surfactant addition on the interfacial structures and behaviour was examined, as well as the influence of surfactant headgroup and polymer molecular architecture were considered.

The effect of surfactant headgroup was studied by using a series of surfactants possessing identical C₁₂H₂₅ hydrocarbon tail and varying the headgroup charge and size: anionic sodium dodecylsulfate (SDS), cationic dodecyltrimethylammonium bromide (DTAB) and non-ionic dodecylpentaethyleneglycol ether (C₁₂E₅). The impact of polymer architecture on these mixed systems was investigated by a variation of the length and number of PVAc grafts in the PEG-*g*-PVAc structure, as well as the length of the PEG backbone, hence also influencing the hydrophobic/hydrophilic balance.

A clear transition from cooperative adsorption at the air-water interface, evidenced by synergistic γ lowering at low surfactant concentration, to competitive adsorption at increasing surfactant concentration was observed, where the polymer seemed to be depleted from the interface. The onset of this competitive behaviour was highly dependent on the surfactant and polymer characteristics, with transition concentration ~ 0.5 cmc in mixtures containing SDS

and DTAB, and ~ 0.1 cmc in the case of C₁₂E₅/polymer mixtures. Even though both competitive and cooperative polymer/surfactant adsorption behaviours are routinely reported in literature [1-3], depending on the polymer and surfactant characteristics, such transition from synergistic to competitive behaviour achieved by increasing surfactant concentration and no other external input (such as pH or temperature control [4]) has not been pinpointed in literature before.

This transition to competitive adsorption was also confirmed by the surface excess (Γ) determined from NR data fitting at low Q range, an emerging method of Γ calculation especially valuable in mixed polymer/surfactant systems [5]; and the interfacial structures were elucidated following NR and XRR data fitting over the whole accessible Q range. At low surfactant concentrations, a single layer model, comprised of a mixed PEG-*g*-PVAc/surfactant layer, was used to fit the interfacial structures well. The thickness (t) of the layer depended largely on the composition. In PEG-*g*-PVAc/SDS system, at low SDS concentration $t \sim 12$ and 24 Å depended largely on the polymer concentration. With increasing SDS concentration to above its cmc, the layer $t \sim 12$ Å independent on the polymer concentration. Similar behaviour was observed in the system containing C₁₂E₅, however the final $t \sim 17$ Å. Both SDS and C₁₂E₅ have been shown to interact relatively strongly with PEG, and hence the backbone of the polymer [6, 7]. The cationic DTAB, on the other hand, was shown to interact with PVAc [8] following partial dissociation of the PVAc carbonyl group resulting in partial negative charge. These electrostatic interactions were demonstrated by the synergistic adsorption at low surfactant concentration, with a layer $t \sim 27$ Å, marginally thicker than the pure polymer layer. Increasing DTAB concentration the layer t resembled that of pure DTAB monolayer at the interface ($t \sim 14$ Å), yet the polymer $\Gamma \sim 0.6$ mg m⁻² confirmed the relative strong DTAB/PEG-*g*-PVAc interactions at the interface.

Using a multilayer model for NR data fitting at high surfactant concentration, the air-water interface was found to be predominantly covered by surfactant monolayer, while the polymer was depleted from the interface forming a thin, non-uniform layer just underneath the surfactant monolayer, free to interact with the surfactant headgroup. This “hanging” polymer layer t was determined to be only ~ 3 Å in the system containing SDS, and $t \sim 5$ Å in the systems containing DTAB and C₁₂E₅. This layer thickness was then correlated to the enhanced foam stability in SDS/polymer system, and no significant effect on foam stability observed in the strongly interacting DTAB/polymer and C₁₂E₅/polymer mixed systems.

The implications of such structural and compositional characteristics of the interfacial layer for foaming behaviour of the polymer/surfactant mixture were also evaluated. It is widely accepted that polymers can be added to surfactant systems to increase foam stability as a result of changing the viscosity of the bulk solution and therefore decreasing the liquid drainage. As an example, a comb co-polymer gel has been shown to enhance foam stability used in oil recovery, while lowering its foamability [9]. The different foam stability observed in this work cannot be attributed solely to an increase in solution viscosity, as the foaming behaviour of PEG-*g*-PVAc mixtures varied depending on the surfactant characteristics. We could therefore argue that the polymer architecture must be considered in such studies as well as the specific polymer/surfactant interactions [10] at the air-water interface, as gauged by a combination of complementary methods [11].

These findings can be exploited in product formulations, where depending on the surfactants present, the PEG-*g*-PVAc co-polymer can act as foam stability enhancer (with SDS, preferred in hand dishwashing detergents) or slight defoamer (with DTAB and C₁₂E₅, preferred in automatic dishwashing detergents).

8.1.2 DEEDMAC/SDS complexes

A comprehensive study of DEEDMAC/SDS complexation was performed in bulk and at interfaces. In the bulk, the interactions between cationic DEEDMAC vesicles and anionic SDS resulted in an increase in the hydrodynamic diameter and charge reversal upon complexation. Additionally, the SDS adsorption onto DEEDMAC vesicle outer layer, as well as aggregation, was also visualised using transmission electron microscopy and confocal microscopy. The SDS/DEEDMAC complexation has been studied before in the bulk [12] and we wished to extend this study to interfaces, specifically the solid-liquid interface relevant to the DEEDMAC applications as fabric softener. Some correlation between vesicle interactions at interfaces and in bulk has been proposed before. However, it was demonstrated that the work of adhesion between vesicles was highly dependent on the vesicle membrane tension and therefore changes of several orders of magnitude have been determined between free vesicles in bulk and at solid-liquid interface [13].

The adsorption of DEEDMAC bilayers at mica surfaces *via* vesicle rupture (also referred to as vesicle fusion) was investigated using XRR and surface force apparatus (SFA). The bilayer thickness t was determined to be ~ 3 -4 nm, consistent with existing literature [14]. Addition of

SDS above its cmc to an adsorbed DEEDMAC bilayer led to a prominent t increase to $t > 30$ nm, consistent with several alternating DEEDMAC/SDS layers. These DEEDMAC/SDS complexes at the solid-liquid interface were stable under normal and shearing forces and following MilliQ rinsing. The high surface roughness and patchiness arising from SDS/DEEDMAC complexation somewhat limited the effectiveness of XRR.

These results can be related to the application of DEEDMAC as a popular fabric softener, where the surfactant adsorbs to the surface of the fabric and then remains adsorbed during the remainder of the wash cycle, as well as during wear time, providing additional softness [15]. The stability of adsorbed DEEDMAC layer in presence of other surfactants is therefore of paramount importance.

8.2 Future work

Several avenues were identified for possible future studies, as well as improved data analysis and interpretation.

8.2.1 PEG-*g*-PVAc polymer/surfactant mixtures

Currently it is not possible to calculate I of surfactant/Polymer B mixtures nor compare the XRR data to NR measurements of surfactant/Polymer B mixtures. It would therefore be desirable to collect NR data of the surfactant mixtures with Polymer B. NR data acquisition over the whole accessible Q range and in different isotopic contrasts is time consuming, however I can be determined from the low Q analysis of two isotopic contrasts measurements (deuterated and hydrogenous surfactant with hydrogenous polymer) in ACMW which largely decreases the time consumption [16].

Furthermore, in the current study we have not employed isotopic contrast matching of the surfactant or polymer structure to the solvent. However, by using solvent with scattering length density matched to a part of the system could add more certainty to our data fitting analysis (*e.g.* at high surfactant concentrations matching out surfactant at the top of the interface and only “seeing” the partially depleted polymer hanging layer). Additionally, co-fitting of the XRR and NR data of polymer/surfactant mixtures would be beneficial to minimise the uncertainties associated with any fitting method.

There has been an ongoing effort to establish a link between foaming behaviour and rheological properties of surfactant systems [17, 18]. It has been shown that the surface dilatational elasticity of two simple non-ionic surfactants measured by oscillating drop method correlated well with their thin film stability [19]. Investigating the effect of polymer addition to surfactant systems and their interfacial rheology directly correlated to the change of surface tension and droplet volume would therefore be of interest.

Finally, dynamic γ data of the surfactant/Polymer B mixtures could be collected to study the fast adsorption dynamics in the systems, especially in mixtures of DTAB/Polymer B where no synergy was observed in equilibrium γ data.

8.2.2 DEEDMAC/SDS complexes

NR of deuterated SDS and hydrogenous DEEDMAC at varying SDS concentrations at interfaces would allow for more precise data analysis regarding the adsorption behaviour of these systems. Additionally, off-specular XRR and/or NR could be used to determine spatial distribution along the interface and would also aid in the XRR and NR data fitting at the interfaces which is currently halted by the non-homogeneity of the interfacial layers and high roughness. The structuring along the air-water interface could also be investigated using Brewster angle microscopy.

Limited shearing data was recorded using the SFA. However, due to the piezoelectric tube wear, it would be advisable to conduct repeat experiments at chosen DEEDMAC/SDS concentrations, and at the shear rate relevant to DEEDMAC use as a fabric softener. The normal force SFA data could be fitted using modified DLVO theory, with modifications needed to account for the electrostatic and hydration forces [14].

Polarised light microscopy (PLM) was attempted, however no structures were observed at the concentrations studied. We would expect to see Maltese crosses from vesicles, SDS micelles and any anisotropic complex structures; therefore, it would be of interest to attempt PLM on higher resolution microscope as an indication of any ordering and formation of lamellar DEEDMAC/SDS phase could be gained from such studies [20].

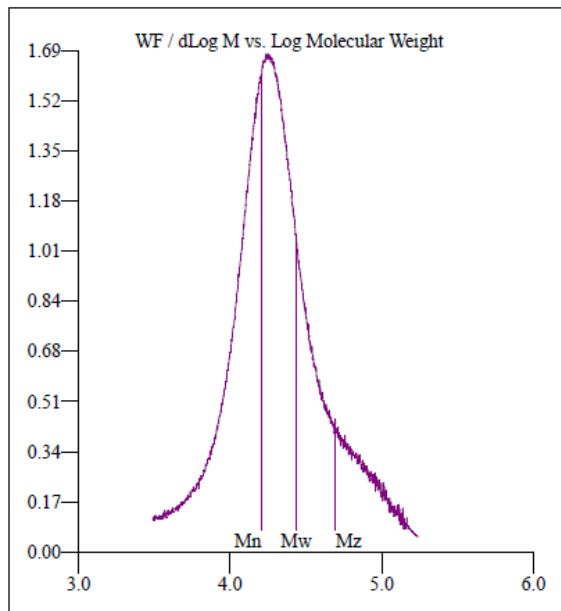
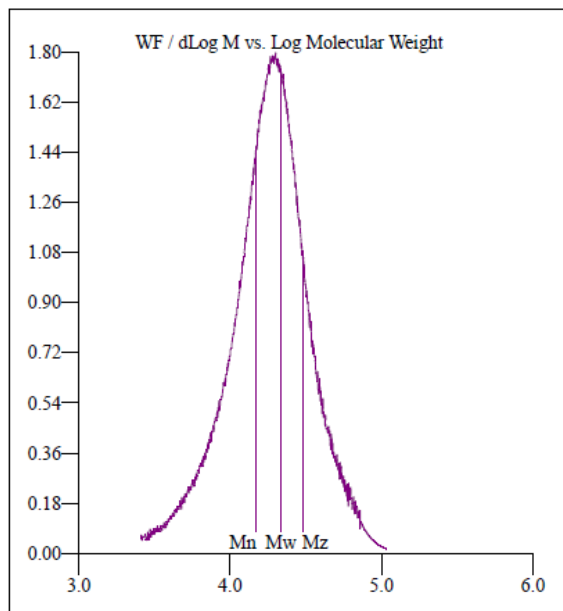
8.3 References

1. Jean, B., Lee, L.-T., and Cabane, B., *Effects of Sodium Dodecyl Sulfate on the Adsorption of Poly(N-isopropylacrylamide) at the Air–Water Interface*. Langmuir, 1999. **15**(22): p. 7585-7590.
2. Jadidi, N., Adib, B., and Malihi, F.B., *Synergism and Performance Optimization in Liquid Detergents Containing Binary Mixtures of Anionic–Nonionic, and Anionic–Cationic Surfactants*. 2013. **16**(1): p. 115-121.
3. Péron, N., et al., *Competitive Adsorption of Neutral Comb Polymers and Sodium Dodecyl Sulfate at the Air/Water Interface*. The Journal of Physical Chemistry B, 2008. **112**(25): p. 7410-7419.
4. Windsor, R., Neivandt, D.J., and Davies, P.B., *Temperature and pH Effects on the Coadsorption of Sodium Dodecyl Sulfate and Poly(ethylenimine)*. Langmuir, 2002. **18**(6): p. 2199-2204.
5. Braun, L., et al., *Polymers and surfactants at fluid interfaces studied with specular neutron reflectometry*. Advances in Colloid and Interface Science, 2017. **247**: p. 130-148.
6. Cabane, B. and Duplessix, R., *Neutron scattering study of water-soluble polymers adsorbed on surfactant micelles*. Colloids and Surfaces, 1985. **13**: p. 19-33.
7. López-Esparza, R., et al., *Interaction between poly(ethylene glycol) and two surfactants investigated by diffusion coefficient measurements*. Journal of Colloid and Interface Science, 2006. **300**(1): p. 105-110.
8. Briddick, A., et al., *Surfactant and Plasticizer Segregation in Thin Poly(vinyl alcohol) Films*. Langmuir, 2016. **32**(3): p. 864-872.
9. Zhao, G., et al., *Enhanced foam stability by adding comb polymer gel for in-depth profile control in high temperature reservoirs*. Colloids and Surfaces A: Physicochemical and Engineering Aspects, 2015. **482**: p. 115-124.
10. Petkova, R., Tcholakova, S., and Denkov, N.D., *Foaming and Foam Stability for Mixed Polymer–Surfactant Solutions: Effects of Surfactant Type and Polymer Charge*. Langmuir, 2012. **28**(11): p. 4996-5009.
11. Fauser, H., et al., *Surface Adsorption of Oppositely Charged SDS:C12TAB Mixtures and the Relation to Foam Film Formation and Stability*. The Journal of Physical Chemistry B, 2015.
12. Cocquyt, J., et al., *Interaction kinetics of anionic surfactants with cationic vesicles*. Colloids and Surfaces A: Physicochemical and Engineering Aspects, 2007. **298**(1): p. 22-26.
13. Frostad, J.M., et al., *Direct measurement of interaction forces between charged multilamellar vesicles*. Soft Matter, 2014. **10**(39): p. 7769-7780.

-
14. Das, S., et al., *Interaction of adsorbed polymers with supported cationic bilayers*. RSC Advances, 2013. **3**(43): p. 20405-20411.
 15. Kumar, A., et al., *Intact deposition of cationic vesicles on anionic cellulose fibers: Role of vesicle size, polydispersity, and substrate roughness studied via streaming potential measurements*. Journal of Colloid and Interface Science, 2016. **473**: p. 152-161.
 16. Campbell, R.A., *Recent advances in resolving kinetic and dynamic processes at the air/water interface using specular neutron reflectometry*. Current Opinion in Colloid & Interface Science, 2018. **37**: p. 49-60.
 17. Heller, J.P. and Kuntamukkula, M.S., *Critical review of the foam rheology literature*. Industrial engineering chemistry research, 1987. **26**(2): p. 318-325.
 18. Langevin, D., *Influence of interfacial rheology on foam and emulsion properties*. Advances in Colloid and Interface Science, 2000. **88**(1-2): p. 209-222.
 19. Stubenrauch, C. and Miller, R., *Stability of Foam Films and Surface Rheology: An Oscillating Bubble Study at Low Frequencies*. The Journal of Physical Chemistry B, 2004. **108**(20): p. 6412-6421.
 20. Bibi, S., et al., *Microscopy imaging of liposomes: From coverslips to environmental SEM*. International Journal of Pharmaceutics, 2011. **417**(1): p. 138-150.

Appendix

A. Polymer GPC



Conventional Calibration - Homopolymers : Results

Peak RV - (ml)	20.207	24.850
Mn - (Daltons)	14,854	0
Mw - (Daltons)	21,568	0
Mz - (Daltons)	29,930	0
Mp - (Daltons)	18,785	0
Mw / Mn	1.452	0.000
Percent Above Mw:	0	100.000
Percent Below Mw:	0	0.000
Mw 10.0% Low	5,797	0
Mw 10.0% High	50,532	0
Wt Fr (Peak)	1.000	0.000
RI Area - (mvm)	10.57	-3.50
UV Area - (mvm)	0.00	0.00

Conventional Calibration - Homopolymers : Results

Peak RV - (ml)	20.267	24.837
Mn - (Daltons)	16,064	0
Mw - (Daltons)	27,193	0
Mz - (Daltons)	49,544	0
Mp - (Daltons)	17,154	0
Mw / Mn	1.693	0.000
Percent Above Mw:	0	100.000
Percent Below Mw:	0	0.000
Mw 10.0% Low	6,241	0
Mw 10.0% High	89,339	0
Wt Fr (Peak)	1.000	0.000
RI Area - (mvm)	17.66	-1.57
UV Area - (mvm)	0.00	0.00

Figure A.1 GPC data of PEG-g-PVAc co-polymers.

B. NMR

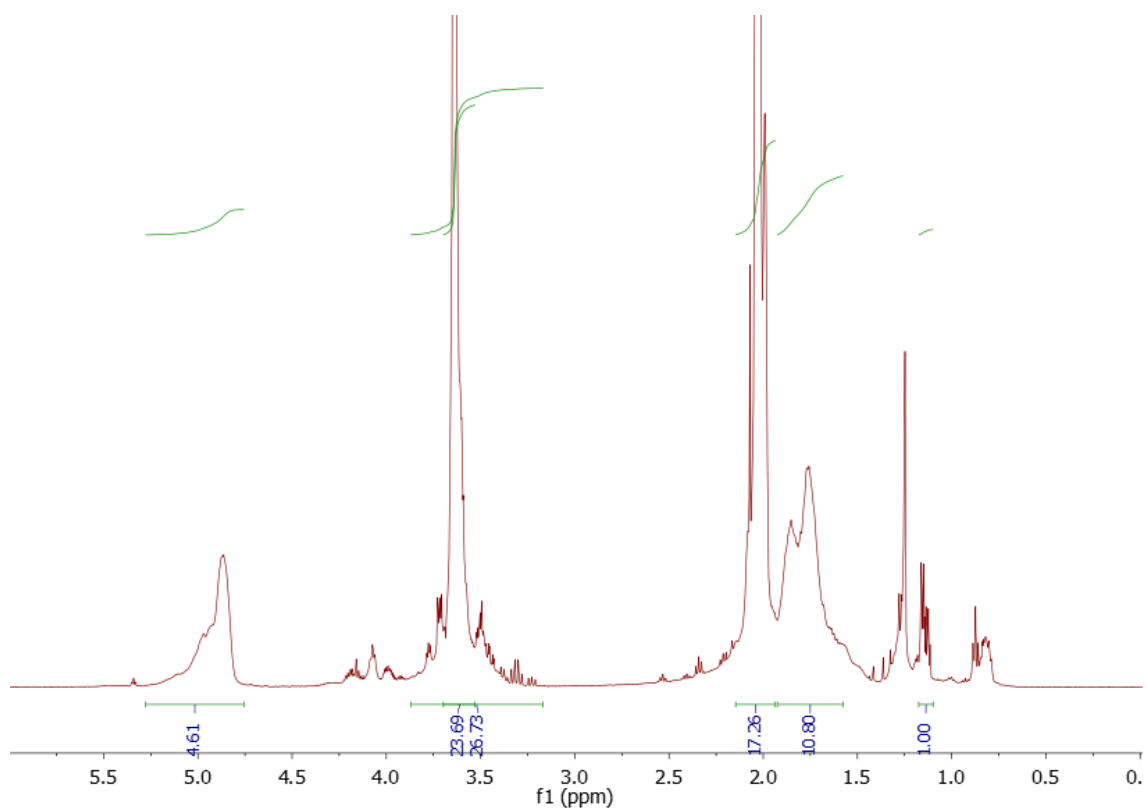


Figure B.1 ^1H NMR of PEG-g-PVAc co-polymer.

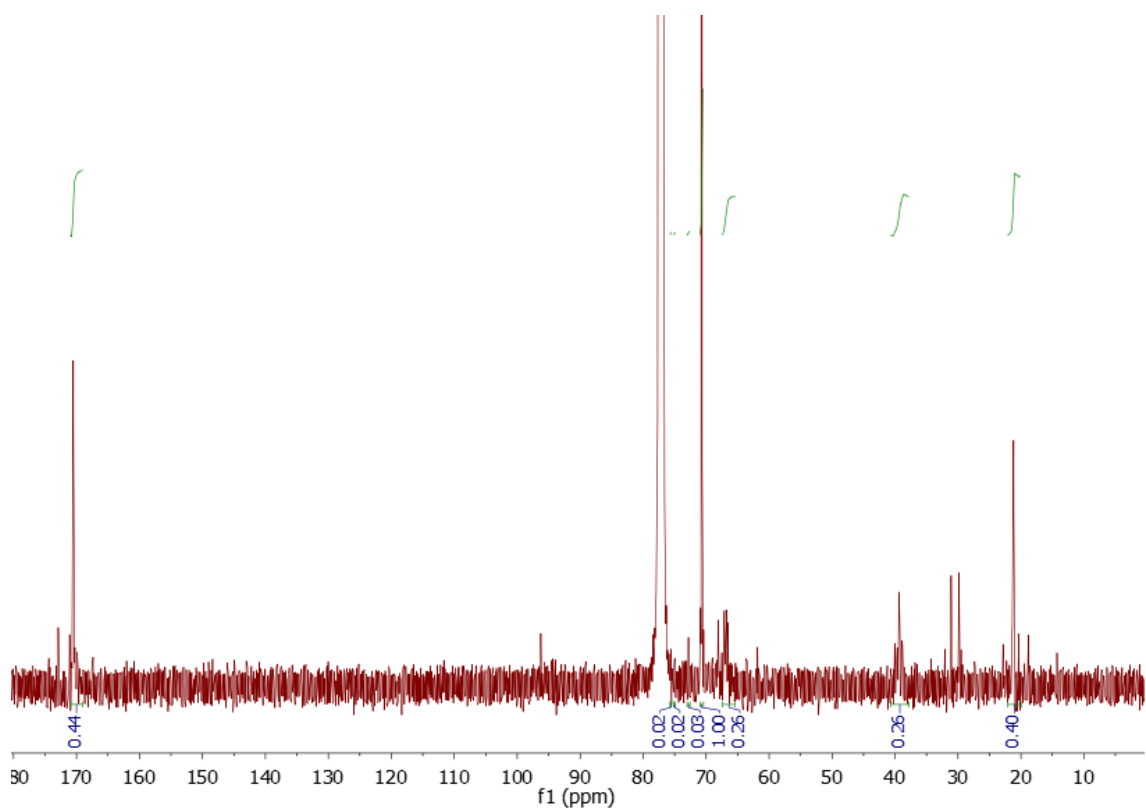


Figure B.2 Inverse gated ^{13}C NMR of PEG-g-PVAc co-polymer.

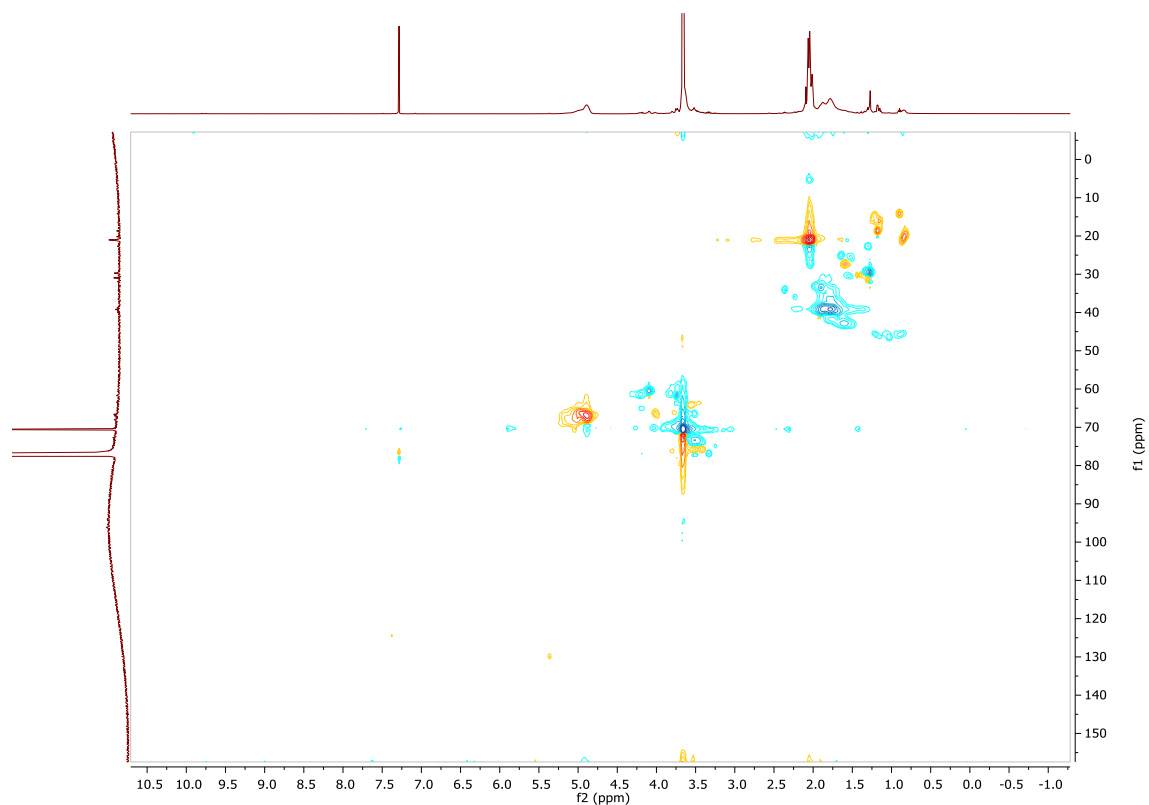


Figure B.3 HSQC NMR of PEG-g-PVAc co-polymer

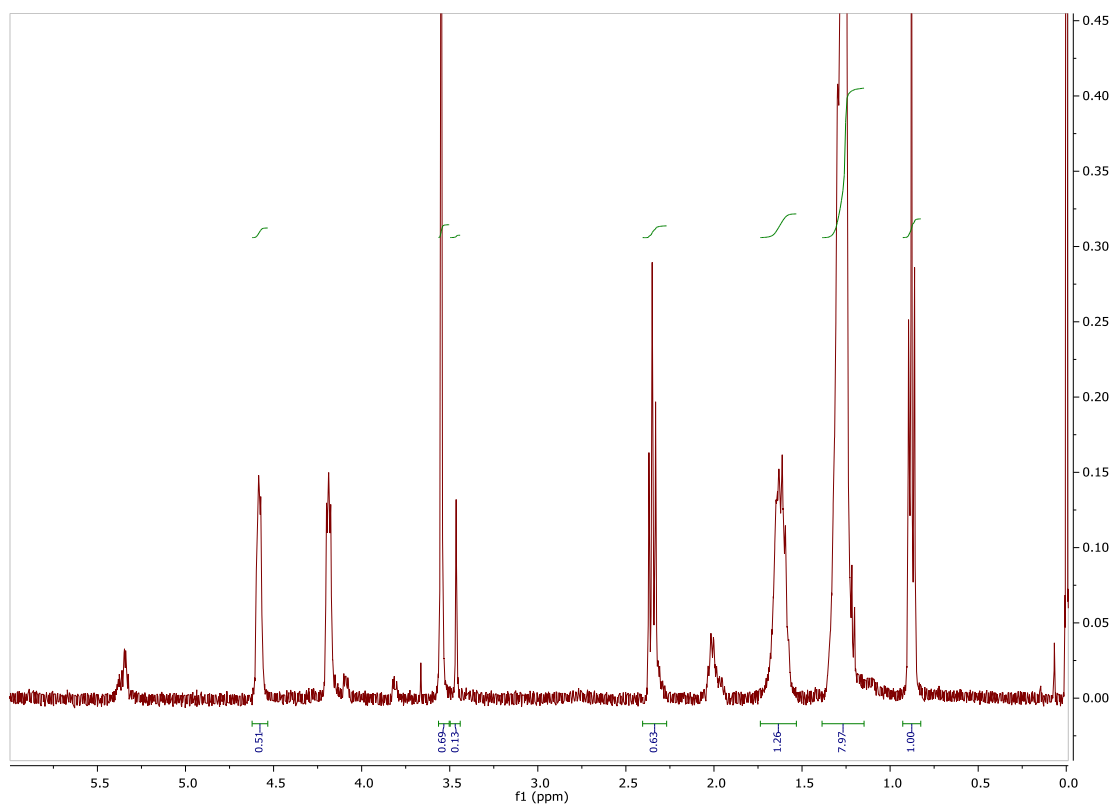


Figure B.4 ^1H NMR of DEEDMAC

C. Supplementary material for Chapter 3

Fitted NR data for PEG-*g*-PVAc at two concentrations (0.2 and 2 cac) is shown in Figure C.1. The data was fitted using a 1-layer model, with the schematics of the interface shown in the inset, and the fitted ρ profiles shown with the fitted parameters (t , σ , and φ_{water}). The interfacial polymer layer thickness increased from $t \sim 10.8 \text{ \AA}$ at 0.2 cac to $t \sim 28.0 \text{ \AA}$ at 2 cac.

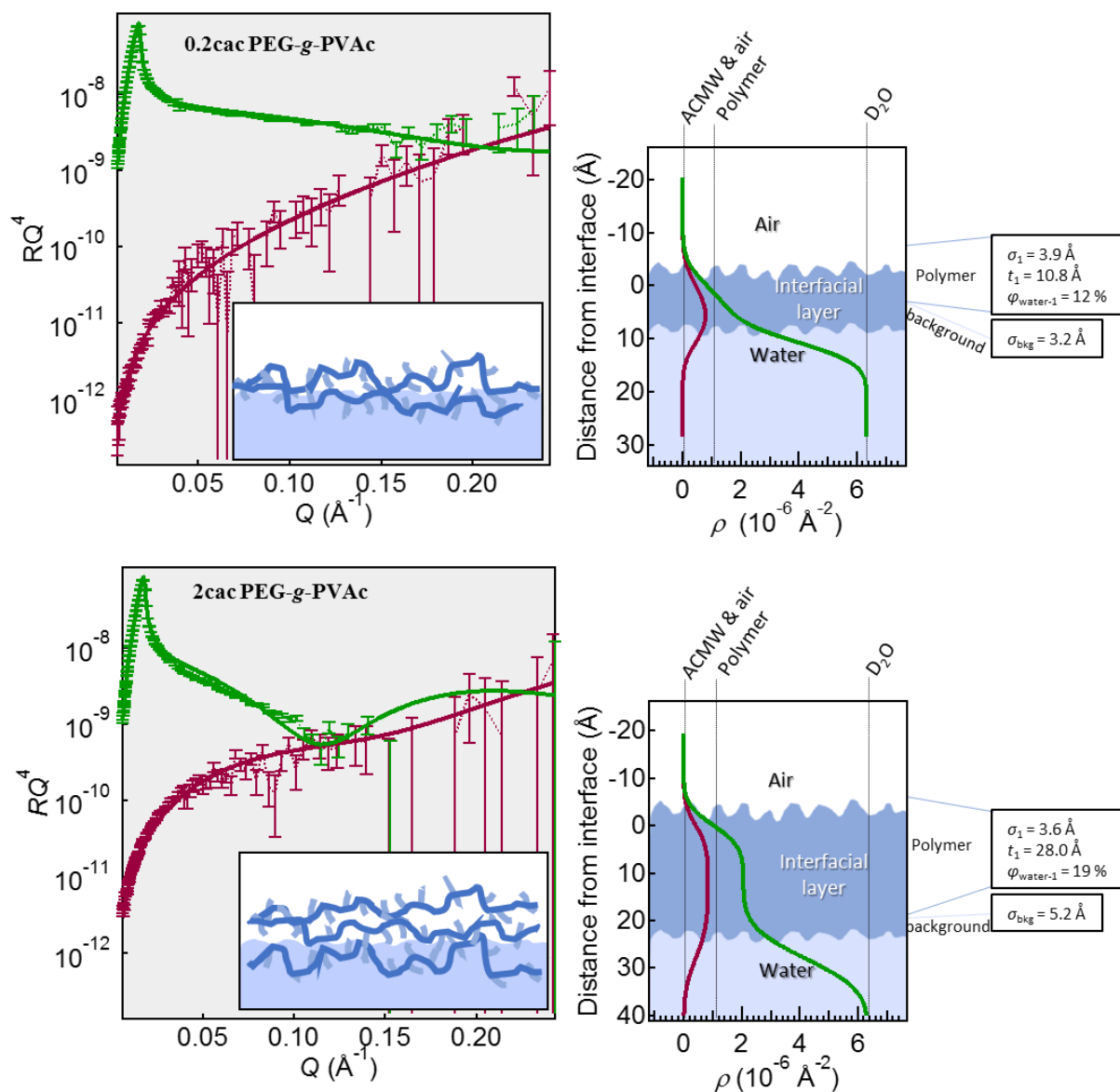


Figure C.1 Fitted NR data for 0.2 and 2 cac PEG-*g*-PVAc, with the fitted ρ profiles and schematic representation based on the fitted parameters. The data is colour coded as follows: green represents PEG-*g*-PVAc in D₂O, and purple represents PEG-*g*-PVAc in ACMW. The error bars associated with the data points were determined from the data reduction, larger at higher Q values due to lower contrast between the solvent and sample. The solid lines show the fitted curve, with the fitted parameters also shown, including thickness (t), solvent volume fraction (φ_{water}), and roughness of the layer (σ).

The NR data and the fitted ρ profiles using a 1-layer model for SDS at 0.1 cmc and a 2-layer model for SDS at 1.2 cmc are shown in Figure C.2.

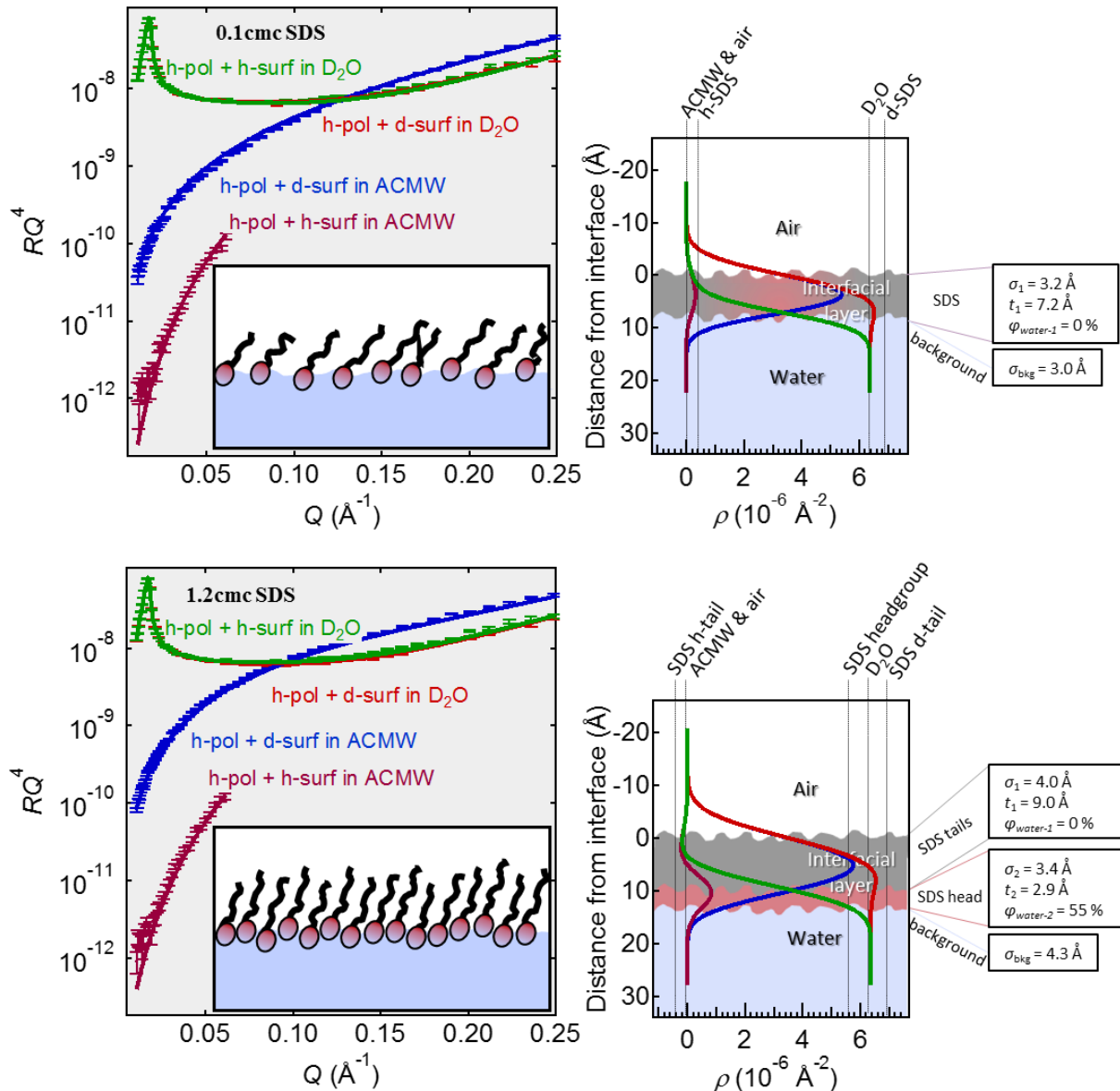


Figure C.2 Fitted NR data for 0.1 and 1.2 cmc SDS, with the fitted ρ profiles and schematic representation based on the fitted parameters. The data is colour coded as follows: **red** represents dSDS in D_2O , **green** represents hSDS in D_2O , **blue** represents dSDS in ACMW, and **purple** represents hSDS in ACMW. The error bars associated with the data points were determined from the data reduction, larger at higher Q values due to lower contrast between the solvent and sample. The solid lines show the fitted curve, with the fitted parameters also shown, including thickness (t), solvent volume fraction (ϕ_{water}), and roughness of the layer (σ).

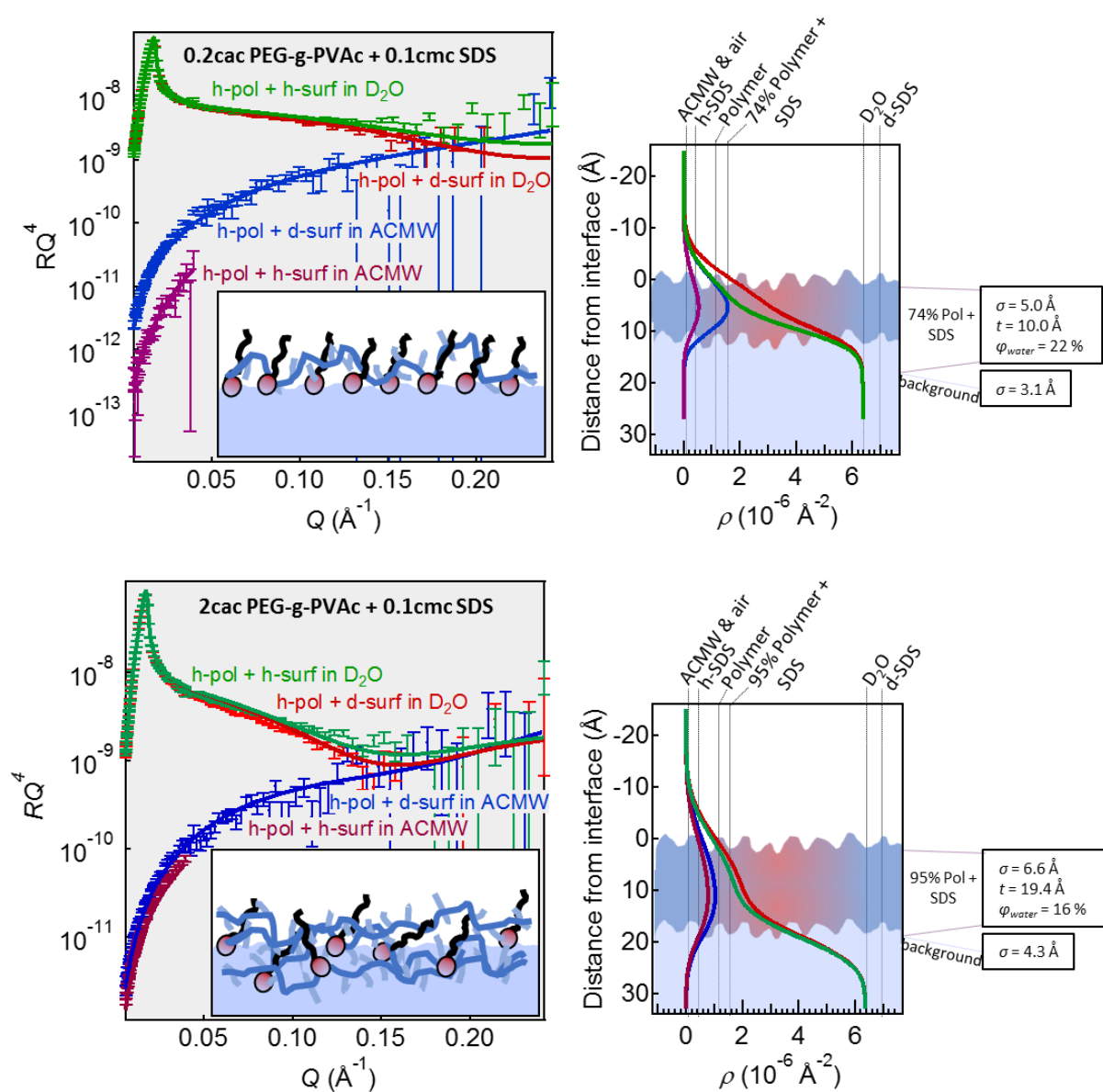


Figure C.3 Fitted NR data for 0.1 cmc SDS with 0.2 and 2 cac PEG-g-PVAc, with the fitted ρ profiles and schematic representation based on the fitted parameters. The data is colour coded as follows: **red** represents mixtures of PEG-g-PVAc and dSDS in D_2O , **green** represents mixtures of PEG-g-PVAc with hSDS in D_2O , **blue** represents mixtures of PEG-g-PVAc with dSDS in ACMW, and **purple** represents mixtures of PEG-g-PVAc with hSDS in ACMW. The error bars associated with the data points were determined from the data reduction, larger at higher Q values due to lower contrast between the solvent and sample. The solid lines show the fitted curve, with the fitted parameters also shown, including thickness (t), solvent volume fraction (φ_{water}), and roughness of the layer (σ).

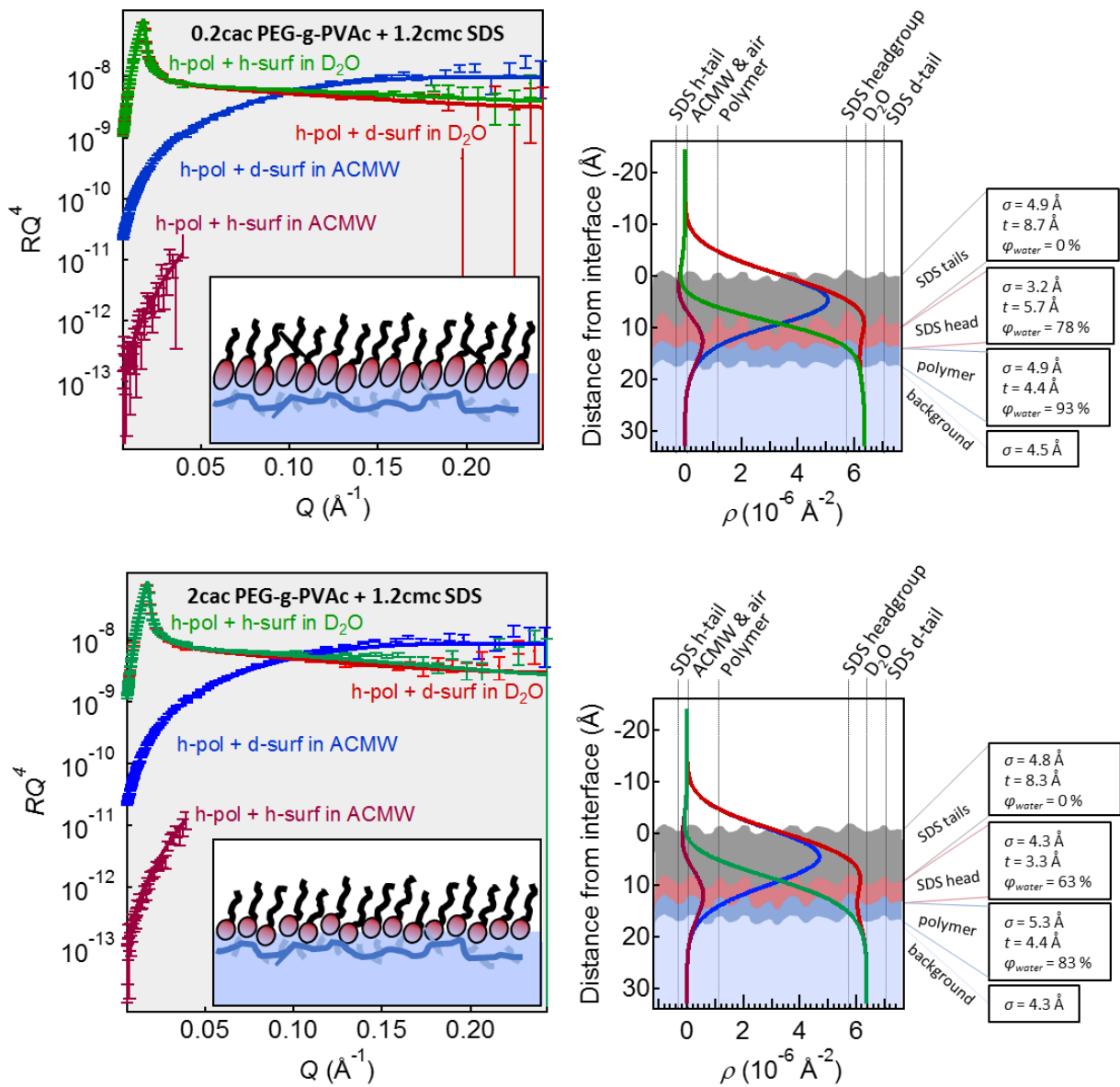


Figure C.4 Fitted NR data for 1.2 cmc SDS with 0.2 and 2 cac PEG-g-PVAc, with the fitted ρ profiles and schematic representation based on the fitted parameters. The data is colour coded as follows: **red** represents mixtures of PEG-g-PVAc and dSDS in D_2O , **green** represents mixtures of PEG-g-PVAc with hSDS in D_2O , **blue** represents mixtures of PEG-g-PVAc with dSDS in ACMW, and **purple** represents mixtures of PEG-g-PVAc with hSDS in ACMW. The error bars associated with the data points were determined from the data reduction, larger at higher Q values due to lower contrast between the solvent and sample. The solid lines show the fitted curve, with the fitted parameters also shown, including thickness (t), solvent volume fraction (φ_{water}), and roughness of the layer (σ).

Appendix

An example of fitted NR data plotted as R vs Q rather than RQ^4 vs Q is shown in Figure C.5.

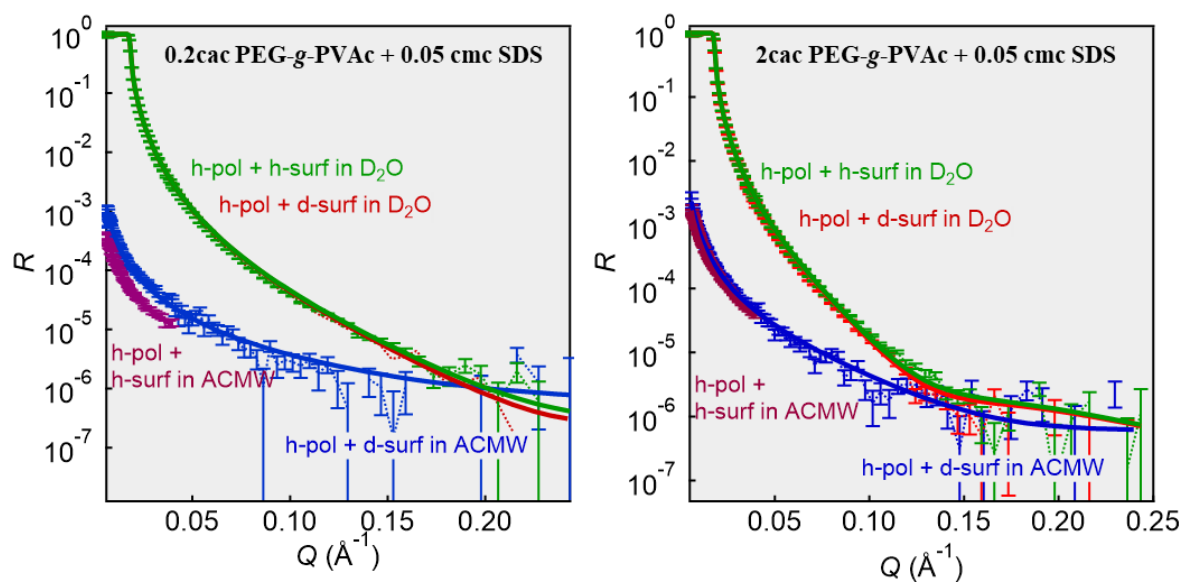


Figure C.5 NR data of PEG-g-PVAc with 0.05 cmc SDS plotted as R vs Q .

For illustration of the different models for fitting NR data of SDS/PEG-*g*-PVAc mixtures, we show a comparison of a 1-layer model fit to 2-layer or 3-layer model fits of mixtures containing 0.05 cmc SDS (Figure C.6), 0.5 cmc SDS (Figure C.7) and 5 cmc SDS (Figure C.8) with the polymer.

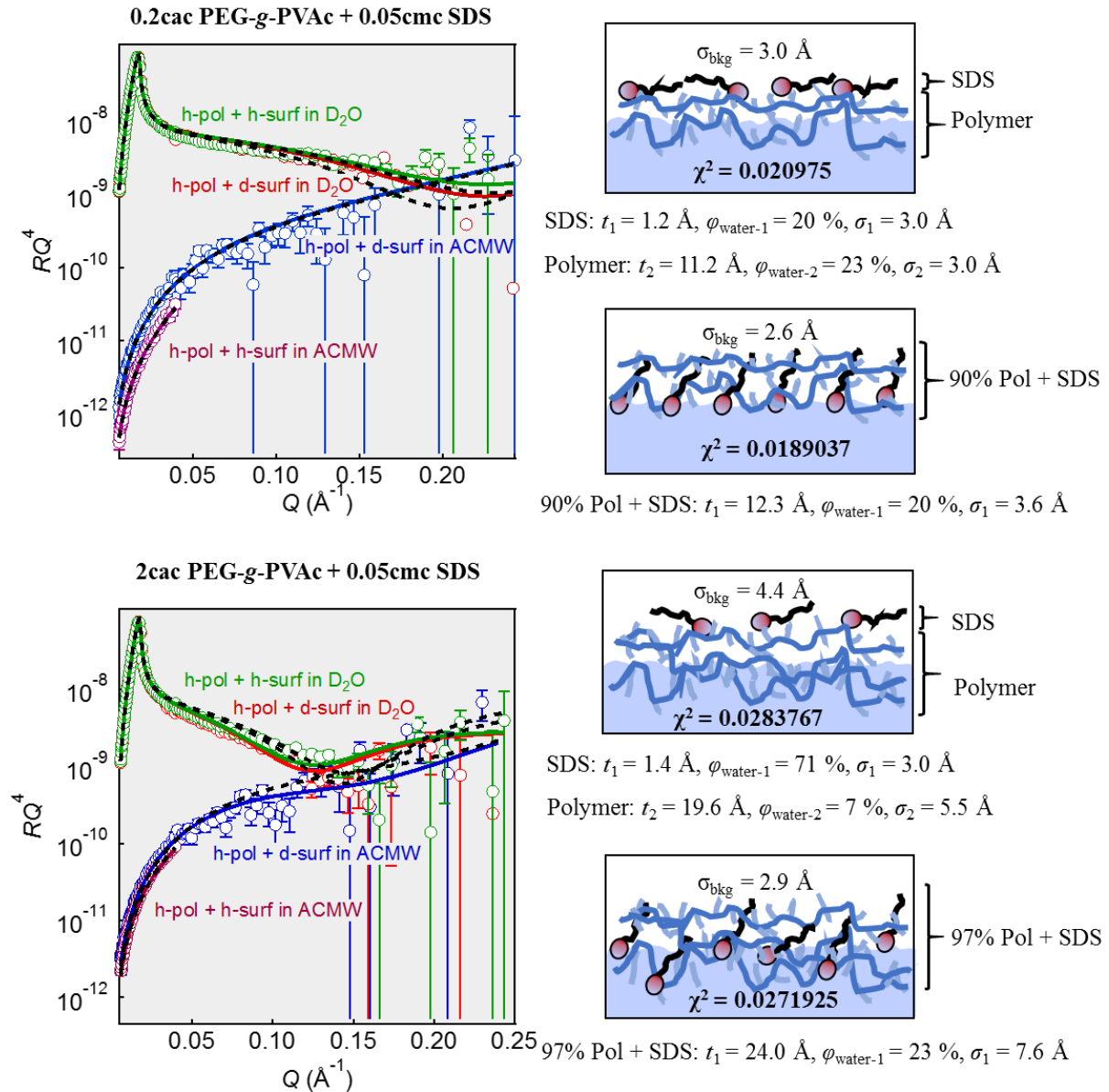


Figure C.6 Fitted NR data for 0.05 cmc SDS with 0.2 and 2 cac PEG-*g*-PVAc. The data is colour coded as follows: **red** represents mixtures of PEG-*g*-PVAc and dSDS in D₂O, **green** represents mixtures of PEG-*g*-PVAc with hSDS in D₂O, **blue** represents mixtures of PEG-*g*-PVAc with dSDS in ACMW, and **purple** represents mixtures of PEG-*g*-PVAc with hSDS in ACMW. The coloured solid lines show the fitted curves using a 1-layer model, while the dashed lines represent the fits using a 2-layer model. The schematic representations and the fitted parameters are also shown, including thickness (t), solvent volume fraction (φ_{water}), and roughness of the layer (σ). Included is also a χ^2 value for each fitted model, which is a measure of the quality of the fit (the lower the value, the more closely is the data fitted). The error bars associated with the data points were determined from the data reduction, larger at higher Q values due to lower contrast between the solvent and sample.

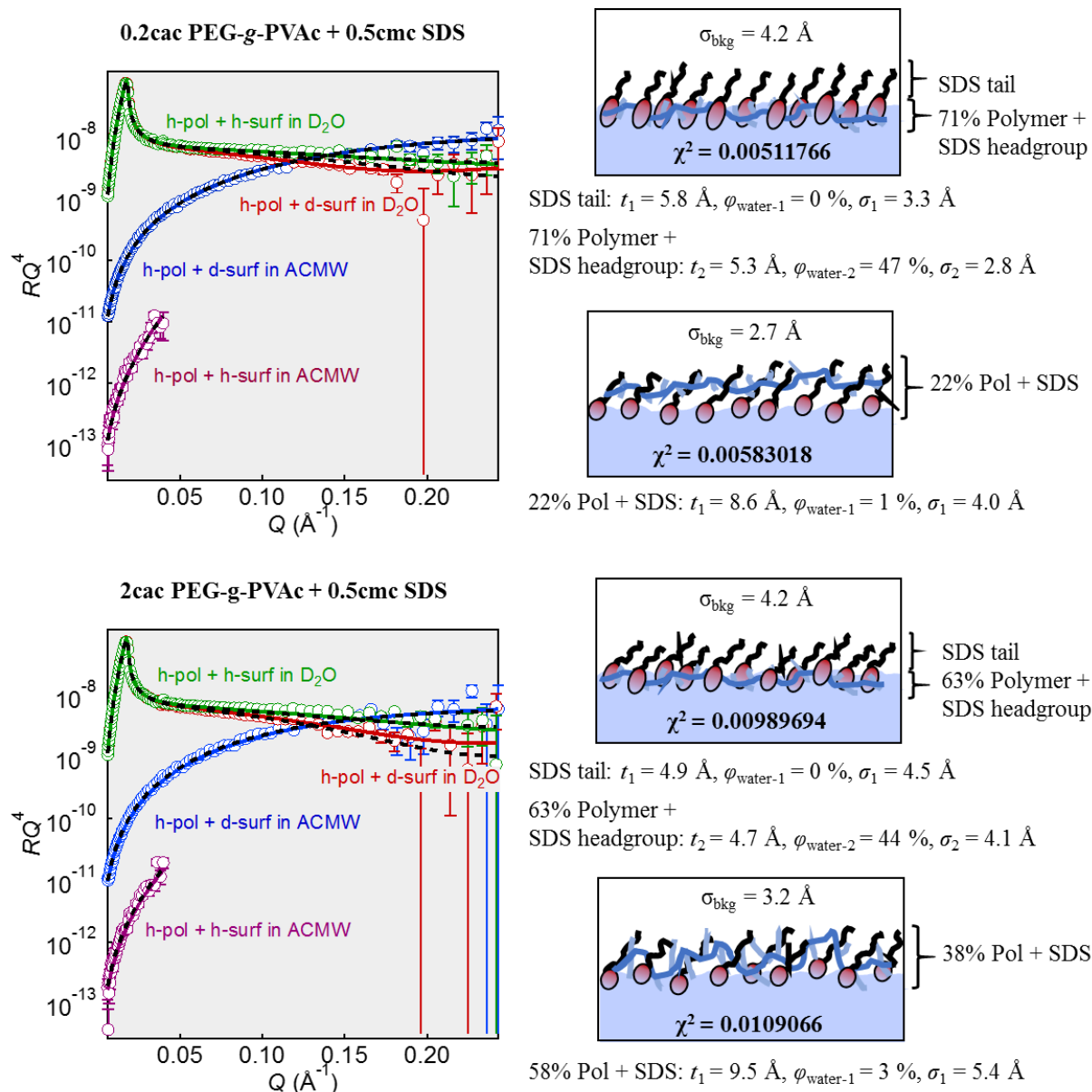


Figure C.7 Fitted NR data for 0.5 cmc SDS with 0.2 and 2 cac PEG-g-PVAc. The data is colour coded as follows: *red* represents mixtures of PEG-g-PVAc and dSDS in D₂O, *green* represents mixtures of PEG-g-PVAc with hSDS in D₂O, *blue* represents mixtures of PEG-g-PVAc with dSDS in ACMW, and *purple* represents mixtures of PEG-g-PVAc with hSDS in ACMW. The coloured solid lines show the fitted curves using a 2-layer model, while the dashed lines represent the fits using a 1-layer model. The schematic representations and the fitted parameters are also shown, including thickness (t), solvent volume fraction (ϕ_{water}), and roughness of the layer (σ). Included is also a χ^2 value for each fitted model, which is a measure of the quality of the fit (the lower the value, the more closely is the data fitted). The error bars associated with the data points were determined from the data reduction, larger at higher Q values due to lower contrast between the solvent and sample.

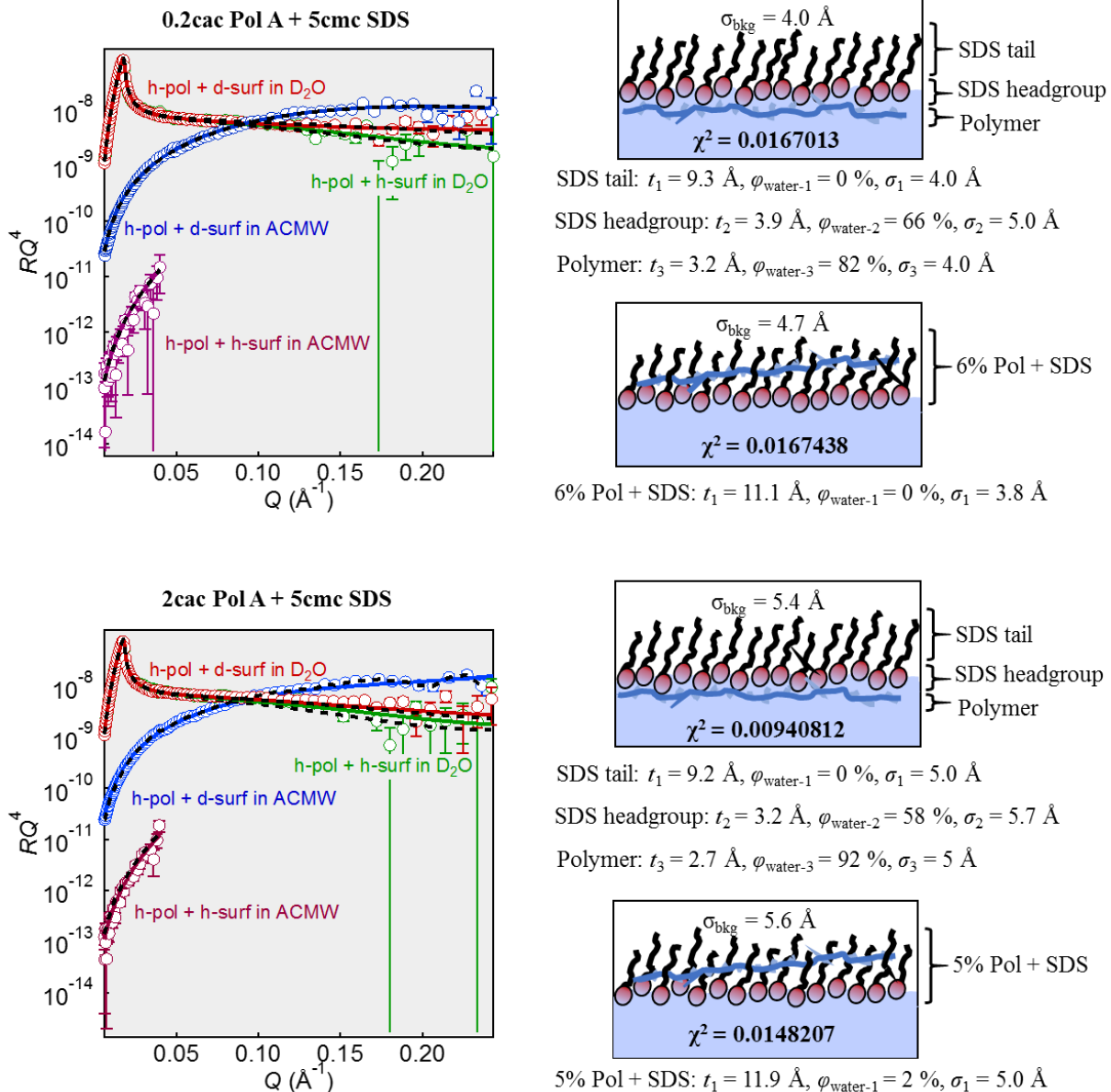


Figure C.8 Fitted NR data for 5 cmc SDS with 0.2 and 2 cac PEG-g-PVAc. The data is colour coded as follows: red represents mixtures of PEG-g-PVAc and dSDS in D_2O , green represents mixtures of PEG-g-PVAc with hSDS in D_2O , blue represents mixtures of PEG-g-PVAc with dSDS in ACMW, and purple represents mixtures of PEG-g-PVAc with hSDS in ACMW. The coloured solid lines show the fitted curves using a 3-layer model, while the dashed lines represent the fits using a 1-layer model. The schematic representations and the fitted parameters are also shown, including thickness (t), solvent volume fraction (φ_{water}), and roughness of the layer (σ). Included is also a χ^2 value for each fitted model, which is a measure of the quality of the fit (the lower the value, the more closely is the data fitted). The error bars associated with the data points were determined from the data reduction, larger at higher Q values due to lower contrast between the solvent and sample.

D. Supplementary material for Chapter 4

The NR data and the fitted ρ profiles using a 1-layer model for DTAB at 0.1 cmc and a 2-layer model for DTAB at 1.2 cmc are shown in Figure .

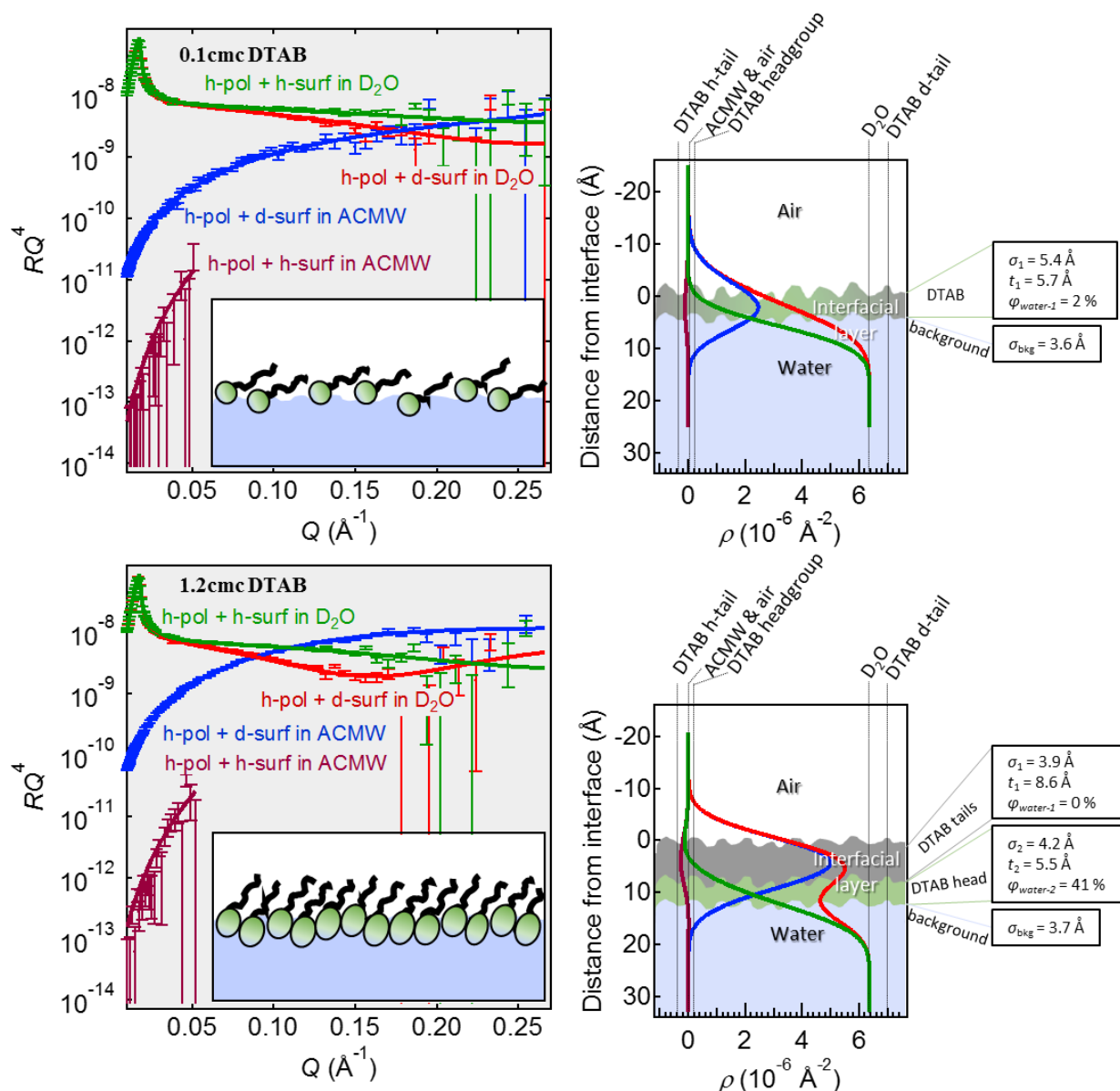


Figure D.1 Fitted NR data for 0.1 and 1.2 cmc DTAB, with the fitted ρ profiles and schematic representation based on the fitted parameters. The data is colour coded as follows: *red* represents dSDS in D_2O , *green* represents hSDS in D_2O , *blue* represents dSDS in ACMW, and *purple* represents hSDS in ACMW. The error bars associated with the data points were determined from the data reduction, larger at higher Q values due to lower contrast between the solvent and sample. The solid lines show the fitted curve, with the fitted parameters also shown, including thickness (t), solvent volume fraction (ϕ_{water}), and roughness of the layer (σ).

E. Supplementary material for Chapter 4

The NR data and the fitted ρ profiles using a 1-layer model for $C_{12}E_5$ at 0.1 cmc and a 2-layer model for $C_{12}E_5$ at 1.2 cmc are shown in Figure .

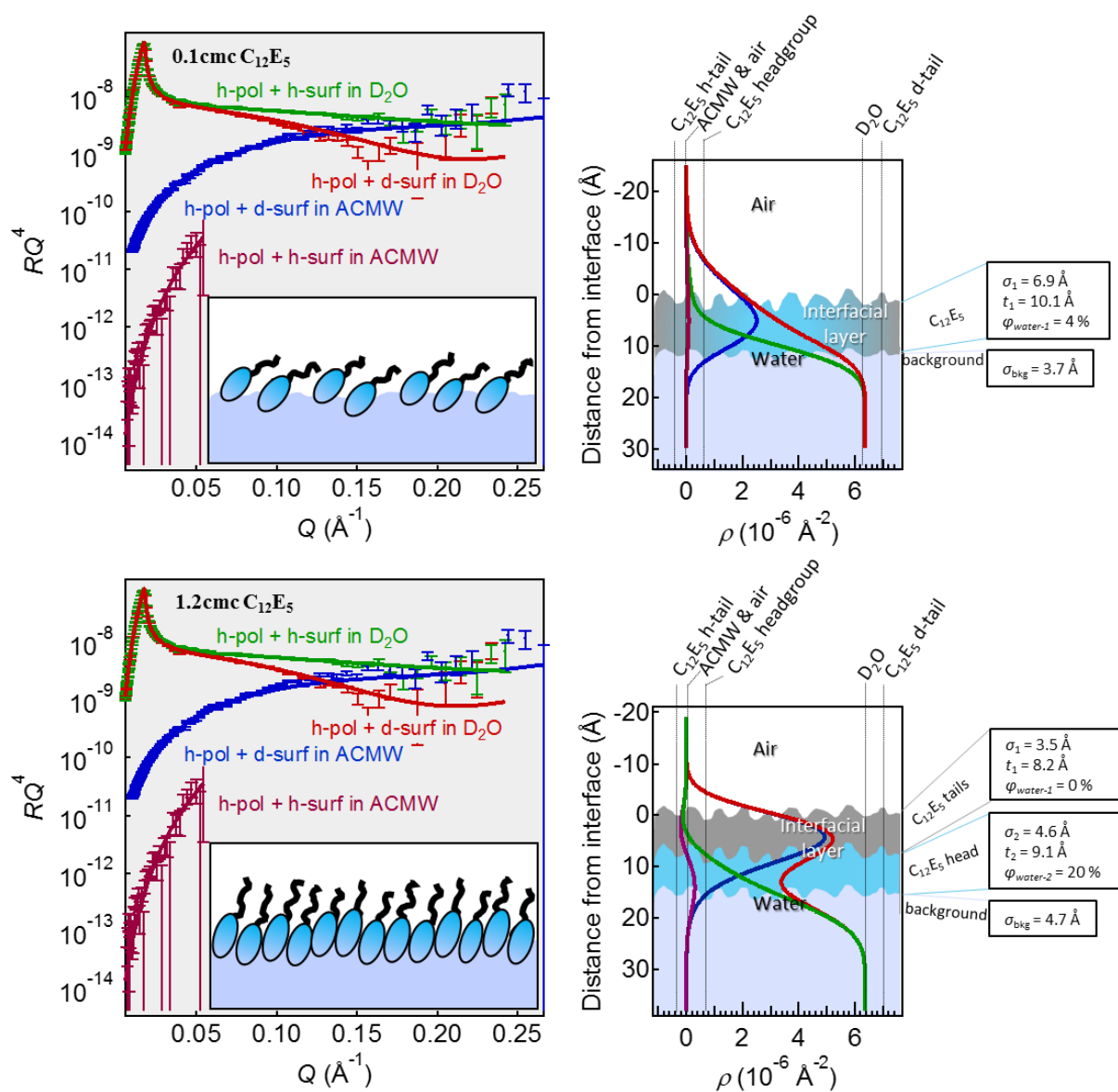


Figure E.1 Fitted NR data for 0.1 and 1.2 cmc $C_{12}E_5$, with the fitted ρ profiles and schematic representation based on the fitted parameters. The data is colour coded as follows: red represents dSDS in D_2O , green represents hSDS in D_2O , blue represents dSDS in ACMW, and purple represents hSDS in ACMW. The error bars associated with the data points were determined from the data reduction, larger at higher Q values due to lower contrast between the solvent and sample. The solid lines show the fitted curve, with the fitted parameters also shown, including thickness (t), solvent volume fraction (ϕ_{water}), and roughness of the layer (σ).

F. Supplementary material for Chapter 7

Gelation was observed after 5 cmc SDS was added to 25 mg mL⁻¹ DEEDMAC vesicular dispersion prepared by sonication at RT. The same concentration mixture but with the vesicles prepared by extrusion has shown a highly hazy and viscous dispersion. The 5 cmc SDS mixtures with 5 mg mL⁻¹ DEEDMAC vesicles prepared by both sonication and extrusion did not show any gel formation (Figure F.1).

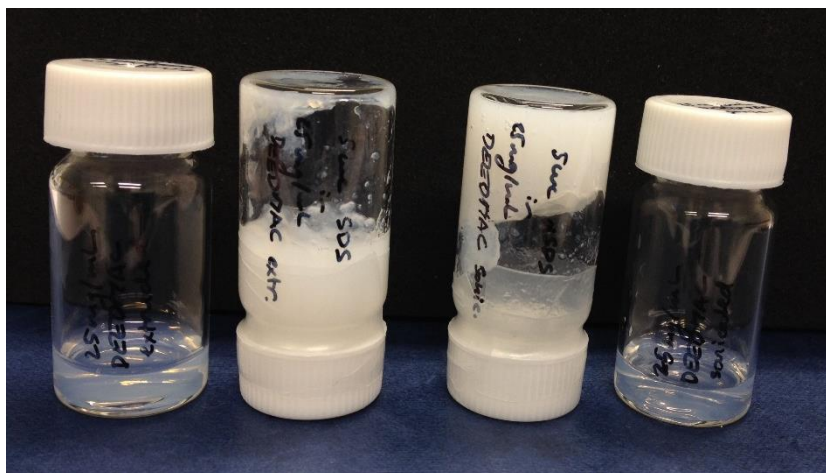


Figure F.1 Gelation of DEEDMAC vesicular dispersions with 5 cmc SDS.

An observation of highly rough and inhomogeneous structures formed on mica surfaces during an SFA experiment following addition of high SDS concentration to an adsorbed DEEDMAC bilayer (Figure F.2).

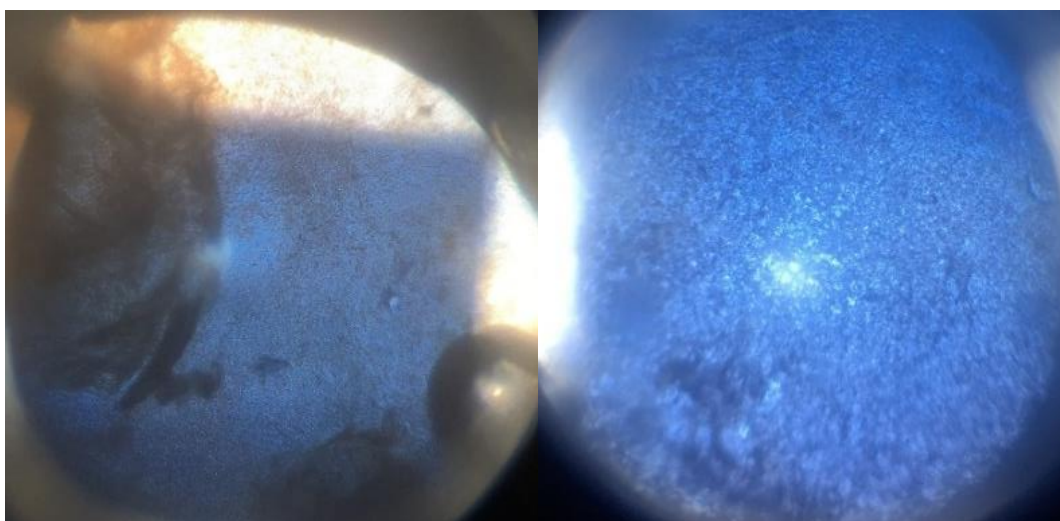


Figure F.2 Observation of rough and inhomogeneous DEEDMAC/SDS structures at mica-water interface.

Raw data collected for off specular NR from a sample of DEEDMAC/SDS mixture in D_2O . The high intensity peaks clearly show the critical edge and Bragg peaks, including the off-specular scatter (Figure F.3).

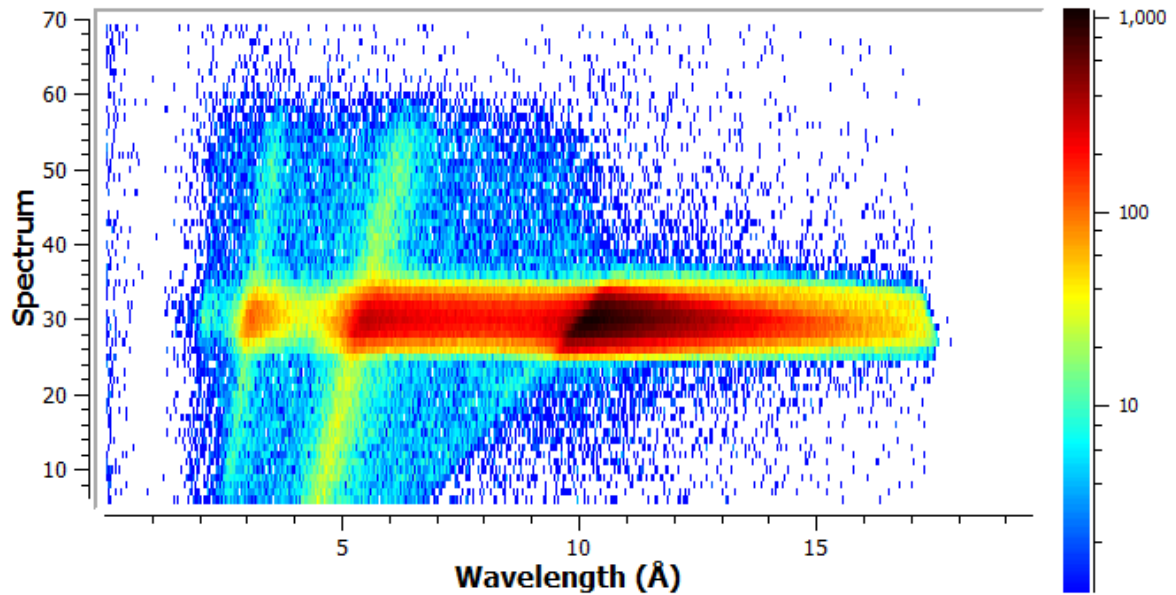


Figure F.3 Linear detector image of DEEDMAC/SDS complex in D_2O at the air-water interface.

